Component Dynamics in Miscible Polymer Blends and Block Copolymers(Dissertation_全文)

AUTHOR(S):

Chen, Quan

Component Dynamics in Miscible Polymer Blends and Block Copolymers

Doctor Thesis

by

Quan Chen

2011

Contents

Chapter 1 INTRODUCTION

1-1 Background

Almost all applications of polymers utilize polymer blends, copolymers, or composites, instead of pure homopolymers. Mixing of different polymers is one of the most efficient ways to tune the properties to meet the application needs. Thus, the dynamic feature of polymer blends has been an active subject in the field of polymer physics in the past two decades. [1-26]

Generally, the equilibrium state of a polymer blend composed of chemical different components, say A and B, is determined from the thermodynamics under a set of conditions, *e.g.*, the temperature T, the concentration w, and the molecular weight M of the A and B components.[27,28] For an A/B blend, the combinatorial entropy of components always favors mixing, but this contribution diminishes with increasing M and becomes almost negligible for high-M. Thus, the miscibility of the A/B pair is closely related to an interacting energy between A and B: the lower the interaction energy, the more favor for A and B to be in contact with each other. When the A/B interacting energy is less than a small positive critical value, E_{crit}, the A/B blend would be thermodynamically miscible. Thus, the phase behavior of the A/B blend strongly depends on a change of the interacting energy with the temperature. If an increase of temperature enhances the favorable A/B interaction and thus leads to an increase of miscibility, the phase behavior is referred to as the upper critical solution temperature (UCST) behavior. In contrast, if the increase of temperature reduces this interaction to give a lower miscibility, the low critical solution temperature (LCST) behavior prevails.[27,28]

The polymer blends in a miscible state have been known to exhibit unique and complex dynamic behavior not observed for pure homopolymers.[1-26] It is now well established that this behavior is related to a *dynamic heterogeneity* existing in different time and length scales.[1-26] The molecular picture of the dynamic heterogeneity can be further extended to disordered block copolymers if an effect of the block junction is properly incorporated.

This chapter summarizes the current understanding for the dynamic behavior of the miscible polymer blends and disordered block copolymers. The first part explains the molecular origin/mechanism of the dynamic heterogeneity. The second part shows how this dynamic heterogeneity is related to the component dynamics at the segmental scale (of several monomers) in the miscible polymer blends and disordered block copolymers. The third part considers the blending effect on the component dynamics at a larger scale in the miscible blend and disordered block copolymers, where several important open questions related to this thesis are outlined.

1-1-1 Molecular origin of dynamic heterogeneity

The heterogeneity is a general issue for all miscible polymer blends if the focus is placed on sufficient small length and time scales. Since a segment of A is *connected* to the other segments of A, it feels a local environment richer for A itself.[1,2,16] This effect is termed as the *self-concentration*, as schematically shown in Figure 1-1, where the circles represent the monomers (with their atomic details being not resolved in this illustration). Due to the chain connectivity, the local average volume fraction at the location of a monomer A (small white circle) changes from $\phi = 1$ in a volume comparable to the monomer size to the macroscopic average volume fraction $<\phi>$ in a volume (grey area) large enough to smear the local heterogeneity. Then, the motion of a *segment* composed of several monomers is controlled by the local effective volume fraction ϕ_{eff}, instead of the macroscopic $<\phi>$.

Lodge-Mcleish (LM) model[3,16] provides a simple theoretical idea for the effect of the chain connectivity explained above. This model assumes that the effective volume fraction ϕ_{eff} in a volume surrounding a segment A is contributed from both the self-concentration ϕ_{self} and the intermolecular volume fraction ϕ:

$$\phi_{eff}=\phi_{self} + (1 - \phi_{self})\phi \qquad (1\text{-}1)$$

The model further assumes that ϕ equals to the average volume fraction $<\phi>$ of the respective component in the system and ϕ_{self} is the volume fraction of A in one Kuhn segment occupying a volume $V = l_K^3$ (white area in Figure 1-1 shows this V). Here, l_K is Kuhn segment length serving as a unit length for the large scale Gaussian conformation of the chain.

Several comments need to be added here for the LM model. Firstly, the choice of $V = l_K^3$ is somehow *arbitrary*.[3,8] Extensive experimental results show that the actual length scale governing the segmental motion may deviate from l_k and depend on both the chemical structure of the components and their local interaction.[3, 5-15] In other words, there appears to be no simple universal rule that governs the length scale for the so-called segmental dynamics.[3] Moreover, the replacement of ϕ appealing in eq 1-1 by an average volume fraction $<\phi>$ may be a harmless approximation if the concentration fluctuation of the component chains is negligible. Nevertheless, this mean field nature may prevent the LM model from giving a reasonable prediction for some experimental results in particular at T close to the glass transition temperature of the components where the concentration fluctuation becomes siginificant.[3,18,19] Namely, ϕ may also fluctuate to some extent depending on

the relative length and time scales for the segmental dynamics and the concentration fluctuation. In relation to this point, there are some theoretical attempts to incorporate the concentration fluctuation mechanism into the LM model.[17,25] However, additional fitting parameters are needed to satisfactorily describe the dynamic feature revealed in experiments. Thus, at this stage, it seems reasonable to regard ϕ_{eff} as a fitting parameter that could vary from system to system.[3,8,24]

1-1-2 Effect of blending on segmental dynamics

The miscible polymer blends exhibit unique segmental dynamics:[1-26] *e.g.*, the broad glass transition process, the broad mode distribution of segmental dynamics, and a change of this distribution with temperature. In general, the segmental dynamics is related to a localized frictional environment and the broad mode distribution of this dynamics reflects a non-uniform frictional environment attributable to the dynamic heterogeneity. Thus, the dynamic heterogeneity can be conveniently studied through analyzing the segmental dynamics.

Experimentally, the component dynamics in the segmental scale can be resolved for model binary blends in which the two components have a large miscible window and different contributions to measurable properties. For example, the polyisoprene/poly (vinyl ethylene) (PI/PVE) system exhibits the LCST behavior but is statistically miscible in a wide range of T and thus has been frequently utilized as a model system.[9,10,11,13] Figure 1-2 shows the dielectric spectra of PI/PVE blend studied by Hirose et al.[9,10] In general, the dielectric relaxation detects the fluctuation of different types of dipoles in the system. For the PI/PVE blend, both components have the so-called type-B dipole perpendicular to the chain backbone and the fluctuation of type-B dipole is generally associated to the segmental motion. The PI chain also has the type-A dipole parallel along the chain backbones.[9,26,29] The sum of type-A dipoles over a chain is proportional to the end-to-end vector of the chain. Thus, the fluctuation of type-A dipole is activated by the global motion of the PI chains. (More detailed explanation of the type-A and B dipoles is given in Section 2-2-1-2.)

For the master curve shown in Figure 1-2, the dielectric dispersions seen at high, middle and low frequencies characterize the segmental motion of PI, the segmental motion of PVE, and the global motion of PI, respectively. The segmental dispersion of PI was faster than that of PVE. This feature could be explained on the basis of the self-concentration: Since the segments of either PI or PVE were in a dynamic environment locally condensed by themselves, the segmental dynamics of each component was biased toward its bulk behavior and PI having a lower glass transition

temperature, T_g, exhibited faster segmental dynamics than PVE having a higher T_g. ($T_{g,PI} \cong -70°C$; $T_{g,PVE} \cong 0°C$)

To construct the master curve shown in Figure 1-2, Hirose et al. shifted the dielectric data obtained at different T horizontally by a factor of a_T to allow a good superposition of dielectric dispersions at high and low frequencies corresponding to the segmental and global relaxation of PI.[9,26] However, this shift led to a failure of superposition for the middle dispersion corresponding to the segmental relaxation of PVE. This failure was partly attributed to the self-concentration effect, which resulted in different frictional coefficients, ζ, and accordingly the different temperature dependence of two components, and also to a magnified concentration fluctuation of PVE at low T.

The molecular picture of self-concentration and concentration fluctuation can be extended to the disordered diblock copolymers through incorporating an effect(s) of the block junction on the dynamic heterogeneity. The comparison of the dynamic behavior of the disordered diblock copolymer and that of the corresponding miscible polymer blend can elucidate this junction effect.[2,5,30-34] Figure 1-3 shows the DSC traces for PI/PVE blends and PI-PVE disordered diblock copolymers with the weight fraction of PVE, w_{PVE}, as indicated.[31,32] Clearly, the PI/PVE blend and the PI-PVE diblock copolymer having the same w_{PVE} exhibit almost indistriguishable glass transition processes. This thermal behavior reflects a dynamic similarity of the segments in the blend and copolymer, which was also observed dielectrically.[10] This dynamic similarity suggests a lack of the junction effect on the segmental dynamics of the copolymer. This lack was observed because most of the segments are too far from the block junction to be influenced by the junction.[2,8,33] (The junction effect can be enhanced by increasing the number of blocks and decreasing the block length.[5,34])

1-1-3 Effect of blending on chain dynamics

The dynamic heterogeneity should modify the dynamics over the chain dimension since the large-scale chain motion results from accumulation of the localized motion. At the same time, it is expected that the large-scale dynamics is not affected by the dynamic heterogeneity in a straightforward way noted for the segmental dynamics, because the local heterogeneity tends to be smeared in the large length and time scales corresponding to the motion of the whole chain.

To explain a hierarchinal dynamic behavior from the segmental to the whole chain level, the focus has been first placed on the simplest example, the homopolymer, and then on the polymer

blends and block copolymers thereby discussing the possible effects of the blending and the block junction.

For homopolymer, the large-scale (global) motion of a chain is quenched in a short time scale where the chain cannot be regarded as a continuous thread. In contrast, a given chain can be regarded as the thread composed of flexible motional units (referred to as subchains) in a time scale long enough for the thermal equilibration of these units. Then, the *friction* of the chain is defined as a sum of the subchain friction.[27]

At the same time, due to the threadlike nature, polymer chains are not allowed to cross each other. Thus, a chain is *topologically constrained* by the surrounding chains if the chains are sufficiently long and effectively packed in space.[29, 35-38] This type of topological constraint is referred to as *entanglement*. Mutually entangled chains can be regarded as a *network*. The network disturbs the lateral motion of the chain over a distance corresponding to the *network mesh size* and the motion of the chain over a large length scale is limited in a direction along the chain backbone. This type of *curvi-linear motion* along the main chain axis, termed as *reptation*, was first proposed by de Gennes.[35] Doi and Edwards extended this molecular picture by regarding the motion of a given chain in the network as being constrained in a *tube-like region* surrounding the chain, and taking the network mesh size as the *tube diameter*.[36] Thus, the *entanglement mesh size* and the *tube diameter* are interchangeably utilized, depending on the specific molecular picture being adopted.[29, 35-38]

For homopolymer, the chain dynamics is in principle predictable with the knowledge of (1) the size and frictional coefficient of the subchains, (2) the *end-to-end distance* of the chain, and (3) the entanglement mesh size/tube diameter.[29, 35-38] The dynamic picture for chain dynamics of the miscible polymer blends and the disordered copolymers is much more complex than that of the homopolymers, because either the thermal equilibration or the release of topological constraint requires a cooperative motion of two components having dynamic asymmetry (different frictional coefficients, for example). This complicated process is highlighted by three open questions specified below.

The first question is: could the chains of the same component feel a uniform frictional environment? For a long time, the term *dynamic heterogeneity* has been utilized to represent exclusively the frictional heterogeneity for *segmental dynamics*, and this dynamic heterogeneity has been considered to be effectively smeared in the global length scale comparable to the chain dimension unless T approaches the phase-separation point.[39] Nevertheless, recent experiments by

Watanabe and coworkers revealed that the dynamic heterogeneity could survive in the length and time scales of the *global* chain dynamics in highly-miscible polymer blends.[40]

Watanabe and coworkers had investigated the dynamic behavior for polyisoprene (PI) and poly (*p-tert* butyl styrene) (PtBS) blend.[40] They chose this blend because of the following features: (1) PI and PtBS exhibit the LCST-type phase behavior but have a surprisingly wide miscible window. Phase separation occurs only at inaccessibly high $T > 250°C$ even for PI and PtBS having the molecular weights $M \cong 10^5$. (2) PI and PtBS have very different glass transition temperatures in bulk state, $T_{g,PI} \cong -70°C$ and $T_{g,PtBS} \cong 150°C$. This difference of bulk T_g is much larger than that for the pair of PI and PVE being extensively studied ($T_{g,PVE} \cong 0°C$).[1,2,4,9,10,13,24,43,44] The large contrast of T_g should result in a strong dynamic asymmetry for the PI and PtBS components in the miscible state. (3) PI has the type-A dipole while PtBS does not. Then, the dielectric relaxation at low frequencies exclusively detects the global motion of PI.

Watanabe and coworkers[40] had noted that the dielectric spectrum corresponding to the global motion of PI broadened with decreasing T, as shown in Figure 1-4. This behavior is obviously different from that of PI/PVE blend shown in Figure 1-2, for which the global motion of PI at different T gave the same dielectric mode distribution. Watanabe and coworkers attributed this broadening to a non-uniform frictional environment for the global motion of PI. Namely, in the PI/PtBS blend, the global motion of PtBS was slower than that of PI. The concentration fluctuation of PtBS was effectively quenched in a time scale of the global motion of PI thereby giving a spatial, frictional heterogeneity for this motion.[40,42] Then, some PI chains were located in a PtBS-rich region to feel a higher friction compared to the other PI chains, leading to the broadening of the dielectric dispersion for the PI chains as a whole ensemble. A decrease of temperature tends to enhance the dynamic asymmetry between PI and PtBS thereby magnifying the degree of broadening.

This finding widens the perspective of dynamic heterogeneity in miscible polymer blends, and intrigues further thoughts on how this heterogeneity is related to the concentration, the chain dimension, and the contrast of effective glass transition temperatures of two components. It is highly desired to understand these relationships.

The second question related to the blending effect is: what is the entanglement mesh size for a given component in a miscible polymer blend? For polymeric liquids, the entanglement mesh size could be resolved experimentally through detecting the *plateau modulus* in a time scale where the local thermal equilibration has been achieved over the strand between the topological constraints while these constraints have not yet relaxed.[29,45,46] Then, a sequence of the equilibrated monomeric

segments behave as a coarse-grained segment referred to as the *entanglement segment*. The plateau modulus, G_N, measures a number density of these entanglement segments. The relationship between the plateau modulus G_N and the molecular weight of the entanglement segment M_e is given on the basis of the classical theory of entropy elasticity of rubbers as:[29,45,46]

$$G_N = \frac{\rho RT}{M_e} \tag{1-2}$$

Here, ρ, R, and T represent the polymer concentration (=density for bulk polymer), the gas constant, and the absolute temperature, respectively. For miscible polymer blend, it is probably more convenient to take the average length of entanglement strands a ($\propto M_e^{0.5}$ for Gaussian chains), not M_e, as a fundamental parameter since two components may have different density of chain backbone but still adopt the same entanglement length a.

The length a has been hardly investigated for miscible polymer blends. Namely, the value of a has been experimentally determined only for miscible blends for which two components have similar a values in their bulk, *e.g.*, systems polyisoprene/poly (vinyl ethylene)[43,44] (PI/PVE, a_{PI}^{bulk} = 5.8nm, a_{PVE}^{bulk} = 5.1nm)[47] and polyisoprene/polybutadiene[48,49] (PI/PB, a_{PI}^{bulk} = 5.8nm, a_{PB}^{bulk} = 4.7nm)[47], or for the blends of PI/PB and polystyrene/poly(vinyl methyl ether) (PS/PVME) in which one component has a low molecular weight and relaxed rapidly thereby behaving as a diluent for the other component in the experimental window examined.[50, 51] For the former case, different mixing rules of the entanglement mesh size give very similar a values between the a^{bulk} values of two bulk components. Thus, the test of mixing rule of a has not been well-settled. For the latter case, the experiments actually detected the average length of the topological constraints among the slower component chains, instead of the whole blend, and no details of the mixing rule have been resolved. Thus, a more informative test for a in the miscible blends should be made under the condition (1) two bulk components have a large contrast of a_{PI}^{bulk} and (2) the chains of both components are sufficient long so that the plateau can be well observed in a wide range of frequency (where the entanglement segment has been thermally equilibrated but the components have not relaxed globally).

It should be emphasized that the topological constraint is not a static issue but a dynamic issue. For a miscible polymer blend composed of the dynamically asymmetric components, the local motion of one component having a higher mobility may be somehow disturbed by the other slow component, and this type of constraint could emerge at various length scales even smaller than a.

This mechanism, being absent in homopolymers, may further complicate the relaxation behavior of each component in a miscible blend.

The third question focuses on the role of the junction point of the disordered block copolymer: how does the block junction influence the chain dynamics for disordered copolymers? As explained in Section 1-1-2, the junction effect on the segmental dynamics is almost negligible for the PI-PVE diblock copolymers, because most of the segments are sufficiently far away from the junction. Nevertheless, it is expected that the global motion of a block copolymer is strongly influenced by the junction since the junction forces the constituent blocks to move cooperatively.

This expectation is in harmony with the global dynamics observed for PI-PVE copolymers and PI/PVE blends. For the PI/PVE blends, the dynamic heterogeneity in the segmental scale appeared to result in different temperature dependence of the terminal relaxation processes of the components so that the viscoelastic relaxation mode distribution of the blend as a whole changed with T.[2,4,7,9,10,13] In contrast, the mode distribution of the PI-PVE was (approximately) insensitive to T,[10,30,33] leading to a qualitative interpretation that the block junction forced the PI and PVE blocks to relax cooperatively.

However, the molecular picture of this cooperative motion may fail if one block has a large segmental friction and exhibits much slower motion compared to the other block. For this case, the slow block would behave effectively as an immobilized anchor for the fast block thereby forcing the latter to relax as a tethered chain. In other words, the disordered copolymer chain may be regarded as a free linear chain relaxing through the cooperative motion of the constituent blocks only when the frictional contrast between these blocks is sufficiently small.

1-2 Scope of this doctoral thesis

Concerning the three questions asked in the previous section, this thesis makes a detailed investigation of the dynamic behavior of miscible blends and disordered copolymer composed of PI and PtBS having a large contrast not only for T_g but also for the entanglement mesh size a^{bulk} (= 5.8nm for PI and 11.7nm for PtBS). The object of this thesis is threefold. Namely, this thesis relates the dynamic heterogeneity for the global motion of PI quantitatively to the chain dimension, concentration, and frictional contrast of two components, makes a quantitative test for different mixing rules of a, and examines the junction effect on dynamic behavior of a PI-PtBS diblock copolymer.

Chapter 2 summarizes the methods of synthesizing and characterizing the samples as well as the principle(s) and operation(s) of the physical measurements.

In Chapter 3, linear viscoelastic and dielectric behavior of PI and PtBS in bulk state is discussed in terms of the modes of motion. The data for polystyrene (PS) are also examined for comparison. Specifically, the focus is placed on the viscoelastic relaxation mode distribution related to the entanglement. This mode distribution serves as a basis for understanding the slow dynamics of PI and PtBS in the blends.

Chapter 4 investigates the entanglement length, a, in the PI/PtBS blends composed of high-M PI and PtBS samples. The PI and PtBS chains behave as the fast and slow (low- and high-friction) components and are well entangled with each other. The relaxation dynamics of these chains changed significantly with temperature T. At high T, the blend exhibited two-step entanglement plateau of the storage modulus $G'(\omega)$, and the plateaus at high and low angular frequencies (ω) were attributed to the entanglement among all component chains (before the relaxation of PI chains) and that between the PtBS chains (after the relaxation of PI chains), respectively. The modulus at the high-ω plateau was well discribed by a simple mixing rule weighing a by the number fraction of the Kuhn segments of the components. At low T, the blend exhibited the power-law behavior of storage and loss moduli, $G' = G'' \propto \omega^{1/2}$, in the range of ω where the high-ω plateau was supposed to emerge. This lack of the high-ω plateau was attributed to retardation of the thermal equilibration of the PI chain over the entanglement length a due to the hindrance from the slow PtBS chains: The PI and PtBS chains appeared to be equilibrated *cooperatively/simultaneously* at a rate essentially determined by PtBS, and the PI chains relaxed soon after this equilibration thereby giving the plateau region too narrow to be detected.

Chapters 5 and 6 are devoted for the dynamic heterogeneity and the corresponding relaxation behavior of PI and PtBS therein. The dynamic heterogeneity in the PI/PtBS blends (explained in Figure 1-4) is related to both dimensional and frictional contrast between the PI and PtBS chains therein. Chapters 5 and 6 attempt to examine the effects of these two types of contrast separately.

Chapter 5 investigates the dynamic behavor of PI/PtBS blends composed of the same pair of PI and PtBS (having the same dimensional contrast) but with different compositions. The focus is placed on a relationship between the frictional contrast and the dynamics of PI and PtBS under the influence of the dynamic heterogeneity. The PI chains appeared to be in a frictionally non-uniform environment and can be regarded as two species: the majority of PI that governs the dielectric peak, and the minority of PI relaxing much slower than the majority. The minority appeared to interact with locally concentrated PtBS chains thereby being responsible for the broadening of the dielectric

mode distribution. A difference of the relaxation rates of the majority and minority, as well as the composition of the slow minority, decreased on a reduction of the frictional contrast between PI and PtBS, *i.e.*, on increases of T and/or the PI concentration C_{PI}. In contrast, the relaxation mode distribution of PtBS did not change with T and C_{PI}, possibly because the fast motion of PI chains smeared the dynamic heterogeneity to allow the PtBS chains to feel a uniform frictional environment. Furthermore, the relaxation of PI and PtBS chains was found to be slower compared to the relaxation in respective iso-frictional bulk states. The retardation of the PI relaxation was in accordance with the molecular picture that the PI chains are forced to *cooperatively/ simultaneously* equilibrated with the slower PtBS chains over the entanglement mesh size (as explained in Chapter 4). The retardation of the PtBS relaxation was different from that expected from the ordinary entanglement effect. A new molecular mechanism referred to as *pseudo-constraint release* mechanism was proposed to explain this difference: the moderately overlapped PtBS chains are stitched/entangled by a PI chain, and the relaxation of the PtBS chains is possibly activated by the PI chain motion.

Chapter 6 investigates the dynamic behavior of PI/PtBS blends with a fixed composition (having the same frictional contrast for two components at a given T) but having different molecular weights of the components. As described in Chapter 5, the PI chains appeared to exhibit the ordinary entanglement relaxation affected by the frictional heterogeneity as well as by the topological constraint from the slow PtBS chains. In the blends containing the same PtBS chains and at a given T, the PI chains with larger M_{PI} exhibited a relaxation mode distribution closer to that in the bulk state, which suggested a more uniform frictional environment for PI chains having larger M_{PI}. This result is in accord to an expectation that the dynamic heterogeneity is smeared over a large length and in a long time scale. In contrast, the PtBS chains exhibited no ordinary entanglement relaxation associated with a plateau of the storage moduli. Instead, the PtBS chains exhibited the relaxation that is similar in the mode distribution but much slower compared to the PtBS relaxation in a non-entangled solution in an iso-frictional state. This retardation was again attributable to the *pseudo-constraint release* mechanism proposed in Chapter 5.

Chapter 7 examines the dynamic feature for a PI-PtBS diblock copolymer. The dielectric spectra detecting the global motion of the PI block broadened significantly with decreasing T. Since the PI and PtBS blocks behaved as the fast and slow blocks at low T while these blocks exhibited equally fast motion at high T, this complexity was related partly to the dynamic frictional heterogeneity for the PI block resulting from this motional difference of the blocks. Nevertheless, it turned out that the complexity was more importantly related to the connectivity between the PI and PtBS blocks: Namely, the PI block essentially behaved as a tethered chain at low T (where the slow

PtBS block effectively anchored the PI block) while the two blocks behaved as portions of a free linear chain at high *T* (where this anchoring effect almost vanished). This change in the motional mode of the PI block appeared to dominate the change of the dielectric relaxation spetra characterizing the global motion of the PI block.

Finally, Chapter 8 gives a summary of this thesis.

References

1. Chung, G. C.; Kornfield, J. A.; Smith, S. D. *Macromolecules* **1994**, 27, 964-973.
2. Chung, G. C.; Kornfield, J. A.; Smith, S. D. *Macromolecules* **1994**, 27, 5729-5741.
3. Colmenero, J.; Arbe, A. *Soft Matter* **2007**, 3, 1474-1485.
4. Haley, J. C.; Lodge, T. P.; He, Y. Y.; Ediger, M. D.; von Meerwall, E. D.; Mijovic, J. *Macromolecules* **2003**, 36, 6142-6151.
5. He, Y. Y.; Lutz, T. R.; Ediger, M. D. *Macromolecules* **2003**, 36, 8040-8048.
6. He, Y. Y.; Lutz, T. R.; Ediger, M. D. *Macromolecules* **2004**, 37, 9889-9898.
7. He, Y. Y.; Lutz, T. R.; Ediger, M. D.; Ayyagari, C.; Bedrov, D.; Smith, G. D. *Macromolecules* **2004**, 37, 5032-5039.
8. He, Y. Y.; Lutz, T. R.; Ediger, M. D.; Pitsikalis, M.; Hadjichristidis, N.; von Meerwall, E. A. *Macromolecules* **2005**, 38, 6216-6226.
9. Hirose, Y.; Urakawa, O.; Adachi, K. *Macromolecules* **2003**, 36, 3699-3708.
10. Hirose, Y.; Urakawa, O.; Adachi, K. *Journal of Polymer Science Part B-Polymer Physics* **2004**, 42, 4084-4094.
11. Pathak, J. A.; Colby, R. H.; Floudas, G.; Jerome, R. *Macromolecules* **1999**, 32, 2553-2561.
12. Pathak, J. A.; Colby, R. H.; Kamath, S. Y.; Kumar, S. K.; Stadler, R. *Macromolecules* **1998**, 31, 8988-8997.
13. Pathak, J. A.; Kumar, S. K.; Colby, R. H. *Macromolecules* **2004**, 37, 6994-7000.
14. Alegria, A.; Colmenero, J.; Ngai, K. L.; Roland, C. M. *Macromolecules* **1994**, 27, 4486-4492.
15. Urakawa, O. *Nihon Reoroji Gakkaishi* **2004**, 32, 265-270.
16. Lodge, T. P.; McLeish, T. C. B. *Macromolecules* **2000**, 33, 5278-5284.

17. Leroy, E.; Alegria, A.; Colmenero, J. *Macromolecules* **2003**, 36, 7280-7288.
18. Arbe, A.; Alegria, A.; Colmenero, J.; Hoffmann, S.; Willner, L.; Richter, D. *Macromolecules* **1999**, 32, 7572-7581.
19. Cendoya, I.; Alegria, A.; Alberdi, J. M.; Colmenero, J.; Grimm, H.; Richter, D.; Frick, B. *Macromolecules* **1999**, 32, 4065-4078.
20. Haley, J. C.; Lodge, T. P. *Journal of Rheology* **2004**, 48, 463-486.
21. Aparicio, R. P.; Arbe, A.; Colmenero, J.; Frick, B.; Willner, L.; Richter, D.; Fetters, L. J. *Macromolecules* **2006**, 39, 1060-1072.
22. Lutz, T. R.; He, Y. Y.; Ediger, M. D.; Cao, H. H.; Lin, G. X.; Jones, A. A. *Macromolecules* **2003**, 36, 1724-1730.
23. Min, B. C.; Qiu, X. H.; Ediger, M. D.; Pitsikalis, M.; Hadjichristidis, N. *Macromolecules* **2001**, 34, 4466-4475.
24. He, Y. Y.; Lutz, T. R.; Ediger, M. D.; Lodge, T. P. *Macromolecules* **2003**, 36, 9170-9175.
25. Shenogin, S.; Kant, R.; Colby, R. H.; Kumar, S. K. *Macromolecules* **2007**, 40, 5767-5775.
26. Watanabe, H.; Urakawa, O. *Korea-Australia Rheology Journal* **2009**, 21, 235-244.
27. Eitouni, H.B.; Balsara, N.P., *Thermodynamics of Polymer Blends*, 2nd ed.; Mark, J. E., Ed.; Springer: New York **2007**; Chapter 19, pp 339-356.
28. Paul, D.R., Buchnail, C.B., Polymer Blends, *Volume 1:Formulation*; John Wiley & Sons, New York **2000**; Chapter 1, pp 1-14.
29. Watanabe, H. *Prog. Polym. Sci.* **1999**, 24, 1253-1403.
30. Arendt, B. H.; Krishnamoorti, R.; Kannan, R. M.; Seitz, K.; Kornfield, J. A.; Roovers, J. *Macromolecules* **1997**, 30, 1138-1145.
31. Roovers, J.; Toporowski, P. M. *Macromolecules* **1992**, 25, 3454-3461.
32. Roovers, J.; Wang, F. J. *Non-Crystalline Solids* **1994**, 172, 698-704.
33. Kanetakis, J.; Fytas, G.; Kremer, F.; Pakula, T. *Macromolecules* **1992**, 25, 3484-3491.
34. He, Y. Y.; Lutz, T. R.; Ediger, M. D.; Lodge, T. P. *Macromolecules* **2003**, 36, 9170-9175.
35. de Gennes PG. *J Chem Phys* **1971**, 55, 572 – 579.
36. Doi, M.: Edwards, S. F. *The Theory of Polymer Dynamics*, Oxford University Press: New York,**1986**.
37. Graessley, W. W. *Adv. Polym. Sci.* **1982**, 47, 67-117.
38. McLeish, T. C. B. *Adv. Phys.* **2002**, 51, 1379-1527.
39. Rizos, A. K.; Fytas, G.; Semenov, A. N. *J. Chem. Phys.* **1995**, 102, 6931-6940.
40. Watanabe, H.; Matsumiya, Y.; Takada, J.; Sasaki, H.; Matsushima, Y.; Kuriyama, A.; Inoue, T.; Ahn, K. H.; Yu, W.; Krishnamoorti, R. *Macromolecules* **2007**, 40, 5389-5399.
41. Yurekli, K.; Krishnamoorti, R. *Journal of Polymer Science Part B-Polymer Physics* **2004**, 42, 3204-3217.

42. Takada, J.; Sasaki, H.; Matsushima, Y.; Kuriyama, A.; Matsumiya, Y.; Inoue, T.; Watanabe, H. *Nihon Reoroji Gakkaishi* **2007**, 35, 221-224.
43. Zawada, J.A.; Fuller G.G., Colby R.H.; Fetters L.J., Roovers J. *Macromolecules* **1994**, 27 (23), 6851-6860
44. Zawada, J.A.; Fuller G.G., Colby R.H.; Fetters L.J., Roovers J. *Macromolecules* **1994**, 27 (23), 6861-6870
45. Ferry, J. D., *Viscoelastic Properties of Polymers*, 3rd ed. Wiley: New York, **1980**.
46. Graessley, W.W., *Polymeric Liquids & Networks: Dynamics and Rheology*, Garland Science: New York, **2008**.
47. Fetters, L. J.; Lohse, D. J.; Colby, R.H. *Chain Dimensions and Entanglement Spacings, in Physical Properties of Polymers Handbook*, 2nd ed.; Mark, J. E., Ed.; Springer: New York **2007**; Chapter 25, pp 445-452.
48. (a)Watanabe, H.; Yamazaki, M.; Yoshida, H.; Adachi, K.; Kotaka, T. *Macromolecules* **1991**, 24 (19), 5365-5371 (b) Watanabe, H.; Yamazaki, M.; Yoshida, K.; Kotaka, T. *Macromolecules* **1991**, 24 (19), 5372-5379
49. Watanabe, H.; Urakawa, O.; Yamada, H.; Yao, M.L. *Macromolecules* **1996**, 29 (2), 755-763.
50. Yang, X.P.; Wang, S.Q.; Ishida, H. *Macromolecules* **1999**, 32 (8), 2638-2645.
51. Kitade, S.; Ochiai, K.; Ida, M.; Takahashi, Y.; Noda, I. *Polymer J.* **1997**, 29 (12), 1034-1036.

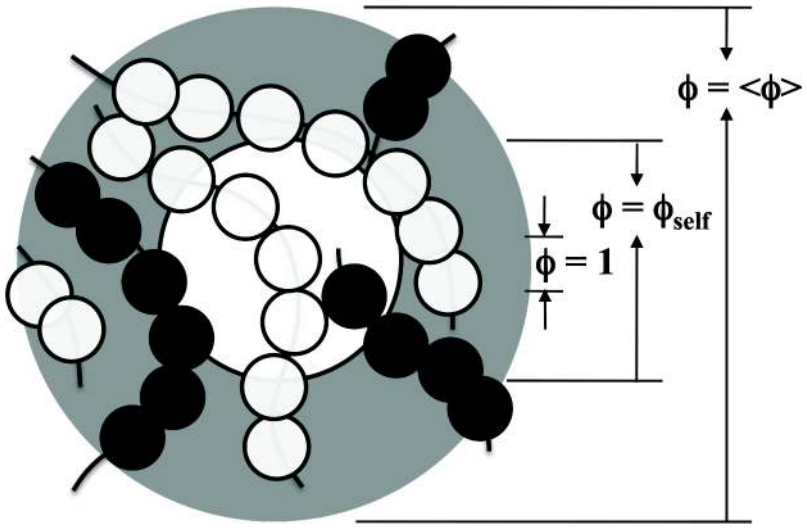

Fig. 1-1: Schematic illustration of chain connectivity effect in miscible blends of the component chains A (white) and B (black). The white and grey areas, respectively, show the volumes corresponding to the Kuhn segment length and a macroscopic length scale, with the latter being large enough to smear the the local heterogeneity.

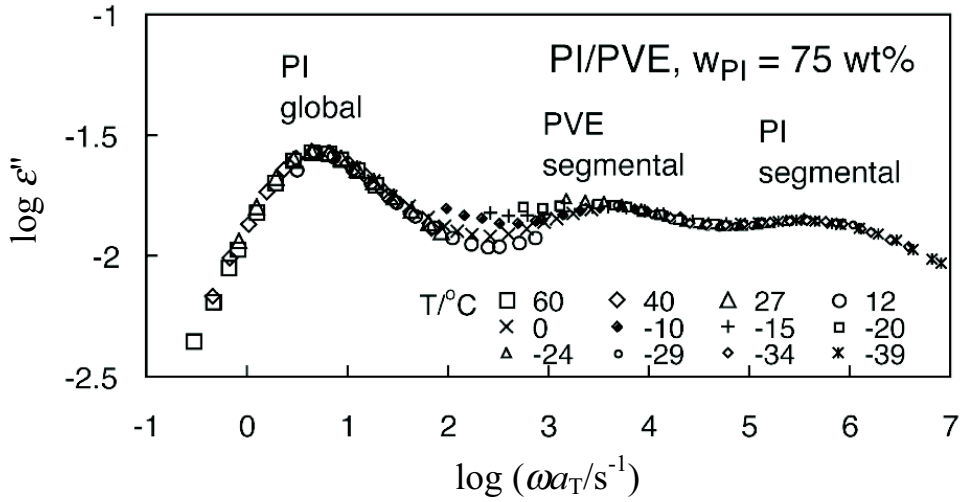

Fig. 1-2: Dielectric loss ε" of PI115/PVE602 blend with weight concentration of PI w_{PI} = 75wt%.[9,15] The raw ε" data are shifted along ω axis so that the superposition is achieved for low-ω and high-ω dielectric dispersions corresponding to the segmental and global dynamics of PI, respectively. The sample code numbers indicate the molecular weights in unit of 10^2.

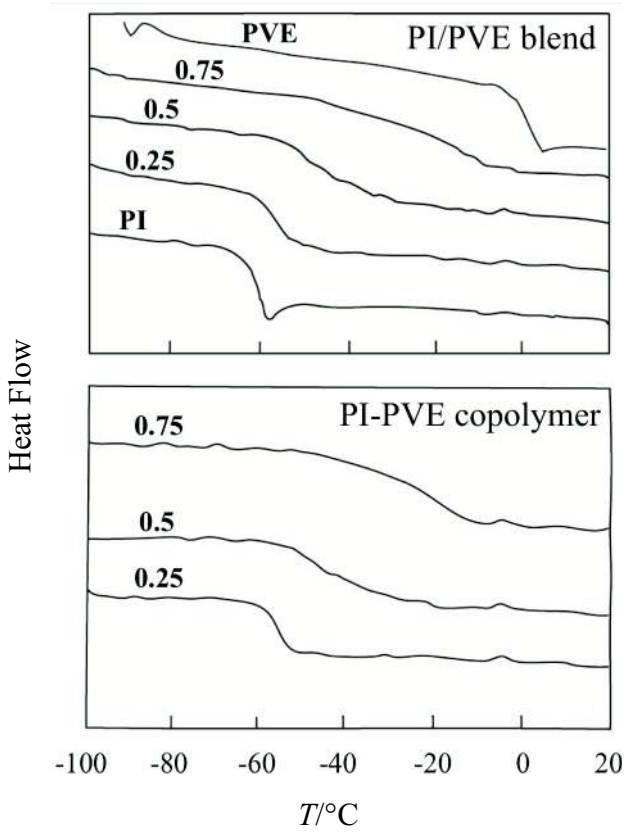

Fig. 1-3: Comparison of DSC traces of PI/PVE blends and PI-PVE copolymers having various weight fractions of PVE, w_{PVE} (numbers in the figure).[31,32] The profiles of bulk PVE and PI are also shown for comparison.

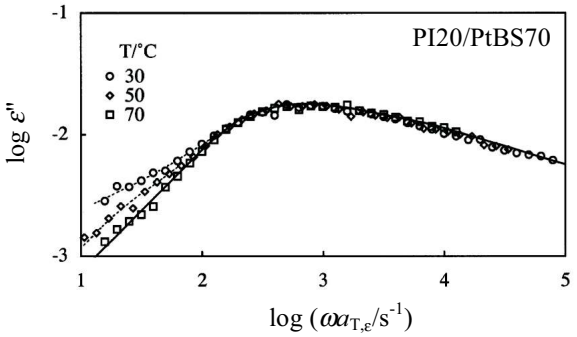

Fig. 1-4: Comparison of dielectric loss ε'' of the miscible PI20/PtBS70 blend with the PI composition of w_{PI} = 80wt% at different T.[40] The ε'' data at 50 and 70°C are shifted along ω axis by a factor of $a_{T,\varepsilon}$ to be compared with that at 30°C. The code numbers indicate the molecular weights in unit of 10^3.

Chapter 2 PRINCIPLES AND EXPERIMENTAL METHODS

2-1 Materials

The PI and PtBS samples as well as a PI-PtBS copolymer sample utilized in this thesis were synthesized anionically through high vacuum techniques with glass constrictions/breakable seals, except a commercially available PI20 sample (from Kuraray Co). Benzene and *sec*-butyllithium were utilized as the solvent and initiator, respectively. In the synthesis of the copolymer, the PtBS block anion was firstly polymerized and split into two portions, one being terminated with methanol to recover the precursor PtBS sample, and the other being copolymerized with isoprene monomer to give the desired PI-PtBS diblock sample.

These samples were characterized with gel-permeation chromatography (GPC) (Co-8020 and DP-8020, Tosoh) equipped with a refractive index (RI)/low-angle light scattering (LALS) monitor (LS-8000, Tosoh Co.) and a ultra-violet (UV) adsorption monitor (UV-8020). Tetrahydrofuran (THF) was utilized as the eluent. The weight-average molecular weight M_w of the PtBS samples, including the percursor of the PI-PtBS copolymer, was determined from the LALS/RI signals, where standard PS samples (Tosoh Co., TSK's) and/or a PtBS sample synthesized/characterized previously were utilized as references.[1,2] M_w of PI was determined by the elution volume calibration, with monodisperse PI samples[3-9] with known M_w being utilized as the elution standards. For the PI-PtBS copolymer sample, the PI content w_{PI} was determined from the RI/UV signals, with the well-characterized PtBS and PI samples being utilized as RI/UV references. The molecular weight of the PI block of the copolymer was evaluated from this w_{PI} and the precursor PtBS molecular weight $M_{w,PtBS}$ (=PtBS block molecular weigth) as $M_{PI} = w_{PI}M_{w,PtBS}/(1-w_{PI})$. The polydispersity indices M_w/M_n of the PI, PtBS and PI-PtBS samples were evaluated from the elution volume calibration, by utilizing the monodisperse PI samples as the standards for the PI and PI-PtBS samples, and the previously synthesized PtBS sample as the standard for the PtBS samples.

The microstructure of the PI samples (dissolved in deuterated chloroform) was determined from ^{1}H-NMR. A Varian MERCURYplus AS400 spectrometer was operated at a static magnetic field of 9.4 T and the resonance frequency of 400.0 MHz. The structure was (almost) the same for PI samples and PI blocks of PI-PtBS samples studied in this thesis, *i.e.*, 1,4-*cis* : 1,4-*trans* : 3,4 = 78:14:8. This microstructure allows PI to be miscible with PtBS at all temperatures ($\leq$ 200°C) examined in this thesis.

The PI/PtBS blends were prepared according to the previous method reported by Yurekli and Krishnamoorti.[10] Prescribed masses of PI and PtBS were dissolved in THF at a total concentration

of about 10wt% and then precipitated in a drop-wise way into an excess methanol/acetone (8wt/2wt) mixture vigorously stirred by a magnetic bar. The blends were recovered *via* decantation and thoroughly dried under vacuum first at room temperature and then at 80-140°C. The blends thus prepared were transparent, which was in accordance with the PI/PtBS miscibility.

2-2 Measurements

In general, the dynamic behavior of polymer chains at different length and time scales can be detected physically through different experimental methods, *e.g.*, the viscoelastic, dielectric, rheo-optical, and nuclear magnetic resonance (NMR).[11-14] One common strategy of these techniques is to apply an excitation/perturbation and to record a corresponding response that reflects the dynamics of the molecules in a specfic range of time and length scales. For a sufficiently weak excitation, the conformation of the polymer chains is just slightly altered from the equilibrium conformation so that the response reflects the equilibrium dynamics of the chains.

Molecular understanding of such response is made on the basis of expressions of physical quantities in terms of the conformational variables of polymer chains. This expression is summarized below for the viscoelastic and dielectric relaxation functions. The details of the experiments are then summarized from two aspects: (1) the concepts and instruments of the measurements, and (2) some basic aspects in the analysis of the data obtained from these measurements.

2-2-1 Molecular expression of relaxation functions

2-2-1-1 Viscoelastic relaxation function

In viscoelastic measurements, a deformation is applied and a corresponding stress is recorded. For a small shear strain γ, the resulting stress $\sigma(t)$ as a function of time t reflects the equilibrium thermal motion of the polymer chains. The relaxation modulus, being independent of the small γ, is referred to as the linear relaxation modulus:

$$G(t) \equiv \sigma(t)/\gamma \tag{2-1}$$

Figure 2-1 shows the relaxation behavior typically observed for monodisperse linear homopolymers.[15] The glassy zone, the glass-to-rubber transition, and the terminal relaxation (flow) zone are observed with increasing time scale. For linear polymers with small molecular weight M, the

terminal relaxation immediately follows the glass-to-rubber transition zone. In contrast, for linear polymers with M higher than a critical value M_c, the rubbery plateau emerges and then the terminal relaxation follows. Here, M_c characterizes the onset of the topological constraint (entanglement) due to the uncrossability of the polymer chains, as explained earlier in eq 1-2.

The molecular interpretation of the linear relaxation modulus is based on the relationship between the conformational variables and the stress. Obviously, the length scale of the thermal motion increases with an increase of time scale of the focus.[15] In a very short time scale, the polymer chain motion is not fully activated and the chain can not be regarded as a continuous thread. Instead, the monomeric segments can be regarded as the mobile planar objects and the origin of the stress is known to be the anisotropy of their planar orientation (orientation of the normal axis of the monomeric plane) as well as distortion of the local atomic packing under the strain.[16-21] The modulus having this molecular origin is referred to as the glassy modulus.

In contrast, in a longer time scale, the motion of the monomeric segments occurs actively to equilibrate successive monomeric segments. Then, the internally equilibrated sequence of the monomeric segments can be coarse-grained as a larger, flexible motional unit for the large-scale motion of the chain. This type of coarse-grained motional unit is referred to as *subchain* or *Rouse segment*. (The Rouse segment, defined as a statistical segment, is composed of ~10 monomeric segments.)[22-24] The hierachinal structure from the monomeric segments to the subchains and to the chain is schematically illustrated in Figure 2-2.[15]

The subchain behaves as an *entropic Gaussian spring* to exhibit a thermal tension $\boldsymbol{f}$ along its end-to-end vector $\mathbf{u}$: $\boldsymbol{f} = -\kappa\mathbf{u}$ where κ is the spring constant given by $\kappa = 3k_BT/gb^2$ with k_B, T, g, and b being the Boltzmann constant, the absolute temperature, the number of monomeric segments per subchain, and the effective step length of the monomeric segment, respectively.[13,14,25] (gb^2 is the mean-square average of $\mathbf{u}$ at equilibrium.)

For monodisperse polymer chains each composed of N subchains, the sum of the thermal tension of the subchains gives the stress tensor:[13,14]

$$\boldsymbol{\sigma}_{\text{chain}} = 3\nu Nk_BT\left\{\frac{1}{N}\sum_{n=1}^{N}\mathbf{S}(n,t)\right\} - p\mathbf{I} \tag{2-2a}$$

with

$$\mathbf{S}(n,t) = \left\langle \frac{\mathbf{u}(n,t)\mathbf{u}(n,t)}{gb^2} \right\rangle \tag{2-2b}$$

Here, ν is the chain number density, **I** is the unit tensor, p is the isotropic pressure, **u**(n,t) is the end-to-end vector of nth subchain at time t, **uu** denotes a dyadic of **u** (with its ij component being given by $u_i u_j$), and <…> represents the average taken over all chains.

The end-to-end vectors of the subchains have distributions in their length and orientation. Eq 2-2 clearly indicates that the deviatoric part (measurable part) of the stress tensor due to the entropy elasticity of the polymer chains, hereafter referred to as the polymeric stress, reflects the orientational anisotropy of the subchains specified by the configuration tensor **S**(n,t).[26] Consequently, the polymeric stress relaxes, even though the material keeps its distorted shape (*e.g.*, sheared shape), when the orientational anisotropy induced by the applied strain relaxes through the thermal motion of the chains. (In this relaxed state, **S**(n,t) is equal to **I**/3 and the subchain tension is transmitted isotropically in all directions to balance with the isotropic pressure.) Thus, the viscoelastic relaxation time of the polymeric liquids is identical to the orientational relaxation time of the chains therein.

A comment needs to be added for the stress expression, eq 2-2. At first sight, the stress given by eq 2-2 may appear to change according to the choice of the subchain size. However, this is not the case: Eq 2-2 gives the same stress irrespective of the subchain size given that the chosen subchain has been internally equilibrated in the time scale of the focus.[13,26]

It is noteworthy that the configuration tensor **S**(n,t) defined by eq 2-2b is a purely structural quantity and its average $(1/N)\Sigma_{n=1}^{n=N}\mathbf{S}(n,t)$ can be directly measured as an optical anisotropy such as the birefringence. This relationship in eq 2-2 is consistent with the stress-optical rule stating that the anisotropic part of the refractive index tensor, $\Delta\mathbf{n}$, is proportional to the anisotropic part of the stress tensor:[16-21]

$$\Delta\mathbf{n} = C\boldsymbol{\sigma} \qquad (2\text{-}3)$$

Here, the factor C is the stress optical coefficient. The proportionality between the mechanical stress and optical anisotropy specified by eq 2-3 holds in long time scales. This fact in turn enables an optical examination of the rheological properties of polymers. (The stress-optical rule does not hold in short time scales where the stress tensor is contributed from not only the polymeric stress due to the entropy elasticity (eq 2-2) but also a glassy stress reflecting torsion/packing of the monomeric segments. A modified stress-optical rule holds in such short time scales.[16-21])

2-2-1-2 Dielectric relaxation functions

In dielectric measurement, the excitaion/perturbation is an electric field **E**. This field orients the molecular dipoles and activates the polarization **P** of the system, and the relaxation of **P** after removal of **E** is recorded as a responce. Thus, from a microscopic view, the dielectric relaxation detects the fluctuation of the miscroscopic polarization given by a sum of the molecular dipoles.[8]

Stockmayer classified the dipoles of flexible chains into three types:[27,28] (1) the type-A dipole attached parallel to the chain backbone, (2) the type-B dipole attached perpendicularly to the chain backbone, and (3) the type-C dipole attached to the side group, as schematically shown in Figure 2-3. The dielectric relaxation processes due to the fluctuation of type-C and type-B dipoles reflect the local motion of the chain backbone and side-groups, respectively. These relaxation processes usually have *M*-indipendent characteristic times unless the polymer has low-*M* to enhance the mobility of the segments and/or side groups. (This enhancement due to the chain ends becomes negligible at moderately high-*M*.) In contrast, the dielectric relaxation due to the fluctuation of the type-A dipole is retarded with increasing *M* because the sum of (non-inverted) type-A dipoles is proportional to an end-to-end vector **R** of the chain, as schematically shown in the bottom part of Figure 2-2. Most of the polymers have the type-B dipoles but some special polymers, *e.g.*, *cis*-polyisoprene (*cis*-PI), have the type-A dipoles. This type of special polymer, being hereafter referred to as the type-A chain, is the target of the molecular expression of the dielectric relaxtion function explained below.

For a weak electric field, the dielectric response reflects the equilibrium thermal motion of the dipoles attached to the polymer chains. The polarization $\mathbf{P}(t)$ is given by a sum of all dipoles $\boldsymbol{\mu}$ in a unit volume:[8,17]

$$\mathbf{P}(t) = \sum_j \boldsymbol{\mu}_j(t) \tag{2-4}$$

The normalized dielectric relaxation function $\Phi(t)$ is defined as an auto-correlation of **P** at two separate times, 0 and t:

$$\Phi(t) = \frac{\langle P_E(t) P_E(0) \rangle}{\langle P_E^2 \rangle} \tag{2-5a}$$

with P_E being the component of **P** in the direction of **E**. If the system is isotropic and homogeneous, Eq 2-5a can be rewritten as:[13,15,28]

$$\Phi(t) = \frac{\langle \mathbf{P}(t) \bullet \mathbf{P}(0) \rangle}{\langle \mathbf{P}^2 \rangle} \tag{2-5b}$$

In a time scale where the fluctuation of the type-A dipole is concerned, the fluctuation of the type-B and C dipoles has usually relaxed completely and negligibly contributes to Φ(t). Moreover, for polymer chains like *cis*-PI having small type-A dipoles, the dipole-dipole interaction energy is negligibly small compared to the thermal energy $k_B T$. Thus, the cross-correlation between type-A dipoles of different polymer chains also negligbibly contributes to the dielectric function. Since the sum of (non-inverted) type-A dipoles over a chain is proportional to the end-to-end vector **R**, the corresponding dielectric relaxation function detects the global motion (end-to-end fluctuation) of the chain and eq 2-5b can be re-written as: [13,15,28]

$$\Phi(t) = \frac{\langle \mathbf{R}(t) \bullet \mathbf{R}(0) \rangle}{\langle R^2 \rangle} \tag{2-6}$$

Correspondingly, the dielectric intensity is related to the mean-square end-to-end distance of the chain $\langle R^2 \rangle$ as: [13,15,28]

$$\Delta\varepsilon = F\left(\frac{4\pi\tilde{\mu}^2}{3k_B T}\right) v \langle R^2 \rangle \tag{2-7}$$

Here, v is the chain number density, F is a factor correcting a difference between the intensities of macroscopic and microscopic electric fields ($F \cong 1$ for global motion of type-A chains), and $\tilde{\mu}$ is a magnitude of the type-A dipoles reduced to the unit length of **u**.

2-2-2 Methods and operations of the measurements

2-2-2-1 Linear viscoelastic measurements

In the linear viscoelastic regime, the Boltzmann superposition principle holds and the shear stress $\sigma(t)$ in respond to an arbitrary strain history $\gamma(t)$ can be expressed in terms of the linear relaxation modulus $G(t)$ as:[11,13]

$$\sigma(t) = \int_{-\infty}^{t} G(t-t') \frac{\mathrm{d}\gamma(t')}{\mathrm{d}t'} \mathrm{d}t' \tag{2-8}$$

In dynamic viscoelastic measurements, a small amplitude oscillatory (sinusoidal) shear is imposed on a material to be tested:[11]

$$\gamma(t) = \gamma_0 \sin\omega t \text{ with } \omega = \text{angular frequency} \tag{2-9}$$

The amplitude γ_0 is kept small ($\gamma_0 \leq 0.1$ for all measurements included in this thesis) so that the linearity is guaranteed. Then, from eqs 2-8 and 2-9, the stress $\sigma(t)$ is also given as a sinusoidal function of t:[11]

$$\sigma(t) = \gamma_0 G_0(\omega)\sin[\omega t+\delta(\omega)] = \gamma_0 G'(\omega)\sin\omega t + \gamma_0 G''(\omega)\cos\omega t \tag{2-10a}$$

Here, δ is a phase angle characterizing a delay of $\sigma(t)$ with respect to $\gamma(t)$. The storage and loss moduli, $G'(\omega)$ and $G''(\omega)$, are related to $\delta(\omega)$ and the magnitude of the complex modulus $G_0(\omega)$ by $G'(\omega) = G_0(\omega)\cos\delta(\omega)$ and $G''(\omega) = G_0(\omega)\sin\delta(\omega)$. $G'(\omega)$ and $G''(\omega)$ are directly related to $G(t)$ as:[11]

$$G'(\omega) = \omega\int_0^\infty G(t)\sin\omega t\,dt\,; \quad G''(\omega) = \omega\int_0^\infty G(t)\cos\omega t\,dt \tag{2-10b}$$

In this thesis, the linear viscoelastic measurements were conducted with a laboratory rotational rheometer (ARES, Rheometric Scientific). The parallel-plate fixture of diameters 4mm and 8mm were utilized for measuring the modulus in the glassy and rubbery zones, respectively. The geometry of the parallel-plate fixture is sketched in Figure 2-4(a). The motor and the transducer are attached to the bottom and top plates, respectively. An angular displacement θ (in unit of radian) is applied by the motor, and a toque of the sample, M_σ (in unit of Nm), in response to the applied deformation, is measured by the transducer. θ and M_σ are converted into the strain γ and the stress σ as:

$$\gamma = \theta K_\gamma;\ \sigma = M_\sigma K_\sigma \tag{2-11}$$

Here, K_γ and K_σ are the strain and stress constants determined by the geometry and the size of the fixture. For the parallel-plate fixture, the expression of K_γ and K_σ are given by:

$$K_\gamma = R/H;\ K_\sigma = 2/[\pi(R/10)^3] \tag{2-12}$$

Here, R and H are the radius of the plate and the gap between the plates, respectively, as shown in Figure 2-4(a).

2-2-2-2 Linear rheo-optical measurements

The stress-optical coefficient C appearing in eq 2-3 is a material constant.[16-21] Thus, the orientational anisotropies of different molecules are differently weighted in $\boldsymbol{\sigma}$ and $\Delta\mathbf{n}$. This feature enables separation of the stress components due to respective components in the blends in a specific time scale. Thus, the rheo-optical measurement is very useful for multi-component systems.

The rheo-optical measurements in this thesis were conducted with a homemade device composed of an oscillating drive and optical/mechanical detectors equipped in Osaka University. A structure of the rheometric and optical parts of the device is sketched in Figure 2-4 (c1) and (c2), respectively.[21]

In the measurement in this thesis, a small amplitude oscillatory deformation $\gamma(t) = \gamma_0 \sin\omega t$ (γ_0 = 0.06) was applied to the sample sandwitched between two glass plates. Under this oscillation, the incident light beam of intensity I_0 was introduced to the sample and the intensity of the transmitted light $I_\omega(t)$ was recorded, with the analyzer being displaced from the cross-nicol position by a small angle $\alpha \ll 1$. (The light path is shown with thick dashed lines in Figure 2-4 (c2).) Then, the birefringence (in the vorticity direction) $\Delta n^{Z}(t)$ is proportional to a ratio between I_ω and I_0 and given by:

$$\Delta n^{Z}(t) = \frac{\lambda}{2\pi d\alpha}\frac{\Delta I_\omega(t)}{I_0}\tan\theta \tag{2-13}$$

Here, λ is the wave length in vacuum, d is the thickness of the sample, and θ is the refraction angle, as indicated in Figure 2-4 (c2). $\Delta I_\omega(t)$ oscillates at the angular frequency ω of the strain, and $\Delta n^{Z}(t)$ is expressed as a sinusoidal function of t:[16-21]

$$\Delta n^{Z}(t) = 2\gamma_0 K_0(\omega)\sin[\omega t+\delta_B(\omega)] = 2\gamma_0 K'(\omega)\sin\omega t + 2\gamma_0 K''(\omega)\cos\omega t \tag{2-14}$$

The phase angle $\delta_B(\omega)$ appearing in eq 2-14 may be different from the viscoelastic $\delta(\omega)$ in eq 2-10a. The coefficient of 2 is needed to convert the measured Δn^{Z} to Δn_{xy} (the xy component of refrective index tensor $\Delta\mathbf{n}$) under small strain.[21] A complex strain-optical coefficient is defined as $K^* = K'+iK''$ with $K'(\omega) = K_0(\omega)\cos\delta_B(\omega)$ and $K''(\omega) = K_0(\omega)\sin\delta_B(\omega)$, as similar to the expression of the complex modulus.

2-2-2-3 Linear dielectric measurements

In the dielectric measurements, an electric field E is applied on a material and the electric displacement $D(t)$ is recorded as a function of time t. $D(t)$ is related to the normalized dielectric function $\Phi(t)$ as:[13,15,28]

$$D(t) = [\varepsilon_0 - \Delta\varepsilon\Phi(t)]E\varepsilon_{vac} \qquad \text{with } \Delta\varepsilon = \varepsilon_0 - \varepsilon_\infty \tag{2-15}$$

Here, ε_0 is the static dielectric constrant, ε_∞ is the unrelaxed dielecrtric constant (at high frequency), $\Delta\varepsilon$ is the dielectric intensity, and ε_{vac} (=8.85 × 10^{-12}Fm^{-1}) is the permittivity of vacuum. (ε_0, ε_∞ and $\Delta\varepsilon$ are defined as the quantities relative to vacuum.)

In the linear dielectric regime, the Boltzmann superposition holds and $D(t)$ against the field $E(t)$ of arbitrary t dependence is expressed as:

$$D(t) = \varepsilon_{vac}\left(\varepsilon_0 E(t) - \Delta\varepsilon\int_{-\infty}^{t}\Phi(t-t')\frac{dE(t')}{dt'}dt'\right) \tag{2-16}$$

In the dynamic linear dielectric measurments, the material is subjected to a sinusoidal electric field $E(t)$ with a small ampltitude E_0:[12,28]

$$E(t) = E_0\sin\omega t \tag{2-17}$$

The electric displacement $D(t)$ against this $E(t)$ is expressed as:[12]

$$D(t) = \varepsilon_{vac}E_0\,[\varepsilon'(\omega)\sin\omega t - \varepsilon''(\omega)\cos\omega t] \tag{2-18a}$$

$$\varepsilon'(\omega) = \varepsilon_0 - \omega\Delta\varepsilon\int_0^\infty\Phi(t)\sin\omega t dt\,; \quad \varepsilon''(\omega) = \omega\Delta\varepsilon\int_0^\infty\Phi(t)\cos\omega t dt \tag{2-18b}$$

Here, the dielectric constant $\varepsilon'(\omega)$ and dielectric loss $\varepsilon''(\omega)$ are the in- and out-phase components of the dynamic complex dielectric constant, $\varepsilon^*(\omega) = \varepsilon'(\omega) - i\varepsilon''(\omega)$.

In the measurements in this thesis, the sample to test was charged in a homemade dielectric cell composed of parallel electrodes and a guard electrode, as sketched in Figure 2-4(b). The measurements were made with an impedance analyzer/dielectric interface system (1260 and 1296, Solatron) and a capacitance bridge (1615A, QuadTech). The capacity C_0 of the empty dielectric cell and the capacity $C^*(\omega)$ of the cell filled with sample were measured at the same T. Then, $\varepsilon^*(\omega)$ of the sample was obtained as:

$$\varepsilon^*(\omega) = C^*(\omega)/C_0 \tag{2-19}$$

2-2-2-4 Differential scanning calorimetry (DSC) measurements

In the DSC measurements, the sample and a reference are supplied with heat energy at different rates to be forced to have the same temperature that increases linearly with time.[29] A difference of the energies supplied to the sample and the reference is recorded against the temperature T to give a DSC trace.

In this thesis, the DSC measurements were conducted with two laboratory calorimeters, DSC2910, TA Instruments (in Chapter 5) and DSC Q20, TA Instruments (in Chapter 7). The main purpose for the thermal measurements was to detect the glass transition processes for the PI/PtBS systems. For this purpose, the samples of known mass (10-20mg) were quenched to −100°C or lower T through liquid nitrogen and heated at a rate of 10-20°C/min up to 200°C or higher T. This process was repeated for two times to remove the thermal history and a third run was also made to check the reproducibility. The second and third runs were reproducible, and the DSC traces shown in this thesis were obtained from the second run.

2-2-3 Analysis of the linear viscoelastic and dielectric data

2-2-3-1 Viscoelastic relaxation mode distribution and relaxation time

Since the flexible chains have a large freedom of their intra-chain motion, the linear relaxation modulus $G(t)$ of these chains has a relaxation mode distribution and can be phenomenologically expressed as:[11,13,26]

$$G(t) = \sum_{p\geq 1} h_{G,p} \exp(t / \tau_{G,p}) \tag{2-20}$$

Here, $h_{G,p}$ and $\tau_{G,p}$ are the intensity and characteristic time for the p-th viscoelastic relaxation mode. Then, from eq 2-10b, the storage and loss moduli, $G'(\omega)$ and $G''(\omega)$, can be expressed in terms of $h_{G,p}$ and $\tau_{G,p}$ as:[13,26]

$$G'(\omega) = \omega^2 \sum_{p\geq 1} h_{G,p} \frac{\tau_{G,p}^2}{1+\omega^2\tau_{G,p}^2}, \quad G''(\omega) = \omega \sum_{p\geq 1} h_{G,p} \frac{\tau_{G,p}}{1+\omega^2\tau_{G,p}^2} \tag{2-21}$$

At low $\omega << 1/\tau_1$ (with τ_1 = longest relaxation time) where all modes have relaxed, $G'(\omega)$ and $G''(\omega)$ exhibit the power-law type terminal tails as:

$$G'(\omega) = \left\{ \sum_{p \geq 1} h_{G,p} \tau_{G,p}^2 \right\} \omega^2 = \eta_0^2 J \omega^2 \propto \omega^2 \quad \text{for } \omega << 1/\tau_1 \tag{2-22}$$

$$G''(\omega) = \left\{ \sum_{p \geq 1} h_{G,p} \tau_{G,p} \right\} \omega = \eta_0 \omega \propto \omega \quad \text{for } \omega << 1/\tau_1 \tag{2-23}$$

Here, η_0 and J are the zero-shear viscosity and steady state recoverable compliance, respectively. Viscoelastic quantities characterizing the terminal relaxation are related to the terminal tails of G' and G'', as summarized below.[13,26]

The zero shear viscosity, η_0, though usually defined in a steady flow state, can be determined from G'' at $\omega << 1/\tau_1$ (where the terminal tail is observed) as

$$\eta_0 = \sum_{p \geq 1} h_{G,p} \tau_{G,p} = \left[\frac{G''}{\omega} \right]_{\omega \to 0} \tag{2-24}$$

Similarly, the steady state recoverable compliance J is determined from the G' and G'' data at $\omega << 1/\tau_1$ as

$$J = \frac{\sum_{p \geq 1} h_{G,p} \tau_{G,p}^2}{\left\{ \sum_{p \geq 1} h_{G,p} \tau_{G,p} \right\}^2} = \left[\frac{G'}{\{G''\}^2} \right]_{\omega \to 0} \tag{2-25}$$

The other quantity characterizing the terminal relaxation is an average relaxation time, $\langle \tau \rangle$. Specifically, the second moment average viscoelastic relaxation time defined below is frequently utilized.

$$\langle \tau_G \rangle_w = \frac{\sum_{p \geq 1} h_{G,p} \tau_{G,p}^2}{\sum_{p \geq 1} h_{G,p} \tau_{G,p}} = \left[\frac{G'}{\omega G''} \right]_{\omega \to 0} \quad (= J\eta_0) \tag{2-26}$$

For entangled polymer chain, the dynamic behavior is strongly related not only to this $\langle \tau_G \rangle_w$ but also to the longest Rouse relaxation time $\tau_{G,R}$. Osaki and coworkers proposed a method to evaluate $\tau_{G,R}$ from the power law behavior, $G' \propto \omega^{1/2}$, in the glass to rubber transition zone.[30] This method can be utilized to estimate the Rouse relaxation time of an entanglement segment, τ_a, as:

$$G'(\omega) = 1.111 \frac{CRT}{M_e} (\omega \tau_a)^{1/2} \tag{2-27}$$

Here, R is the gas constant, T is the temperature, C is the mass concentration, and M_e is the molecular weight of the entanglement segment, respectively.

A method of the graphical evaluation of the characteristic quantities, η_0, J, $\langle\tau_G\rangle_w$, and τ_a is shown in Figure 2-5(a). [13,26,30] The lines attached to $G'(\omega)$ and $G''(\omega)$ data in the terminal relaxation region (low ω) show the terminal tails (of slope = 2 for G' and 1 for G'' in the double-logarithmic scale). The line attached to G' data in the glass to rubbery transition region (high ω) shows the power law behavior $G'(\omega) = \alpha\omega^{1/2}$. The $1/J$ and $1/\langle\tau_G\rangle_w$ values are evaluated as the G' and ω values at a cross-point of the teminal tails, respectively. In addition, the $1/\tau_a$ value is obtained as the ω value where $G'(\omega)$ in the power law zone has a value of $1.111CRT/M_e$ (=$1.111G_N$).

2-2-3-2 Dielectric relaxation mode distribution and relaxation time

As similar to the viscoelastic relaxation function (eq 2-20), the normalized dielectric relaxation function can be expressed phenomelogically in terms of relaxation modes as:

$$\Phi(t) = \sum_{p\geq 1} h_{\varepsilon,p} \exp(t/\tau_{\varepsilon,p}) \qquad (\sum_{p\geq 1} h_{\varepsilon,p} = 1) \tag{2-28}$$

Here, $h_{\varepsilon p}$ and $\tau_{\varepsilon p}$ are the normalized intensity and characteristic time for the p-th dielectric relaxation mode, respectively. From eqs 2-18b and 2-28, the decrease of dielectric constant from its static value ε_0, $\Delta\varepsilon'(=\varepsilon_0-\varepsilon')$, and dielectric loss, ε'', are expressed in terms of $h_{\varepsilon p}$ and $\tau_{\varepsilon p}$ as:

$$\frac{\Delta\varepsilon'(\omega)}{\Delta\varepsilon} = \omega^2 \sum_{p\geq 1} h_{\varepsilon,p} \frac{\tau_{\varepsilon,p}^2}{1+\omega^2\tau_{\varepsilon,p}^2}, \quad \frac{\varepsilon''(\omega)}{\Delta\varepsilon} = \omega \sum_{p\geq 1} h_{\varepsilon,p} \frac{\tau_{\varepsilon,p}}{1+\omega^2\tau_{\varepsilon,p}^2} \tag{2-29}$$

The dielectric intensity $\Delta\varepsilon$ can be evaluated through integration of the ε'' data and/or extrapolation of the $\Delta\varepsilon'$ data as (cf. eq 2-28):

$$\Delta\varepsilon = \frac{2}{\pi}\int_{-\infty}^{\infty} \varepsilon'' \mathrm{d}\ln\omega = \lim_{\omega\to\infty} \Delta\varepsilon'(\omega) \tag{2-30}$$

The second-moment average dielectric relaxation time, defined in a way similar to $\langle\tau_G\rangle_w$, is obtained from the $\Delta\varepsilon'$ and ε'' data as:[13,28]

$$\langle\tau_\varepsilon\rangle_w = \frac{\sum_{p\geq 1} h_{\varepsilon,p}\tau_{\varepsilon,p}^2}{\sum_{p\geq 1} h_{\varepsilon,p}\tau_{\varepsilon,p}} = \left[\frac{\Delta\varepsilon'}{\omega\varepsilon''}\right]_{\omega\to 0} \tag{2-31}$$

A method of the graphical evaluation of $\langle \tau_\varepsilon \rangle_w$ is shown in Figure 2-5(b).[6] The solid lines attached to the ε'' and $\Delta\varepsilon'$ ($=\varepsilon_0 - \varepsilon'$) data show the terminal tails (of slope = 2 for $\Delta\varepsilon'$ and 1 for ε'' in the double logarithmic scale). The ω at a cross-point of these lines coincides with $1/\langle \tau_\varepsilon \rangle_w$. Thus, in later chapters, $\langle \tau_\varepsilon \rangle_w$ of PI is easily evaluated from the dielectric data.

The dielectric terminal relaxation time is frequently evaluated from the frequency of the dielectric ε'' peak as:[13,28]

$$\tau_\varepsilon = 1/\omega_{\varepsilon\text{-peak}} \tag{2-32}$$

For monodisperse PI samples in bulk, the ε'' peak is sharp and governed by the slowest relaxation mode to give $\omega_{\varepsilon\text{-peak}} \cong 1/\langle \tau_\varepsilon \rangle_w$ (as noted in Figure 2-5(b)). Then, $1/\omega_{\varepsilon\text{-peak}}$ can be utilized as the dielectric terminal relaxation time. (However, this is not the case for materials exhibiting a broad ε'' peak, for which $\langle \tau_\varepsilon \rangle_w \gg 1/\omega_{\varepsilon\text{-peak}}$.)

2-2-3-3 Time-temperature superposition

The linear viscoelastic behavior is fully specified by the relaxation spectrum $\{h_{G,p}, \tau_{G,p}\}$, as explained earlier in eq 2-20. The mode relaxation time and intensity, $\tau_{G,p}$ and $h_{G,p}$, generally change with T. If this change is common for all relaxation modes, the spectra at two different temperatures T and T_r are related as:[26]

$$\tau_{G,p}(T) = a_{T,G}\tau_{G,p}(T_r), \quad h_{G,p}(T) = b_{T,G}h_{G,p}(T_r) \tag{2-33}$$

where $a_{T,G}$ and $b_{T,G}$ are functions of T (and T_r) being independent of the mode index p. For this case, the modulus at T is related to that at the reference T_r as:

$$G(t,T) = b_{T,G}G(t/a_{T,G}, T_r) \qquad \text{in time } t \text{ domain} \tag{2-34a}$$

$$G^*(\omega,T) = b_{T,G}G^*(\omega a_{T,G}, T_r) \qquad \text{in frequency } \omega \text{ domain} \tag{2-34b}$$

For this case, the data at different T can be superposed into a master curve at T_r. This superposition is referred to as the time-temperature superposition (tTs).

Figure 2-6 shows an example of tTs. The left panel shows the raw G' data obtained for a PI sample at different T as indicated. These data are corrected by an intensity factor, b_T^{-1}, and shifted along the ω axis by a factor of $a_{T,G}$, to give the master curve shown in the right panel. Clearly, the G' data are well superposed, meaning that tTs works for this sample. For this case, the material is

referred to as a thermo-rheologically simple material. (A material not obeying tTs is referred to as a thermo-rheologically complex material.)

For polymeric materials, slow and fast viscoelastic relaxation modes usually detect global and local motions of the stress-sustaining units therein, as explained earlier. Thus, eq 2-34 holds when the following criteria/conditions are satisfied:[26] (1) the motion in various length scales is accelerated to the same extent (by a factor $a_{T,G}$) on heating, and (2) a type of the molecular/structural dynamics, that determines the distribution of the elastic free energy to respective viscoelastic modes, does not change with T thereby giving the same $b_{T,G}$ to all modes. Homopolymer melts are an example of the materials satisfying these criteria: Slow viscoelastic relaxation of the melts, reflecting the global motion of the polymer chains, occurs through accumulation of local motion of subchain (or Rouse segments) so that all viscoelastic modes are accelerated to the same extent and the relaxation intensity increases by the same factor for those modes. Thus, the melt obeys tTs, as demonstrated in Figure 2-6.

For the homopolymer melts at T in a range between T_g+20 K and T_g+100K (or a little higher), the shift factor $a_{T,G}$ and the intensity reduction factor $b_{T,G}$ are well described by empirical equations:[11,26,31]

$$\log a_{T,G} = -\frac{C_1(T - T_r)}{C_2 + (T - T_r)} \quad \text{(Williams-Landel-Ferry (WLF) equation)} \tag{2-35}$$

$$b_{T,G} = \frac{T\rho(T)}{T_r\rho(T_r)} \tag{2-36}$$

Here, C_1 and C_2 are the constants essentially determined by a separation of the reference temperature T_r from the glass transition temperature T_g, and ρ is the mass density of the melt (that decreases on thermal expansion). Eq 2-35 is often related to thermal expansion of a free volume in melts,[26,32] while eq 2-36 is directly connected to the entropy elasticity of polymer chains (cf. eq 2-2). Eqs 2-35 and 2-36 are satisfactorily valid for a variety of homopolymer melts. However, there still remains a controversy about their molecular meaning. Specifically, a correction to eq 2-36 due to temperature dependence of the chain dimension and packing length has been proposed,[11,26] although this correction is rather small in a numerical sense.

The tTs can hold also for the dielectric spectra $\{h_{\varepsilon,p};\ \tau_{\varepsilon,p}\}$. If the change of $\{h_{\varepsilon,p};\ \tau_{\varepsilon,p}\}$ is common for all dielectric relaxation modes,

$$\tau_{\varepsilon,p}(T) = a_{\mathrm{T},\varepsilon}\tau_{\varepsilon,p}(T_\mathrm{r}),\ h_{\varepsilon,p}(T) = b_{\mathrm{T},\varepsilon}h_{\varepsilon,p}(T_\mathrm{r}) \tag{2-37}$$

the dielectric data at different temperatures T and T_r are related through relationships

$$\varepsilon(t,T) = b_{\mathrm{T},\varepsilon}\varepsilon(t/a_{\mathrm{T},\varepsilon}, T_\mathrm{r}) \qquad \text{in time } t \text{ domain} \tag{2-38a}$$

$$\varepsilon''(\omega,T) = b_{\mathrm{T},\varepsilon}\varepsilon''(\omega a_{\mathrm{T},\varepsilon}, T_\mathrm{r});\ \Delta\varepsilon'(\omega,T) = b_{\mathrm{T},\varepsilon}\Delta\varepsilon'(\omega a_{\mathrm{T},\varepsilon}, T_\mathrm{r}) \ \text{in frequency } \omega \text{ domain} \tag{2-39b}$$

For type-A chains, the dielectric data at low ω detects the global chain motion and the corresponding shift factor $a_{\mathrm{T},\varepsilon}$ and intensity reduction factor $b_{\mathrm{T},\varepsilon}$ are well described by empirical equations:[13,28]

$$\log a_{\mathrm{T},\varepsilon} = -\frac{C_1(T - T_\mathrm{r})}{C_2 + (T - T_\mathrm{r})} \ \text{(Williams-Landel-Ferry (WLF) equation)} \tag{2-39}$$

$$b_{\mathrm{T},\varepsilon} = \frac{T_\mathrm{r} v(T)\left\langle R(T)^2\right\rangle}{T v(T_\mathrm{r})\left\langle R(T_\mathrm{r})^2\right\rangle} \tag{2-40}$$

Here, v and $\left\langle R^2\right\rangle$ are the number density and mean-square end-to-end distance of the chains (cf. eq 2-7).

The changes of v and $\left\langle R^2\right\rangle$ with T are usually much smaller than a change of T itself. Similarly, in eq 2-36, the change of ρ with T is always much smaller than a change of T itself. Thus, the intensity factors can be safely approximated as:

$$b_{\mathrm{T,G}} = T/T_\mathrm{r} \tag{2-41a}$$

$$b_{\mathrm{T},\varepsilon} = T_\mathrm{r}/T \tag{2-41b}$$

There is no *a priori* reason for a given material to be thermo-rheologically simple.[26] In particular, for materials containing two or more components (such as polymer blends), the acceleration of molecular motion on heating is usually different for different components thereby leading to failure of the tTs. Since tTs works only under restricted conditions explained above, the test of time-temperature superposition in turn enables a test of changes of the molecular dynamics (a change of the mode of motion) with T.

References

1. Watanabe, H.; Matsumiya, Y.; Takada, J.; Sasaki, H.; Matsushima, Y.; Kuriyama, A.; Inoue, T.; Ahn, K. H.; Yu, W.; Krishnamoorti, R. *Macromolecules* **2007**, 40, 5389-5399.
2. Takada, J.; Sasaki, H.; Matsushima, Y.; Kuriyama, A.; Matsumiya, Y.; Inoue, T.; Watanabe, H. *Nihon Reoroji Gakkaishi* **2007**, 35, 221-224.
3. Watanabe, H.; Urakawa, O.; Kotaka, T. *Macromolecules* **1993**, 26, 5073-5083
4. Matsumiya, Y.; Watanabe, H.; Osaki, K. *Macromolecules* **2000**, 22, 499-506
5. Watanabe, H.; Matsumiya, Y.; Inoue, T. *Macromolecules* **2002**, 35, 2339-2357
6. Watanabe, H.; Ishida, S.; Matsumiya, Y.; Inoue, T. *Macromolecules* **2004**, 37, 1937-1951
7. Watanabe, H.; Ishida, S.; Matsumiya, Y.; Inoue, T. *Macromolecules* **2004**, 37, 6619-6631
8. Qiao, X.Y.; Sawada, T.; Matsumiya, Y.; Watanabe, H. *Macromolecules* **2006**, 39, 7333-7341
9. Sawada, T.; Qiao, X.Y.; Watanabe, H. *Nihon Reoroji Gakkaishi* **2007**, 35, 11-20

10. Yurekli, K.; Krishnamoorti, R. *Journal of Polymer Science Part B-Polymer Physics* **2004**, 42, 3204-3217.
11. Graessley, W.W. *Polymeric Liquids & Networks: Dynamics and Rheology, Garland Science:* New York, **2008**.
12. Kremer, F.; Schönhals, A. *Boardband Dielectric Spectroscopy*, Springer: Berlin, **2002**.
13. Watanabe, H. *Prog. Polym. Sci*. **1999**, 24, 1253-1403.
14. McLeish, T. C. B. *Adv. Phys.* **2002**, 51, 1379-1527.
15. Watanabe, H. *Polymer Journal*. **2009**, 41, 925-950
16. Inoue T.; Okamoto H.; Osaki K. *Macromolecules* **1991**, 24, 5670-5675.
17. Okamoto, H.; Inoue, T.; Osaki, K. J. *Polym. Sci. Part B: Polym. Phys.* **1995**, 33, 417-424.
18. Inoue T.; Mizukami Y.; Okamoto T.; Matsui H.; Watanabe H.; Kanaya T.; Osaki K. *Macromolecules* **1996**, 29, 6240-6245.
19. Inoue T.; Matsui H.; Osaki T. *Rheol Acta* **1997**, 36, 239-244.
20. Inoue T. *Nihon Reoroji Gakkaishi* **2000**, 28, 167-175.
21. Hayashi, C.; Inoue, T. *Nihon Reoroji Gakkaishi* **2009**, *37*, 205-210.
22. Inoue, T.; Osaki, K. *Macromolecules* **1996**, 29, 1595-1599
23. Inoue, T. *Nihon Reoroji Gakkaishi* **2000**, 28, 167-175
24. Inoue, T.; Uematsu T.; Osaki, K. *Macromolecules* **2002**, 35, 820-826
25. Doi, M.; Edwards, S. F. *The Theory of Polymer Dynamics*, Oxford, Clarendon, **1986**.
26. Watanabe, H.; Matsumiya, Y.; Chen, Q.; and Yu, W. Comprehensive Polymer Science, 2nd Ed., Elsevier, Oxford, UK, **2010**, in press

27. Stockmayer, W.H. Pure Appl. Chem. 1967, 15, 539-554.
28. Watanabe, H. *Macromol. Rapid Commun*. **2001**, 22, 127-175.
29. Sperling, L.H. *Introduction to Physical Polymer Science, 4th Ed*., John Wiley&Sons: New Jersey, **2006**.
30. Osaki, K.; Inoue, T.; Uematsu, T.; Yamashita, Y. *J. Polym. Sci. Part B: Polymer Phys*. **2001**, 39, 1704-1712.
31. Rubinstein, M.; Colby R.H. *Polymer Physics*, Oxford University Press Inc., New York **2003**
32. Ferry, J. D.; *Viscoelastic Properties of Polymers, 3rd Ed.*, Wiley, New York **1980**

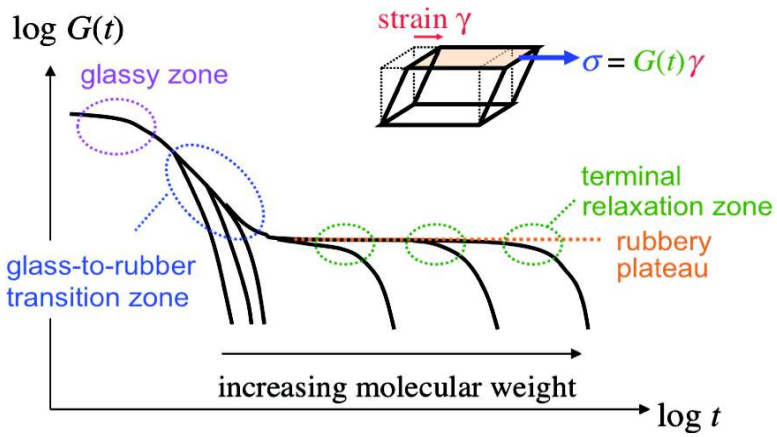

Fig. 2-1: A schematic illustration of the viscoelastic relaxation modulus, $G(t)$, of flexible linear polymers. (Figure 1 in Ref.15)

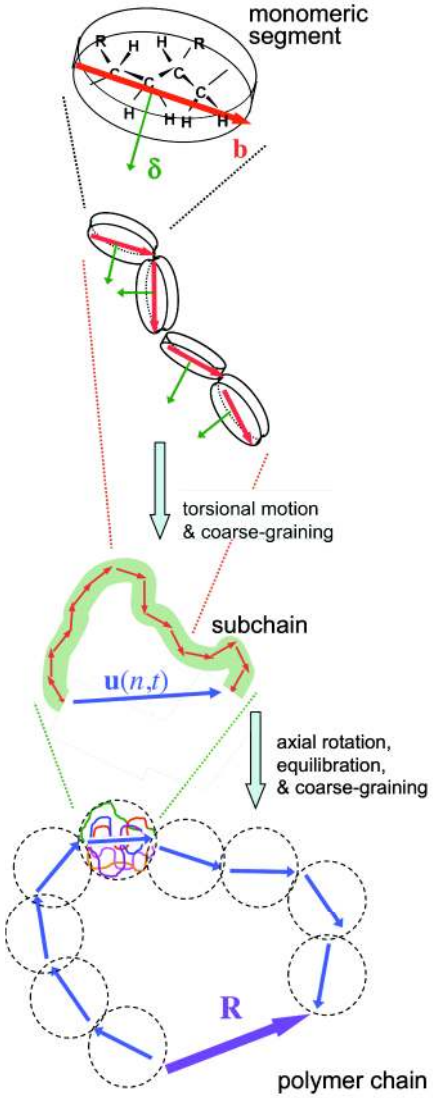

Fig. 2-2: A schematic illustration of hierachinal structure of flexible linear polymers. (Figure 2 in Ref.15)

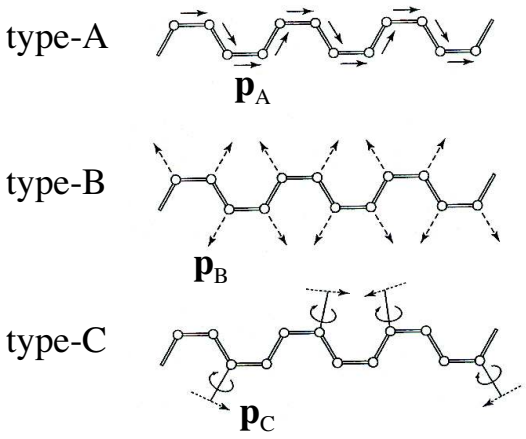

Fig. 2-3: A schematic illustration of different types of dipoles of polymer chains. The type-A and B dipoles are attached parallel and perpendicularly to the chain backbone, respectively. The type-C dipole is attached to the sider group. (Figure 1 in Ref.28)

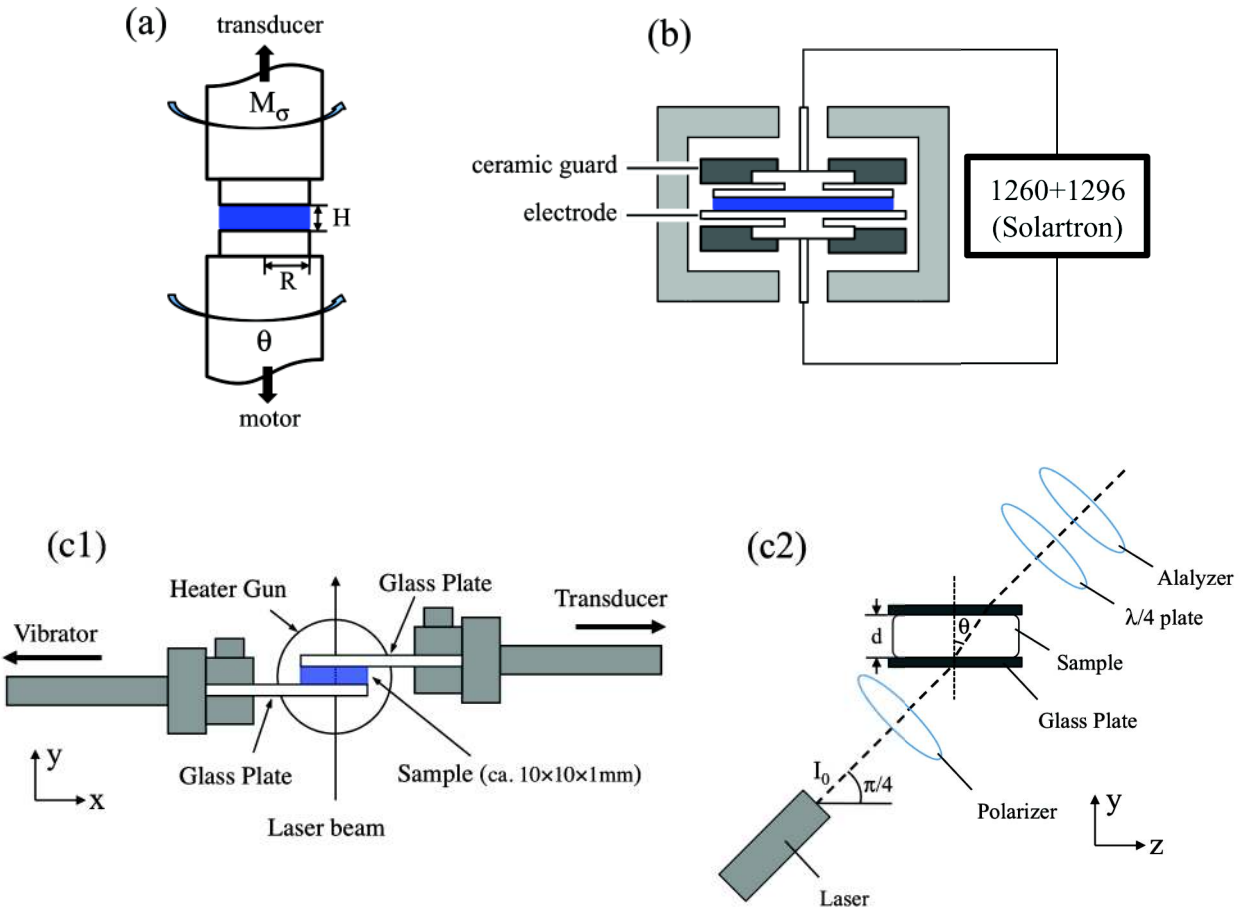

Fig. 2-4: Schemetic illustration of **(a)** the parellel-plate fixture for viscoelastic measurements, **(b)** the dielectric cell for dielectric measurements, **(c1)** the viscometric parts and **(c2)** the optical parts of the parallel-plate fixture for birefringence measurements.[21]

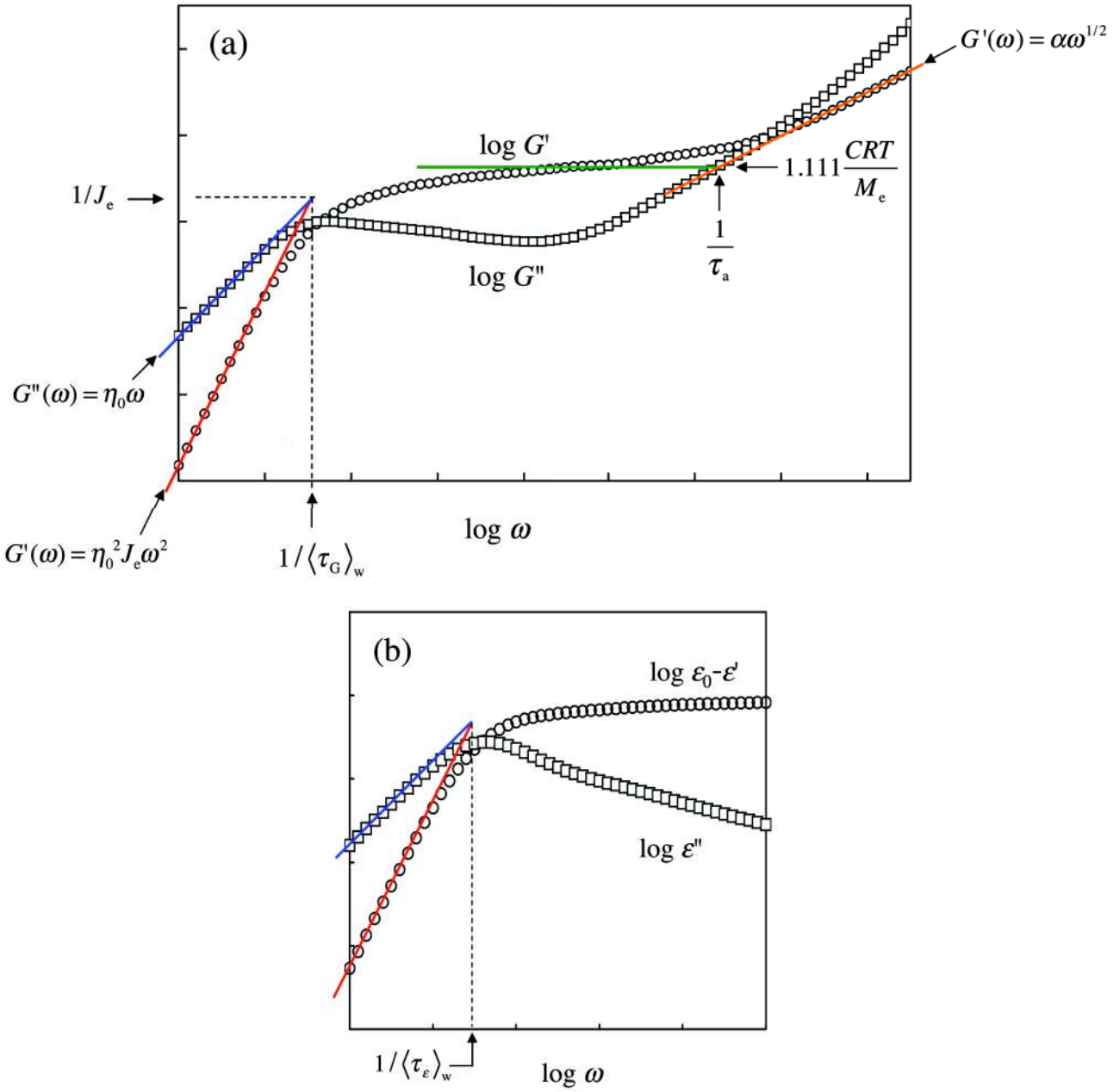

Fig. 2-5: Schematic illustration of viscoelastic and dielectric quantities evaluated from viscoelastic and dielectric data.

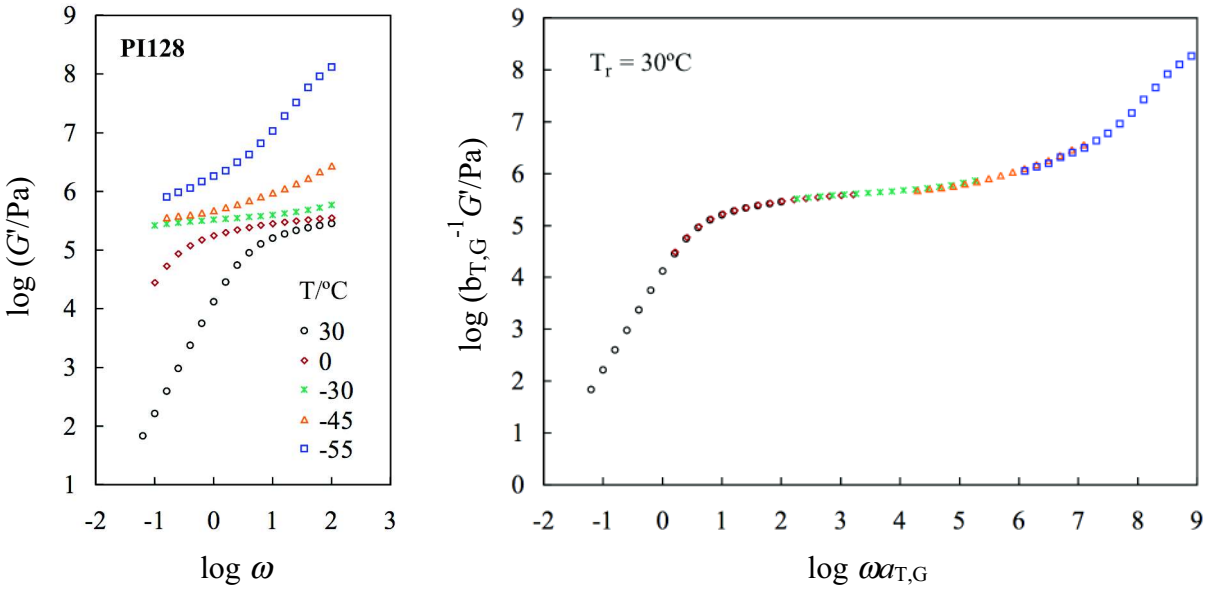

Fig. 2-6 Test of time-temperature superposition of storage modulus, G', obtained for the PI128 sample (M = 128×10^3). The left panel shows the raw G' data, and the right panel shows the master curve of G' reduced at T_r = 30°C.

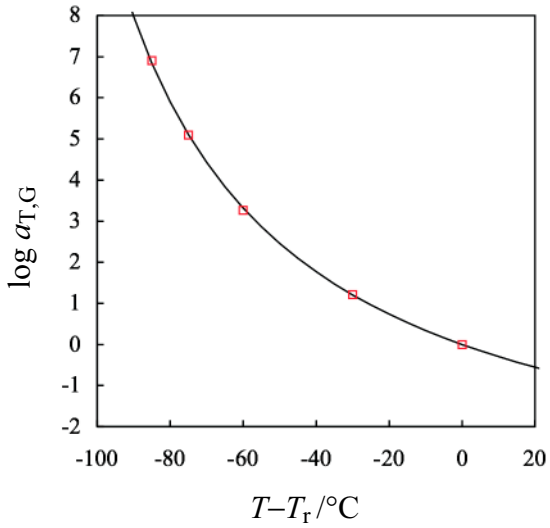

Fig. 2-7 The shift factor $a_{T,G}$ obtained for the G' data of PI128 in Figure 2-6. The $a_{T,G}$ data are plotted against the $T-T_r$, with T_r = 30°C. The solid curve shows the WLF equation for PI.

Chapter 3 DYNAMICS OF BULK PI AND PTBS

3-1 Introduction

Linear viscoelastic behavior of entangled, monodisperse bulk polymers has been extensively studied in the past decades to establish some universal features not affected by the chemical structure of the polymers. For example, the molecular weight (M) dependence of the steady state recoverable compliance J of those polymers can be summarized as[1,2]

$$J \propto M^1 \text{ for } 2M_e < M < M_c' \tag{3-1a}$$

$$J \propto M^0 \text{ for } M > M_c' \tag{3-1b}$$

where M_c' (= $4M_e$ - $6M_e$) and M_e, respectively, are the characteristic molecular weight defined for J and the entanglement molecular weight (cf. eq 1-2). The universal behavior summarized by eq 3-1 has been interpreted to reflect the crossover from the non-entangled, Rouse-like behavior (eq 3-1a) to the entangled, reptation-like behavior (eq 3-1b) occurring in the range of $2M_e < M < M_c'$. This interpretation is consistent with the experimental observation[1,2] that the J value in the lightly to moderately entangled regime ($2M_e < M < M_c'$) is close to that expected for the Rouse chain. Furthermore, for well entangled polymers with $M > M_c'$, the angular frequency (ω) dependence of the storage and loss moduli, G' and G'', in the terminal relaxation regime is insensitive to M to give the M-insensitive J (= $[G'/G''^2]_{\omega \to 0}$). This behavior is qualitatively consistent with the reptation-based molecular models.[3,4]

However, the above interpretation of the Rouse-to-reptation crossover should not be regarded as a rigorous and quantitative crossover because of several factors that affect the J data. First of all, a considerable scatter is noted even for the most reliable set of the J data,[1,2] which would be partly due to small but non-zero polydispersities of the polymer samples so far examined. More importantly, the stress is contributed from different motional modes of a chain, so that the G' and G'' data of lightly to moderately entangled polymers are influenced by all these motional modes instead of reflecting a simple crossover from Rouse to reptaion behavior. The available motional modes of the linear polymer chains are summarized below.

The hiearachinal relaxation behavior of linear polymer chains has been explained in Figures 2-1 and 2-2: In a short time scale, only the local motion is activated, and the glassy modulus reflecting an anisotropy of the disk-like monomeric segments is observed.[5-9] In contrast, in a long time scale, the linear polymer chain can be regarded as a thread-like chain composed of internally equilibrated

subchains. The stress relaxation of the thread-like chains, particularly for the entangled chains, is further contributed from different motional modes of the chain, as briefly summarized below.

The polymer chain behaves as a Rouse chain before it feels the topological constraints. In a longer time scale where the entanglement effect prevails, the reptation mechanism appears to govern the terminal relaxation of the monodisperse linear chains. However, the reptation model, originally proposed by de Gennes[10] and fully formulated by Doi and Edwards[11], can not fully describe the relaxation behavior of monodisperse linear polymers at long times. For example, the reptation model predicts that the relaxation time scales with the molecular weight of linear chains as $\tau \propto M^3$, but extensive experiments show $\tau \propto M^{3.5\pm0.2}$. It has been widely accepted that this 3.5th power-law behavior reflects some relaxation modes that are faster than the reptation and becomes less important with an increase of M. For example, the contour length of a probe chain in a tube, measured along the tube axis, fluctuates due to the Rouse motion of the chain along the tube. This contour length fluctuation (CLF) process accelarates the relaxation (release of orientational anisotropy) of subchains near the chain ends.[3,4,11] Moreover, the tube for the probe chain moves due to the motion of the tube-forming matrix chains. The tube motion accelerates the probe relaxation through two different but related mechanisms: the tube motion allows a large-scale motion of the probe in a direction lateral to the backbone to enhance the probe relaxation.[3,4,12] This mechanism is referred to as the *constraint release* (CR).[3,4,12] The lateral motion can be coarse-grained to give an increase of the effective tube diameter, which is referred to as the *dynamic tube dilation* (DTD).[3,4,13]

Thus, it is desired to analyze the G' and G'' data of linear polymer chains in terms of the motional modes, in particularly for the entangled polymer chains. For linear polystyrene (PS), polyisoprene (PI), and poly(*p*-*tert*-butyl styrene) (PtBS) in a wide range of M, this chapter makes this analysis with the aid of the glassy modulus reported in literature[5,7,9]. It turned out that the terminal entanglement relaxation mode distribution and the corresponding compliance J_{ent} are rather insensitive to M even for $M < M_c'$ and close to those of well entangled high-M polymers, in particular for the case of PI and PS. In addition, the mode distribution of the viscoelastic data of PI was in accordance to that of the dielectric data within the framework of the DTD mechanism. Details of these results are presented below.

3-2 Experimental

For bulk, linear polystyrene (PS) samples with small polydispersities ($M_w/M_n < 1.1$), Schausberger et al.[14] reported the G' and G'' data in a wide range of M up to 2450×10^3. Their data

were utilized in the analysis in this chapter. In addition, previously published data for low-M PS samples ($10^{-3}M$ = 23 and 39) were utilized.[15] Furthermore, for commercially available PS samples (Tosoh TSK; $10^{-3}M$ = 9.5 and 96), dynamic viscoelastic measurements were conducted to determine G' and G''. The details of the measurements were explained in Section 2-2. The data for all these samples were compared at a reference temperature utilized by Schausberger et al.,[14] $T_{r,bulk}$ = 180°C. A Williams-Landel-Ferry (WLF) correction for the segmental friction (reduction of the G' and G'' data to the *iso*-frictional state[2]) was made for the lowest-M sample, as explained in Appendix 3-1.

Linear polyisoprene (PI) and poly(*p-tert*-butyl styrene) (PtBS) samples, including two PtBS samples previously studied by Watanabe and coworkers,[16,17] were anionically synthesized and then characterized with low-angle laser light scattering combined with GPC (Tosoh LS-8000, CO-8020, and DP8020), as explained in Section 2-1.

Dynamic viscoelastic and dielectric measurements were conducted for the PI and PtBS samples. Details of these measurements were explained in Section 2-2. The data of PI and PtBS samples were reduced at $T_{r,bulk}$ = 30°C and 180°C, respectively, with the data for low-M PI and PtBS being subjected to the WLF correction for the segmental friction.

For all samples, the value for M_w, M_w/M_n and $T_{r,bulk}$ after the WLF correction are listed in Table 3-1 ($T_{r,bulk}$ = 180, 30, and 180°C, respectively, for high-M PS, PI and PtBS samples; no WLF correction was needed for these samples.) .

3-3 Results and Discussion

3-3-1 Overview

Figures 3-1(a), (b) and (c), respectively, show the angular frequency (ω) dependence of the G' and G'' data of PS, PI and PtBS bulk samples (symbols). The numbers attached to the G' curves indicate $10^{-3}M$ of respective samples. The solid curves indicate literature data for the glassy modulus,[5,7,9] as explained later in more detail.

The entanglement molecular weight M_e determined from the entanglement plateau modulus G_N (eq 1-2) is 18.0×10^3, 5.0×10^3 and 37.6×10^3 for PS[1,2], PI,[3] and PtBS,[18] respectively. Thus, in Figure 3-1, PS samples with $M \le 23\times10^3$ ($\cong M_e^{PS\ bulk}$), the PI sample with $M = 3\times10^3$ ($\cong M_e^{PI\ bulk}$), and the PtBS samples with $M \le 42\times10^3$ ($\cong M_e^{PtBS\ bulk}$) are in the non-entangled state. These low-M samples exhibit the well-known behavior,[1,2] the high-ω glassy (or segmental) mode relaxation that is followed by the Rouse-like relaxation (glass to rubber transition) at intermediate ω and by the

terminal relaxation at low ω; cf. Figures 3-1 (a), (b), and (c). The higher-M samples are in the entangled state to show the other type of well-known behavior,[1,2] the existence of the entanglement plateau between the Rouse-like regime and the terminal regime and the extension of this plateau with increasing M.

PI, PS, and PtBS have type-B dipole perpendicular to the chain backbone thus their segmental (glassy) relaxation seen at high ω is dielectrically active. In addition, PI also has the type-A dipole parallel along its chain backbone, and its global motion activates both viscoelastic and dielectric relaxation.

Figure 3-2 shows the dielectric loss $\varepsilon''(\omega)$ data obtained as functions of ω for (a) PI and (b) PtBS. The sense of symbols is the same as that in Figure 3-1. For PI samples, ε'' exhibit low-ω and high-ω dispersions corresponding to the fluctuation of type-A dipole due to the global motion and the flucutation of type-B dipole due to the segmental motion. In contrast, PtBS has no type-A dipole and thus its global motion is dielectrically inert. The dielectric dispersion seen at high-ω reflects the segmental motion of PtBS, with the dielectric intensity $\Delta\varepsilon_{\rm seg}^{\rm PtBS}$ (cf. eq 2-30) being considerably smaller than $\Delta\varepsilon_{\rm seg}^{\rm PI}$ of PI and even smaller compared to the intensity $\Delta\varepsilon_{\rm global}^{\rm PI}$ of the global relaxation of PI ($\Delta\varepsilon_{\rm seg}^{\rm PtBS} \cong 0.27\Delta\varepsilon_{\rm seg}^{\rm PI} \cong 0.21\Delta\varepsilon_{\rm global}^{\rm PI}$ when reduced at the same T).

The viscoelastic and dielectric shift factors for PI and for PtBS are plotted against $T-T_{\rm r,bulk}$ in the top and bottom panels of Figure 3-3. The sense of symbols is the same as in Figure 3-1. The values of $T_{\rm r,bulk}$ of PI and PtBS are listed in Table 3-1 (a) and (b), respectively.

For PI samples, the viscoealstic and dielectric shift factors (top panel of Figure 3-3) agree well with each other and are excellently described by the WLF equation of PI shown with the solid curve:

$$\log\ a_{\rm T} = -\frac{4.425\times(T-T_{\rm r,bulk})}{140.0+T-T_{\rm r,bulk}} \tag{3-2}$$

Similarly, the viscoelastic and dielectric shift factors of PtBS samples (bottom panel of Figure 3-3) agree well with each other and are described by the WLF equation of PtBS shown with the solid curve:

$$\log\ a_{\rm T} = -\frac{10.0\times(T-T_{\rm r,bulk})}{116.5+T-T_{\rm r,bulk}} \tag{3-3}$$

The viscoelastic terminal relaxation time, $\tau_{\rm G} = [G'/\omega G'']_{\omega\to 0}$ (eq 2-26) and the steady state recoverable compliance, $J = [G'/G''^2]_{\omega\to 0}$ (eq 2-25), were obtained from the G' and G'' of the PS, PI

and PtBS samples at respective $T_{r,bulk}$ shown in Figure 3-1. For the PI samples, the dielectric terminal relaxation time was evaluated as $\tau_\varepsilon = [\Delta\varepsilon'/\omega\varepsilon'']_{\omega\to 0}$ (eq 2-31). These τ_G and τ_ε data are well defined with respect to the relaxation spectra, as explained in Section 2-2-3. The M dependence of these τ_G and J data is shown with the plus symbols in Figures 3-4 (a), (b), and (c). The τ_ε data for PI are shown with the filled circles in Figure 3-4 (b) for comparison. For PI samples, τ_ε and τ_G are close to each other. This feature confirms that dielectric and viscoelastic relaxation processes of PI detect the same global motion of the chain. However, a non-negligible difference is noted between τ_ε and τ_G. This small difference is due to the different feature of the dielectric and viscoelastic relaxation functions, as explained in Section 2-2-1 and discussed later in more detail.

In Figure 3-4, the unfilled circles and squares indicate the data obtained after subtraction of the moduli due to the glassy mode and the Rouse-fluctuation mode, as explained later. The M dependence of τ_G data exhibits the well-known crossover,[1,2] from $\tau_G \propto M^2$ for low-M to $\tau_G \propto M^{3.5}$ for high-M; cf. Figure 3-4. The J data of PS and PI show the crossover explained earlier for eq 3-1 (Figures 3-4 (a) and (b)), while this crossover is not very clearly observed for PtBS because the maximum M_{PtBS} examined is only 10 times larger than $M_e^{PtBS\ bulk}$.

J is sensitive to the mode distribution and the terminal relaxation intensity. Thus, the changes of J with M seen in Figure 3-4 are indicative of changes of the intensity/mode distribution occurring in the moderately entangled regime (up to $M = M_c'$). These changes can be most clearly noted in Figures 3-5 (a), (b), and (c), where the G' and G'' data for the entangled PS, PI and PtBS samples with $M \geq 1.5M_e$ were shifted along the ω axis and compared with each other. (The sense of symbols is the same as that in Figure 3-1). The PS, PI and PtBS samples with $10^{-3}M$ = 2450, 99 and 348 were chosen as references of the shift. For each polymer species, a set of the G' and G'' data for the other sample was shifted along the ω axis until the low-ω tail of G' ($\propto\omega^2$) of this sample was superposed on the tail of the reference sample. As seen in Figure 3-5, the data for PS and PI at frequencies lower than the G''-peak frequency are satisfactorily superposed only for high-M samples, *i.e.*, $10^{-3}M$ = 186-2450 for PS and $10^{-3}M$ = 53-179 for PI. A non-negligible deviation is noted for middle-M PS ($M \leq 125\times10^3 \cong 7\,M_e^{PS\ bulk}$) and middle-$M$ PI ($M \leq 21\times10^3 \cong 4\,M_e^{PI\ bulk}$). For PtBS examined in Figure 3-5(c), a similar deviation is noted even between the two high-M samples having $10^{-3}M$ = 186 ($\cong 5\,M_e^{PtBS\ bulk}$; unfilled circle) and 348 ($\cong 10\,M_e^{PtBS\ bulk}$; plus symbol). The onset of this deviation (increase of the terminal relaxation intensity) can be noted, but less clearly, also in the plots of J shown in Figure 3-4. Thus, the change of the relaxation mode distribution/intensity with M is most sensitively detected through the comparison of the G' and/or G'' data shifted in this way.

All above features are well established for flexible polymer melts.[1,2] However, the storage and loss moduli due to the glassy mode, G_G' and G_G'' shown with the solid curves in Figure 3-1, do not vanish in the glass-to-rubber regime and even in the terminal regime. Instead, the low-ω tails of these moduli, $G_G' \propto \omega^2$ and $G_G'' \propto \omega$, contribute to the G' and G'' data in those regimes in particular for low-M polymers, as clearly noted in Figure 3-1: For example, G_G'' is as large as 20%, 25% and 30% of the raw G'' data in the terminal regime for the lowest-M PS, PI and PtBS samples, respectively. Consequently, in the range of $M < M_c'$, the J data sensitively characterizing the terminal mode distribution has this non-negligible contribution from the glassy mode. Thus, the Rouse-like, approximate proportionality between the raw J data and M (cf. Figure 3-4) should not be regarded as a rigorous/quantitative evidence of the Rouse proportionality.

3-4 Data Analysis

3-4-1 Viscoelastic moduli contributed from all motional modes

The rheo-optical studies by Inoue et al.[5-8] revealed that the complex modulus G^* (= $G' + iG''$) of flexible polymer melts is contributed from the glassy and rubbery modes (specified by subscripts "G" and "R" below) and expressed as

$$G^*(\omega) = G_G^*(\omega) + G_R^*(\omega) \tag{3-4}$$

Here, the glassy modulus G_G^*, shown with the solid curves in Figure 3-1, reflects the anisotropy of planar orientation (orientation of the normal of the monomeric plane) as well as distortion of the local atomic packing under strain.[5-8] Thus, G_G^* relaxes through the torsional motion of the segments around the chain backbone. In contrast, the rubbery modulus G_R^* detects the anisotropy of axial orientation (orientation of the bond vectors connecting the centers of neighboring segments) and relaxes through the axial rotation of the polymer chain.[5-8] The classical stress-optical rule (eq 2-3) specifies the proportionality between the modulus and the optical anisotropy due to the axial orientation and thus holds in long time scales where the segmental relaxation has completed.

For entangled linear polymers, the rubbery modulus G_R^* can be further divided into two components, G_{Rf}^* due to the entanglement-free Rouse-like fluctuation of the chain length and G_{ent}^* due to the larger-scale motion under the entanglement constraint. G_{ent}^* can be related to both reptation and CR/DTD mechanisms, as discussed later in detail. Since non-entangled chains relax through the Rouse mechanism equivalent to the Rouse-fluctuation mechanism for the entangled

chains, a non-entangled chain of a given molecular weight M_r (< $1.5M_e$) serves as a reference for the entangled chain of the molecular weight M to experimentally evaluate $G_{Rf}^*(\omega, M)$ for the latter:

$$G_{Rf}^*(\omega, M) = b_M\{G^*(\omega', M_r) - G_G^*(\omega')\}_{\omega'=\lambda_M\omega} \quad (3\text{-}5)$$

$$\text{with} \quad b_M = M_r/M \text{ and } \lambda_M = (M/M_r)^2 \quad (3\text{-}6)$$

The raw $G^*(\omega, M_r)$ data for the low-M reference sample appearing in eq 3-5 are contributed from the glassy modulus $G_G^*(\omega)$ so that the subtraction of $G_G^*(\omega)$ is necessary in eq 3-5. The factors b_M and λ_M, respectively, reflect the M dependence of the terminal Rouse relaxation intensity ($\propto M^{-1}$) and the terminal Rouse relaxation time ($\propto M^2$).

A comment needs to be added for eqs 3-5 and 3-6. As seen in Figures 3-1 (a), (b), and (c), the raw G' data of all samples exhibit the M-independent Rouse-type power-law behavior ($G' \propto \omega^{1/2}$) in the low-ω side of the rubber-to-glass transition zone where the glassy G_G' negligibly contributes to the G' data. For entangled linear polymers, Osaki et al.[19-21] evaluated the longest Rouse fluctuation time by extrapolating this Rouse-type power-law behavior of the G' data to lower ω where a G' value expected for a hypothetical non-entangled Rouse chain of the same molecular weight was obtained, as explained earlier for eq 2-27. Thus, the method of evaluating of G_{Rf}^* shown in eqs 3-5 and 3-6 is in harmony with the method of Osaki et al.[19-21] In relation to this point, it is worth mentioning that a reptation-based molecular model of Milner and McLeish[22] argued that the Rouse fluctuation is the one dimensional motion (along the tube representing the entanglement mesh) thereby assuming that the Rouse fluctuation intensity is one third of the intensity for the hypothetical high-M Rouse chain (one third of the intensity adopted by Osaki et al.[19-21]) in a time scale longer than the thermal equilibration time of a entanglement strand. However, the longest Rouse fluctuation time evaluated by Osaki et al. successfully described both the linear and nonlinear relaxation behavior[19,21] of well entangled polymers. (In addition, the argument by Milner and McLeish[22] appears to fail for entangled star-branched chains that is considered to fully relax through the *one dimensional* arm length fluctuation.[3,4]) For this reason, eqs 3-5 and 3-6 can be safely adopted for the evaluation of the Rouse fluctuation modulus for the entangled PS, PI and PtBS.

Thus, for the entangled PS, PI and PtBS chains of the molecular weight M, $G_{ent}^*(\omega,M)$ due to the large scale motion under the entanglement constraint can be evaluated from their raw $G^*(\omega, M)$ data, the $G_G^*(\omega)$ data reported by Inoue et al.[5,7,9] (cf. solid curves in Figure 3-1), and the raw $G^*(\omega, M_r)$ data for the non-entangled reference chain of the molecular weight M_r as (cf. eqs 3-4 to 3-6):

$$G_{ent}^*(\omega, M) = G^*(\omega, M) - G_G^*(\omega) - G_{Rf}^*(\omega) \quad (3\text{-}7a)$$

with $G_{Rf}^*(\omega, M) = \{M_r/M\}\{G^*(\omega', M_r) - G_G^*(\omega')\}_{\omega'=(M/M_r)^2\omega}$ (3-7b)

The $G^*(\omega, M_r)$ data for non-entangled PS with $M_r = 23\times10^3$ ($\cong M_e^{PS\ bulk}$), PI with $M_r = 3\times10^3$ ($\cong M_e^{PI\ bulk}$), and PtBS with $M_r = 42\times10^3$ ($\cong M_e^{PtBS\ bulk}$) shown in Figure 3-1 were utilized as the reference modulus appearing in eq 3-7b to evaluate $G_{ent}^*(\omega, M)$ in the terminal regime for the entangled PS, PI and PtBS samples. Figure 3-6 demonstrates an example of this evaluation for a PS sample with $M = 61\times10^3$. From the raw G^* data of this PS shown with the cross and plus symbols for G' and G'', the G_G^* data (dotted curve for G_G''; G_G' is smaller than 10^1 Pa at ω examined in Figure 3-6), and the G_{Rf}^* data (solid curves) were subtracted to give G_{ent}' (circles) and G_{ent}'' (squares). The plateau and peak, respectively, are observed for G_{ent}' and G_{ent}'' much more clearly than for the raw G' and G'' data (because of the subtraction in eq 3-7a). Similar results were found for all entangled PS, PI and PtBS samples.

In Figures 3-7 (a), (b), and (c), respectively, G_{ent}^* thus obtained for the entangled PS, PI and PtBS samples are shifted along the ω axis, as done for the raw G^* data in Figure 3-5. (The sense of symbols is the same as that in Figure 3-1.) The solid curves in Figure 3-7(b) were calculated from the ε'' data of a reference PI with $10^{-3}M = 99$. The details of this calculation are explained later. In Figure 3-4, the relaxation time τ_{ent} ($= [G_{ent}'/\omega G_{ent}'']_{\omega\to0}$) and compliance J_{ent} ($= [G_{ent}'/G_{ent}''^2]_{\omega\to0}$) corresponding to those G_{ent}^* data are shown with the unfilled squares. Comparison of Figures 3-7(a), (b), and (c) with Figures 3-5(a), (b), and (c) reveals that the terminal relaxation mode distribution and relaxation intensity of G_{ent}^* are much more insensitive to M compared to those of the raw G^* data, in particular in the lightly to moderately entangled regime ($2M_e < M < M_c'$). It is remarkable that G_{ent}^* of PI and PS is essentially independent of M in the entire range of $M \geq 1.5M_e$. This behavior of G_{ent}^* is well reflected in the M-insensitivity of the J_{ent} data shown in Figure 3-4 (squares). The corresponding relaxation time τ_{ent} obeys the $M^{3.5}$ proportionality better than τ evaluated from the raw G^* data (cf. Figures 3-4 (a), (b), and (c)). All these results suggest that the crossover from the non-entangled, Rouse behavior to the entangled, reptation-like behavior occurring in the range of $2M_e < M < M_c'$ reflects appearance of the entanglement relaxation mode having *M-insensitive mode distribution* superposed onto the Rouse fluctuation mode.

Here, a comment needs to be made for the rubbery relaxation of non-entangled chains. This relaxation is identical to that due to the Rouse fluctuation and characterized by $G_R^*(\omega) = G^*(\omega) - G_G^*(\omega)$ (cf. eq 3-4). The G_G^* data (solid curves in Figure 3-1) were utilized to obtain G_R^*, the corresponding compliance J_R ($= [G_R'/G_R''^2]_{\omega\to0}$), and the relaxation time τ_R ($= [G_R'/\omega G_R'']_{\omega\to0}$). In Figures 3-4 (a), (b), and (c), J_R and τ_R for the non-entangled chains are shown with the circles. Non-negligible deviation is noted for J and τ (symbols) and J_R and τ_R (circles) for non-entangled chains.

This fact in turn demonstrates the importance of the glassy modulus for the terminal relaxation of non-entangled low-M chains.

3-4-2 Test of DTD/CR mechanism for the relaxation of well-entangled PI chains

The relationship between the slow dielectric and viscoelastic relaxation processes has been discussed extensively for the PI chains in bulk, solutions and blends by Watanabe and coworkers.[3, 23-25] In general, the normalized dielectric relaxation function $\Phi(t)$ (cf. eq 2-6) and the normalized viscoelastic relaxation function $\mu(t)$ (= $G(t)/G(0)$ with $G(0)$ being the initial modulus; $G(0) = G_N$ if the focus is placed on the entanglemental relaxation) reflect the same global motion of PI chains from different aspects, *i.e.*, $\Phi(t)$ characterizes the *orientation correlation* of the end-to-end vector of the PI chains at two separate times 0 and t (eq 2-6), while $\mu(t)$ characterizes the *isochronal orientational anisotropy* of the individual segments (eqs 2-1 and 2-2). The relationship between $\Phi(t)$ and $\mu(t)$ is not unique and strongly depends on the details of the relaxation dynamics of PI. Chapters 4, 5, and 6 discuss this relationship for PI in the PI/PtBS blends. Here, a brief summary is given for the relationship for entangled linear PI melts derived by Matsumiya et al. under the concept of the dynamic tube dilation/constraint release (DTD/CR).[24]

In the molecular picture of DTD, the relaxed portions of the chain are regarded as a solvent. The dielectric relaxation function $\Phi(t)$ is related to the auto-correlation of end-to-end vector for the *portion of backbone remaining in the initial tube.* On the other hand, the viscoelastic relaxation function $\mu(t)$ is proportional to the *number of entanglements surviving in a hypothetical, equivalent solution* with the concentration $\cong \Phi(t)$. Then, $\Phi(t)$ and $\mu(t)$ satisfy a relationship:

$$\mu(t) \cong [\Phi(t)]^{1+\alpha} \quad \text{with the dilation factor } \alpha \cong 1 \tag{3-8}$$

The validity of this DTD relationship has a pre-requisite: the lateral motion of chains due to the CR mechanism occurs actively so that the equilibration is always achieved over a length scale of a' ($=a/\Phi(t)^{\alpha/2}$), the effective entanglement mesh size of the respective chains in the equivalent solution.[3,24,25]

Eq 3-8 can be converted in the frequency domain. The complex dielectric constant $\varepsilon^*(\omega)$ is the Fourier transformation of $\Phi(t)$ and can be expressed in terms of the intensity $h_{\varepsilon,p}$ and relaxation time $\tau_{\varepsilon,p}$ of the p-th dielectric mode associating to $\Phi(t)$ (cf. eq 2-29):

$$\frac{\Delta\varepsilon' + i\varepsilon''(\omega)}{\Delta\varepsilon} = \sum_p h_{\varepsilon,p} \frac{\omega^2 \tau_{\varepsilon,p}{}^2 + i\omega\tau_{\varepsilon,p}}{1 + \omega^2 \tau_{\varepsilon,p}{}^2} \tag{3-9}$$

From eq 3-8, the viscoelastic moduli can be expressed with the same set of $h_{\varepsilon,p}$ and $\tau_{\varepsilon,p}$ as:

$$\frac{G'(\omega) + iG''(\omega)}{G_N} = \sum_{p,q} h_{pq} \frac{\omega^2 \tau_{pq}{}^2 + i\omega\tau_{pq}}{1 + \omega^2 \tau_{pq}{}^2} \tag{3-10}$$

with $h_{pq} = h_{\varepsilon,p} h_{\varepsilon,q}$ and $\tau_{pq} = [\tau_{\varepsilon,p}{}^{-1} + \tau_{\varepsilon,q}{}^{-1}]^{-1}$.

Eqs 3-9 and 3-10 allow a test of the validity of the DTD/CR mechanism (eq 3-8) through comparison of the $G^*(\omega)$ and $\varepsilon''(\omega)$ data. In the studies of Matsumiya et al.,[24] this test was made at frequencies where $G_G^*(\omega)$ and $G_{Rf}^*(\omega)$ were negligibly contributing to the $G^*(\omega)$ data. The modulus $G_{ent}^*(\omega)$ resolved in this chapter enables the comparison in a wider frequency window.

Figure 3-8 compares the raw $\varepsilon''(\omega)$ data obtained for entangled PI samples with $10^{-3}M$=9-128. The sense of symbols is the same as in Figure 3-1. The raw ε'' data are shifted along the ω axis by a factor of Λ to superpose the ε'' peak on that of the reference sample with $10^{-3}M$ = 99. Clearly, the mode distribution of ε'' is quite insensitive to M for entangled PI, as reported by Watanabe et al.[23,24] The solid curve is the fit of $\varepsilon''(\omega)$ of the reference PI sample with eq 3-9. The intensity $h_{\varepsilon,p}$ and relaxation time $\tau_{\varepsilon,p}$ were evaluated by the iteration method explained by Watanabe et al.[25] The same sets of $h_{\varepsilon,p}$ and $\tau_{\varepsilon,p}$ were utilized to calculate $G^*(\omega)/G_N$ given by eq 3-10. The $G^*(\omega)$ data thus obtained, shown with the solid curve in Figure 3-7(b), agree well with the $G_{ent}^*(\omega)$ data for the reference PI ($10^{-3}M$=99). Furthermore, Λ utilized in Figure 3-8 is very close to λ utilized in Figure 3-7(b) (within a difference of 0.1 in the logarithmic scale). Thus, the M insensitivity of G_{ent}^* and ε'' and the validity of the DTD/CR molecular picture found for the reference PI are concluded for all entangled PI samples examined in this chapter.

3-5 Concluding Remarks

The viscoelastic terminal relaxation mode distribution was examined for linear PS, PI and PtBS chains. The viscoelastic mode distribution, reflected in the ω dependence of the raw G^* data and the corresponding J data, considerably changed with M in the light to moderately entangled regime ($2M_e < M < M_c'$). However, this change of the mode distribution was largely contributed from the glassy relaxation and Rouse fluctuation occurring in prior to the entanglement relaxation. The modulus G_{ent}^* exclusively reflecting the entanglement relaxation, obtained after subtraction of the

moduli due to the glassy relaxation and Rouse fluctuation, and the corresponding J_{ent} were rather insensitive to M even in the light to moderately entangled regime and close to those of well entangled high-M polymers, in particular for the case of PS and PI. Thus, the crossover from the non-entangled behavior to the entangled behavior occurring in that regime appears to reflect the emergence of the entanglement relaxation having *M-insensitive* mode distribution superposed onto the Rouse fluctuation mode.

For PI chains having non-inverted type-A dipole, the DTD/CR mechanism was examined through comparison of the G_{ent}* data and the dielectric data, the latter detecting the fluctuation of end-to-end vector. This mechanism was found to be valid for all monodispersed entangled PI samples examined in this chapter.

Appendix 3-1 WLF analysis

For homopolymer, the characteristic time of the Rouse segments τ_s depends not only on the temperature but also on the concentration of chain ends. This effect vanishes for samples with sufficient high-M, for which an increase of τ_s with M has been saturated. Then, for samples with low-M and unsaturated τ_s, a WLF correction is needed to compensate the chain end effect. This correction allows a comparison of data for homopolymer samples in the iso-τ_s state over a wide range of M.

The WLF-type shift factor a_T (cf. eq 2-35) of homopolymer, defined with respect to an arbitrarily chosen reference temperature $T_{r,bulk}$, exhibits the temperature dependence:[2,13,22]

$$\log a_T = -\frac{C_1(T - T_{r,bulk})}{C_2 + T - T_{r,bulk}} \qquad \text{(A3-1-1)}$$

C_1 and C_2 are the WLF coefficients that are related, within the *free volume model*, to the fractional free volume $f(T_{r,bulk})$ at $T_{r,bulk}$ and the thermal expansion coefficient of the free volume α_f as $C_1 = 0.4343/f(T_{r,bulk})$ and $C_2 = f(T_{r,bulk})/a_f$. These coefficients can be determined from plots of $(\log a_T)^{-1}$ data gainst $(T–T_{r,bulk})^{-1}$: The plots give a straight line with a slope of $–C_2/C_1$ and an intercept of $–1/C_1$ (as long as a_T obeys the WLF eq A3-1-1).

For low-M samples with unsaturated τ_s, the values of f and a_f can be determined from the C_1 and C_2 data. Obviously, f of low-M samples is different from f^∞ of high-M samples at the same T. Then, for low-M samples, a new reference temperature $T^\infty_{r,bulk}$ having $f(T^\infty_{r,bulk}) = f^\infty$ can be calculated as $T^\infty_{r,bulk} = T_{r,bulk} + \{f^\infty - f(T_{r,bulk})\}/\alpha_f$. $T^\infty_{r,bulk}$ thus determined is termed as iso-τ_s temperature (or iso-fractional free volume temperature since the fractional free volume f has been corrected).

For the high-M bulk PS, PI, and PtBS samples, the WLF eqs 3-2, 3-3 and WLF equation (for PS) in Ref 15 give $f^\infty(T^{PI}_{r,bulk} = 30°C) = 0.098_1$, $f^\infty(T^{PtBS}_{r,bulk} = 180°C) = 0.043_4$, and $f^\infty(T^{PS}_{r,bulk} = 180°C) = 0.070_7$, respectively.[15,17,26] These values enable an evaluation of $T^\infty_{r,bulk}$ for the low-M samples as listed in Table 3-1 ($T^\infty_{r,bulk} = T_{r,bulk}$ for high-M samples).

Here, a comment is needed for the $T^\infty_{r,bulk}$ determined from the standard WLF analysis explained above: $T^\infty_{r,bulk}$ is also referred to as the iso-frictional (or iso-ζ_s) temperature in literature.[16,17] Strictly speaking, it is the characteristic time of Rouse segments τ_s ($\propto \zeta_s/T$) not ζ_s, that has the same value after the WLF analysis of the shift factor (cf. Section 2-2-3-3). Nevertheless, the T dependence of ζ_s is usually much stronger than that of $1/T$ (with T in K unit) so that the friction coefficient ζ_s is almost the same at $T^\infty_{r,bulk}$.

The WLF analysis can be also utilized for a component being plascitized or anti-plasticized in polymer solutions/blends. If a component is plascitized/anti-plasticized, an iso-τ_s temperature T_{iso} lower/higher than $T_{r,bulk}$ should be chosen for this component in the solutions/blends to achieve the same τ_s as the bulk component at $T_{r,bulk}$. The method for determining T_{iso} is essentially the same as the method explained above.

References

1. Graessley W.W. *Adv Polym Sci* **1974**, 16, 1-179.
2. Ferry J.D., *Viscoelastic Properties of Polymers*, 3rd ed, Wiley, New York, **1980**.
3. Watanabe H., *Prog Polym Sci* **1999**, 24, 1253-1403.
4. McLeish T.C.B., *Adv Phys* **2002**, 51, 1379-1527.
5. Inoue T.; Okamoto H.; Osaki K., *Macromolecules* **1991**, 24, 5670-5675.
6. Inoue T.; Mizukami Y.; Okamoto T.; Matsui H.; Watanabe H.; Kanaya T.; Osaki K., *Macromolecules* **1996**, 29, 6240-6245.
7. Inoue T.; Matsui H.; Osaki T., *Rheol Acta* **1997**, 36, 239-244.
8. Inoue T., *Nihon Reoroji Gakkaishi* **2000**, 28, 167-175.
9. Okamoto H.; Inoue T.; Osaki K., *J Polym Sci Part B Polym Phys* **1995**, 33, 417-424.
10. de Gennes PG. *J Chem Phys* **1971**, 55, 572 – 579.
11. Doi, M.: Edwards, S. F. *The Theory of Polymer Dynamics*, Oxford University Press: New York,**1986**.
12. Graessley, W. W. *Adv. Polym. Sci.* **1982**, 47, 67-117.
13. Marrucci, J. *Polym. Sci., Polym. Phys. Ed.* **1985**, 23, 159-177
14. Schausberger A.; Schindlauer G.; Janeschitz-Kriegl H.; *Rheol Acta* **1985**, 24, 220-227.
15. Watanabe H.; Sakamoto T.; Kotaka T., *Macromolecules* **1985**, 18, 1436-1442.
16. Watanabe H.; Matsumiya Y.; Takada J.; Sasaki H.; Matsushima Y.; Kuriyama A.; Inoue T., Ahn K.H.; Yu W., Krishnamoorti R., *Macromolecules* **2007** , 40, 5389-5399.
17. Chen Q.; Matsumiya Y.; Masubuchi Y.; Watanabe H.; Inoue T., *Macromolecules* **2008**, 41, 8694-8711.
18. Fetters L.J.; Loshe D.J.; Colby R.H., *Chain Dimensions and Entanglement Spacings, in Mark JE ed Physical Properties of Polymers Handbook,* 2nd ed, Springer, New York, **2007**.
19. Osaki K.; Inoue T.; Isomura T., *J Polym Sci Part B Polym Phys* **2000**, 38, 2043-2050.
20. Osaki K.; Inoue T.; Isomura T., *J Polym Sci Part B Polym Phys* **2000**, 38, 3271-3276.
21. Osaki K.; Inoue T.; Uematsu T.; Yamashita Y., *J Polym Sci Part B Polym Phys* **2001**, 39, 1704-1712.

22. Milner S.T.; McLeish T.C.B., *Phys Rev Lett* **1998**, 81, 725-728.
23. Watanabe, H., *Macromol. Rapid Commun.* **2001**, 22, 127-175.
24. Matsumiya, Y.; Watanabe, H.; Osaki K. *Macromolecules* **2000**, 33, 499-506.
25. Watanabe, H.; Matsumiya, Y.; Inoue T. *Macromolecules* **2002**, 35, 2339-2357.
26. Colby, R.H.; Fetters, L.J.; Graessley, W.W. *Macromolecules* **1987**, 20, 2226-2237
27. Fetters, L.J.; Loshe, D.J.; Colby, R.H. *Chain Dimensions and Entanglement Spacings, in Mark JE ed Physical Properties of Polymers Handbook,* 2nd ed, Springer, New York, **2007**.

Table 3-1(a). Characteristics of PI samples

Code	$10^{-3}M_w$	M_w/M_n	$T^{\infty}_{r,bulk}$ /°C	R_{PI}/nm [a]
PI3	3.0	1.07	25	4.5
PI9	8.8	1.03	29	7.7
PI21	21.0	1.04	30	11.9
PI53	53.4	1.03	30	19.0
PI99	98.5	1.04	30	25.9
PI128	128	1.03	30	29.5
PI179	179	1.06	30	34.9

Table 3-1(b). Characteristics of PtBS samples

Code	$10^{-3}M_w$	M_w/M_n	$T^{\infty}_{r,bulk}$ /°C	R_{PtBS}/nm
PtBS16	16.4	1.02	171	7.7
PtBS27	27.2	1.02	180	9.9
PtBS42	41.8	1.04	180	12.3
PtBS70	69.5	1.03	180	15.8
PtBS91	91.1	1.03	180	18.1
PtBS186	186	1.02	180	25.9
PtBS348	348	1.05	180	35.4

Table 3-1(c). Characteristics of PS samples

Code	$10^{-3}M_w$	M_w/M_n	$T^{\infty}_{r,bulk}$ /°C	R_{PS}/nm
PS10	9.5	1.02	175	6.4
PS23	23.4	1.07	180	10.1
PS39	38.9	1.07	180	13.0
PS61	61	1.06	180	16.3
PS96	96.4	1.03	180	20.5
PS125	125	1.05	180	23.3
PS292	292	1.07	180	35.7
PS757	757	1.07	180	57.5
PS2450	2450	1.05	180	103.4

a: The end-to-end distance of the chain was calculated by $R_X^2=[<R^2>/M]_X M_X$ (X = PI, PtBS and PS), with $[<R^2>/M]_X$ = 6.79×10^{-3}, 3.61×10^{-3} and 4.37×10^{-3}nm^2 for PI, PtBS and PS, respectively.[27]

b: The overlapping concentration, $C_{PtBS}^* = \{M_{PtBS}/N_A\}/\{4\pi R_{g,PtBS}^3/3\}$, was evaluated from the root-mean-square radius of gyration $R_{g,PtBS}= \sqrt{R_{PtBS}^2/6}$.

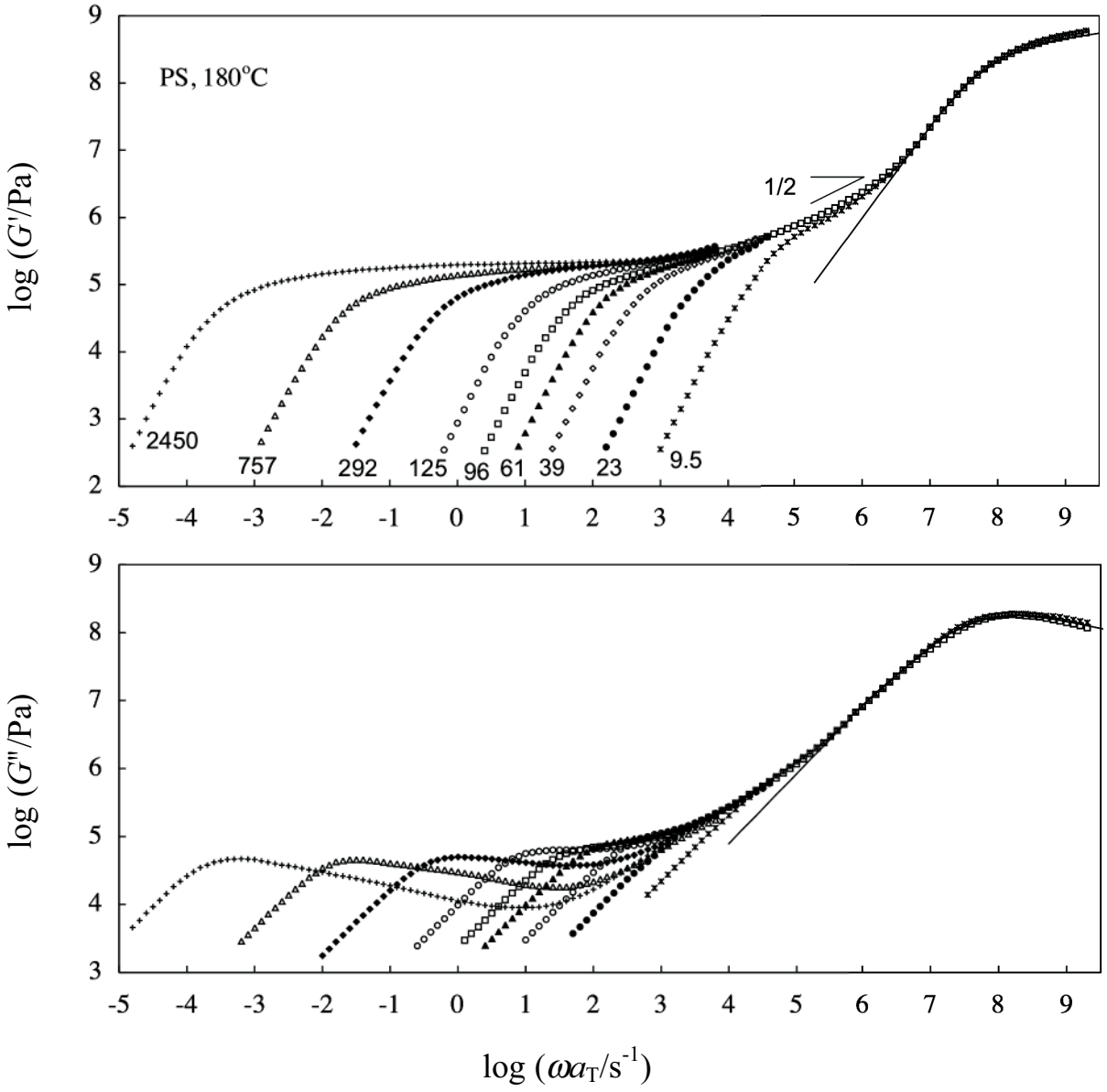

Fig. 3-1 (a): Linear viscoelastic modulus of monodisperse PS samples at 180°C.[14,15] The numbers attached to the G' curves indicate $10^{-3}M$. The solid curves indicate the literature data[5] for the modulus due to the glassy mode.

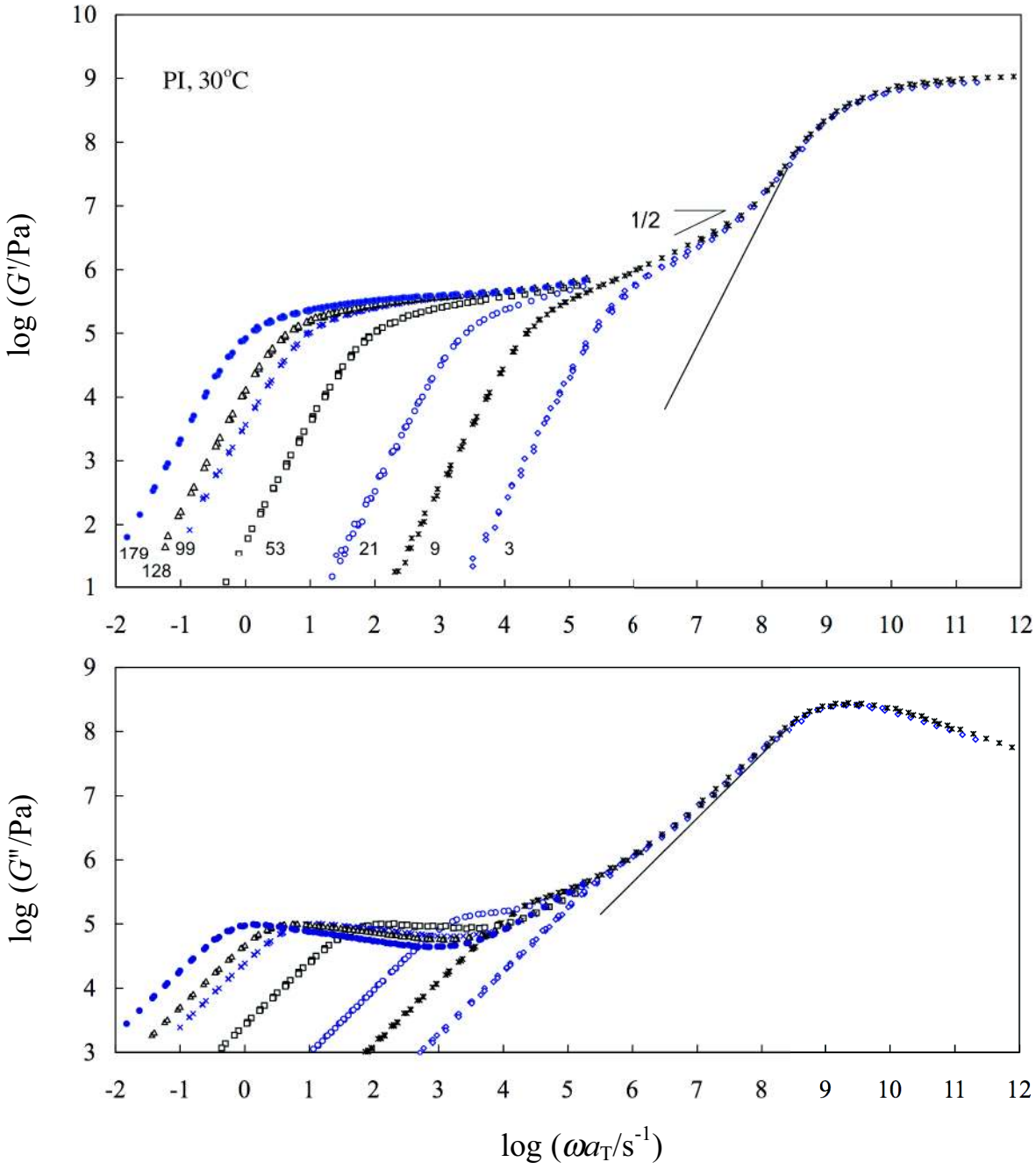

Fig. 3-1 (b): Linear viscoelastic modulus of monodisperse PI samples at 30°C. The numbers attached to the G' curves indicate $10^{-3}M$. The solid curves indicate the literature data[9] for the modulus due to the glassy mode.

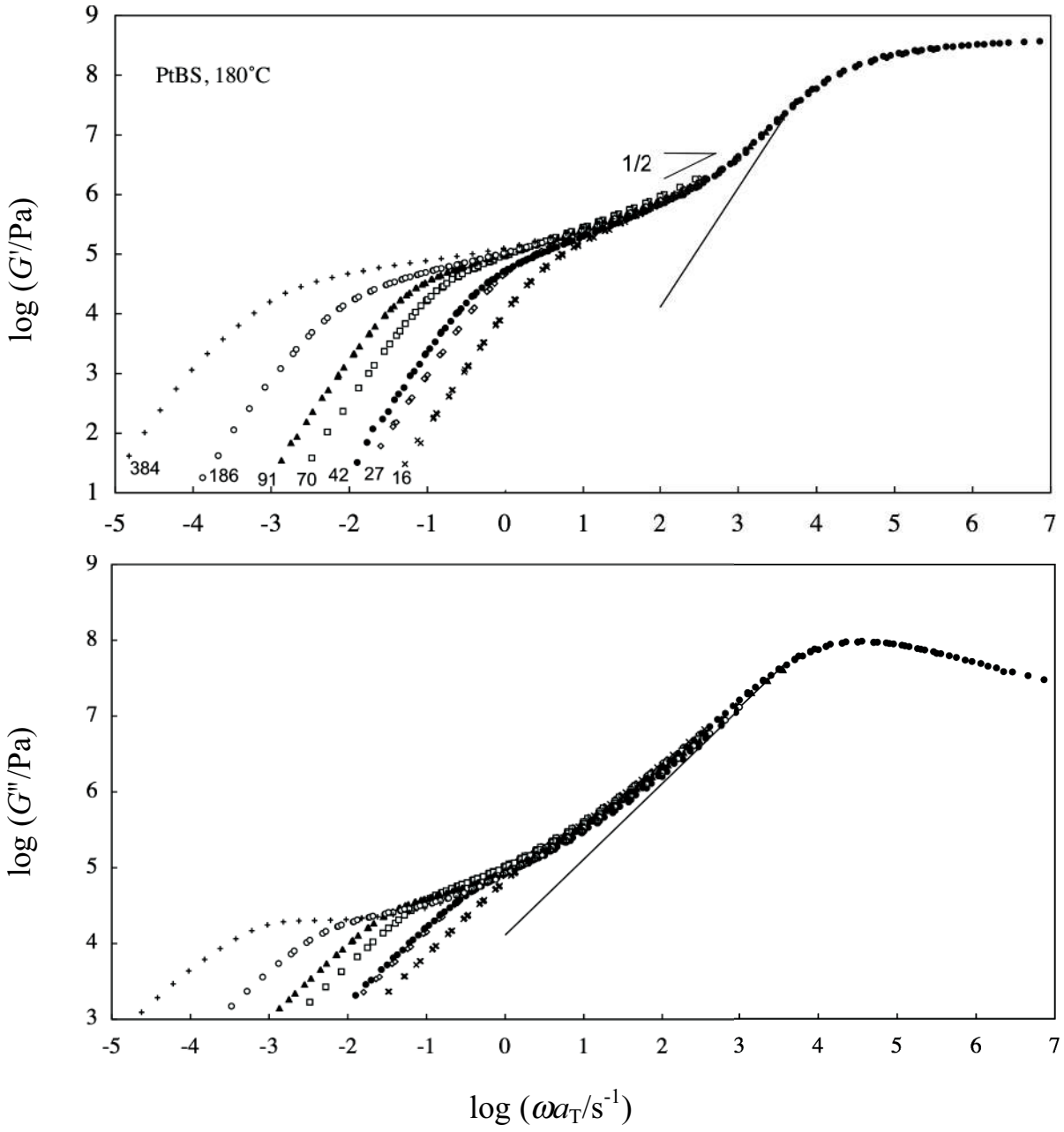

Fig. 3-1 (c): Linear viscoelastic modulus of monodisperse PtBS samples at 180°C. The numbers attached to the G' curves indicate $10^{-3}M$. The solid curves indicate the literature data[7] for the modulus due to the glassy mode.

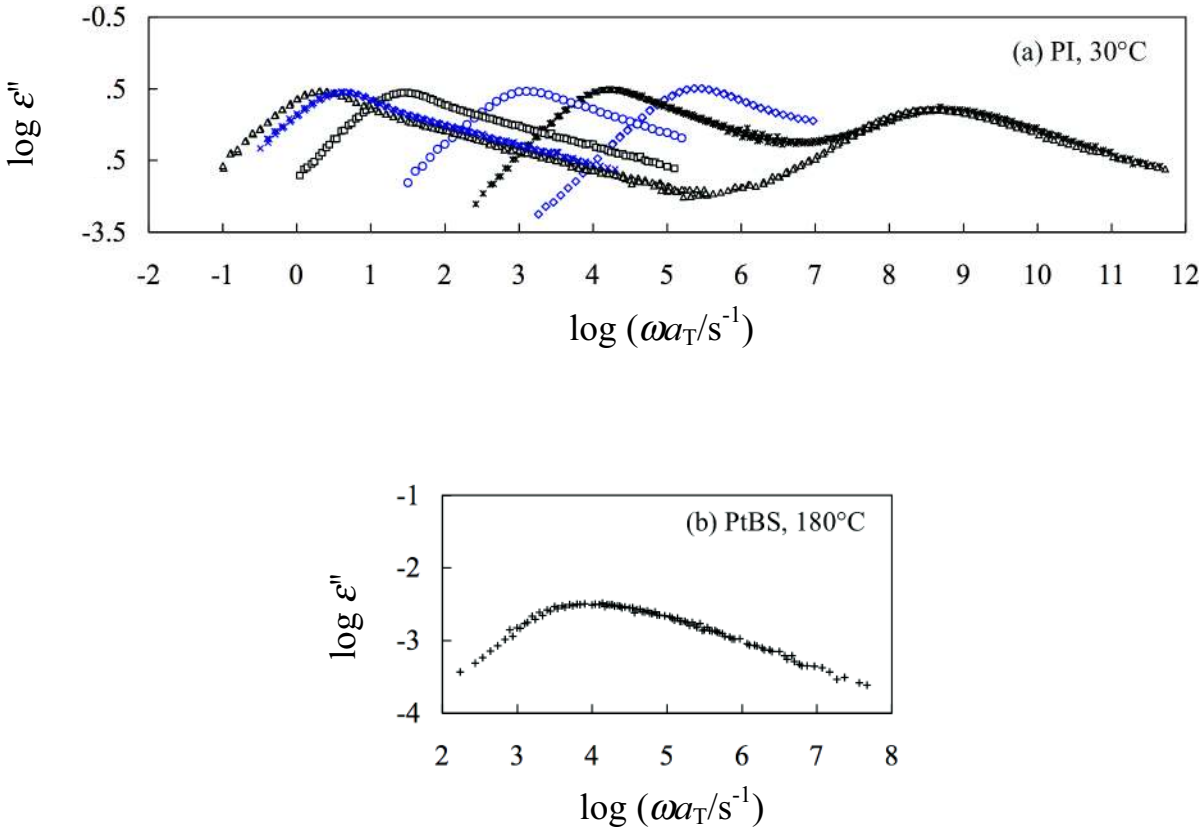

Fig. 3-2: Dielectric loss, ε'', of (a) the PI samples at 30°C, and (b) PtBS sample at 180°C. The sense of symbols is the same as in Figure 3-1.

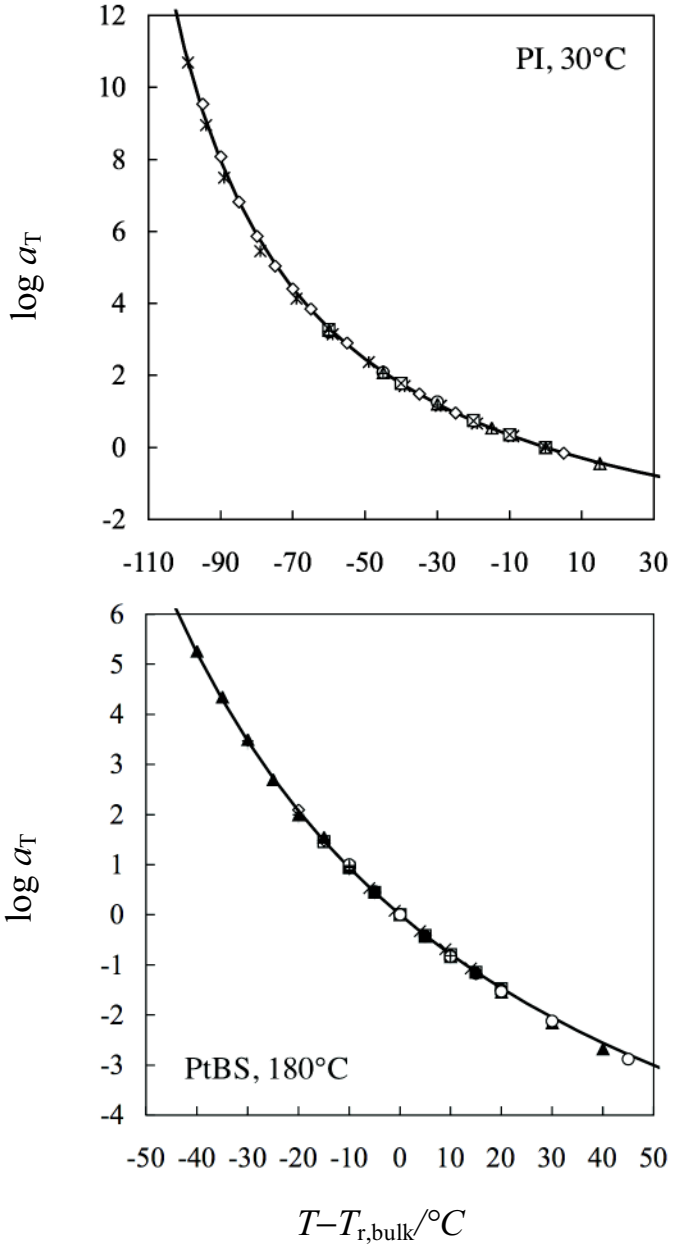

Fig. 3-3: Shift factor a_T obtained for viscoelastic data (Figure 3-1) and dielectric data (Figure 3-2) for the PI and PtBS samples. a_T is plotted against $T-T_{r,bulk}$, with the reference temperature $T_{r,bulk}$ = 30°C and 180°C for PI and PtBS, respectively. The sense of symbols is the same as in Figure 3-1. The solid curves indicate the WLF equation for PI (eq 3-2, top panel) and PtBS (eq 3-3, bottom panel).

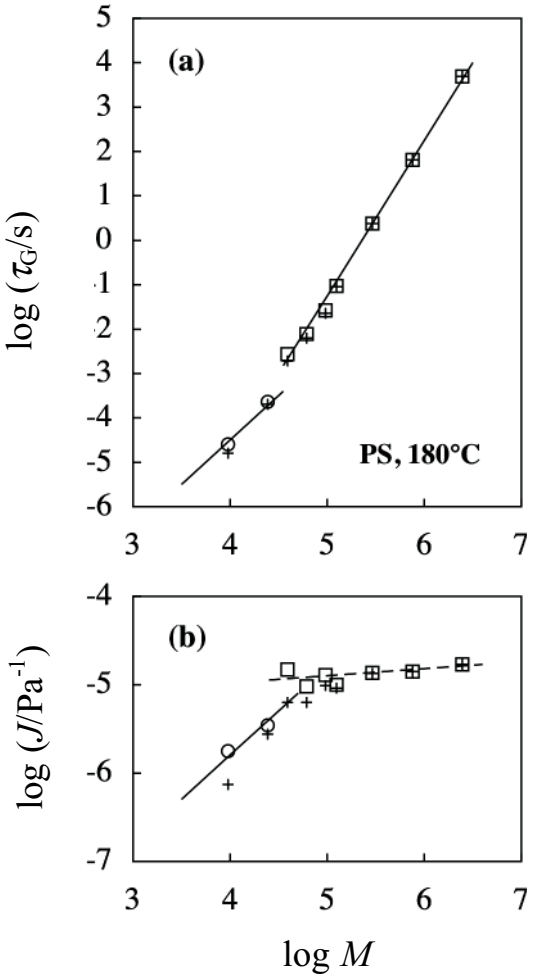

Fig. 3-4 (a): Molecular weight dependence of **(a)** terminal viscoelastic relaxation time τ_G and **(b)** steady state recoverable compliance J of monodisperse PS samples at 180°C. The plus symbol indicates τ_G and J evaluated from the raw G' and G'' data shown in Figure 3-1, the square shows τ_{ent} and J_{ent} of entangled PS obtained after subtraction of the moduli due to the glassy and Rouse fluctuation modes from the G' and G'' data, and the circle denotes τ_R and J_R of non-entangled PI obtained after subtraction of the modulus due to the glassy mode.

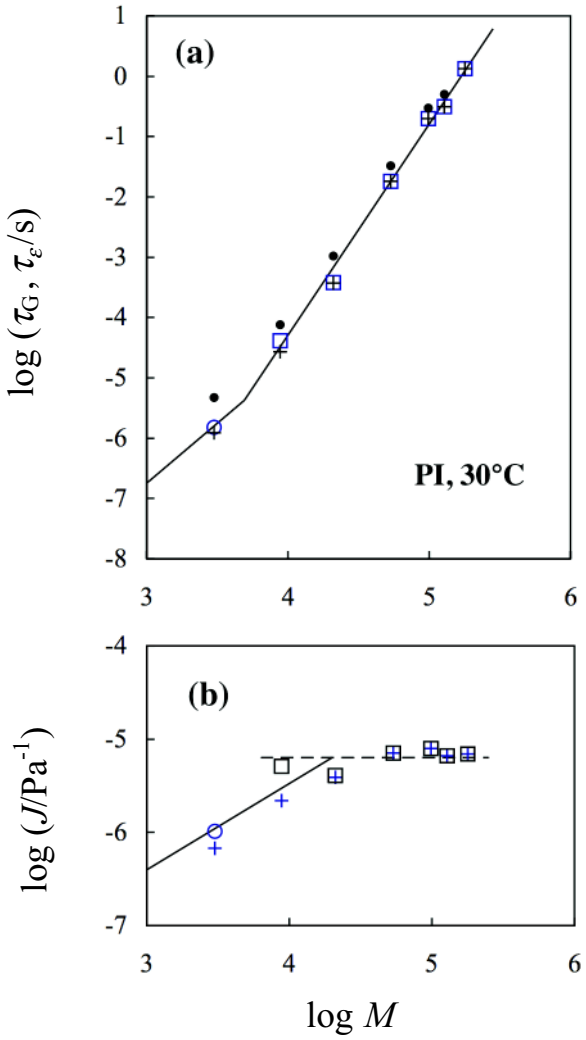

Fig. 3-4 (b): Molecular weight dependence of **(a)** terminal viscoelastic relaxation time τ_G and **(b)** steady state recoverable compliance J of monodisperse PI samples at 30°C. The plus symbol indicates τ_G and J evaluated from the raw G' and G'' data shown in Figure 3-1(b), the square shows τ_{ent} and J_{ent} of entangled PI obtained after subtraction of the moduli due to the glassy and Rouse fluctuation modes from the G' and G'' data, and the circle denotes τ_R and J_R of non-entangled PI obtained after subtraction of the modulus due to the glassy mode. The dielectric terminal relaxation time τ_ε of PI samples is added for comparison (filled circles).

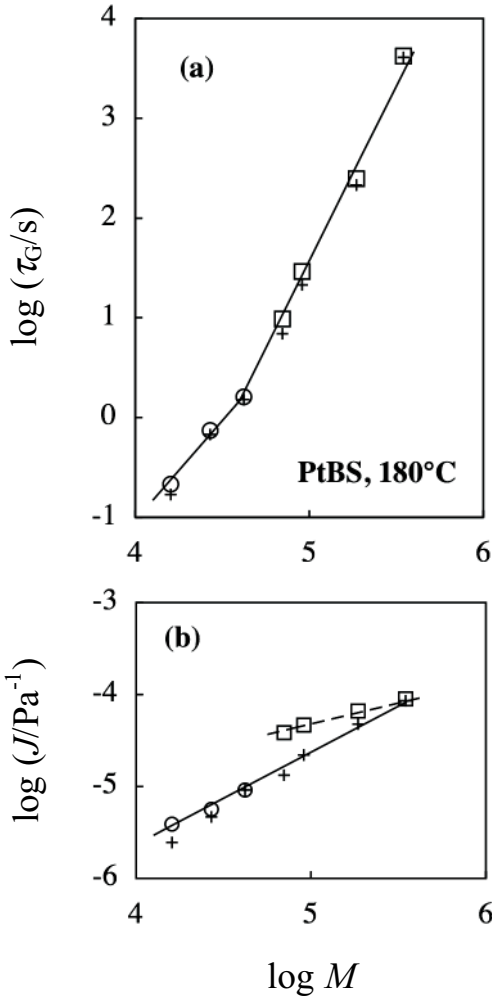

Fig. 3-4 (c): Molecular weight dependence of **(a)** terminal viscoelastic relaxation time τ_G and **(b)** steady state recoverable compliance J of monodisperse PtBS samples at 180°C. The plus symbol indicates τ_G and J evaluated from the raw G' and G'' data shown in Figure 3-1(c), the square shows τ_{ent} and J_{ent} of entangled PtBS obtained after subtraction of the moduli due to the glassy and Rouse fluctuation modes from the G' and G'' data, and the circle denotes τ_R and J_R of non-entangled PtBS obtained after subtraction of the modulus due to the glassy mode.

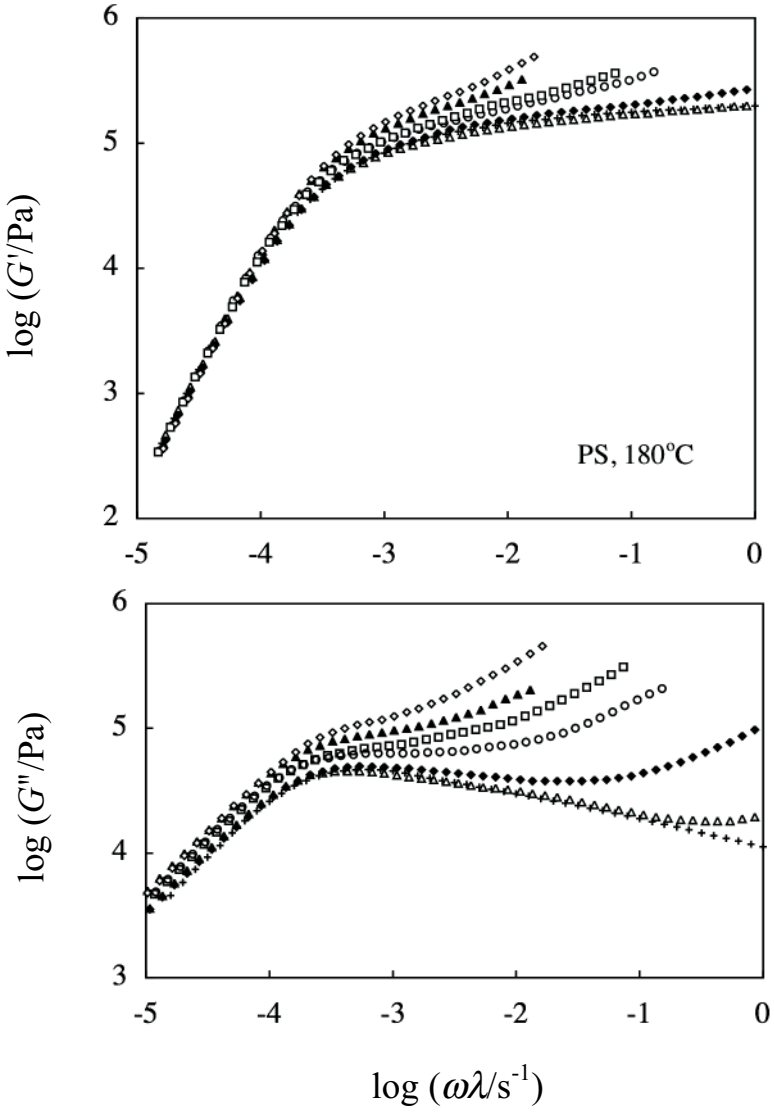

Fig. 3-5 (a): Comparison of terminal viscoelastic relaxation mode distribution for PS samples at 180°C. The sense of the symbols is the same as in Figure 3-1(a). The G^* data are shifted along the ω axis by appropriate factors λ to superpose the low-ω tails of the G' data.

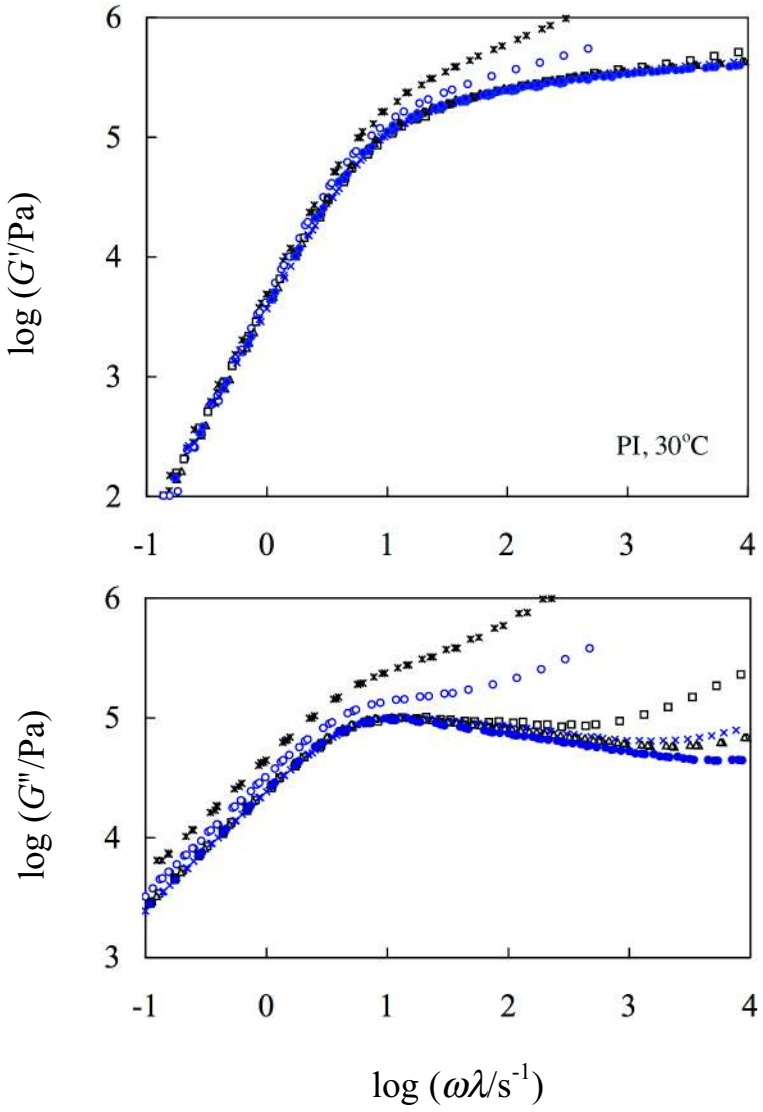

Fig. 3-5 (b): Comparison of terminal viscoelastic relaxation mode distribution for PI samples at 30°C. The sense of the symbols is the same as in Figure 3-1(b). The G^* data are shifted along the ω axis by appropriate factors λ to superpose the low-ω tails of the G' data.

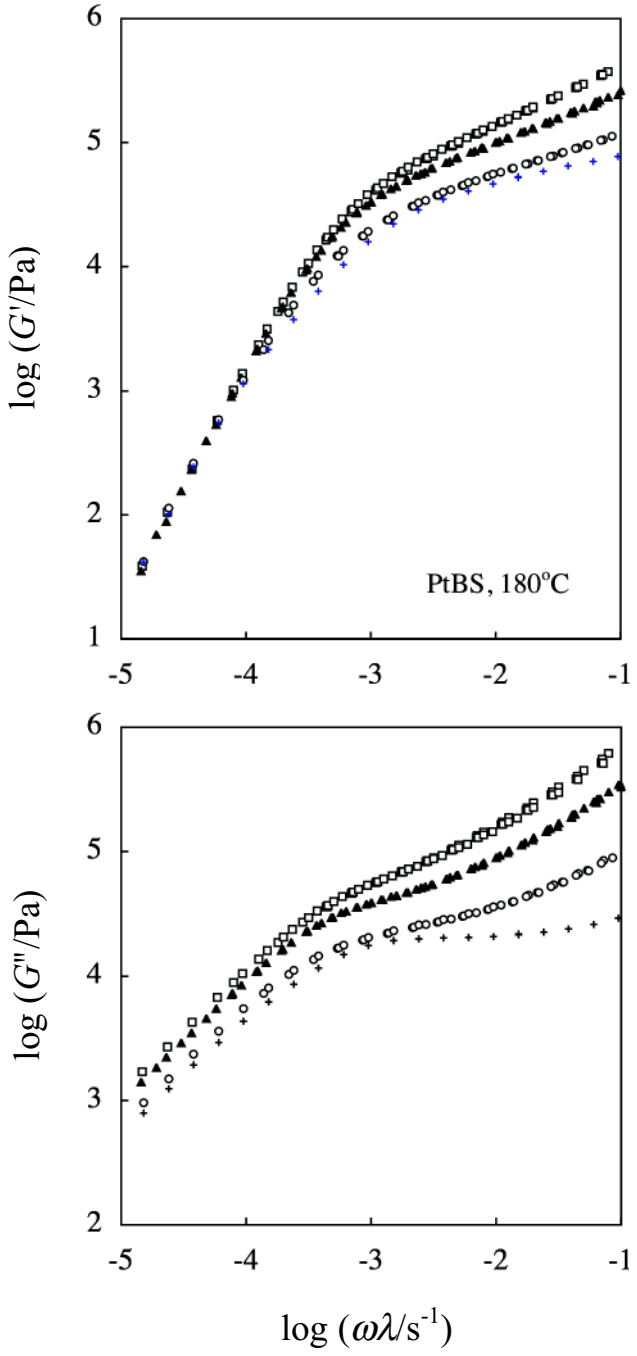

Fig. 3-5 (c): Comparison of terminal viscoelastic relaxation mode distribution for PtBS samples at 180°C. The sense of the symbols is the same as in Figure 3-1(c). The G^* data are shifted along the ω axis by appropriate factors λ to superpose the low-ω tails of the G' data.

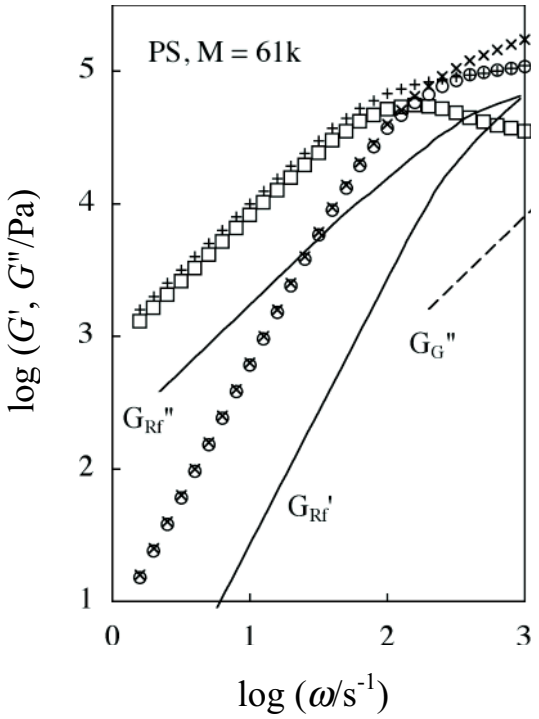

Fig. 3-6: Evaluation of G_{ent}' (circle) and G_{ent}'' (square) exclusively reflecting the entanglement relaxation of a PS sample with $M = 61\times10^3$ at 180°C.

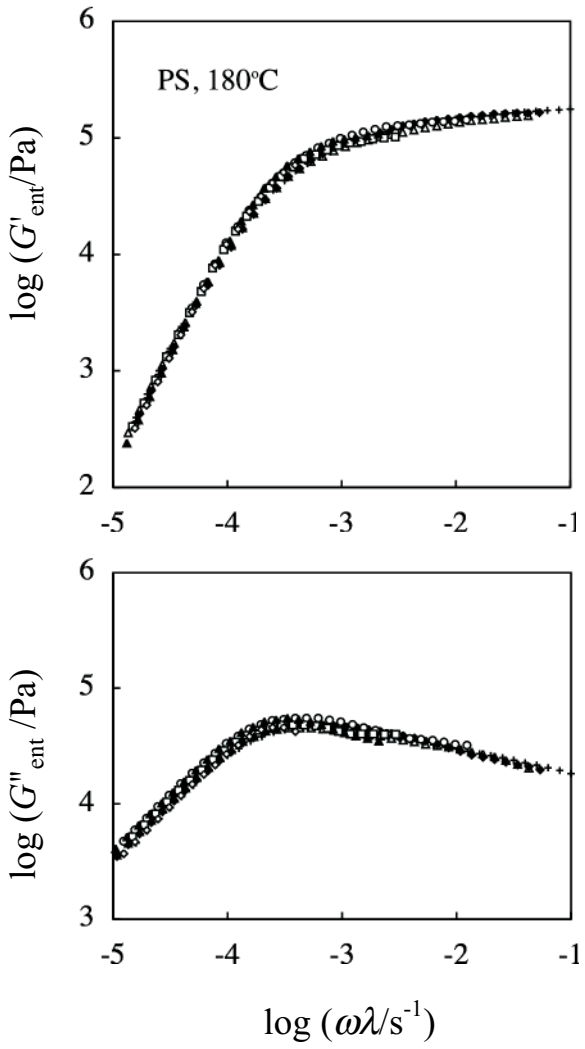

Fig. 3-7 (a): Comparison of terminal viscoelastic mode distribution due only to the entanglement relaxation of PS samples at 180°C. The sense of the symbols is the same as in Figure 3-1(a). The G_{ent}* data exclusively reflecting the entanglement relaxation are shifted along the ω axis by appropriate factors λ to superpose the low-ω tails of the G_{ent}' data.

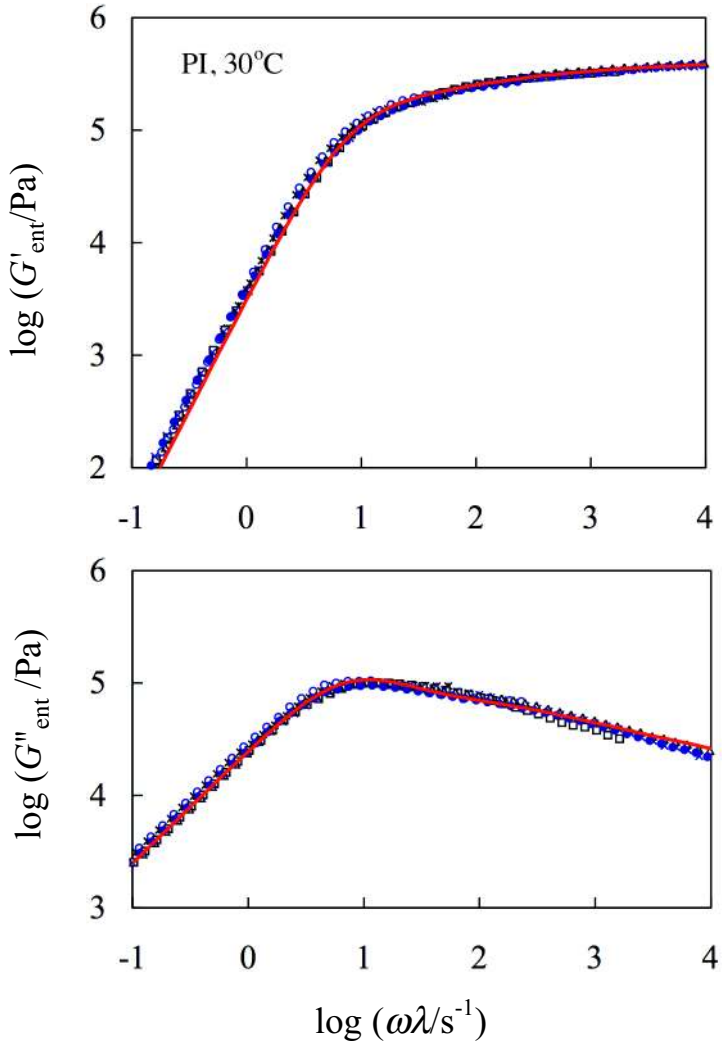

Fig. 3-7 (b): Comparison of terminal viscoelastic mode distribution due only to the entanglement relaxation of PI samples at 30°C. The sense of the symbols is the same as in Figure 3-1(b). The G_{ent}* data exclusively reflecting the entanglement relaxation are shifted along the ω axis by appropriate factors λ to superpose the low-ω tails of the G_{ent}' data. The curves are calculated from ε" data of the reference PI with $M/10^3$ = 99 through the DTD relationship.

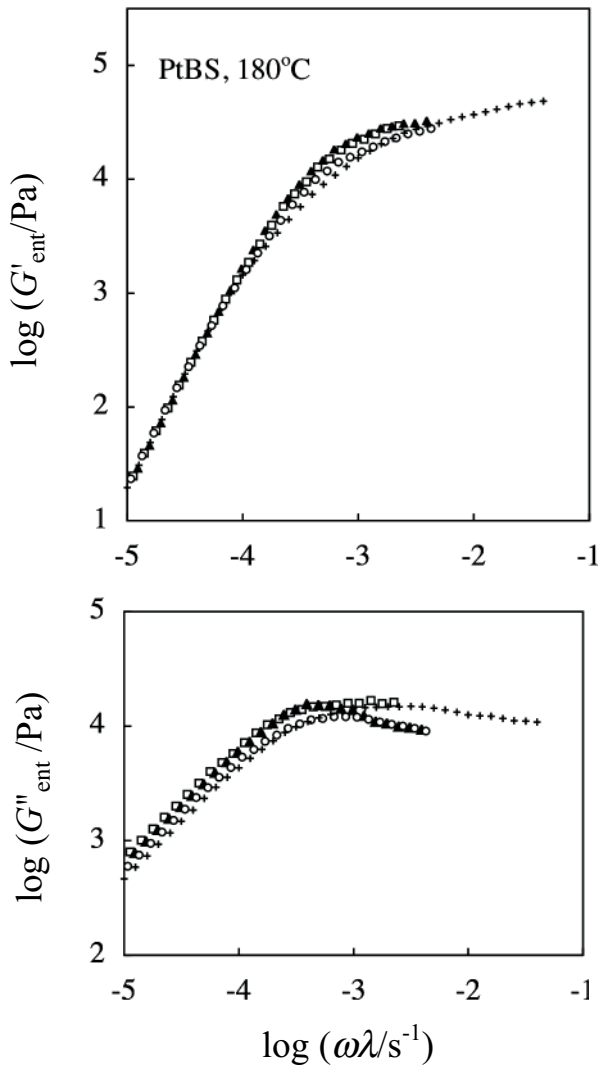

Fig. 3-7 (c): Comparison of terminal viscoelastic mode distribution due only to the entanglement relaxation of PtBS samples at 180°C. The sense of the symbols is the same as in Figure 3-1(c). The G_{ent}* data exclusively reflecting the entanglement relaxation are shifted along the ω axis by appropriate factors λ to superpose the low-ω tails of the G_{ent}' data.

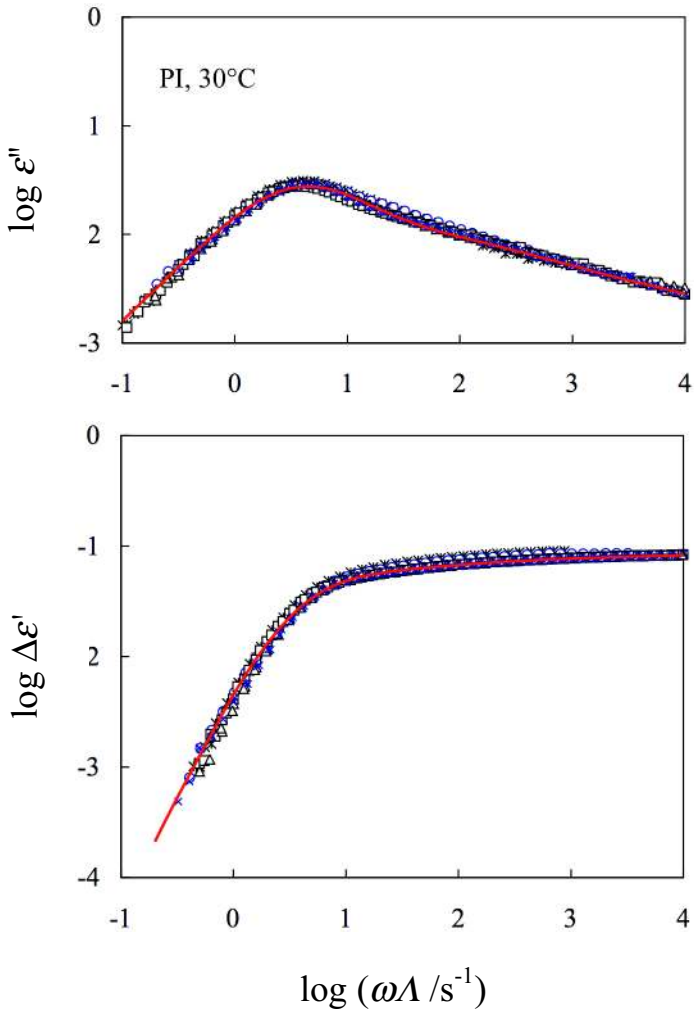

Fig. 3-8: Comparison of mode distribution of the dielectric ε'' and $\Delta\varepsilon'$ data for entangled PI samples at 30°C. The sense of the symbols is the same as in Figure 3-1(b). The ε'' and $\Delta\varepsilon'$ data are shifted along the ω axis by appropriate factors Λ to achieve the best superposition at the ε'' peak. This solid curves are calculated from the dielectric spectra (eq 3-9).

Chapter 4 ENTANGLEMENT DYNAMICS IN PI/PTBS BLENDS

4-1 Introduction

The entanglement dynamics of long flexible polymer chains is one of the central research subjects in the field of polymer physics. For homopolymer systems, this dynamics has been extensively investigated from experimental and theoretical aspects to reveal some specific mechanisms that govern the global relaxation of the chain. For example, within the content of the tube model, the terminal viscoelastic relaxation of linear chains is activated mainly by the reptation mechanism and accelerated/broadened by the contour length fluctuation (CLF) and constraint release (CR) mechanisms as explained in Chapter 3.[1-5] In particular, the CR mechanism is essential in binary blends of chains having same chemical structure and widely separated molecular weights (M).[2,3] Similar effects are naturally expected for miscible blends of chemically different chains. However, an interesting and important difference is noted between the blends of chemically identical chains (homopolymer systems) and of chemically different chains. Namely, the local segmental friction ζ_s and the entanglement molecular weight M_e, the basic parameters affecting the entanglement relaxation, are common for all component chains in the former type of blends but not in the latter. Thus, it is very interesting to examine ζ_s and M_e in the miscible blends of chemically different chains.

For such miscible blends of two components, say A and B, motion of the monomeric segments has been extensively investigated[6-23] in relation to the concepts of the self-concentration[6] and the local composition fluctuation explained in Chapter 1.[7] The global, entanglement dynamics in miscible blends has been also investigated[22,24-29] but less clearly understood compared to the local segmental dynamics. These blends often exhibit two-step entanglement relaxation qualitatively similar to that observed for binary blends of chemically identical chains. However, the temperature dependence of ζ_s is different for the two components in the miscible blends, which results in the thermo-rheologically complexity of the entanglement relaxation of these blends. This complexity has been incorporated in the tube model (originally developed for chemically uniform systems) to reformulate the model for the miscible blends on the basis of the molecular picture of *double reptation* (DR)[26] and *dynamic tube dilation* (DTD).[29] (The molecular picture of double reptation assumes that the disentanglement is a binary event involving two chains and the stress sustained by an entanglement relaxes immediately after any one of the two chains diffuse away.)[2] The reformulated models semi-quantitatively describe the slow viscoelastic relaxation of miscible blends such as *cis*-polyisoprene (PI)/poly(vinyl ethylene) (PVE) blends. However, no full agreement was found between the model and the data, quite possibly because the DR/DTD

formulation utilized in the models does *not* accurately apply even to chemically uniform homopolymer systems.[23,30-34] (For chemically uniform binary blends of long and short chains, the DR/DTD molecular picture is valid only when the length and time scales involved in this picture are consistently coarse-grained on the basis of the *Rouse-CR process* (cf. Appendix 4-1) of the whole sequence of long-short entanglements.[30-32,34])

The above models for the miscible blends include the entanglement length a (or the entanglement molecular weight $M_e \propto a^2$) as a parameter determining the entanglement plateau modulus G_N as well as the component relaxation times (cf. eq 1-2). The comparison of the model prediction and data was based on the a (or M_e) value estimated from a mixing rule(s), for example, $1/a = \phi_A / a_A^{bulk} + \phi_B / a_B^{bulk}$ where a_X^{bulk} is the entanglement length of the component X (X = A, B) in bulk and ϕ_X is the volume fraction of this component in the blend.[26] Since a_X^{bulk} is not significantly different for the components so far examined (*e.g.*, PI and PVE), the other choices of the mixing rule would have given nearly the same a (or M_e) value in the blend and thus have hardly affected the model predictions. It is highly desired to distinguish several mixing rules and specify the most appropriate rule.

PI and poly(*p-tert*-butyl styrene) (PtBS) are miscible in a wide range of temperature[35-38] and have quite different a_X^{bulk} and M_e^{bulk} values in bulk:[39]

bulk PI: $a_{PI}^{bulk} = 5.8$ nm, $M_{e,PI}^{bulk} = 5.0 \times 10^3$ (4-1)

bulk PtBS: $a_{PtBS}^{bulk} = 11.7$ nm, $M_{e,PtBS}^{bulk} = 37.6 \times 10^3$ (4-2)

(The M_e values shown in eqs 4-1 and 4-2 were evaluated from the plateau modulus G_N through eq 1-2). Different mixing rules give considerably different a (or M_e) values for the PI/PtBS blends, which enables specification of the most appropriate rule. Furthermore, PI has the type-A dipole parallel along the chain backbone and its global motion activates the dielectric relaxation,[2,40] while PtBS has no type-A dipole and its global motion is dielectrically inert at low ω (cf. Figure 3-2).[36-38] Thus, the dielectric data of PI/PtBS blends can be utilized to unequivocally determine the terminal relaxation time τ_ε^{PI} of the PI chains therein.[36-38] The viscoelastic modulus of PI in the blend, evaluated from the τ_ε^{PI} data and the modulus data of bulk PI, is helpful for accurately specifying the most appropriate mixing rule.

Thus, viscoelastic, dielectric, and rheo-optical measurements were conduced for the blends of high-M PI and PtBS to test the mixing rule of a. At all temperatures examined, the blends were in the miscible state and the PI and PtBS chains therein behaved as the fast and slow (low- and high-

friction) components in the blends. The viscoelastic, dielectric, and rheo-optical data revealed that the blends exhibit two-step entanglement relaxation at high T and the high frequency (ω) plateau of the modulus at $\omega > 1/\tau_e^{PI}$, being sustained by both PI and PtBS, is most appropriately described by the simplest mixing rule of a based on the number fraction of the Kuhn segments of PI and PtBS. The data also suggested that the Rouse equilibration of PI at length scales $\leq a$ is significantly retarded by PtBS at low T thereby narrowing the high-ω plateau zone to an undetectable width (and forcing this zone to almost merge into the retarded Rouse relaxation zone). This chapter presents details of these results, placing its emphasis on the fundamental aspects of polymer rheology, *i.e.*, the role of the Rouse equilibration in determining the stress and the necessity of this equilibration for the appearance of the entanglement plateau.

4-2 Experimental

4-2-1 Materials

The high-M PtBS348 and high-M PI99 and PI128 samples utilized in this chapter were synthesized anionically, as explained in Section 2-1.[36-38,41,42] The characteristics of these samples are summarized in Table 4-1.

The materials subjected to the viscoelastic, dielectric, and rheo-optical measurements were the blends of PtBS348 with PI99 and PI128. The method for preparing the blend sample was explained in Section 2-1.[35,38]

4-2-2 Measurements

Linear viscoelastic and dielectric measurements were conducted for the PI99/PtBS348 and PI128/PtBS348 blends having the PI content of w_{PI} = 40, 50, and 56 wt% in a range of T between 20°C and 120°C. (The dielectric and viscoelastic data of the bulk PI and PtBS samples have been shown in Figures 3-1 and 3-2, respectively.) For comparison, the viscoelastic measurement was conducted also for a 46.7 wt% solution of PtBS348 in a low-M solvent, dibutyl phthalate (DBP), utilized as a reference system for the 50 wt% PI/PtBS348 blends. Rheo-optical (dynamic birefringence) measurements were conducted for the 50 wt% PI128/PtBS348 blend at T /°C $\leq$ 100 with a home-made device composed of an oscillating drive and optical/mechanical detectors.[43-46] The principles and operations of the viscoelastic, dielectric, and rheo-optical measurements were explained in Section 2-2-2.

4-3 Results and Discussion

4-3-1 Overview

For the PI99/PtBS348 blend with w_{PI} = 50 wt%, Figure 4-1 shows the angular frequency (ω) dependence of the storage and loss moduli, G' and G'', and the dielectric loss, ε'', at temperatures T as indicated. For clarity of the plots, only the data at representative T are shown. The blend was miscible at all T examined. The raw ε'' data are multiplied by a factor of 10^4 and shown in a range of ω where the direct current (dc) conduction negligibly contributes to the data (the estimation of dc conduction is explained later in the top panel of Figure 5-3).[38] The component molecular weights are significantly larger than M_e^{bulk} in respective bulk systems (cf. eqs 4-1 and 4-2), which allows the PI and PtBS chains to be well entangled in the blend. Since PI has the type-A dipoles while PtBS does not, the dielectric relaxation seen in Figure 4-1 is exclusively attributed to the global motion (end-to-end vector fluctuation) of the PI chains in the blend. At all T examined, the blends exhibit two-step viscoelastic relaxation, and the terminal (second step) relaxation is much slower than the dielectric relaxation. Thus, PI99 and PtBS348 are unequivocally assigned as the fast and slow components in the blends, and the terminal viscoelastic relaxation is attributed to the global motion of the PtBS chains.

The two-step viscoelastic relaxation behavior (Figure 4-1) was noted for all PI/PtBS blends examined. This behavior is qualitatively similar to that seen for chemically uniform binary blends such as PI/PI blends.[30,31] However, an important difference is noted, *i.e.*, the thermo-rheological complexity of the viscoelastic data of the PI/PtBS blend. This complexity is demonstrated in Figure 4-2, where a reference temperature is chosen to be T_r = 303 K (30°C). The modulus data are corrected with the intensity factor $b_T = T/T_r$ and shifted along the ω axis to achieve the best superposition of the $b_T^{-1}G''$ data at $\omega a_T \cong 10^{-3}$ s^{-1}. (For clarity of the plots, the $b_T^{-1}G''$ data are multiplied by a factor of $10^{-1.5}$.) For comparison, the dielectric $b_T\varepsilon''$ data, corrected with the intensity factor b_T, are multiplied by a factor of 10^4 and shifted *independently from the modulus data* to achieve the best superposition at the ε'' peak.

The thermo-rheological complexity of the modulus data (failure of the superposition) seen in Figure 4-2 is partly attributed to a fact that PI and PtBS contributing to the modulus have different T dependence of the friction coefficient of their Rouse segments (= smallest motional unit for the global motion), $\zeta_{s,PI}$ and $\zeta_{s,PtBS}$: $\zeta_{s,PtBS}$ decreases with increasing T much more strongly compared to $\zeta_{s,PI}$, as explained in more detail later in Chapter 5. More importantly, Figure 4-1 demonstrates that

the blend at high T (100°C) exhibits a plateau of G' and a peak of G'' at high $\omega > 20$ s^{-1} where the terminal relaxation process of PI is dielectrically detected, while the blend at low T (30°C) shows neither G'-plateau nor G''-peak in the PI relaxation zone at $\omega > 0.1$ s^{-1}. Instead, the G' and G'' data at low T exhibit the Rouse-type power-law behavior, $G' = G'' \propto \omega^{1/2}$ (shown with the dotted line in Figure 4-1), and monotonically increase beyond the levels of G'-plateau/G''-peak seen at high T. Similar behavior was observed for all PI/PtBS blends examined.

The above results strongly suggest that the relaxation mechanism and the corresponding viscoelastic mode distribution of PI change with T and this change largely contributes to the thermo-rheological complexity of the blend. In relation to this point, it is noted in Figure 4-1 that the PI/PtBS blend at high T exhibits the two-step plateau of G' and the corresponding double peak/shoulder of G''. This behavior is very similar to that of the chemically uniform binary blends[30,31] (reflecting the reptation/CLF mechanism combined with the CR/tube dilation mechanism). Thus, the PI/PtBS blends at high T serve as the good model system for the test of the mixing rule of the entanglement length a. In the next section, this test is made for the G' and G'' data of those blends at high ω. The rheo-optical data are also utilized to check the results of the test.

After this test, a change of the relaxation mechanism(s) in the PI/PtBS blends on the decrease of T is examined to discuss why the high-ω Rouse-like behavior is observed at low T instead of the plateau and peak of G' and G'' (cf. Figure 4-1). In relation to this discussion, Figure 4-2 demonstrates that the time-temperature superposition satisfactorily works for the ε'' data of PI in the blend despite the failure of the superposition for the G^* data and that the superposed ε'' data are close to the data of bulk PI corrected for the temperature and the PI volume fraction in the blend (solid curve). Thus, the relaxation mechanisms of PI at high and low T are different but should be still associated with the same dielectric mode distribution, which provides a clue for discussing those mechanisms.

4-3-2 Test of mixing rule of entanglement length

The test of the mixing rule of the entanglement length a can be made unequivocally for the PI/PtBS blends at high T if the behavior of those blends is very similar to that of the chemically uniform blends (such as PI/PI blends[30,31]). It is well known that the chemically uniform blends have the entanglement plateau G_N being independent of the component molecular weights M and the volume fraction ϕ, since this plateau are sustained by chemically identical components.

Moreover, the relaxation behavior of the slow component therein is insensitive to M_{fast} of the fast component and close to the behavior in the solution having the same ϕ_{slow} if the fast and slow components have widely separated relaxation times.

These features were examined for the 50 wt% PI99/PtBS348 and PI128/PtBS348 blends (ϕ_{PtBS} = 0.47 as evaluated under the assumption of volume additivity) at 100°C and the 46.7 wt% PtBS348/DBP solution having the same ϕ_{PtBS}. The results are shown in Figure 4-3. The solution data at 20°C corrected for the intensity factor b_T (= T/T_r = 293/373), $b_T^{-1}G_{sol}$*, were shifted along the ω axis to match the viscosity with that of the blends. Clearly, the data of the blends in the low-ω plateau zone are insensitive to M_{PI} of PI (fast component) and agree well with the solution data. Furthermore, G_N of the blends in the high-ω plateau zone is insensitive to M_{PI} and the relaxation from this plateau is slower for larger M_{PI}. All these features are very similar to those of the chemically uniform blends, confirming that the PI/PtBS blends at high T do serve as the good model system for the test of the mixing rule of a.

Now, a test is made for the empirical mixing rules of the entanglement length a,

$$\frac{1}{a} = \frac{\phi_A}{a_A^{bulk}} + \frac{\phi_B}{a_B^{bulk}} \quad \text{(ref. 26)} \tag{4-3}$$

$$a = n_A a_A^{bulk} + n_B a_B^{bulk} \quad \text{(proposed in this thesis)} \tag{4-4}$$

$$\frac{1}{M_e^{1/2}} = \frac{\phi_A}{\left\{M_e^{bulk\ A}\right\}^{1/2}} + \frac{\phi_B}{\left\{M_e^{bulk\ B}\right\}^{1/2}} \quad \text{(ref. 29)} \tag{4-5}$$

a_X^{bulk} denotes the entanglement length in the bulk system of the component X (= A, B), and n_X is the number fraction of the Kuhn segments of the component X in the blend. (Eq 4-5 is similar but not identical to eq 4-3 because a ratio $\left(a^{bulk}\right)^2 / M_e^{bulk}$ is not the same for all polymer species.)

The mixing rules, eqs 4-3 and 4-4, is based on a molecular picture that the high-ω plateau is sustained by both A and B (PI and PtBS) chains and these chains are cooperatively equilibrated to have the same a value. This molecular picture sounds very reasonable (although it is impossible to fully rule out the other possibility that the component chains are separately equilibrated.)

A few comments need to be made for the mixing rule, eq 4-4, proposed in this thesis. For homopolymers, the criterion of entanglement can be characterized by the number P_e of entanglement strands within a volume a^3, where a is the entanglement mesh size (or tube diameter). The value of P_e is nearly constant for a variety of flexible homopolymers including PI and PtBS:[39]

$$P_e \equiv \frac{a^3}{V_e} = \frac{a}{p} = 20 \pm 3 \tag{4-6}$$

In eq 4-6, V_e represents the occupied volume of the entanglement strand; $V_e = M_e/(\rho N_A)$ with ρ and N_A being the polymer density and Avogadro constant. p is the packing length[39,47,48] defined as a ratio of the occupied volume of the Kuhn segment υ_0 to square of the Kuhn length b:

$$p \equiv \frac{\upsilon_0}{b^2} \tag{4-7}$$

Since the Kuhn segment is the fundamental unit for description of the flexible polymer conformation, the average of p should include the number fractions of these segments as the weighing factors as

$$p = p_A a_A^{bulk} + p_B a_B^{bulk} \tag{4-8}$$

where p_A and p_B are packing length of A and B in bulk. A small variation in the p/a ratio among polymer species can be safely neglected, and eq 4-7 can be re-written for a to give eq 4-4.

Eqs 4-3, 4-4, and 4-5 can be tested on the basis of a formal blending law of the complex modulus, $G^*(\omega) = \Sigma_{X=A,B} G_X^{bld}*(\omega)$ with $G_X^{bld}*(\omega)$ being the complex modulus of the component X *in the blend.* In general, $G_X^{bld}*(\omega)$ does not coincide with $G_X^{bulk}*(\omega)$ of bulk component X because of the CR effect on $G_X^{bld}*(\omega)$, and this formal blending law merely represents the stress additivity of the components. Nevertheless, in the high-ω plateau zone where the mixing rules of a are to be tested, the fast component has hardly relaxed thereby activating no significant CR relaxation for the fast and slow components. In this zone, $G_X^{bld}*$ can be approximated to have the same relaxation mode distribution as $G_X^{bulk}*$, and the above blending law can be cast in a form,

$$G*(\omega) = \sum_{X=A,B} \phi_X I_X G_X^{bulk}*(\omega\lambda_X) \quad \text{in the high-}\omega\text{ plateau zone} \tag{4-9}$$

with

$$\lambda_X = \frac{\tau_G^X}{\tau_G^{bulk\,X}} \tag{4-10}$$

and

$$I_X = \left(\frac{a_X^{bulk}}{a} \right)^2 \text{ (when eqs 4-3 and 4-4 are utilized)} \tag{4-11a}$$

$$I_X = \frac{M_e^{\text{bulk X}}}{M_e} \text{ (when eq 4-5 is utilized)} \qquad (4\text{-}11b)$$

Here, λ_X denotes a difference of the viscoelastic relaxation times of the component X in bulk ($\tau_G^{\text{bulk X}}$) and in the blend (τ_G^X), and I_X represents a difference of the entanglement plateau heights normalized to unit volume fraction of the component X in bulk and blend. I_X is determined according to the mixing rules.

A comment needs to be added for λ_X. For the PI chains (fast component) exhibiting a narrow dielectric mode distribution in the PI/PtBS blends, the terminal dielectric relaxation time τ_ε^{PI} can be experimentally determined from the angular frequency $\omega_{\varepsilon\text{-peak}}$ for the ε'' peak as $\tau_\varepsilon^{PI} = 1/\omega_{\varepsilon\text{-peak}}$ (= 0.04 s at 100°C; cf. Figure 4-1). Since the PI chains relax much faster than the PtBS chains, the entanglement constraint from the PtBS chains is effective throughout the terminal relaxation of the PI chains. For this case, the viscoelastic τ_G^{PI} of PI in the blend can be safely replaced by the dielectric τ_ε^{PI} and experimentally evaluate λ_{PI} from the data of τ_ε^{PI} and $\tau_G^{\text{bulk PI}}$ (= 0.2 s at 30°C; obtained from the G_{PI}^{bulk} * shown in Figure 3-1(b) via eq 2-26) as $\lambda_{PI} = \tau_\varepsilon^{PI}/\tau_G^{\text{bulk PI}}$:[48] Indeed, from the empirical equation 5-7 (eq 5-7 explained later in Chapter 5) for τ_G^{PI} of the fast component,[38] the difference between τ_G^{PI} and τ_ε^{PI} for the PI/PtBS blends studied in this chapter was estimated to be less than 5% and can be safely neglected. It is also noted that the first step relaxation of the slow PtBS chains is activated by the terminal relaxation of PI (through the CR mechanism). Thus, τ_G^{PtBS} of PtBS appearing in eq 4-10 can be safely replaced by τ_G^{PI} (= τ_ε^{PI}) of PI, and λ_{PtBS} is evaluated from τ_ε^{PI} and the $\tau_G^{\text{bulk PtBS}}$ data of bulk PtBS as $\lambda_{PtBS} = \tau_\varepsilon^{PI}/\tau_G^{\text{bulk PtBS}}$.

From the G_{PI}^{bulk} * and G_{PtBS}^{bulk} * data shown in Figure 3-1 and the λ_{PI} and λ_{PtBS} values obtained above, the modulus $G^*(\omega)$ of the blend (eq 4-9) were calculated on the basis of respective mixing rules, eqs 4-3, 4-4 and 4-5. For the PI/PtBS blends examined, Figure 4-4 compares the calculated G^* (solid curves) with the G^* data (circles) at high T. Clearly, eqs 4-3 and 4-5 (curves in the left and right columns of panels) considerably underestimate the modulus, *i.e.*, over estimate a and/or M_e in the blends. In contrast, eq 4-4 (curves in the middle column of panels) well describes the G^* data in the high-ω plateau zone where eq 4-4 is to apply. The difference of G^* predicted from eq 4-4 and from eqs 4-3 and 4-5 becomes larger with decreasing w_{PI} (because n_{PI} appearing in eq 4-4 decreases rather weakly with decreasing w_{PI}.)

Here, a comment needs to be added for the validity of eq 4-4. The number fractions n of the Kuhn segments were utilized in eq 4-4 as the weighing factors. The molecular weight of the Kuhn segment M_{Kuhn} is considerably larger for PtBS ($M_{Kuhn}^{PtBS} \cong 1500$)[49,50] than for PI ($M_{Kuhn}^{PI} \cong 130$)[39] to give $n_{PtBS} << n_{PI}$ so that the a value for the PI/PtBS blends obtained from eq 4-4, a = 6.2, 6.3 and

6.5 nm for w_{PI} = 56, 50 and 40 wt%, is much smaller than the a_{PtBS}^{bulk} value of bulk PtBS (11.7 nm) and close to a_{PI}^{bulk} of bulk PI. (5.8 nm) Such small a values are necessary to reproduce the high-ω plateau level seen for the PI/PtBS blends.

It should be emphasized that eq 4-4 could be distinguished from the other mixing rules, eqs 4-3 and 4-5, because PI and PtBS have quite different a^{bulk} values. For the other pairs of components such as PI and poly(vinyl ethylene), the difference of a^{bulk} is much smaller and all blending rules give nearly the same a (or M_e). In other words, the validity of eq 4-4 confirmed in this chapter does not significantly change the results of the previous studies based on eqs 4-3 and 4-5. Nevertheless, eq 4-4 is most straightforwardly related to the molecular picture of the entanglement based on the packing length concept, which in turn indicates the physical soundness of eq 4-4.

The rheo-optical measurements were conducted to further examine the validity of eq 4-4. Since the glassy (segmental) relaxation of the PtBS and PI in the blend at 100°C occurs at high ω (>> 10^4 s^{-1}), this relaxation negligibly contributes to the complex modulus G^* and the complex shear optical coefficient K^* of the PI/PtBS blend. Then, G^* and K^* are related to each other through the stress-optical rule (cf. eq 2-3),[43-46]

$$K^*(\omega) = C_R^{PI} G_{PI}^{bld}{}^*(\omega) + C_R^{PtBS} G_{PtBS}^{bld}{}^*(\omega) \tag{4-12a}$$

$$G^*(\omega) = G_{PI}^{bld}{}^*(\omega) + G_{PtBS}^{bld}{}^*(\omega) \tag{4-12b}$$

C_R^{PI} and C_R^{PtBS} are the stress optical coefficients of PI and PtBS in the Rouse/rubbery/flow zones. Eq 4-12b is equivalent to the formal blending rule (eq 4-9) explained earlier.

Figure 4-5(a) shows the ω dependence of the K^* (= $K'+iK''$) data obtained for the PI128/PtBS348 blend at 100°C. Both K' and K'' were negative in the entire range of ω examined, and their absolute values $|K'|$ and $|K''|$ are shown with the circle and square. In the terminal relaxation regime at low ω, the PI chains have fully relaxed to have $G_{PI}^{bld}{}^*(\omega) << G_{PtBS}^{bld}{}^*(\omega)$ so that eq 4-12 is simplified as $K^*(\omega) = C_R^{PtBS} G^*(\omega)$. Thus, the K'' data at low ω (≤ 0.1 s^{-1}) are utilized to evaluate the coefficient for PtBS, $C_R^{PtBS} = K''(\omega)/G''(\omega) = -6.1\times10^{-9}$ Pa^{-1} at 100°C. This C_R^{PtBS} value is very close to that of bulk PtBS (-5.6×10^{-9} Pa^{-1}) evaluated from the data at 150°C ($C_R^{bulk\ PtBS}$ = -4.9×10^{-9} Pa^{-1})[46] after a correction of T; $C_R \propto T^{-1}$. The coefficient for PI, $C_R^{PI} = 1.3\times10^{-10}$ Pa^{-1} at 100°C, was estimated from the bulk PI data,[45] $C_R^{bulk\ PI} = 2.0\times10^{-10}$ Pa^{-1} at –40°C, after the same correction. With these C_R values at 100°C utilized in eqs 4-12a and 4-12b, the component moduli $G_{PI}^{bld}{}^*$ and $G_{PtBS}^{bld}{}^*$ were calculated from the K^* data and G^* data (obtained simultaneously in the rheo-optical test.). Figures 4-5(b) and (c) show plots of $G_{PI}^{bld}{}^*$ and $G_{PtBS}^{bld}{}^*$, respectively. The dotted

curves in Figure 4-5(c) show the G^* data of the blend at low ω. The rheo-optically calculated $G^{bld}_{PtBS}*$ coincides with those data because C_R^{PtBS} was determined from those data.

In Figures 4-5(b) and (c), the solid curves indicate the component moduli $\phi_X I_X G^{bulk}_X*(\omega\lambda_X)$ (X = PI, PtBS) evaluated on the basis of the blending law, eq 4-9 combined with eq 4-4. For PI, $\phi_{PI} I_{PI} G^{bulk}_{PI}*(\omega\lambda_{PI})$ agrees surprisingly well with the rheo-optically determined $G^{bld}_{PI}*(\omega)$; cf. Figure 4-5(b). A minor deviation seen between $\phi_{PI} I_{PI} G^{bulk}_{PI}*$ and $G^{bld}_{PI}*$ would be mostly due to the approximate use of G^{bulk}_X* in eq 4-9, *i.e.*, the approximate replacement of the fast mode distribution in the blend by that in bulk. At high ω (> 10 s^{-1}) where eq 4-9 applies, the deviation between $\phi_X I_X G^{bulk}_X*$ and G^{bld}_X* is larger for PtBS than for PI partly because of this approximation and, more importantly, because of the difference in the magnitudes of $G^{bld}_{PtBS}*$ and $G^{bld}_{PI}*$ (> $G^{bld}_{PtBS}*$): Since the sum $\phi_{PI} I_{PI} G^{bulk}_{PI}* + \phi_{PtBS} I_{PtBS} G^{bulk}_{PtBS}*$ agrees well with G^* (Figure 4-4) while the sum $G^{bld}_{PtBS}* + G^{bld}_{PI}*$ is forced to coincide with G^* (eq 4-12b), the minor deviation of $\phi_{PI} I_{PI} G^{bulk}_{PI}*$ is compensated by a magnified deviation of $\phi_{PtBS} I_{PtBS} G^{bulk}_{PtBS}*$. Nevertheless, the deviation of $\phi_{PtBS} I_{PtBS} G^{bulk}_{PtBS}*$ is still acceptably small, and the results seen in Figures 4-5(b) and (c) lend support to eq 4-4 utilized in the blending law approach.

A comment needs to be made for the validity of eq 4-12. For homopolymers, the orientation of bond vector of the monomeric segments and that of Rouse segments are proportional to give a stress-optical rule in eq 2-3. However, this proportionality is not necessarily satisfied for each component in a blend if the orientational (nematic) coupling emerges in a monomeric level.[51] This kind of nematic coupling of the components may affects the optical data but not the modulus data.[52-54] In fact, this coupling (with a magnitude ε = 0.3-0.4) has been noted for miscible blends of PI and PVE.[52-54] However, the stress-optical coefficient agreed well for PtBS in bulk and the blend studied in this chapter. This agreement is not expected for the case of strong nematic coupling. Furthermore, the stress optical rule (eq 4-12) with this C_R^{PtBS} value and the C_R^{PI} value for bulk PI (after the T correction) gave the PI modulus $G^{bld}_{PI}*$ that full relaxed at $\omega > 1/\tau_\varepsilon^{PI}$; cf. Figure 4-5(b). This full relaxation never occurs but a second-step slow relaxation should emerge for the rheo-optically evaluated $G^{bld}_{PI}*$ if PI (fast component) has a strong nematic coupling with PtBS (slow component).[51] These facts suggest that the nematic coupling is weak in the PI/PtBS blends. For this reason, the rheo-optical analysis presented in this chapter did not consider this coupling (although some minor coupling could have occurred).

4-3-3 Mechanism of Rouse-like behavior (lack of high-ω plateau) at low temperatures

At first sight, the lack of the high-ω entanglement plateau at low T (Figures 4-1 and 4-2) might appear to be due to a large contribution of the glassy (segmental) relaxation of PtBS348 to the modulus of the blend. However, this is not the case, as explained below. As seen in Figures 3-1(c) and 3-2 (b) of Chapter 3, bulk PtBS348 exhibits the dielectric and viscoelastic relaxation due to the segmental motion at high ω. On completion of this segmental relaxation, G'' of bulk PtBS decreases almost in proportion to ω and becomes considerably larger than G', and G' decreases more strongly down to $\cong 3\times10^6$ Pa. (On a further decrease of ω, the segmental contribution to G^* is overwhelmed by the contribution from the Rouse/rubbery mode and the well-known behavior of entangled polymers prevails.) These features should be observed for the G^* data of the PI99/PtBS348 blend at low T (30°C) *if* the data are dominated by the segmental relaxation of PtBS348. However, as clearly noted in Figure 4-1, G'' of the blend at 30°C is not proportional to ω but exhibits the Rouse-like power-law behavior together with G' ($G'=G''\propto\omega^{1/2}$). Furthermore, a decrease of ω to the low-ω end ($\cong 0.01$ s^{-1}) of this power-law behavior results in a decrease of G' down to $\cong 5\times10^4$ Pa, a value much smaller than the minimum value of $0.47\times3\times10^6\cong1.4\times10^6$ Pa expected for the modulus sustained by the segmental mode of PtBS348 (having the volume fraction $\phi_{PtBS} = 0.47$ in the blend). Thus, the power-law behavior of the moduli and the corresponding lack of the high-ω entanglement plateau observed for the PI99/PtBS348 blend at 30°C cannot be attributed to the segmental (glassy) relaxation of PtBS. This conclusion was found for all PI/PtBS blends examined. Furthermore, the glassy relaxation of PtBS is associated with a positive stress optical coefficient[46] but the components of the complex shear optical coefficient, K' and K'', had negative values in the Rouse-like power-law zone, as explained later for Figure 4-7. This fact also suggests that the glassy relaxation negligibly contributes to the Rouse-like power-law behavior.

Here, it is informative to specify a condition for the entanglement plateau to be observed. This plateau emerges when the Rouse equilibration within the entanglement length a is much faster than the global motion of the chain at a length scale >> a. Consequently, the plateau is not clearly observed if the time required for the Rouse-equilibration and terminal relaxation processes are not widely separated. For high-M homopolymers, these times are well separated because the equilibration rate is determined just by the friction coefficient ζ_s of the Rouse segment without being subjected to a topological constraint. In contrast, in the PI/PtBS blends at low T, ζ_s is much larger for PtBS than for PI and thus the *intrinsic* Rouse equilibration time over the length a, $\tau_a = \zeta_s a^2 N_R/6\pi^2 k_B T \propto \zeta_s$ with N_R being the segment number *per* entanglement of the size a ($= b_R N_R^{1/2}$ with b_R = segment step length), is much longer for PtBS. Then, the slow PtBS chains should hinder the PI chain from exploring all local conformations at length scales $\leq a$ within its *intrinsic* $\tau_{a,PI}$. For

this case, the Rouse equilibration of the PtBS chain should become the rate-determining step for the equilibration of the PI chain. This retarded Rouse equilibration of PI is not identical but similar, in a sense that the motion of the constraining chains determines the equilibration rate, to the equilibration during the constraint release process.[30-32,34] If $\tau_{a,\mathrm{PtBS}}$ of PtBS is not very shorter than the terminal relaxation time of PI, the PI chain fully relaxes soon after its retarded Rouse equilibration is completed at this $\tau_{a,\mathrm{PtBS}}$ thereby exhibiting no clear entanglement plateau. This could be the mechanism of the lack of the high-ω entanglement plateau observed for the PI/PtBS blends at low *T*.

This molecular picture can be tested for the data shown in Figure 4-1. For a chain of the molecular weight *M* and mass concentration *C*, the power-law type Rouse behavior of *G*' and *G*" can be compactly described, in a continuous form, as[55]

$$G'(\omega) = G''(\omega) = 1.111\frac{CRT}{M}\left(\omega\tau_{\mathrm{G,R}}\right)^{1/2} \tag{4-13}$$

where *R* is the gas constant and $\tau_{\mathrm{G,R}}$ is the viscoelastic Rouse relaxation time. Eq 4-13 is essentially identical to eq 2-27 explained in Chapter 2. For the PI99/PtBS348 blend with w_{PI} = 50 wt%, the entanglement length described by eq 4-13 has a value, a = 6.3 nm. Replacement of *M* in eq 4-13 by $M_{\mathrm{e}}^{\mathrm{X}} = \{a/a_{\mathrm{X}}^{\mathrm{bulk}}\}^2 M_{\mathrm{e}}^{\mathrm{bulk\,X}}$ for the component X in the blend (X = PI, PtBS) gives the blend modulus corresponding to the Rouse equilibration over the length *a*:

$$G'(1/\tau_a) = G''(1/\tau_a) = 1.111G_{\mathrm{N}} \equiv 1.111\left\{\frac{C_{\mathrm{PI}}RT}{M_{\mathrm{e}}^{\mathrm{PI}}} + \frac{C_{\mathrm{PtBS}}RT}{M_{\mathrm{e}}^{\mathrm{PtBS}}}\right\} = 3.6\times10^5 \text{ Pa} \tag{4-14}$$

Here, τ_a is the Rouse equilibration time that is common for PI and PtBS (as discussed above), and $1/\tau_a$ (= ω_a) is the corresponding frequency. (This method of determination of $1/\tau_a$ was graphically shown in Figure 2-5(a).) For the PI99/PtBS348 blend at 30°C, the *G*' and *G*" values specified by eq 4-14 are 3.6×10^5 Pa. The corresponding ω_a value evaluated from the *G*' and *G*" data (Figure 4-1) is 0.4 s^{-1}. The Rouse equilibration time thus obtained, $\tau_a = 1/\omega_{\mathrm{a}}$ = 2.5 s, is only moderately shorter than the dielectrically evaluated terminal relaxation time of PI, $\tau_\varepsilon^{\mathrm{PI}}$ = 10 s. Namely, the PI chain exhibits the terminal relaxation soon after its retarded Rouse equilibration is completed. This result, found for all PI/PtBS blends at low *T*, lends support to the above molecular picture attributing the lack of the high-ω plateau to the retardation of the Rouse equilibration of the PI chains.

In relation to this molecular picture, it is noted that the G' data at *high T* shown in Figures 4-1 and 4-4 have values smaller than the $G'(1/\tau_a)$ value specified by eq 4-14; $10^{-5}G'(1/\tau_a)$/Pa =4.5, 4.4, and 4.2 for (w_{PI}/wt%, T/°C) = (56, 80), (50, 100), (40, 120), respectively. This result indicates that at high T the PI and PtBS chains had been already Rouse-equilibrated over the length a in the range of ω examined. Under this situation, the PI chains had $\tau_\varepsilon^{PI} >> \tau_a$, which allowed the PI and PtBS chains to cooperatively exhibit the high-ω plateau seen in Figure 4-4. Thus, the existence of the high-ω plateau at high T is in harmony with the above molecular picture.

4-3-4 Model for the blend modulus at low temperatures

From the molecular picture of the retarded Rouse equilibration over the entanglement length a, the complex modulus of the PI chains in the PI/PtBS blends at low T can be modeled as

$$G_{PI}^{bld}*(\omega) = \frac{C_{PI}RT}{M_e^{PI}}\sum_{p=1}^{N_R}\frac{i\omega\tau_a/r_p^2}{1+i\omega\tau_a/r_p^2} + \phi_{PI}I_{PI}G_{PI}^{bulk}*(\omega\lambda_{PI}') \quad (4\text{-}15a)$$

with

$$r_p = \sin\left\{\frac{p\pi}{2(N_R+1)}\right\}\sin^{-1}\left\{\frac{\pi}{2(N_R+1)}\right\} \quad (4\text{-}15b)$$

Here, $M_e^{PI} = \{a/a_{PI}^{bulk}\}^2 M_e^{bulk\,PI}$ is the entanglement molecular weight for PI in the blend, and N_R is the number of Rouse segments (more accurately, the number of the Rouse bond vectors, as explained in Appendix 4-1) per entanglement segment of the size a. Since the Rouse and Kuhn segments of flexible PI chains are similar in size, this number can be estimated as $N_R = M_e^{PI}/M_{Kuhn}^{PI}$. The first summation term including these parameters represents the discrete Rouse process with the equilibration time τ_a (common with PtBS). The second term represents the terminal entanglement relaxation of PI occurring at the dielectric relaxation time in the blend, τ_ε^{PI}. (Since the global motion is much faster for PI than for PtBS, the terminal viscoelastic relaxation time of PI can be safely replaced by the dielectric τ_ε^{PI}, as explained earlier.) As explained for eq 4-9, the second term is approximately expressed in terms of the bulk PI modulus $G_{PI}^{bulk}*$, the PI volume fraction ϕ_{PI}, the relaxation time shift factor $\lambda_{PI}' = \tau_\varepsilon^{PI}/\tau_G^{bulk\,PI}$, and the correction factor I_{PI} (given by eq 4-11a) representing a change of the entanglement plateau on blending.

Now, the focus is placed on $G^{\text{bld}}_{\text{PtBS}}$ * of the PtBS chains in the blend. These chains are also Rouse-equilibrated over the entanglement length a with the characteristic time τ_a. Since the PtBS and PI chains are equilibrated cooperatively to have the common τ_a, the onset time of the Rouse equilibration, $\tau_a / r^2_{N_R}$ (cf. eq 4-15b), would be also common for these chains. Thus, the number of the Rouse segment per entanglement segment of PtBS in the blend would be close to N_{R} of the PI chain. After this equilibration, the global motion of PI chains activates the CR relaxation of the PtBS chain thereby dilating the entanglement mesh size for PtBS from a (described by eq 4-4) to the size in the PtBS solution having the same volume fraction ϕ_{PtBS} as the blend, $a_{\text{soln}} = a^{\text{bulk}}_{\text{PtBS}} / \phi^{0.65}_{\text{PtBS}}$. After this CR/dilation process, the effective entanglement molecular weight for PtBS agrees with that in the solution, $M^{\text{soln}}_{\text{e}} = M^{\text{bulk PtBS}}_{\text{e}} / \phi^{1.3}_{\text{PtBS}}$, and PtBS exhibits the terminal relaxation in the dilated entanglement mesh characterized by this $M^{\text{soln}}_{\text{e}}$. Thus, in a range of ω where this terminal relaxation has *not* occurred at all, the complex modulus of PtBS can be modeled as

$$G^{\text{bld}}_{\text{PtBS}}*(\omega) = \frac{C_{\text{PtBS}}RT}{M^{\text{PtBS}}_{\text{e}}} \sum_{p=1}^{N_{\text{R}}} \frac{i\omega\tau_a / r_p^2}{1 + i\omega\tau_a / r_p^2}$$

$$+ \frac{C_{\text{PtBS}}RT}{M^{\text{soln}}_{\text{e}}} \sum_{p=1}^{N_{\text{CR}}-1} \frac{i\omega\tau_{\text{CR}} / q_p^2}{1 + i\omega\tau_{\text{CR}} / q_p^2} + \frac{C_{\text{PtBS}}RT}{M^{\text{soln}}_{\text{e}}} \qquad \text{(4-16a)}$$

with

$$q_p = \sin\left\{\frac{p\pi}{2N_{\text{CR}}}\right\} \sin^{-1}\left\{\frac{\pi}{2N_{\text{CR}}}\right\} \qquad \text{(4-16b)}$$

Here, $M^{\text{PtBS}}_{\text{e}} = \{a / a^{\text{bulk}}_{\text{PtBS}}\}^2 M^{\text{bulk PtBS}}_{\text{e}}$ is the PtBS entanglement molecular weight in the blend (in the high-ω plateau zone), and r_p is given by eq 4-15b. In eq 4-16a, the first term represents the Rouse equilibration of the PtBS chain over the entanglement length a, and the second term, the Rouse-type CR process[2,3,56] having the longest characteristic time τ_{CR}. The third term denotes the dilated entanglement plateau identical to that in the solution. The number of the CR segments N_{CR}, specifying the upper bound of the second summation in eq 4-16a and determining the q_p factor in eq 4-16b, is taken to be the number of the entanglement segments of PtBS *per* dilated entangled mesh and evaluated as $N_{\text{CR}} = M^{\text{soln}}_{\text{e}} / M^{\text{PtBS}}_{\text{e}}$. Since the local CR hopping of the PtBS chain is activated by the global motion of the PI chains, the onset time for the CR process, $\tau_{\text{CR}} / q^2_{N_{\text{CR}}-1}$, should be proportional to $\tau^{\text{PI}}_{\varepsilon}$ of PI. Within the Graessley model (explained in Appendix 4-1),[56] $\tau_{\text{CR}} / q^2_{N_{\text{CR}}-1}$ is related to $\tau^{\text{PI}}_{\varepsilon}$ as

$$\tau_{CR}/q_{N_{CR}-1}^2 = \Lambda(z)\,\tau_\varepsilon^{PI} \text{ with } \Lambda(z) = \frac{1}{z}\left(\frac{\pi^2}{12}\right)^z \tag{4-17}$$

Here, z is the local jump gate number typically in a range of z = 2-4. z is treated as an adjustable parameter (z = 2 as shown later).

The basic times appearing in eqs 4-15 and 4-16, τ_a and τ_ε^{PI}, have been determined from the viscoelastic and dielectric data as explained in the previous section. The other parameters, M_e^X (X = PI, PtBS), N_R, N_{CR}, and τ_{CR} were evaluated from a (eq 4-4), a_X^{bulk} and $M_e^{bulk\,X}$ (eqs 4-1 and 4-2), M_{Kuhn}^{PI} (= 130), M_e^{soln} (= $M_e^{bulk\,PtBS}/\phi_{PtBS}^{1.3}$), and τ_ε^{PI}. The values of these parameters are summarized in Table 4-2. With the aid of those values, the blend modulus can be calculated from the model (eqs 4-15 and 4-16) and compared with the $G^*(\omega)$ data at 30°C. The results of this comparison are shown in Figure 4-6. Since the model approximates the modulus of PI in the blend by the bulk modulus (cf. eq 4-15a), no perfect agreement is expected between the model and experiments. Nevertheless, Figure 4-6 demonstrates that the modulus calculated from the model with a reasonable value of z = 2 (solid curves) is surprisingly close to the data for all blends examined (symbols).[57] This result lends further support to the molecular picture underlying the model, the cooperative Rouse equilibration of the PI and PtBS chains that is slower than the intrinsic Rouse equilibration of PI and leads to the lack of high-ω plateau at low T.

The model can be further tested on the basis of the rheo-optical data. Figure 4-7(a) shows the complex shear optical coefficient K^* (= $K'+iK''$) measured for the PI128/PtBS348 blend with w_{PI} = 50 wt % at 30°C. K' was negative in the entire range of ω examined and K'' was also negative at ω < 100 s^{-1} where the blend exhibited the Rouse-like power-law behavior. Thus, the plots are shown for their absolute values, $|K'|$ and $|K''|$. The segmental relaxation of PtBS hardly contributes to the blend modulus in the experimental window, as noted from these K' and K'' values and also from the G' and G'' values as explained earlier. Thus, the K^* and G^* data can be safely analyzed within the framework of the stress-optical rule, eq 4-12, to give the component moduli.

For this purpose, the C_R values at 30°C, $C_R^{PtBS} = -5.0\times10^{-9}$ Pa^{-1} and $C_R^{PI} = 1.0\times10^{-9}$ Pa^{-1}, were evaluated after the temperature correction ($C_R \propto T^{-1}$) to the C_R values at 100°C (utilized for Figure 4-5): $G_{PI}^{bld}{}^*(\omega)$ and $G_{PtBS}^{bld}{}^*(\omega)$ evaluated from eq 4-12 with the C_R values at 30°C are shown with the symbols in Figures 4-7(b) and (c), respectively. These rheo-optically obtained moduli are very close to the moduli deduced from the model (eqs 4-15 and 4-16) shown with the curves.[58] This result demonstrates the basic validity of the model.

Finally, the dielectric mode distribution of the PI chains in the blends is to be discussed. The slow dynamics of PI changes from the reptation-like dynamics in the equilibrated entanglement mesh to the retarded Rouse-like dynamics (under the hindrance from the slow PtBS chains) with decreasing T, as discussed earlier. Nevertheless, the dielectric mode distribution of PI is insensitive to this change thereby allowing the ε'' data to obey the time-temperature superposition (Figure 4-2). This result can be related to a fact that the dielectric mode distribution of PI, equivalent to the distribution of the end-to-end vector fluctuation modes, is very similar for the reptation-like and Rouse-like dynamics.[2,34] Thus, the change of the slow dynamics of PI still allowed the ε'' data to obey the superposition.

In Figure 4-2, the solid curve shows the ε'' data of bulk PI99 at $T_r = 30°C$ corrected for the PI volume fraction in the blend ($\phi_{PI} = 0.53$) and shifted along the ω axis to match the ε'' peak frequency with that for the data in the blend. The dielectric mode distribution of PI in the blend is close to but a little broader than that of bulk PI. This delicate difference may be related to motional constraint from PtBS and the frictional heterogeneity, both resulting from the concentration fluctuation essentially quenched in the time scale of PI relaxation.[36,38]

4-3-5 Additional comments

In all high-M blends examined in this chapter, the terminal relaxation of PI was dielectrically observed at ω where the modulus was below $G^*(1/\tau_a)$ for the Rouse equilibration over the entanglement length a (cf. eq 4-14), although the terminal relaxation time τ_ε^{PI} was not significantly longer than the equilibration time τ_a at low T (cf. Table 4-2). This situation was confirmed also for most of low-M, lightly entangled PI/PtBS blends examined in Chapter 6.[36,38] For such cases, it is reasonable to utilize the $G_{PI}^{bulk}*(\omega)$ data of bulk PI to approximate the modulus of PI in the blend at $\omega < 1/\tau_a$ as $G_{PI}^{bld}*(\omega) = \phi_{PI} I_{PI} G_{PI}^{bulk}*(\omega\lambda_{PI})$ (cf. eqs 4-9 and 4-15). Then, $G_{PtBS}^{bld}*(\omega)$ of PtBS at $\omega < 1/\tau_a$ can be safely evaluated after subtraction of this $G_{PI}^{bld}*(\omega)$ from the $G^*(\omega)$ data of the blend. This subtraction is made in Chapters 5 and 6[36,38] to examine the thermo-rheological behavior of PtBS in the low-M blend.

4-3 Concluding Remarks

Viscoelastic, dielectric, and rheo-optical behavior was examined for well-entangled high-M PI/PtBS blends in the miscible state. The component dynamics therein, in particular that of PI (fast component), changed with T significantly.

At high T, the blend exhibited two-step entanglement plateau of the storage modulus G'. The high-ω and low-ω plateaus were attributed to the entanglement among all component chains and that between the PtBS chains (slow component), respectively. The entanglement length a characterizing the high-ω plateau was well described by the simple mixing rule based on the number fraction n of the Kuhn segments of the components, $a = n_{\mathrm{PI}} a_{\mathrm{PI}}^{\mathrm{bulk}} + n_{\mathrm{PtBS}} a_{\mathrm{PtBS}}^{\mathrm{bulk}}$. This result is consistent with the current molecular picture that relates the entanglement density to the packing length p ($\cong 1/20a$). Furthermore, in the high-ω plateau zone, the component moduli obtained from a blending law combined with this mixing rule of a were close to the rheo-optically determined moduli. This result lent further support to the above mixing rule.

At low T, the blend exhibited the Rouse-like power-law behavior of moduli ($G' = G'' \propto \omega^{1/2}$) at ω where the high-ω plateau was supposed to emerge. This lack of the high-ω plateau was attributed to retardation of the Rouse equilibration of the PI chain over the entanglement length a due to the hindrance from the slow PtBS chains. In other words, the PI and PtBS chains were equilibrated cooperatively/simultaneously at a rate essentially determined by PtBS. This equilibration time τ_a, evaluated from the G^* data of the blend, was shorter than the dielectrically detected terminal relaxation time of PI $\tau_\varepsilon^{\mathrm{PI}}$, but the difference between τ_a and $\tau_\varepsilon^{\mathrm{PI}}$ was rather small. Thus, the high-ω plateau zone was too narrow to be resolved experimentally, and the PI chains relaxed almost immediately after their Rouse equilibration (hindered by PtBS). This PI relaxation activated the CR relaxation of PtBS to dilate the entanglement mesh size for PtBS to that in the corresponding PtBS solution. A simple model considering the Rouse equilibration and CR/tube dilation processes described the G^* data of the blend surprisingly well, lending support to the molecular picture underlying the model, the cooperative/simultaneous Rouse equilibration of PI and PtBS chains. The model prediction was consistent with the rheo-optical data, which lent further support to this picture.

Finally, it should be emphasized that the cooperative Rouse equilibration is intimately related to the fundamental aspect of polymer rheology that the mechanical stress reflects the orientational anisotropy of subchains exploring all local conformations in a given time scale. At low T, the PI chain cannot explore all conformations at the length scale a within its intrinsic Rouse time $\tau_{\mathrm{a,PI}}$ because the slow PtBS chains behave as uncrossable obstacles in this time scale thereby hindering

the PI chain from this exploration. The chain motion is accelerated with increasing T more significantly for PtBS than for PI, which enables this exploration to occur within the intrinsic $\tau_{a,PI}$. The PI/PtBS blends exhibit the high-ω plateau only at such high T.

Appendix 4-1 Rouse Model and Thermal Constraint Release Model

Rouse model is formulated for a linear chain composed of N Gaussian subchains that are placed in a frictional medium. Each subchain, composed of g momoners, is modeled as a bead having a friction coefficient $\zeta_s = g\zeta_0$ (ζ_0 is the frictional coefficient of a monomer) and the neighboring beads are connected by a Gaussian spring with a spring constant $\kappa = 3k_BT/b_R^2$, with b_R being the average end-to-end distance of the subchain/Rouse segments. ($b_R^2 = gb^2$, where g and b are the number of monomers per Rouse segment and the effective step length of the monomer, respectively.) This bead-spring chain is schematically shown in Figure 4-8(a).[1,2]

The Rouse model is originally formulated for an isolated, non-entangled chain. However, this model can be utilized in other situation where the local interactions affect the chain dynamics. For example, the constraint release dynamics considers the chain moving through a local jump process, as schematically shown in Figure 4-8(b). The accumulation of these jumps results in a motion of the tube basically described by the Rouse dynamics. Thus, the Rouse model is valid in the long time scale even in the presence of local interaction, which is analogous to the static conformation described by the Gaussian function even in the presence of local attraction/repulsion.[1]

In the Rouse model, a time evolution of the position of each bead is determined by a balance of the frictional, elastic, and Brownian forces. From this time evolution, the orientation function $\mathbf{S}(n,t)$ (cf. eq 2-2) under the step strain γ is calculated to be:

$$\mathbf{S}(n,t) = \frac{2\gamma}{3N}\sum_{p=1}^{N}\sin^2\left(\frac{p\pi n}{N}\right)\exp\left(-\frac{t}{\tau_{R,p}}\right)$$

$$\text{with } \tau_{R,p} = \frac{\tau_R^G}{r_p^2} \text{ and } r_p = \sin\left\{\frac{p\pi}{2(N+1)}\right\}\sin^{-1}\left\{\frac{\pi}{2(N+1)}\right\} \qquad \text{(A4-1-1)}$$

In eq A4-1-1, τ_R^G is the longest viscoelastic Rouse relaxation time:

$$\tau_R^G = \frac{\zeta_s b_R{}^2 N^2}{6\pi^2 k_B T} \qquad \text{(A4-1-2)}$$

and $\tau_{R,p}$ is the characteristic time of the p-th relaxation mode, $\tau_{R,p} \cong \tau_R^G / p^2$ for large N. For monodisperse Rouse chains having a number density of ν, combination of eqs A4-1-1, 2-1 and 2-2 gives:

$$G(t) = \nu k_B T \sum_{p=1}^{N} \exp\left(-\frac{t}{\tau_{R,p}} \right) \qquad \text{(A4-1-3)}$$

For $N \gg 1$ and $t \ll \tau_R^G$ and/or $\omega \gg 1/\tau_R^G$, eq A4-1-3 gives a power law form $G(t) \propto t^{-1/2}$ and $G'(\omega) = G''(\omega) \propto \omega^{1/2}$.

Accumulation of the local CR jumps result in the Rouse-like feature of $G(t)$ and $G^*(\omega)$. A mean waiting time τ_w for the local CR jump, determining an effective local friction, is proportional to the relaxation time τ_{mat} of the tube forming matrix chains. Thus, in the Graessley model, τ_w is expressed as:[56]

$$\tau_w = \Lambda(z)\,\tau_{mat} \text{ with } \Lambda(z) = \frac{1}{z}\left(\frac{\pi^2}{12} \right)^z \qquad \text{(A4-1-4)}$$

where z is the average number of constraints per entanglement segment (= number of the local jump gates). The accumulation of the local CR jumps with characteristic time τ_w leads to a Rouse like relaxation until an effect of different type of topological constraints such as the probe-probe entanglement emerges.

References and Notes

1. Doi, M.; Edwards, S. F. *The Theory of Polymer Dynamics*, Oxford, Clarendon, **1986**.
2. Watanabe, H. *Prog. Polym. Sci.* **1999**, 24, 1253-1403.
3. McLeish, T. C. B. *Adv. Phys.* **2002**, 51, 1379-1527.
4. Rubinstein, M.; Colby, R. H. *Polymer Physics*, Oxford, New York, **2003**.
5. Graessley, W. W. *Polymeric Liquids and Networks: Dynamics and Rheology*, Garland Science, New York, **2008**.
6. Lodge, T. P.; McLeish, T. C. B. *Macromolecules* **2000**, 33, 5278-5284.
7. Zetsche, A.; Fischer, E. W. *Acta Polym.* **1994**, 45, 168-175.
8. Miller, J. B.; McGrath, K. J.; Roland, C. M.; Trask, C. A.; Garroway, A. N. *Macromolecules* **1990**, 23, 4543-4547.
9. Chung, G. C.; Kornfield, J. A.; Smith, S. D. *Macromolecules* **1994**, 27, 964-973.
10. Alegria, A.; Colmenero, J.; Ngai, K. L.; Roland, C. M. *Macromolecules* **1994**, 27, 4486-4492.
11. Kumar, S. K.; Colby, R. H.; Anastasiadis, S. H.; Fytas, G. *J. Chem. Phys.* **1996**, 105, 3777-3788.
12. Wetton, R. E.; Macknight, W. J.; Fried, J. R.; Karasz, F. E. *Macromolecules* **1978**, 11, 158-165.
13. Liang, K. M.; Banhegyi, G.; Karasz, F. E.; Macknight, W. J. *J. Polym. Sci. Part B: Polym. Phys.* **1991**, 29, 649-657.
14. Miura, N.; MacKnight, W. J.; Matsuoka, S.; Karasz, F. E. *Polymer* **2001**, 42, 6129-6140.
15. He, Y. Y.; Lutz, T. R.; Ediger, M. D. *Macromolecules* **2003**, 36, 8040-8048.
16. He, Y. Y.; Lutz, T. R.; Ediger, M. D. *Macromolecules* **2004**, 37, 9889-9898.
17. Zhao, J. S.; Ediger, M. D.; Sun, Y.; Yu, L. *Macromolecules* **2009**, 42, 6777-6783.
18. Angell, C. A. *J. Phys. Chem. Solids* **1988**, 49, 863-971.
19. Hodge, I. M. *J. Non-Cryst. Solids* **1996**, 202, 164-172.
20. Roland, C. M.; Ngai, K. N. *J. Non-Cryst. Solids* **1997**, 212, 74-76.
21. Hirose, Y.; Urakawa, O.; Adachi, K. *Macromolecules* **2003**, 36, 3699-3708.
22. Urakawa, O. *Nihon Reoroji Gakkaishi* **2004**, 32, 265-270.
23. Watanabe, H.; Urakawa, O. *Korean-Australian Rheol. J.* **2009**, 21, 235-244.
24. Pathak, J. A.; Colby, R. H.; Floudas, G.; Jerome, R. *Macromolecules* **1999**, 32, 2553-2561.
25. Pathak, J. A.; Colby, R. H.; Kamath, S. Y.; Kumar, S. K.; Stadler, R. *Macromolecules* **1998**, 31, 8988-8997.
26. Pathak, J. A.; Kumar, S. K.; Colby, R. H. *Macromolecules* **2004**, 37, 6994-7000.
27. Haley, J. C.; Lodge, T. P.; He, Y. Y.; Ediger, M. D.; von Meerwall, E. D.; Mijovic, J. *Macromolecules* **2003**, 36, 6142-6151.
28. Haley, J. C.; Lodge, T. P. *J. Rheol.* **2004**, 48, 463-486.

29. Haley, J. C.; Lodge, T. P. *J. Rheol.* **2005**, 49, 1227-1302.
30. Watanabe, H.; Ishida, S.; Matsumiya, Y.; Inoue, T. *Macromolecules* **2004**, 37, 1937-1951.
31. Watanabe, H.; Ishida, S.; Matsumiya, Y.; Inoue, T. *Macromolecules* **2004**, 37, 6619-6631.
32. Watanabe, H.; Sawada, T.; Matsumiya Y. *Macromolecules* **2006**, 39, 2553-2561.
33. Qiao, X.; Sawada, T.; Matsumiya, Y.; Watanabe, H. *Macromolecules* **2006**, 39, 7333-7341.
34. Watanabe, H. *Polymer J.* **2009**, 41, 929-950.
35. Yurekli, K.; Krishnamoorti, R. *J. Polym. Sci. Part B: Polym. Phys.* **2004**, 42, 3204-3217.
36. Watanabe, H.; Matsumiya, Y.; Takada, J.; Sasaki, H.; Matsushima, Y.; Kuriyama, A.; Inoue, T.; Ahn, K. H.; Yu, W.; Krishnamoorti, R. *Macromolecules* **2007**, 40, 5389-5399.
37. Takada, J.; Sasaki, H.; Matsushima, Y.; Kuriyama, A.; Matsumiya, Y.; Watanabe, H.; Ahn, K. H.; Yu, W. *Nihon Reoroji Gakkaishi* **2008**, 36, 35-42.
38. Chen, Q.; Matsushima, Y.; Masubuchi, Y.; Watanabe, H.; Inoue, T. *Macromolecules* **2008**, 41, 8694-8711.
39. Fetters, L. J.; Lohse, D. J.; Colby, R.H., *Chain Dimensions and Entanglement Spacings*, in *Physical Properties of Polymers Handbook*, 2nd ed.; Mark, J. E., Ed.; Springer: New York, 2007; Chapter 25, pp 445-452.
40. Watanabe, H. *Macromol. Rapid Commun.* **2001**, 22, 127-175.
41. Chen, Q.; Uno, A.; Matsumiya, Y.; Watanabe, H. *Nihon Reoroji Gakkaishi* **2010**, 38, 187-193.
42. T. Sawada, T.; Qiao, X.; Watanabe, H. *Nihon Reoroji Gakkaishi* **2007**, 35, 11-20.
43. Hayashi, C.; Inoue, T. *Nihon Reoroji Gakkaishi* **2009**, *37*, 205-210.
44. Inoue, T.; Okamoto. H.; Osaki, K. *Macromolecules* **1991**, 24, 5670-5675.
45. Okamoto, H.; Inoue, T.; Osaki, K. *J. Polym. Sci. Part B: Polym. Phys.* **1995**, 33, 417-424.
46. Inoue, T.; Matsui, H.; Osaki K. *Rheol. Acta* **1997**, 36, 239-244.
47. Within the context of the tube model, the PI relaxation in the blends at high *T* occurs in the fixed entanglement mesh formed by the slow PtBS chains as well as by the PI chains themselves.
48. Fetters, L. J.; Lohse, D. J.; Richter, D.; Witten, T. A.; Zirkel, A. *Macromolecules* **1994**, 27, 4639-4647.
49. Fetters, L. J.; Lohse, D. J.; Graessley, W. W. *J. Polym. Sci. Part B: Polym. Phys.* **1999**, 37, 1023-1033.
50. **a)** The Kuhn molecular weight of PtBS, $M_{\mathrm{Kuhn}}^{\mathrm{PtBS}} \cong 1500$, was evaluated from the data for the characteristic ratio ($C_\infty = 13.0 \pm 0.7$)[50b] and a ratio of the mean-square end-to-end distance to molecular weight reported for PtBS,[39] $\left\langle R_{\mathrm{PtBS}}^2 \right\rangle / \mathrm{nm}^2 = 3.6_1 \times 10^{-3} M_{\mathrm{PtBS}}$. **b)** Mays, J. W.; Ferry, W. M.; Hadjichristidis, N.; Funk, W. G.; Fetters, L. J. *Polymer* **1986**, 27, 129-132.
51. Kornfield, J. A.; Fuller, G. G.; Pearson, D. S. *Macromolecules* **1989**, *22*, 1334-1345.
52. Zawada, J. A.; Fuller, G. G.; Colby, R. H.; Fetters, L. J.; Roovers, J. *Macromolecules* **1994**, 27, 6851-6860.

53. Zawada, J. A.; Fuller, G. G.; Colby, R. H.; Fetters, L. J.; Roovers, J. *Macromolecules* **1994**, 27, 6861-6870.
54. Arendt, B. H.; Krishnamoorti, R.; Kornfield, J. A.; Smith, S. D. *Macromolecules* **1997**, 30, 1127-1137.
55. Osaki, K.; Inoue, T.; Uematsu, T.; Yamashita, Y. *J. Polym. Sci. Part B: Polymer Phys.* **2001**, 39, 1704-1712.
56. Graessley, W. W. *Adv. Polym. Sci.* **1982**, 47, 67-117.
57. The model (eqs 4-15 and 4-16) had also been modified by incorporating a minor contribution from the segmental (glassy) relaxation. The resulting model prediction remained close to that shown in Figure 4-6 (solid curves).
58. For the rheo-optical analysis, an attempt had also been given to incorporate the segmental (glassy) contribution in eq 4-12. The resulting component moduli were hardly different from those shown in Figure 4-7(b) (symbols).

Table 4-1. Characteristics of samples

Code	$10^{-3}M_w$	M_w/M_n	$T^{\infty}_{r,bulk}$/°C	R/nm [a]
PI99	98.5	1.04	30	25.9
PI128	128	1.03	30	29.5
PtBS348	348	1.05	180	35.4

a: The end-to-end distance of the chain was calculated by $R_X^2=[<R^2>/M]_X M_X$ (X = PI, PtBS) with $[<R^2>/M]_X$ = 6.79×10^{-3} and 3.61×10^{-3} for PI and PtBS, respectively.[39]

Table 4-2. Parameter values utilized in the model.

	PI99/PtBS348 w_{PI} = 50 wt% 30°C	PI128/PtBS348 w_{PI} = 50 wt% 30°C	PI128/PtBS348 w_{PI} = 40 wt% 60°C
a/nm [a]	6.3	6.3	6.5
τ_a/s [b]	2.5	2.5	1.0
τ_ε^{PI}/s [c]	10	20	2.8
$10^{-3}M_e^{PI}$ [d]	5.8	5.8	6.2
$10^{-3}M_e^{PtBS}$ [d]	10.8	10.8	11.5
N_R [e]	44	44	47
N_{CR} [f]	9	9	7
$10^{-2}\tau_{CR}$/s [g]	2.7	5.5	0.47

a: determined from eq 4-4; b: evaluated from G^* data (cf. eq 4-14)

c: evaluated from ε'' data; d: $M_e^X=\{a/a_X^{bulk}\}^2 M_e^{bulk\,X}$ (X = PI, PtBS)

e: $N_R = M_e^{PI}/M_{Kuhn}^{PI}$; f: $N_{CR} = M_e^{soln}/M_e^{PtBS}$;

g: $\tau_{CR}=\Lambda(z)\tau_\varepsilon^{PI}q_{N_{CR}}^2$ (cf. eqs 4-16a and 4-17)

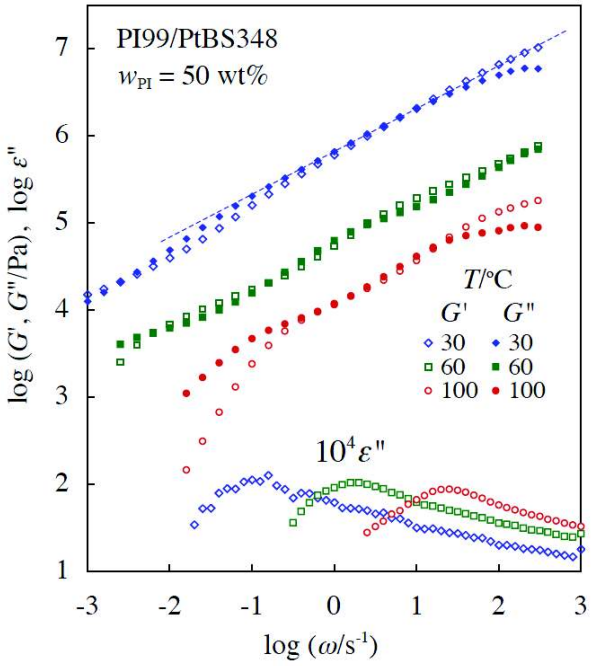

Fig. 4-1: Viscoelastic and dielectric behavior of PI99/PtBS348 blend with w_{PI} = 50 wt% at temperatures as indicated. The ε" data shown are the raw data without the dc correction. The dotted line attached to the modulus data at 30°C indicates the Rouse-like power-law behavior, $G' = G'' \propto \omega^{1/2}$.

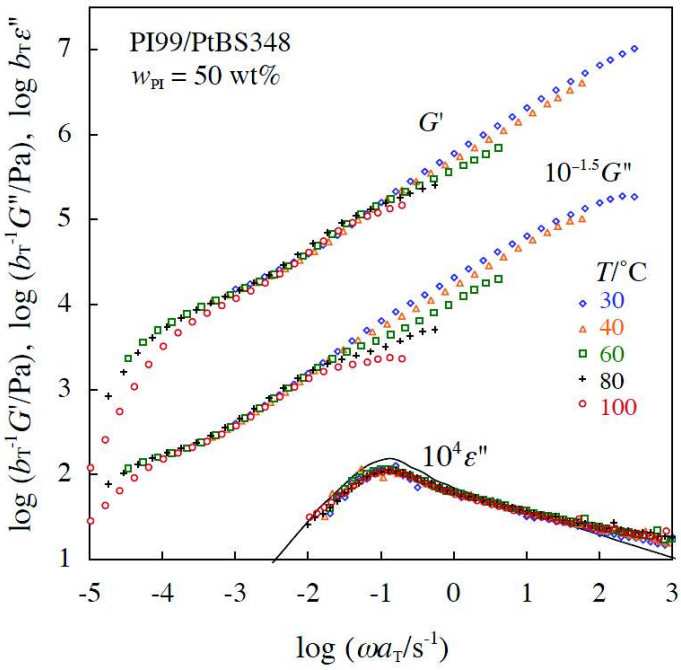

Fig. 4-2: Test of time-temperature superposition for the PI99/PtBS348 blend with w_{PI} = 50 wt%. The solid curve shows the ε" data of bulk PI99 corrected for the temperature and the PI volume fraction in the blend.

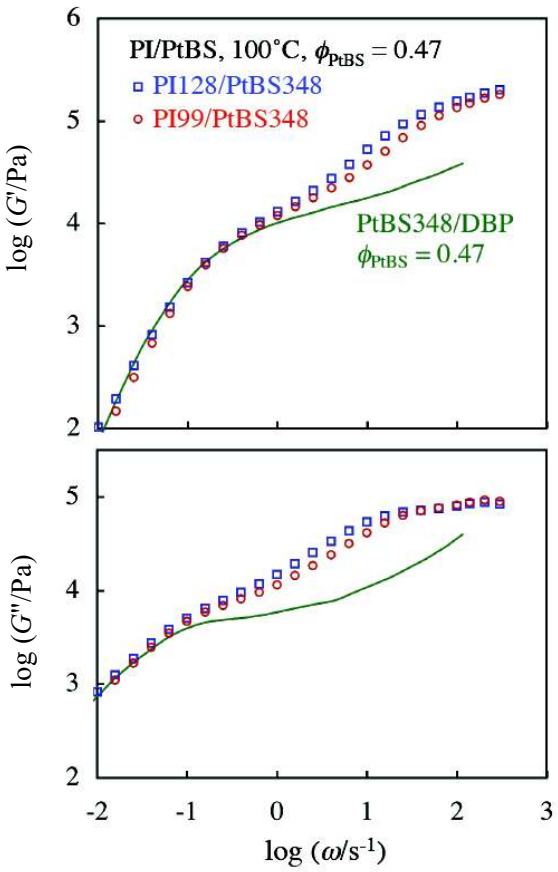

Fig. 4-3: Comparison of the viscoelastic behavior of PI99/PtBS348 and PI128/PtBS348 blends with that of a PtBS/DBP solution. All systems have the same PtBS volume fraction, ϕ_{PtBS} = 0.47.

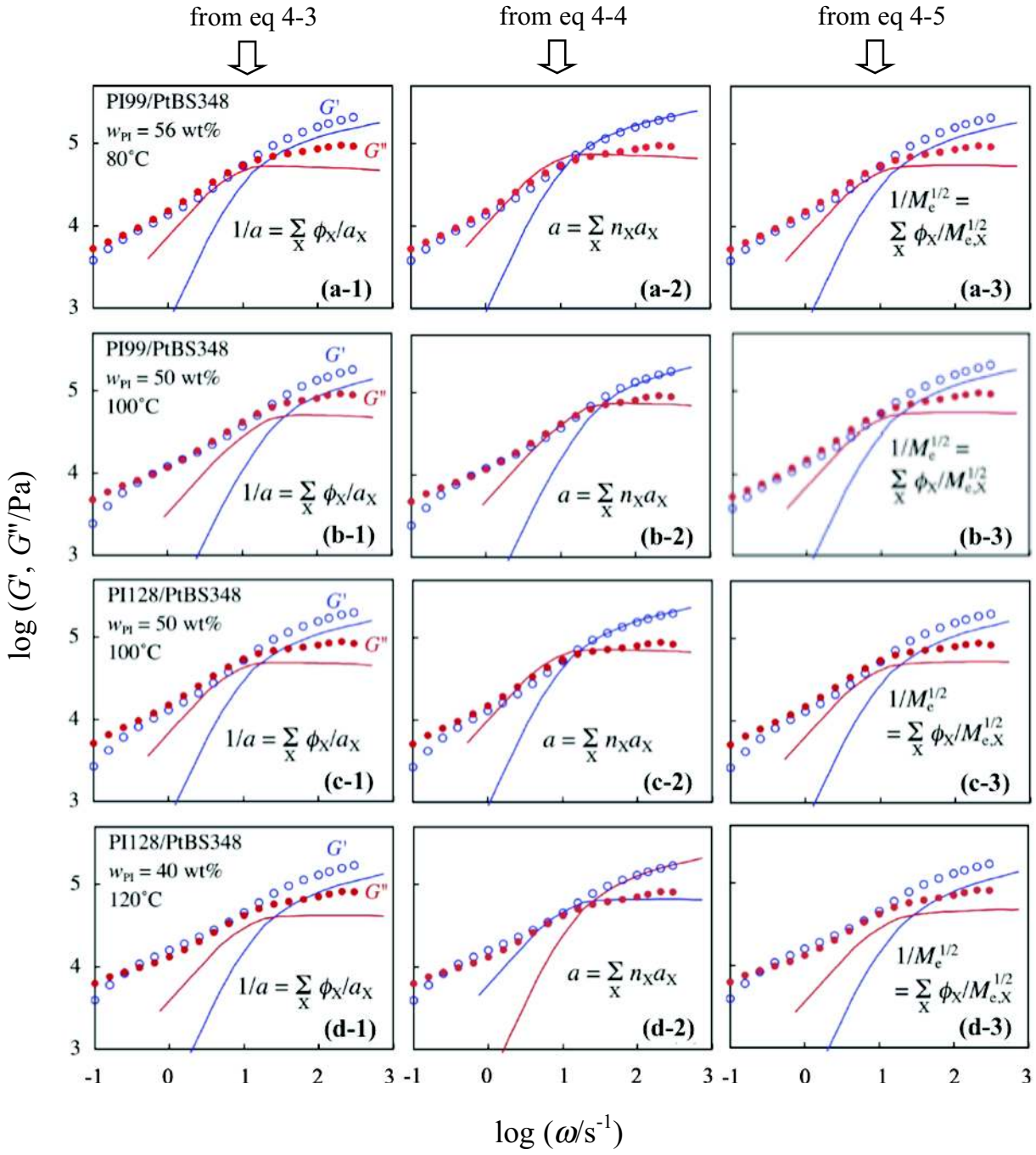

Fig. 4-4: Comparison of the G^* data of **(a)** PI99/PtBS348 blend (w_{PI} = 56 wt%) at 80°C, **(b)** PI99/PtBS348 blend (w_{PI} = 50 wt%) at 100°C, **(c)** PI128/PtBS348 blend (w_{PI} = 50 wt%) at 100°C, and **(d)** PI128/PtBS348 blend (w_{PI} = 40 wt%) at 120°C with the prediction of eqs 4-3, 4-4, and 4-5 combined with eq 4-9.

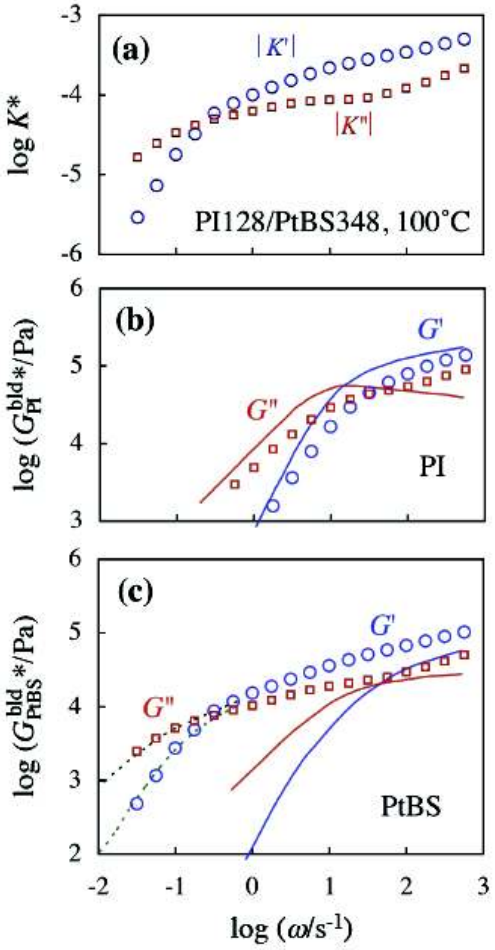

Fig. 4-5: **(a)** Complex shear optical coefficient of PI128/PtBS348 blend (w_{PI} = 50 wt%) at 100°C. **(b)**, **(c)** Comparison of the rheo-optically determined component moduli (symbols) with the moduli obtained on the basis of the blending rule, eq 4-9 combined with eq 4-4 (solid curves). The dotted curves in part c indicate the G^* data of the blend.

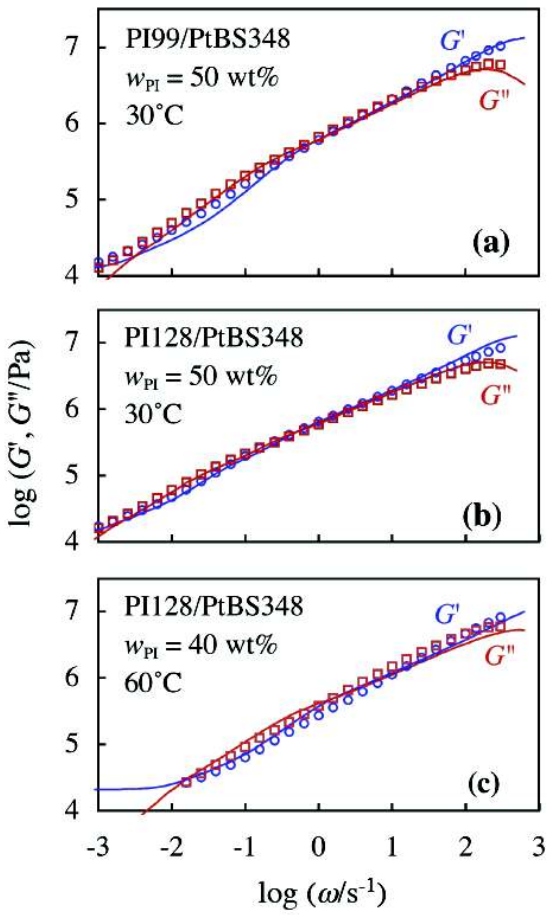

Fig. 4-6: Comparison of the model prediction (eqs 4-15 and 4-16; solid curves) with the G^* data measured for the PI/PtBS blends at T as indicated.

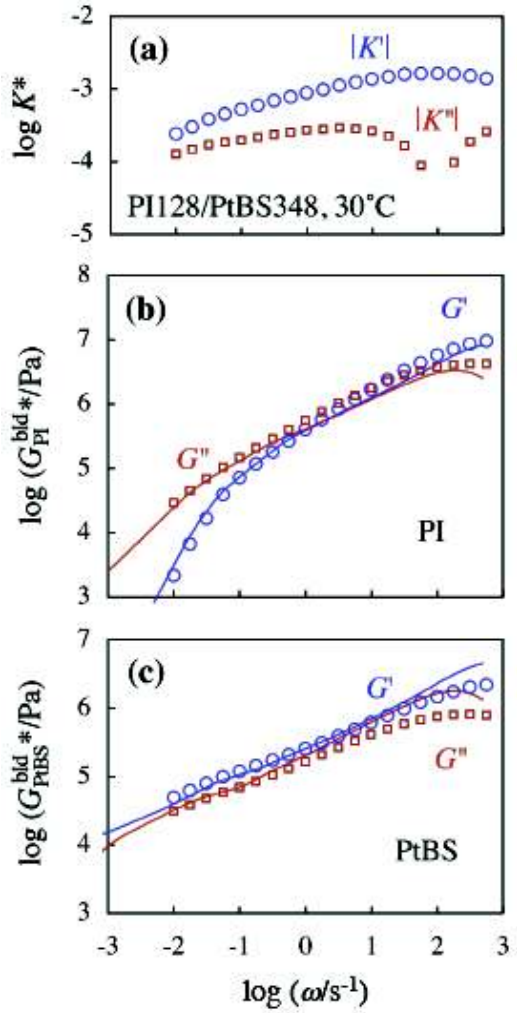

Fig. 4-7: **(a)** Complex shear optical coefficient of PI128/PtBS348 blend (w_{PI} = 50 wt%) at 30°C. **(b)**, **(c)** Comparison of the rheo-optically determined component moduli (symbols) with the moduli deduced from the model, eqs 4-15 and 4-16 (curves).

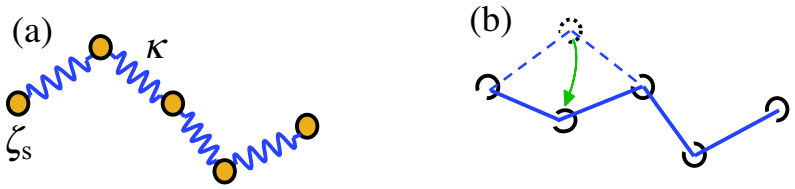

Fig. 4-8: Schematical illustration of **(a)** bead-spring chain and **(b)** local jump in the constraint release process.

Chapter 5 THERMO-RHEOLOGICAL BEHAVIOR OF PI/PTBS BLENDS: I

5-1 Introduction

As explained in Chapter 1, blends of *cis*-polyisoprene (PI) and poly(vinyl ethylene) (PVE) having a large miscible window have been frequently utilized as model systems to discuss the components dynamics.[1-6] For the PI/PVE blends, the thermo-rheologically simple behavior had been noted for the *terminal relaxation* of the components resolved through the dielectric[6,7] (cf. Figure 1-2) and rheo-optical measurements.[7,8] Correspondingly, Haley and coworkers[9,10] and Pathak and coworkers[5] treated each component as a thermo-rheologically simple component in long time scales to combine the concept of "double reptation" and "self-concentration" in their attempts of describing the viscoelastic data of PI/PVE blends. In particular, Haley and coworkers[9,10] observed changes of terminal mode distribution with the blend composition attributable to the composition dependence of the entanglement molecular weight and segmental friction, not to the *dynamic heterogeneity*.

In contrast, the thermo-rheological complexity attributable to the *dynamic heterogeneity* has been observed by Watanabe and coworkers for a LCST-type blend of *cis*-polyisoprene (PI20; $10^{-3}M_{PI} = 19.9$, $R_{PI} = 12$ nm, and $T_{g,bulk}^{PI} \cong -70°C$) and poly(*p-tert* butyl styrene) (PtBS70; $10^{-3}M_{PtBS} = 69.5$, $R_{PtBS} = 16$ nm, and $T_{g,bulk}^{PtBS} \cong 150°C$) with the PtBS concentration of $w_{PtBS} = 20$ wt%, as shown in Figure 1-4.[11] This complexity was attributed to the conditions:[11] (1) the concentration C of the PtBS70 chains is *not* much larger than the overlapping concentration C^*, $C_{PtBS70} \sim 2C_{PtBS70}^*$, (2) the average end-to-end distance R of the PI20 chians is *not* much larger than that of the PtBS70 chains, and (3) PI and PtBS have widely separated glass transition temperatures T_g in respective bulk states. The same degree of overlapping with the PtBS70 chains cannot be simultaneously achieved for all PI20 chains under the conditions (1) and (2). Then, some PI20 chains interacting with the locally condensed PtBS70 chains feel a higher friction compared to the others. This frictional distribution changes with temperature to result in the thermo-rheological complexity of the *terminal* relaxation of the PI20 chains as a whole ensemble.[11] It is worth noting that the time-temperature superposition held for the same PI20 chains blended with a lower-M PtBS16 ($10^{-3}M_{PtBS} = 16.4$ and $R_{PtBS} = 7.7$ nm) with the same PtBS concentration, $w_{PtBS} = 20$ wt%, quite possibly because PI20 was the *slow* component in this blend and the frictional heterogeneity due to PtBS16 was smeared in the time scale of the terminal relaxation of PI20.[12]

In relation to this point, it is expect that the superposition fails even in the PI20/PtBS16 blend on an increase of the weight fraction of PtBS, w_{PtBS}, that enhances a difference of effective T_g of PI20 and PtBS16 therein and forces PI20 to behave as the fast component. In addition, the

molecular picture of the *cooperative/simultaneous Rouse equilibration* over entanglement mesh for PI and PtBS components (as discussed in Chapter 4) is also expected for the low-M PI20/PtBS16 blends if both components have the chain size larger than the entanglement mesh size.

This chapter examines the linear viscoelastic and dielectric behavior of the PI20/PtBS16 blends with $w_{PtBS} > 20$ wt% to test these expectations. The failure of the time-temperature superposition was indeed observed for the PI20 chains in the blends with $w_{PtBS} = 30$ and 50 wt% (where PI20 behaved as the fast component). Furthermore, the relaxation of either PI20 or PtBS16 in these blends was delayed compared to its *iso*-τ_s bulk. The delay of the PI relaxation is in accordance with the molecular picture that the Rouse equilibration of PI chains over the entanglement mesh size is disturbed by the immobilized PtBS chains (as discussed in Chapter 4). The retardation of the PtBS relaxation was attributable to *pseudo-constraint release* mechanism activated by the global motion of the PI chains entangling with the PtBS chains. Details are explained below.

5-2 Experimental

An anionically synthesized atactic poly(*p-tert*-butyl styrene) sample (PtBS16)[12] and a commercially available high-*cis* polyisoprene sample[11] (PI20; supplied from Kuraray Co.) were used. Their molecular characteristics are summarized in Table 5-1. The microstructure of PI20, determined from ^{1}H-NMR, was 1,4-*cis* : 1,4-*trans* : 3,4 = 79 : 14 : 7. This microstructure enables the PI sample to be miscible with PtBS16 in a wide range of T ($\leq$ 250°C).

PI20/PtBS16 blends with the PtBS16 concentration of w_{PtBS} = 30 and 50 wt% were prepared according to the precipitation method reported by Yurekli and coworkers, as explained earlier in Section 2-1.[13]

For the PI20/PtBS16 blends with w_{PtBS} = 30 and 50 wt%, thermal (differential scanning calorimetry: DSC), viscoelastic, and dielectric measurements were conducted. In the thermal measurements, the DSC traces were recorded for respective specimen (~10mg) at a heating rate of 20°C/min in a range from −100°C to 200°C. The principle(s) and operation(s) of these measurements were explained in detail in Section 2-2.

5-3 Results and Discussion

5-3-1 Dynamic behavior of bulk components

The linear viscoelastic modulus of the PtBS16 sample was shown in Figure 3-1(b).[12] For bulk PI20, the storage and loss moduli, $G'(\omega)$ and $G''(\omega)$, a decrease of dielectric constant from is static value, $\Delta\varepsilon' = \varepsilon_0 - \varepsilon'(\omega)$, and dielectric loss, $\varepsilon''(\omega)$, are shown as functions of the angular frequency ω in the top panel Figure 5-1. The time-temperature superposition held for those data, with the shift factors a_T well described by WLF equation of bulk PI (solid curve, cf. eq 3-2),[11] as shown in the bottom panel of Figure 5-1.[11]

Here, a comment needs to be made for the entanglement in bulk PI20 and PtBS16 systems. The entanglement molecular weight defined within the classical rubber elasticity theory, $M_e = \rho RT/G_N$ (cf. eq 1-2), is $M_e^{\text{PI bulk}} = 5.0 \times 10^3$ and $M_e^{\text{PtBS bulk}} = 37.6 \times 10^3$ for bulk PI and bulk PtBS,[14] respectively. Thus, PI20 chains ($M_{PI} = 19.9 \times 10^3 \cong 4\, M_e^{\text{PI bulk}}$) are moderately entangled while the PtBS16 chains ($M_{PtBS} = 16.4 \times 10^3 \cong 0.4\, M_e^{\text{PtBS bulk}}$) are not entangled in respective bulk systems, as can be also noted from the ω dependence of their moduli; cf. cross of the G' and G'' curves seen in the top panel of Figure 5-1 and the Rouse/Zimm-like shape of the modulus of PtBS16 seen in Figure 3-1(b). The lack of entanglement (or motional constraint) for the PtBS16 chain, noted in the bulk state, is not necessarily an intrinsic property of this low-M PtBS chain but would be affected on blending with more flexible PI20. In relation to this point, Chapter 4 had concluded that the entanglement modulus of high-M PI/PtBS blends is satisfactorily described with a mixing rule weighing the entanglement mesh size a by the number fraction of Kuhn segments (cf. eq 4-4). This mixing rule gives a = 6.0, 6.0, and 6.3nm for PI/PtBS blends with w_{PtBS} = 20, 30, and 50wt%, respectively. These values are considerably smaller than the end-to-end distance of PtBS16 (R_{PtBS16} = 7.7nm), suggesting that a PtBS16 chain may feel some topological constraint from the surrounding PI20 chains. Meanwhile, the motional constraint for PI20 may be also affected on blending. Chapter 4 had concluded that PI and PtBS are coorperatively/simultaneously equilibrated over entanglement mesh at a rate essentially determined by PtBS. This mechanism may further affect the terminal relaxation of PI chains. These points are later discussed for the viscoelastic and dielectric data of the PI20/PtBS16 blends.

5-3-2 Overview of behavior of PI20/PtBS16 blends

Figure 5-2 shows the DSC profiles measured for the PI20/PtBS16 blends with w_{PtBS} = 30 and 50 wt%. For comparison, the profiles are shown also for bulk PI20 and PtBS16. The dashed lines

indicate the high-T baselines, and the thin solid and dotted arrows indicate the glass transition temperatures T_g for bulk PI20 and bulk PtBS16, respectively ($T_{g,PI}^{bulk}$ = –67°C and $T_{g,PtBS}^{bulk}$ = 138°C, chosen as the middle-point temperatures for respective glass transition zones). The thick solid and dotted arrows indicate *effective* T_g for PI20 and PtBS16 in the blends expected from the WLF analysis explained later. It is noted that the blends exhibit broad, almost two-step glass transition (in particular at w_{PtBS} = 50 wt%), despite their *static* homogeneity explained earlier. This broad glass transition reflects the dynamic heterogeneity affecting the segmental dynamics in the blends, as noted for a variety of miscible blends.[1-6]

Figure 5-3 shows the viscoelastic and dielectric data measured for the PI20/PtBS16 blends with w_{PtBS} = 30 and 50 wt%. The raw dielectric loss (ε") data are multiplied by a factor of 10^3 and compared with the storage and loss moduli (G' and G") data. For clarity of the plots, the data are shown only at representative temperatures. Since PtBS16 has no type-A dipole, the dielectric relaxation of the blends detected through the ε" data are exclusively attributed to the global motion of the PI20 chains therein. In Figure 5-3, the terminal dielectric relaxation characterized by the power-law tail, $\varepsilon'' \propto \omega$, is clearly observed without being disturbed by the direct current (dc) conduction due to ionic impurities giving $\varepsilon_{dc}'' = \sigma / \omega \propto \omega^{-1}$ (with σ = dc conductivity). In fact, the dc contribution to the ε" data was observed at high T; cf. the dashed line attached to the ε" data at 100°C shown in the top panel of Figure 5-3. However, even for this case, the dielectric relaxation is completed at relatively high ω where the dc contribution is negligibly small. Thus, throughout this chapter, only the raw ε" data having negligible dc contribution are utilized for discussing the PI20 global dynamics in the blends. The quality of those raw ε" data was checked in the following way. Whenever the dc contribution was detected at high T, changes of σ by ±30% is allowed to fit the low-ω ε" data with $\varepsilon_{dc}'' = \sigma / \omega$, subtracted this ε_{dc}" from the raw ε" data, and compared the residue $\varepsilon'' - \varepsilon_{dc}''$ with the raw data. At moderately high ω, the residue was quite insensitive to the ±30% changes of σ and indistinguishable from the raw data, as shown with the small filled circles (residue) and large unfilled circles (raw data) in the top panel of Figure 5-3. This chapter utilizes only the raw data at such moderately high ω where the terminal behavior was readily detected.

As seen in Figure 5-3, the blends as a whole (almost) exhibit the terminal viscoelastic relaxation characterized by the power-law tails of their storage and loss moduli data, $G_B' \propto \omega^2$ and $G_B'' \propto \omega$ (cf. dashed lines attached to the low ω data). From these tails, the second-moment average viscoelastic relaxation frequency[15] of the blends can be evaluated by (cf. eq 2-26):

$$\omega_G = \left[\frac{\omega G_B''}{G_B'} \right]_{\omega \to 0} \tag{5-1}$$

For monodisperse linear PI chains, the relaxation frequency can be simply estimated as the angular frequency $\omega_{\varepsilon\text{-peak}}$ for the ε'' peak (cf. eq 2-32).[15-20] Thus, comparison between viscoelastic ω_G and dielectric $\omega_{\varepsilon\text{-peak}}$ of the blends allows a specification of the fast component therein. At low T, ω_G (shown with the thick arrows) is located at low frequencies where the ε'' data are proportional to ω and the global relaxation of PI20 has completed. This fact unequivocally indicates that PI20 relaxes faster than the blend as a whole and thus PI20 and PtBS16 are the fast and slow components in the blends with w_{PtBS} = 30 and 50 wt% at those T. However, ω_G approaches $\omega_{\varepsilon\text{-peak}}$ and the difference of the terminal relaxation frequencies of PI20 and PtBS16 becomes smaller with increasing T. (Consequently, the PI20 relaxation would become slower than the PtBS16 relaxation at higher T not tested in this chapter.) In the PI20/PtBS16 blend with smaller w_{PtBS} (= 20 wt%), ω_G agreed well with $\omega_{\varepsilon\text{-peak}}$ in a range of T between 30 and 70°C and thus PI20 was the slow component, as found in the previous study of Watanabe and coworkers.[11] These changes of the relative relaxation rates of PI20 and PtBS16 strongly influence the thermo-rheological behavior of the PI20 chains in the blends, as discussed in the following section.

The horizontal dashed lines in Figure 5-3 indicate the plateau modulus G_N estimated as $G_N = C_{PI}RT/M_e^{PI} + C_{PtBS}RT/M_e^{PtBS}$ (cf. eq 4-14) for the blend at lowest T ($G_N = 3.7\times10^5$ and 3.2×10^5Pa for PI/PtBS blends with w_{PtBS} = 30wt% at 20°C and 50wt% at 30°C, respectively). Nevertheless, no plateau is noted for the PI20/PtBS16 blend with w_{PtBS} = 50wt% at 30°C where G_N is expected. The lack of plateau is attributable to the fact that the full relaxation of PI occurs immediately after the equilibration over a. This feature is noted in Figure 5-3: The characteristic frequency ω_a, where $G_B' = 1.111G_N$ (shown with thin arrow) is very close to the onset frequency for the terminal tail, $\varepsilon'' \propto \omega$. For such a case, the frequency window for the PI chain after its equilibration over a and before its terminal relaxation is too narrow (almost negligible) to allow the plateau to be resolved, as fully discussed in Chapter 4. This point is again examined in more detail in Chapter 6.

5-3-3 Dynamic behavior of PI chains in blends

5-3-3-1 Thermo-rheological behavior of PI

Figure 5-4 shows the master curves of the ε'' data measured for the PI20/PtBS16 blends with w_{PtBS} = 30 and 50 wt%; cf. top two panels. The data at respective temperatures T are multiplied by

an intensity correction factor, $b_T = T/T_r$ with T and T_r being represented in K unit, and shifted along the ω axis by a factor of $a_{T,\varepsilon}$ to achieve the best superposition around the ε'' peak with the data at a reference temperature T_r: T_r was chosen to be 343 and 393K (70 and 120°C) for w_{PtBS} = 30 and 50 wt%, respectively. (As explained in Section 2-2-3-3, changes of the density and a mean-square end-to-end distance of PI, much smaller than the change of T (in K) itself, have been safely neglected in this b_T factor as well as the $b_T°$ factor explained below.) For comparison, the master curve (with T_r = 30°C) is also shown for the blend with w_{PtBS} = 20 wt% examined in the previous work.[12] The $a_{T,\varepsilon}$ data for these blends are shown later in the top panel of Figure 5-7.

In all panels of Figure 5-4, the solid curve represents the normalized dielectric loss of bulk PI20 at $T_{r,bulk}$ = 303 K (30°C), $\phi_{PI} b_T° \varepsilon''_{PI}{}^{bulk}(\omega/\Lambda_{PI})$, plotted against ω. Here, ϕ_{PI} is the volume fraction of PI in the blends, and $b_T° = T_{r,bulk}/T_r$ with T_r being the reference temperature of PI20 in the blends; (ϕ_{PI}, T_r/K) = (0.53, 393), (0.73, 343), and (0.81,303) for w_{PtBS} = 50, 30, and 20 wt%. The frequency reduction factor Λ_{PI}(= 7.3, 2.0, and 0.44 for w_{PtBS} = 50, 30, and 20 wt%) was chosen to give the best superposition of the $\phi_{PI} b_T° \varepsilon''_{PI}{}^{bulk}(\omega/\Lambda_{PI})$ data on the ε'' peaks of the blends.

At low T, the dielectric mode distribution of PI20 in the blends with w_{PtBS} = 50 and 30 wt% agrees with that of bulk PI20 at $\omega \geq \omega_{\varepsilon\text{-peak}}$ but broadens at lower ω; cf. Figure 5-4. This low-ω mode distribution narrows with increasing T and finally coincides with that of bulk PI20 at sufficiently high T, demonstrating the thermo-rheological complexity of the PI20 chains in the blends. This behavior strongly suggests that the PI20 chains split into the majority and minority components, the former governing the observed ε'' peak and relaxing faster than the latter, and that the difference of the relaxation rates of these components decreases with increasing T.[11] This difference appears to be sufficiently small in the entire range of T examined for the blend with w_{PtBS} = 20 wt% (bottom panel), which possibly led to the thermo-rheological simplicity seen at those T.

The splitting of the PI20 chains into the majority and minority, seen at w_{PtBS} = 30 and 50 wt%, can be related to the frictional non-uniformity due to the PtBS16 chains (that relax more slowly even compared to the minority PI20 at low T where the splitting/mode broadening is observed). This effect of PtBS16 on the PI20 relaxation is further discussed later in Figure 5-7 in relation to the terminal relaxation times of PI20 in the blends.

5-3-3-2 Separate examination of behavior of majority and minority PI

This section attempts to separate the ε'' data of the blends into contributions from the majority and minority components of PI20 therein and examine the relaxation behavior of respective

components. It is well known that the dielectric mode distribution for the global relaxation (end-to-end vector fluctuation) of PI chains is insensitive to their molecular weight and changes of the environment (*e.g.*, dilution with a solvent) unless they are subjected to strong thermodynamic/spatial confinements.[16,21] Thus, the dielectric mode distribution (observed as the relative ω dependence of ε'') can be safely approximated to be the same for each component in the blends and bulk PI20. Then, the $\varepsilon''(\omega,T)$ data of the blends at a given T can be expressed in terms of the $\varepsilon_{PI}^{bulk}''(\omega)$ data of bulk PI20 at its reference temperature, $T_{r,bulk} = 303$K, as:

$$\varepsilon''(\omega,T) = b_T'\phi_{PI}\left[\upsilon_{maj}\varepsilon_{PI}^{bulk}''(\omega/\lambda_{PI}^{maj}) + \{1-\upsilon_{maj}\}\varepsilon_{PI}^{bulk}''(\omega/\lambda_{PI}^{min})\right]$$

$$\text{with } b_T' = T_{r,bulk}/T \qquad (5\text{-}2)$$

Here, ϕ_{PI} is the PI20 volume fraction in the blend, λ_{PI}^{maj} and λ_{PI}^{min} are the frequency reduction factors for the fast and slow components of PI20 (majority and minority), respectively, and υ_{maj} is the majority component fraction in the ensemble of PI20 chains.

A comment needs to be added to eq 5-2. In general, $\varepsilon''(\omega,T)$ is written as a sum of the contributions from more than two components. However, the close coincidence of the ε'' data of the blends and bulk PI20 seen at $\omega \geq \omega_{\varepsilon\text{-peak}}$ (Figure 5-4) suggests that the data of the blends at those ω are dominated by a single fast component (majority). Furthermore, the ε'' data of the blends at lower ω were larger than the bulk data only by a factor < 5 (because of this coincidence at $\omega \geq \omega_{\varepsilon\text{-peak}}$), which did not allow a fine resolution of the minority into several slow components contributing to the blend data at $\omega < \omega_{\varepsilon\text{-peak}}$. For this reason, the minority is represented as a single component in eq 5-2. In fact, the ε'' data of the blends were successfully described by eq 5-2 within experimental uncertainty, as explained below.

The blend data are fitted with eq 5-2 to determine the three parameters therein, λ_{PI}^{maj}, λ_{PI}^{min}, and υ_{maj}, in the following way: Since the ε'' data of the blend and bulk PI20 are close to each other at $\omega \geq \omega_{\varepsilon\text{-peak}}$ (cf. Figure 5-4), λ_{PI}^{maj} should be close to the $\Lambda_{PI}/a_{T,\varepsilon}$ ratio with Λ_{PI} and $a_{T,\varepsilon}$ being the frequency reduction factor utilized in Figure 5-4 and the shift factor shown in the top panel of Figure 5-7, respectively. The close coincidence of the blend and bulk data also indicates that υ_{maj} is close to a ratio r_ε of the ε'' peak height of the blend to that of bulk PI20 (after the correction of the PI volume fraction and temperature). Thus, in the fitting procedure, λ_{PI}^{maj} and υ_{maj} were varied from the known values of $\Lambda/a_{T,\varepsilon}$ and r_ε in a stepwise way; a few percent change for either λ_{PI}^{maj} or υ_{maj} in each step and less than 30% change in total (after several steps). For given values of λ_{PI}^{maj} and υ_{maj} in each step, the blend data were fitted by eq 5-2 utilizing the $\varepsilon_{PI}^{bulk}''$ data and an appropriately chosen λ_{PI}^{min} value, and the fitting quality was examined. Indeed, a good fit was achieved for λ_{PI}^{maj}

and υ_{maj} close to $\Lambda/a_{T,\varepsilon}$ and r_ε, respectively, and λ_{PI}^{min} smaller than λ_{PI}^{maj}; for example, $\lambda_{PI}^{maj} = \Lambda_{PI}/a_{T,\varepsilon}$ (= 0.042), $\upsilon_{maj} = 0.73 r_\varepsilon$ (= 0.66), and $\lambda_{PI}^{min} = 0.14\,\lambda_{PI}^{maj}$ (= 0.006) for the blend with w_{PtBS} = 50 wt% at 40°C. In the fitting procedue, just the single parameter λ_{PI}^{min} was required to be varied in a wide range and thus no significant ambiguity emerged.

Figure 5-5 shows the best-fit results thus obtained for the blends with w_{PtBS} = 50 and 30wt%. The dotted and dashed curves show the contribution from the fast and slow components of PI20, respectively, and the solid curves indicate the sum of these contributions (eq 5-2). This sum agrees well with the $\varepsilon''(\omega,T)$ data (symbols), which demonstrates that the PI20 chains in the blends can be classified into the fast component (majority) and slow component (minority), with the latter being the representative of various slow components.

From the frequency reduction factors λ_{PI}^{maj} (almost identical to Λ_{PI}/a_T) and λ_{PI}^{min} determined from the fitting, the dielectric relaxation time of PI20 in the blends was evaluated as:

$$\tau_\varepsilon = \{\omega_{\varepsilon\text{-peak}}^{bulk}\lambda_{PI}^{j}\}^{-1} \text{ with } j = \text{(fast) majority and (slow) minority} \qquad (5\text{-}3)$$

where $\omega_{\varepsilon\text{-peak}}^{bulk}$ (= 1.5×10^3 s^{-1}) is the angular frequency for the ε'' peak of bulk PI20 at its $T_{r,bulk}$ (= 30°C). Top three panels of Figure 5-6 show plots of the τ_ε data of the majority and minority components of PI20 in the blends against the temperature T; cf. large and small circles. The bottom panel shows the plots of the majority fraction υ_{maj} (determined from the fitting together with λ's). For the blend with w_{PtBS} = 20 wt%, the ε'' data exhibited the thermo-rheological simplicity and their mode distribution was indistinguishable from that of bulk PI20; cf. bottom panel of Figure 5-6. Thus, for this blend, υ_{maj} was set to be unity and τ_ε was evaluated only for the majority.

In the top two panels of Figure 5-6, large filled squares indicate the viscoelastic relaxation time of the PtBS16 chains with w_{PtBS} = 50 and 30 wt% evaluated from their modulus G_{PtBS}^{bld}* (the superscript "bld" indicates the modulus in the blend), $\tau_{G,PtBS} = [G_{PtBS}^{bld}'/\omega G_{PtBS}^{bld}'']_{\omega\to0}$. G_{PtBS}^{bld}* was obtained by subtracting the modulus G_{PI}^{bld}* of the PI20 chains in the blends from G_B* of the blends as a whole, as explained later in detail. (For the blends with w_{PtBS} = 20 wt%, G_{PI}^{bld}* was very close to G_B* and this subtraction could not be made accurately.[11] For this reason, no $\tau_{G,PtBS}$ data are shown in the third panel.)

In the blends with w_{PtBS} = 30 and 50 wt%, the viscoelastic $\tau_{G,PtBS}$ of PtBS16 is considerably longer than the dielectric τ_ε of the coexisting PI20 at most of the temperatures examined (cf. top two panels of Figure 5-6). This result confirms that PtBS16 and PI20 are the slow and fast components therein. Furthermore, the PI20 chains in the PI/PtBS blends should have $\tau_G \cong \tau_\varepsilon/2$ at

high T where the difference of the PI20 and PtBS16 relaxation rates is reduced, as similar to the behavior of bulk monodisperse PI systems in which all chains relax at the same rate.[16-18] (The PI chains in the monodisperse systems relax partly through the dynamic tube dilation (DTD) mechanism to have $\tau_G \cong \tau_\varepsilon/2$.[16-18]). Thus, the difference of the relaxation rates of the PtBS16 and PI20 chains in the PI/PtBS blends is more significant than it appears in Figure 5-6, given that the τ_G/τ_ε ratio for PI20 ($\cong$ 1/2 at high T) is taken into account.

5-3-3-3 Origin of thermo-rheological complexity of PI

The PI20/PtBS16 blends with w_{PtBS} = 30 and 50 wt% satisfy the conditions explained earlier:[11] (1) The concentration C_{PtBS} of PtBS16 (the slow chain) is not much larger than its overlapping concentration C_{PtBS}*; C_{PtBS}/C_{PtBS}* = 0.9, 1.4, and 2.3 for PI20/PtBS16 blend with w_{PtBS} = 20wt%, 30wt%, and 50wt%, respectively, as summarized in Table 5-2. (2) The average end-to-end distance R_{PI} of PI20 (the fast chain) is not much larger than R_{PtBS} of PtBS16; $R_{PI}/R_{PtBS} \cong 1.6$. (3) PI20 and PtBS16 have widely separated bulk T_g (Figure 5-2), which leads to a difference of their effective T_g in the blends and to the corresponding difference of their local friction coefficients. Thus, the dynamic heterogeneity of the PtBS concentration should be effectively frozen over the length scale of R_{PI} ($\sim R_{PtBS}$) in the time scale of the global relaxation of PI20, which naturally results in the splitting of the PI20 chains into the majority and minority components. The minority should be in the transiently PtBS-enriched region to have a higher effective T_g and feel a higher friction compared to the majority, which leads to the observed difference of their τ_ε and mode broadening at low T. Since the acceleration of the relaxation with T would be stronger for the minority component having the higher effective T_g (as expected from the WLF equation for a_T utilizing T_g as a reference temperature[22]), the whole ensemble of the PI20 chains should exhibit the thermo-rheological complexity and its mode distribution approaches that of bulk PI20 at high T, which is in harmony with the observation. In addition, the majority fraction increases with increasing T (cf. bottom panel of Figure 5-6), which also contributes to this complexity. This increase of the majority fraction may be partly due to the decrease of the difference between the relaxation times of PtBS16 and the minority PI20; cf. top two panels of Figure 5-6: This decrease enhances a probability for the escape of the minority PI20 chains from the PtBS-rich region before completion of their global relaxation. Then, some of the PI chains behaving as the minority at low T would become indistinguishable from the majority (defined as the component governing the ε'' peak), which possibly results in the increase of the majority fraction.

All above results confirm the molecular scenario proposed in the previous work.[11] In relation to this point, it should be emphasized that the PI20 chains in the blend with w_{PtBS} = 20 wt% exhibit the thermo-rheological simplicity (cf. Figure 5-4) because they relax more slowly than the coexisting PtBS16 chains.[12] This simplicity corresponds to the high-T asymptotic behavior seen for larger w_{PtBS}. It is informative to consider why PI20 behaves as the slow component at w_{PtBS} = 20 wt%. The glass transition zone of the blend becomes narrower with decreasing w_{PtBS}, suggesting that the difference of the effective T_g of PI20 and PtBS16 significantly decreases with decreasing w_{PtBS} due to the strong plasticization of PtBS16 by PI20; cf. Figure 5-2. In the blend with w_{PtBS} = 20 wt%, PI20 and PtBS16 seem to have rather similar effective T_g values. (In fact, no broad glass transition was clearly detected in DSC measurements for this blend.) Then, the PtBS16 chains relax faster than PI20 just because of their low-M_{PtBS} value (< M_{PI}), thereby smearing the frictional non-uniformity for the global relaxation of PI20 and allowing PI20 to exhibit the thermo-rheological simplicity at T = 30-70°C. This argument is consistent with the observation that the simplicity vanishes in the same range of T when PI20 is blended with a *high-M* PtBS70 at the same composition (w_{PtBS} = 20 wt%).[11] The *high-M* PtBS70 chains relaxed more slowly than PI20 even when PI20 and PtBS70 have rather similar effective T_g values (at w_{PtBS} = 20 wt%), thereby forcing PI20 to violate the simplicity.

5-3-3-4 Further discussion of dynamics of majority PI in iso-τ_s state

At a given T, the PI20 relaxation in the PI20/PtBS16 blends with w_{PtBS} = 30 and 50 wt% is slower than that in the bulk PI20 system. This difference of the PI20 relaxation rates in the blends and bulk should emerge through several different mechanisms, as briefly summarized below: (1) the PI20 chains are anti-plasticized by the PtBS16 chains to have the characteristic time of the Rouse segment, τ_s, higher than PI20 bulk at the same T. (2) the dynamic tube dilation (DTD)/constraint release (CR) mechanism[16,18,23] working in the moderately entangled bulk PI20 system should be restricted by the PtBS16 chains to retard the PI20 relaxation compared to that in the bulk system, given that the PtBS16 chains are concentrated and relaxing much more slowly than the PI20 chains. (3) the Rouse equilibration of the PI20 chain over the entanglement mesh size is disturbed by the surrounding PtBS16 chains. The shift factor $a_{T,\varepsilon}$ (top panel of Figure 5-7) obtained for the majority of the PI20 chains in the PI20/PtBS16 blends should reflect all of these effects.

An empirical method to correct the rectriction of DTD/CR mechanism is formulated below. The correction is minor in a numerical sense but is important conceptually. Then, WLF analysis is made for the $a_{T,\varepsilon}$ data corrected for this restriction to determine an iso-τ_s temperature $T_{iso\text{-}PI}$ for PI20.

(This iso-τ_s temperature is frequently referred to as the iso-ζ_s temperature in literature because a change of $\tau_s \sim \zeta_s /T$ is dominated by a change of ζ_s.) Finally, the dielectric τ_ε data of PI20 in the blend and bulk is compared in the iso-τ_s state to discuss an effect of PtBS16 chains on the motion of PI20 chains.

Relaxation time data obtained for binary blends of low-*M* and high-*M* PI chains are free from the anti-plasticization effect and thus helpful for making the correction for the restriction of DTD/CR on blending. Specifically, increases of the viscoelastic and dielectric relaxation times $\tau_{G1}(\phi_2)$ and $\tau_{\varepsilon 1}(\phi_2)$ of the fast component 1 (low-*M* PI), resulting from this restriction due to the slow component 2 (high-*M* PI having the volume fraction ϕ_2), was found to be well correlated with a ratio of the viscoelastic relaxation times of the two components in the blend, $\tau_{G2}(\phi_2)/\tau_{G1}(\phi_2)$; as explained in Appendix 5-1. At this moment, no DTD/CR theory describing this correlation accurately and enabling the above correction rigorously is available. Thus, the restriction of the DTD/CR mechanism is corrected here by utilizing empirical equations (Appendix 5-1) that satisfactorily quantify the correlation,

$$\log\left(\frac{\tau_{G1}(\phi_2)}{\tau_{G1}(0)}\right) = B\ \tanh\left\{\alpha\left[\log\left(\frac{\tau_{G2}(\phi_2)}{\tau_{G1}(\phi_2)}\right)\right]^q\right\} \tag{5-4}$$

$$Q \equiv \left(\frac{\tau_{\varepsilon 1}(\phi_2)}{\tau_{\varepsilon 1}(0)}\right) = \left(\frac{\tau_{G1}(\phi_2)}{\tau_{G1}(0)}\right)^{0.3} > 1 \tag{5-5}$$

Here, $\tau_{G1}(0)$ and $\tau_{\varepsilon 1}(0)$ denote the viscoelastic and dielectric relaxation times of the fast component in its monodisperse state, and the coefficients (B, α, q) are (0.2, 0,23, 3) and (0.41, 0.2, 2.5) for ϕ_2 = 0.27 and 0.47, respectively. Since the dielectric relaxation of monodisperse PI is hardly affected while the viscoelastic relaxation is considerably accelerated (by a factor $\cong$ 2) by the DTD mechanism (cf. Appendix 5-1), the restriction of DTD for the fast component in the blends leads to an increase less significant for $\tau_{\varepsilon 1}(\phi_2)$ than for $\tau_{G1}(\phi_2)$. Namely, a relationship $\tau_{\varepsilon 1}(\phi_2)/\tau_{\varepsilon 1}(0) < \tau_{G1}(\phi_2)/\tau_{G1}(0)$ holds. The empirical exponent of 0.3 (< 1) appearing in eq 5-5 is a consequence of this relationship.

The factor Q given by eq 5-5 specifies the increase of the dielectric τ_ε of the fast component due only to the restriction of DTD/CR. Eqs 5-4 and 5-5 can be utilized for the PI/PtBS blends to evaluate Q for the PI chains (fast component therein) and then correct the raw $a_{T,\varepsilon}$ data (top panel of Figure 5-7). For this purpose, the viscoelastic relaxation time of the slow component (PtBS) in the blends, $\tau_{G2}(\phi_2)$ appearing in eq 5-4, can be well approximated by $\tau_{GB}(\phi_2)$ of the blend as a whole.

Although $\tau_{GB}(\phi_2)$ should be somewhat smaller than $\tau_{G2}(\phi_2)$ in a rigorous sense, the Q values obtained from the following analysis changed less than a few percent even $\tau_{GB}(\phi_2)$ is increased artificially by a factor of 2. Thus, this approximation was quite harmless, allowing a replacement of the $\tau_{G2}(\phi_2)/\tau_{G1}(\phi_2)$ term in eq 5-4 by

$$\frac{\tau_{G2}(\phi_2)}{\tau_{G1}(\phi_2)} \cong \frac{\tau_{GB}(\phi_2)}{\tau_{G1}(\phi_2)} = \left\{\frac{\tau_{GB}(\phi_2)}{\tau_{\varepsilon 1}(\phi_2)}\right\} \times \left\{\frac{\tau_{\varepsilon 1}(\phi_2)}{\tau_{G1}(\phi_2)}\right\} = \left\{\frac{\tau_{GB}(\phi_2)}{\tau_{\varepsilon 1}(\phi_2)}\right\} \times \left\{\frac{\tau_{\varepsilon 1}(0)}{\tau_{G1}(0)}\right\} \times Q^{-2.33} \qquad (5\text{-}6)$$

(A relationship obtained from rearrangement of eq 5-5, $\tau_{\varepsilon 1}(\phi_2)/\tau_{G1}(\phi_2) = Q^{-2.33}\tau_{\varepsilon 1}(0)/\tau_{G1}(0)$, has been utilized in eq 5-6.) Insertion of eqs 5-5 and 5-6 into eq 5-4 gives an equation that expresses Q only in terms of directly measurable quantities,

$$\log Q = 0.3B \tanh\left\{\alpha\left[\log\left(\frac{\tau_{GB}(\phi_2)}{\tau_{\varepsilon 1}(\phi_2)}\right) + \log\left(\frac{\tau_{\varepsilon 1}(0)}{\tau_{G1}(0)}\right) - 2.33\log Q\right]^q\right\} \qquad (5\text{-}7)$$

For the known $\tau_{GB}(\phi_2)$ and $\tau_{\varepsilon 1}(\phi_2)$ data, known $\tau_{\varepsilon 1}(0)/\tau_{G1}(0)$ ratio ($\cong$ 2 for bulk PI), and the known parameter values (B, α, q), eq 5-7 can be numerically solved to evaluate Q for the majority of PI in the PI/PtBS blends (in which PI is the fast component). From the Q factor thus obtained, the shift factor is corrected as $a_{T,\varepsilon}^{cor} = a_{T,\varepsilon}/Q$. This $a_{T,\varepsilon}^{cor}$ reflects exclusively a change of τ_s with T for the majority of the PI chains. A standard WLF analysis (cf. Appendix 3-1) was made on $a_{T,\varepsilon}^{cor}$ to determine the iso-τ_s temperature $T_{iso\text{-}PI}$ for the majority of PI20 in the blends. These $T_{iso\text{-}PI}$ values, corresponding to $T_{iso\text{-}PI}$ (bulk) = 30°C (=$T_{r,bulk}$) of bulk PI20, are summarized in Table 5-2.

For the PI20/PtBS16 blends with w_{PtBS} = 30 and 50 wt%, the shift factor $a_{T,iso}$ re-evaluated with respect to $T_{iso\text{-}PI}$ is plotted against $T - T_{iso\text{-}PI}$ in the middle panel of Figure 5-7; cf. square and triangle. For comparison, $a_{T,iso}$ is also shown for the previously examined PI20/PtBS16 blend with w_{PtBS} = 20 wt% (cf. circle).[11] In this 20 wt% blend, PI20 relaxed slower than PtBS16 and thus $T_{iso\text{-}PI}$ (= 41°C) was determined from the WLF analysis of the raw $a_{T,\varepsilon}$ data[11] (without the correction for the restriction of DTD/CR). The solid curve indicates the WLF eq 3-2 that excellently describes the a_T data for bulk PI20 with $T_{iso\text{-}PI}^{bulk} = T_{r,bulk}$ = 30°C. The plots for the PI20/PtBS16 blends with w_{PtBS} = 20-50 wt% are indistinguishable from this solid curve, lending support to the WLF-determination of $T_{iso\text{-}PI}$ in the blends.

The difference of the iso-τ_s temperatures in the blends and bulk, $\Delta T_{iso} = T_{iso\text{-}PI} - T_{iso\text{-}PI}^{bulk}$, can be regarded as a difference of the effective glass transition temperatures in these systems. Then, the ΔT_{iso} data may be utilized to *estimate* the effective T_g of PI20 in the blend as $T_{g,PI}^{eff} = T_{g,PI}^{bulk} + \Delta T_{iso}$ (with $T_{g,PI}^{bulk}$ = –67°C). These estimates, shown in Figure 5-2 with thick solid arrows attached to the

DSC traces, are well located at the low-T side of the broad glass transition zone, as expected. It should be noted that $T_{g,PI}^{eff}$ defined for the Rouse segments is not necessarily identical to the thermal glass transition detecting the onset of motion of the monomeric segments.[1] These two types of segments are not identical to each other and exhibit different T dependence of the friction coefficient at low T (~ T_g), as well known from the fact[24-26] that G^* data of homopolymers are thermo-rheologically complex and associated with complicated changes of the rheo-optical data at low T. Nevertheless, a reasonable agreement is noted between T_g^{eff} (for the Rouse segment) and the DSC traces (for the monomeric segment).

In the bottom panel of Figure 5-7, the raw τ_ε data for w_{PtBS} = 30 and 50 wt% (that are a little affected by the restriction of DTD/CR) are plotted against $T-T_{iso\text{-}PI}$. cf. square and triangle. For comparison, the τ_ε data in the previously examined PI20/PtBS16 blend with w_{PtBS} = 20 wt% are also shown; cf. circle. The solid curve indicates the $\tau_{\varepsilon,bulk}$ data of bulk PI20 plotted against $T-T_{iso\text{-}PI}$ (= $T-T_{r,bulk}$), and the dashed curve shows these bulk $\tau_{\varepsilon,bulk}$ data multiplied by a factor of 2.4.

Clearly, the τ_ε data of the blend (=τ_ε of majority PI20) for w_{PtBS} = 30 and 50 wt% is larger than $\tau_{\varepsilon,bulk}$ of iso-τ_s bulk PI20 by a factor of 2.4. The anti-plasticization effect for PI20 due to PtBS has been compensated in this iso-τ_s plot, and the effect the restriction of DTD/CR on the PI20 relaxation is too small to give the difference by a factor of 2.4: The Q factor representing this effect (cf. eq 5-10) is smaller than 1.31 for the blends at all T. Furthermore, τ_ε in the blend with w_{PtBS} = 20 wt% agrees with $\tau_{\varepsilon,bulk}$ (cf. circles and solid curve), although this blend can be regarded, in the *simplest* case, as an entangled 80 wt% *solution* of PI20 (PI volume fraction ϕ_{PI} = 0.81) because PtBS16 therein relaxed faster than PI20.[12] For entangled PI solutions in an oligomeric solvent, experiments[23] indicated $\tau_\varepsilon \propto \zeta\phi_{PI}^{\beta}$ with $\beta \cong 1.6$. Thus, in the simplest case, τ_ε for w_{PtBS} = 20 wt% is expected to be smaller than $\tau_{\varepsilon,bulk}$ in the iso-ζ bulk by a factor of $0.81^{1.6}$ = 0.71, which is large enough to be resolved in the plot shown in the bottom panel of Figure 5-7. These results suggest a further delay of PI in the blend compared to PI bulk in the iso-τ_s state, which is in harmony with the molecular picture that the PtBS16 chains disturb the PI20 chain to exhibit the free Rouse motion over its entanglement mesh size a in the blend, as explained in Chapter 4. This disturbance surely occurs if the PtBS motion is much slower than the PI motion. In fact, the relative mobility between the PI and PtBS chains can be estimated from a ratio of the frictional coefficients for the entanglement segments of PI and PtBS in blend at T, $\zeta_{e,PI}(T)/\zeta_{e,PtBS}(T)$. The method for determining this ratio is explained later in Appendix 7-2 of Chapter 7. The ratio in the PI20/PtBS16 blends with w_{PtBS} = 30wt% and 50wt% was estimated to be $\zeta_{e,PI}^{bld}(T)/\zeta_{e,PtBS}^{bld}(T) \geq 10$ at all T examined. Thus, the PtBS chains quite possibly behave as immobilized object during the time scale of PI relaxation at all T. Then, the magnitude of motional constraint for PI should be insensitve to T

and hardly affect the WLF-determination of $T_{\text{iso-PI}}$. This T-insensitivity is reflected also in the $\tau_e/\tau_{\varepsilon,\text{bulk}}$ ratio being almost constant (≅2.4) for those blends.

5-3-4 Dynamic behavior of PtBS chains in blends

Obviously, the viscoelastic modulus G_B* of the blends is contributed from both PI20 and PtBS16 chains. Since these chains have different effective T_g's, the G_B* data (shown in Figure 5-3) do not exhibit the thermo-rheological simplicity. However, the modulus G_{PtBS}* of the PtBS16 chains in the blends could exhibit this simplicity if the mechanism of PtBS relaxation does not change with T. In the remaining part of this section, the modulus of PtBS16 in the blends $G_{\text{PtBS}}^{\text{bld}}$* (= G_B* − $G_{\text{PI}}^{\text{bld}}$*) is evaluated, the time-temperature superposition is tested for $G_{\text{PtBS}}^{\text{bld}}$*, and the shift factor for $G_{\text{PtBS}}^{\text{bld}}$* is utilized to determine the iso-τ_s temperature $T_{\text{iso-PtBS}}$ for PtBS16. Finally, an effect of PI20 on the relaxation of PtBS16 chains in the iso-τ_s state (at $T_{\text{iso-PtBS}}$) is examined.

The modulus $G_{\text{PI}}^{\text{bld}}$* of PI20 chains in the blends, required for evaluation of $G_{\text{PtBS}}^{\text{bld}}$* (= G_B* − $G_{\text{PI}}^{\text{bld}}$*) of the PtBS16 chains, can be approximated as the modulus corresponding to the entanglement relaxation, $G_{\text{PI,e}}^{\text{bld}}$*, in a range of ω where the entanglement segments have been internally equilibrated and behave as the basic motional units. $G_{\text{PI,e}}^{\text{bld}}$* can be obtained from the $G_{\text{PI}}^{\text{bulk}}$*($\omega$) data of bulk PI20 if a ratio is known for the viscoelastic $\tau_G(T)$ of PI in the blends at a given temperature T and $\tau_{\text{G,bulk}}(T_{\text{r,bulk}})$ of bulk PI at $T_{\text{r,bulk}}$, as well as for the terminal viscoelastic relaxation intensities I_G in the blends and bulk. These ratios are experimentally determined below to evaluate $G_{\text{PI.e}}^{\text{bld}}$* and $G_{\text{PtBS}}^{\text{bld}}$*.

5-3-4-1 Ratio of viscoelastic relaxation times of PI in blend and bulk

The PI chains split into the majority and minority components in the PI/PtBS blends. The $\tau_G(T)/\tau_{\text{G,bulk}}(T_{\text{r,bulk}})$ ratio for each component can be conveniently expressed as a product of three ratios,

$$\frac{\tau_{\text{G},j}(T)}{\tau_{\text{G,bulk-PI}}(T_{\text{r,bulk}})} = \left\{\frac{\tau_{\varepsilon,\text{bulk-PI}}(T_{\text{r,bulk}})}{\tau_{\text{G,bulk-PI}}(T_{\text{r,bulk}})}\right\} \times \left\{\frac{\tau_{\varepsilon,j}(T)}{\tau_{\varepsilon,\text{bulk-PI}}(T_{\text{r,bulk}})}\right\} \times \left\{\frac{\tau_{\text{G},j}(T)}{\tau_{\varepsilon,j}(T)}\right\}$$

$$\text{with } j = \text{majority, minority} \qquad (5\text{-}8)$$

Here, τ_ε is the dielectric relaxation time (in the environments and at the temperatures as indicated). The first ratio is known from the data for bulk PI; $\tau_{\varepsilon,\text{bulk-PI}}(T_{\text{r,bulk}})/\tau_{\text{G,bulk-PI}}(T_{\text{r,bulk}}) \cong 2$. The second ratio, $\{\tau_{\varepsilon,j}(T)/\tau_{\varepsilon,\text{bulk-PI}}(T_{\text{r,bulk}})\}$, is identical to $1/\lambda_{\text{PI}}^{j}$ with λ_{PI}^{j} being the frequency reduction factors already utilized in eq 5-2. Thus, analysis of the third ratio, $\tau_{\text{G},j}(T)/\tau_{\varepsilon,j}(T)$, allows a evaluation of the $\tau_{\text{G}}(T)/\tau_{\text{G,bulk}}(T_{\text{r,bulk}})$ ratio.

For the majority of PI, the dielectric and viscoelastic relaxation is affected by PtBS through the three mechanisms explained earlier, anti-plasticization, restriction of DTD/CR (compared to bulk PI), and motional constraint due to PtBS that occurs for the Rouse equilibration of PI over *a*. The anti-plasticization just enhances the local friction of PI and thus retards the dielectric and viscoelastic relaxation of PI to the same extent with respect to the relaxation of bulk PI. In other words, the anti-plasticization has no influence on the $\tau_{\text{G},j}(T)/\tau_{\varepsilon,j}(T)$ ratio. Similarly, the motional constraint due to PtBS should equally retard the dielectric and viscoelastic relaxation to give no effect on this ratio (at least in the range of T examined). In contrast, the restriction of DTD/CR retards the viscoelastic relaxation more significantly than the dielectric relaxation because the latter is insensitive to DTD, as explained earlier for eq 5-5. The retardation due to this restriction has been quantified through eq 5-5 as $\tau_{\text{G,maj}}(T) = Q_{\text{maj}}^{3.33}\,\tau_{\text{G,bulk-PI}}(\text{iso-}\tau_{\text{s}})$ and $\tau_{\varepsilon,\text{maj}}(T) = Q_{\text{maj}}\,\tau_{\varepsilon,\text{bulk-PI}}(\text{iso-}\tau_{\text{s}})$, where $\tau_{\text{G,bulk-PI}}(\text{iso-}\tau_{\text{s}})$ and $\tau_{\varepsilon,\text{bulk-PI}}(\text{iso-}\tau_{\text{s}})$ are the viscoelastic and dielectric relaxation times in the iso-τ_{s} bulk and the factor Q has been determined by eq 5-7. This quantification gives a relationship, $\tau_{\text{G,maj}}(T)/\tau_{\varepsilon,\text{maj}}(T) = Q_{\text{maj}}^{2.33}\,\{\tau_{\text{G,bulk-PI}}(\text{iso-}\tau_{\text{s}})/\tau_{\varepsilon,\text{bulk-PI}}(\text{iso-}\tau_{\text{s}})\} = Q_{\text{maj}}^{2.33}\,\{\tau_{\text{G,bulk-PI}}(T_{\text{r,bulk}})/\tau_{\varepsilon,\text{bulk-PI}}(T_{\text{r,bulk}})\}$ where the T-insensitivity of the $\tau_{\text{G,bulk-PI}}/\tau_{\varepsilon,\text{bulk-PI}}$ ratio ($\cong 1/2$) for bulk PI has been utilized. From this relationship and the other relationship explained earlier, $\tau_{\varepsilon,j}(T)/\tau_{\varepsilon,\text{bulk-PI}}(T_{\text{r,bulk}}) = 1/\lambda_{\text{PI}}^{j}$, eq 5-8 is rewritten for the majority PI as:

$$\frac{\tau_{\text{G,maj}}(T)}{\tau_{\text{G,bulk-PI}}(T_{\text{r,bulk}})} = Q_{\text{maj}}^{2.33} / \lambda_{\text{PI}}^{\text{maj}} \quad \text{for majority of PI} \tag{5-9}$$

Thus, this ratio can be evaluated from the known values of Q_{maj} (cf. eq 5-7) and $\lambda_{\text{PI}}^{\text{maj}}$ (cf. eq 5-2).

Similarly, eq 5-8 can be re-written for the slow minority as:

$$\frac{\tau_{\text{G,min}}(T)}{\tau_{\text{G,bulk-PI}}(T_{\text{r,bulk}})} = Q_{\text{min}}^{2.33} / \lambda_{\text{PI}}^{\text{min}} \quad \text{for minority of PI} \tag{5-10}$$

It is noteworthy that the restriction of DTD/CR due to PtBS should be weaker for the slow minority than for the fast majority of PI because the relaxation time difference from PtBS is smaller for the

former. Actually, the restriction of DTD/CR, just moderate for the majority (as quantified by $Q_{maj} \leq$ 1.3), becomes negligibly weak to give $Q_{min} \cong 1$ for the minority.

5-3-4-2 Ratio of viscoelastic relaxation intensities of PI in blend and bulk

Since the majority of PI is the fastest component in the PI/PtBS blend, its terminal viscoelastic relaxation intensity $I_{G,maj}(T)$ is simply proportional to T, the volume fraction of the majority $\phi_{PI}\upsilon_{maj}$, and a correction factor I_{PI} ($=a_{PI}^{bulk\ 2}/a^2$) for a change of entanglement plateau modulus G_N ($\propto M_e^{-1} \propto a^{-2}$, cf. eq 1-2) on blending. Thus, the $I_{G,maj}(T)/I_{G,bulk\text{-}PI}(T_{r,bulk})$ ratio is given by:

$$\frac{I_{G,maj}(T)}{I_{G,bulk\text{-}PI}(T_{r,bulk})} = \frac{1}{b_T'} I_{PI}\phi_{PI}\upsilon_{maj} \text{ with } b_T' = T_{r,bulk}/T \text{ for majority of PI} \quad (5\text{-}11)$$

As explained in Section 2-2-3-3, the change in the density, being much less significant compared to the change of T (in unit of K), has been safely neglected for b_T' shown in eq 5-11 as well as in eqs 5-12 and 5-13 explained later.

A little more detailed consideration is needed for the evaluation of $I_{G,min}(T)$ for the minority of PI. If the majority relaxes *much* faster than the minority, the former behaves as a simple solvent for the relaxation of the latter to dilute the entanglement mesh. In fact, this type of dilution and the corresponding decrease of I_G are known for binary blends of chemically identical, high-M and low-M chains with their relaxation times in the blends differing by a factor >> 10.[23,27] However, if their relaxation times differ only by a factor of 10 or less, the low-M chains (fast component) does not behave as the solvent for the high-M chains (slow component) and the terminal relaxation intensity of the latter is proportional to its volume fraction.[27] This should be the case for the minority PI in the blends studied in this chapter, since τ_e is longer for the minority than for the majority by a factor $\lambda_{PI}^{maj}/\lambda_{PI}^{min} < 10$. Furthermore, the PtBS chains relaxing slower than the minority never behave as the solvent for the minority. Thus, $I_{G,min}(T)$ should be simply proportional to the minority volume fraction, $\phi_{PI}(1-\upsilon_{maj})$. Then, the $I_{G,maj}(T)/I_{G,bulk\text{-}PI}(T_{r,bulk})$ ratio is given by

$$\frac{I_{G,min}(T)}{I_{G,bulk\text{-}PI}(T_{r,bulk})} = \frac{1}{b_T'} I_{PI}\phi_{PI}(1-\upsilon_{maj}) \text{ with } b_T' = T_{r,bulk}/T \text{ for minority of PI} \quad (5\text{-}12)$$

5-3-4-3 Thermo-rheological behavior of PtBS in blend

On the basis of eqs 5-9 to 5-12, the modulus of PtBS in the blend is expressed as:

$$G_{\mathrm{B}}^{*}(\omega) = G_{\mathrm{PI,e}}^{\mathrm{bld}\,*}(\omega) + G_{\mathrm{PtBS}}^{\mathrm{bld}\,*}(\omega) \tag{5-13}$$

with $G_{\mathrm{PI,e}}^{\mathrm{bld}\,*}$ being the modulus corresponding to the entanglement relaxaion of PI in the blend:

$$G_{\mathrm{PI,e}}^{\mathrm{bld}\,*}(\omega;\, T) = \frac{\phi_{\mathrm{PI}} I_{\mathrm{PI}}}{b_{\mathrm{T}}'} \{\upsilon_{\mathrm{maj}} G_{\mathrm{PI}}^{\mathrm{bulk}\,*}(\omega Q_{\mathrm{maj}}^{2.33} / \lambda_{\mathrm{PI}}^{\mathrm{maj}};\, T_{\mathrm{r,bulk}}) + (1-\upsilon_{\mathrm{maj}}) G_{\mathrm{PI}}^{\mathrm{bulk}\,*}(\omega Q_{\mathrm{maj}}^{2.33} / \lambda_{\mathrm{PI}}^{\mathrm{min}};\, T_{\mathrm{r,bulk}})\} \tag{5-14}$$

Eqs 5-13 and 5-14 include no conceptual ambiguity in a range of ω where $G_{\mathrm{B}}'(\omega;\, T) < G_{\mathrm{N}}(T)$ and the entanglement segments have been internally equilibrated to behave as the basic motional units.

Figure 5-8 shows the master curves of the $G_{\mathrm{PtBS}}^{\mathrm{bld}}{}^{*}(\omega,T)$ data thus obtained. The dotted curve shows the shifted modulus of bulk PtBS16 explained later. The $G_{\mathrm{PtBS}}^{\mathrm{bld}}{}^{*}(\omega;\, T)$ data at respective T are reduced by an intensity correction factor, $b_{\mathrm{T}} = T/T_{\mathrm{r}}$ (with T and T_{r} in K unit), and shifted along the ω axis by a factor of $a_{\mathrm{T,G}}$ to achieve the best superposition with the data at the reference temperature T_{r} (=70 and 120°C for w_{PtBS} = 30 and 50 wt%, respectively). The $a_{\mathrm{T,G}}$ data with respect to these T_{r} are shown in the top panel of Figure 5-9. The solid lines attached to the $G_{\mathrm{PtBS}}^{\mathrm{bld}\,*}$ at low ω indicate the viscoelastic terminal tails, $G_{\mathrm{PtBS}}^{\mathrm{bld}}{}' \propto \omega$ and $G_{\mathrm{PtBS}}^{\mathrm{bld}}{}'' \propto \omega^2$. These tails were utilized to determine the viscoelastic relaxation time at T_{r}, $\tau_{\mathrm{G,PtBS}}(T_{\mathrm{r}})$ (cf. eq 2-26), and furtherly τ_{G} of PtBS for PI20/PtBS16 blends as $\tau_{\mathrm{G}}(T) = \tau_{\mathrm{G,PtBS}}(T_{\mathrm{r}}) \times 10^{a_{\mathrm{T,G}}}$, as shown earlier in Figure 5-6.

As noted in Figure 5-8, the time-temperature superposition works (within an experimental resolution) for the $b_{\mathrm{T}}^{-1} G_{\mathrm{PtBS}}^{\mathrm{bld}}{}^{*}(\omega,T)$ data for the blends with w_{PtBS} = 30 and 50 wt%. Thus, the frictional non-uniformity due to the dynamic heterogeneity appears to be smeared by the PI20 chains (relaxing faster than the PtBS16 chains) thereby allowing all PtBS chains to feel the same frictional environment during their terminal relaxation and relaxing through the same mechanism at all T examined. This thermo-rheological simplicity is further discussed later in Chapter 6.

5-3-4-5 Relaxation mechanism of PtBS in iso-frictional state

The relaxation of PtBS16 in the blends is affected by PI20 possibly through several different mechanisms. First of all, PtBS16 is strongly plasticized by PI20 and the relaxation time of the PtBS Rouse segments, τ_{s}, is largely reduced compared to that in the bulk PtBS16 system at the same T.

In addition, the PtBS16 chains may be subjected to some (topological) constraint from the surrouding flexible PI20 chains, since the entanglement length a estimated for PI/PtBS blends with w_{PtBS} = 30 and 50wt% is considerably smaller than R_{PtBS16}. The shift factor $a_{T,G}$ for PtBS16 (top panel of Figure 5-9) could, in principle, reflect the plasticization effect as well as the constraint from the PI20 chains. However, the magnitude of the constraint from the PI20 chains appeared to hardly change with T, as discussed/explained later in more details. Thus, it is reasonable to assume that the T dependence of $a_{T,G}$ for PtBS16 is equivalent to the T dependence of τ_s. Consequently, the WLF analysis (cf. Appendix 3-1) was made for the raw $a_{T,G}$ data of PtBS in the top panel of Figure 5-9.

For the PtBS16 chains in the blends, the iso-τ_s temperature $T_{iso\text{-}PtBS}$ corresponding to $T_{r,bulk}$ of bulk PtBS16 was obtained from the WLF analysis. The value of $T_{iso\text{-}PtBS}$ was summarized in Table 5-2. The shift factor $a_{T,iso}$ for PtBS16 in the blends, re-evaluated with respect to this $T_{iso\text{-}PtBS}$, is plotted against $T-T_{iso\text{-}PtBS}$ in the middle panel of Figure 5-9. The solid curve indicates WLF eq 3-3 that describes the a_T data for bulk PtBS16 with $T_{r,bulk}$ = 171°C. The plots excellently agree with this solid curve, confirming that $T_{iso\text{-}PtBS}$ was successfully evaluated for PtBS16 in the blends.

From this agreement, the difference of the iso-τ_s temperatures in the blends and bulk, $\Delta T_{iso} = T_{iso\text{-}PtBS} - T_{iso\text{-}PtBS}^{bulk}$, can be regarded as a difference of the effective glass transition temperatures for PtBS16 in these systems. This ΔT_{iso} is utilized to estimate the effective T_g of PtBS16 in the blends as $T_{g,PtBS}^{eff} = T_{g,PtBS}^{bulk} + \Delta T_{iso}$ (with $T_{g,PtBS}^{bulk}$ = 138°C). These estimates, shown in Figure 5-2 with thick dotted arrows attached to the DSC traces, are well located at the high-T side of the broad glass transition zone as expected.

In the bottom panel of Figure 5-9, the $\tau_{G,PtBS}$ data for the blends (w_{PtBS} = 30 and 50 wt%) are plotted against $T-T_{iso\text{-}PtBS}$ and compared with the $\tau_{G,PtBS}$ data of bulk PtBS16 plotted against $T-T_{r,bulk}$ (= $T-T_{iso\text{-}PtBS}^{bulk}$). The dotted and dashed curves show the bulk $\tau_{G,PtBS}$ data multiplied by factors of 4.8 and 14.0, respectively. Clearly, $\tau_{G,PtBS}$ is significantly larger in the blends than in the bulk PtBS system in the iso-τ_s state.

This difference of $\tau_{G,PtBS}$ can be noted also for the $G_{PtBS}^{bld}{}^*$ data. The modulus data of bulk PtBS16 at $T_{r,bulk}$ = 444K (= 171°C; cf. Figure 3-1(c)) were multiplied by the PtBS16 volume fraction in the blends (ϕ_{PtBS} = 0.47 and 0.27 for w_{PtBS} = 50 and 30 wt%) and reduced by the intensity correction factor, $b_T^\circ = T_{r,bulk}/T_r$ with T_r being the reference temperatures of the blends utilized in Figure 5-8 (T_r = 393 K and 343K for w_{PtBS} = 50 and 30 wt%). As judged from the $T_{iso\text{-}PtBS}$ data, the bulk PtBS16 chains at 248 and 240°C are in the iso-τ_s state with respect to the PtBS16 chains in the blends at these T_r. The modulus data of bulk PtBS16 thus corrected, $b_T^{\circ -1}\phi_{PtBS}G_{PtBS}^{bulk}{}^*$, were shifted

from $T_{r,bulk}$ to 248°C and 240°C with the aid of WLF equation of PtBS (eq 3-3). This shifted iso-τ_s modulus is shown in Figure 5-8 with the dotted curves. Clearly, the PtBS16 relaxation in the blends is significantly delayed compared to that shown by these curves.

The delay noted in Figures 5-8 and 5-9 suggests an effect of the topological constraint for PtBS16. A important difference is noticed for the relaxation behavior of PtBS and that expected from ordinary CR relaxation: In homopolymer blends, the CR relaxation of the probe chain is activated by the global motion of the matrix chains and thus the CR relaxation time of the probe is essentially proportional to the matrix relaxation time, as expected theoretically[28-30] and confirmed experimentally.[16] This proportionality emerges because the probe exhibits the local CR jump over the entanglement mesh size a immediately after the global motion of the matrix chain occurs, *i.e.*, the probe has the local CR-jump time close to the matrix relaxation time. These conditions are not satisfied for the PtBS16 chains in the blends: As seen in Figure 5-6, the relaxation time of PtBS16 (probe), $\tau_{G,PtBS}$, is not at all proportional to the relaxation time of PI20 (matrix), τ_ε. Furthermore, if the PtBS16 chains relax through the usual Rouse CR mechanism, their local CR-jump time for the length scale of a ($\cong 0.8R_{PtBS}$ as discussed earlier) is given by $\tau^{**} \cong \{a/R_{PtBS}\}^4\tau_{G,PtBS} \cong 0.4\tau_{G,PtBS}$. This τ^{**} is longer than τ_ε of PI20 in particular at low T; cf. Figure 5-6.

The above argument leads to a hypothesis that a focused PtBS16 chain (probe) in the blends with $C_{PtBS} > C_{PtBS}^*$ relaxes when the constraint from the overlapping PtBS16 chains (matrix) is released through the matrix motion. This constraint for the probe emerges because a flexible PI20 chain simultaneously penetrates the random coils of the probe and matrix PtBS16 chains. In other words, the PI20 chains seem to just create the topological constraint for the PtBS16 chains by stitching the random coils of the PtBS16 chains, and the rate-determining step for release of this constraint is the motion of the PtBS16 chains themselves (not the motion of the PI20 chains). This relaxation mechanism of PtBS16 is considerably different from the usual CR mechanism and hereafter referred to as *pseudo-CR* just for convenience of discussion.

The local pseudo-CR jump frequency in the iso-τ_s state would decrease and the terminal relaxation time $\tau_{G,PtBS}$ of PtBS16 would increase with increasing volume fraction ϕ_{PI} of the PI20 chains stitching the PtBS16 random coils. Since ϕ_{PI} is larger for smaller w_{PtBS} (ϕ_{PI} = 0.73 and 0.53 for w_{PtBS} = 30 and 50 wt%), a difference of $\tau_{G,PtBS}$ in the blend and iso-τ_s bulk is expected to be larger for smaller w_{PtBS}. This expectation is in harmony with the observation ($\tau_{G,PtBS}$ is larger for w_{PtBS} = 30 wt% than for w_{PtBS} = 50 wt%; cf. the bottom panel of Figure 5-9).

If the PtBS16 chains relax through the pseudo-CR mechanism, the T dependence of the shift factor $a_{T,G}$ for PtBS16 would not be affected by the motion of the PI20 chains because the PI20

chains stitch the PtBS16 random coils to the same extent irrespective of T. Then, the raw $a_{T,G}$ data of the PtBS16 chains just reflect the change of their τ_s with T, *i.e.*, $a_{T,G} = \tau_s(T) / \tau_s(T_r)$, which is consistent with the $T_{iso\text{-}PtBS}$ determination through the WLF analysis for the raw $a_{T,G}$ data (cf. top panel of Figure 5-9).

5-4 Concluding Remarks

The viscoelastic and dielectric behavior was examined for statistically homogeneous PI20/PtBS16 blends with w_{PtBS} = 50% and 30% at several different temperatures ($\leq$ 120°C). PI20 (with $M_{PI} \cong 4M_e^{PI\ bulk}$) was moderately entangled, while PtBS16 (with $M_{PtBS} \cong 0.4M_e^{PtBS\ bulk}$) was not entangled in respective bulk systems. The dielectric relaxation of these blends exclusively reflected the global motion of the PI20 chains. In contrast, the viscoelastic relaxation was contributed from the motion of both of the PI20 and PtBS16 chains. Comparison of the dielectric and viscoelastic data indicated that the PI20 chains relaxed faster than the PtBS16 chains in the blends at the temperatures examined.

The failure of the time-temperature superposition observed for the dielectric data was related to the non-uniform frictional environment for PI20 due to the motion of the slow PtBS16 chains that was effectively quenched over a length scale of R_{PI} in the time scale of the global relaxation of the PI20 chains. The dielectric data indicated that the PI20 chains in the blends split into the majority and minority components, the former feeling a smaller friction and relaxing faster compared to the latter. The difference of the relaxation rates of these components decreased and the majority fraction increased with increasing temperature, thereby resulting in the failure of the time-temperature superposition. (The dielectric data of the blends approached the data of bulk PI20 at sufficiently high temperatures).

In contrast, the superposition was approximately valid for the terminal relaxation of the PtBS16 chains. In this time scale, the faster PI20 chains appeared to have erased the dynamic heterogeneity to allow the PtBS16 chains to relax in a uniform frictional environment through the same mechanism in the entire range of T examined.

Detailed analysis of the relaxation times of PI20 and PtBS16 chains in the blends suggested that both of these chains relaxed slower in the blends than in respective iso-τ_s bulk systems. The PtBS16 chains were less mobile than the PI20 chains. Thus, the PtBS16 chains appeared to behave

as immobilized obstacle that effectively retarded the Rouse equilibration of the PI20 chains over the entanglement mesh size a. This retardation is certainly possible since PtBS16 have chain size larger than entanglement mesh size, $R_{PtBS16} > a$. For the same reason, the faster PI20 chains can impose a topological contraint for the motion of PtBS. The PtBS16 chains affected by the topological constraint probably relax through a *pseudo-CR* mechanism activated by the motion of a PI chain stitching/entangling with the PtBS chains.

Appendix 5-1 Retardation of Relaxation due to Restriction of DTD/CR

Within the current molecular model (tube model) for the entanglement dynamics of linear homopolymers,[16,28-30] the moderately entangled bulk PI chains relax through several mechanisms including reptation, contour length fluctuation, and dynamic tube dilation (DTD)/constraint release (CR). The DTD/CR contribution to the relaxation is restricted when the PI chains are blended with slower chains. This is the case for the PI chains in the PI/PtBS blends exhibiting the viscoelastic relaxation much slower than the dielectric relaxation. However, the PI relaxation in those blends should be also affected by the other mechanisms, the anti-plasticization and extra constraints from PtBS chains during the Rouse equilibration over the entanglement mesh. The viscoelastic and dielectric data obtained for binary blends of low-M and high-M PI chains[23,31] are free from these mechanisms and thus helpful for quantifying the effect of the restriction of DTD/CR on the PI relaxation. This Appendix organizes these data into a form of empirical equations.

For PI/PI binary blends with the component molecular weights $M_1 = 21.4\times10^3$ (PI21; component-1) and $M_2 = 30.8\times10^4$ (PI308; component-2), the angular frequency (ω) dependence of the viscoelastic and dielectric losses,[23] G'' and ε'', are shown in the top panels of Figures 5-10 and 5-11, respectively. The data are also shown for monodisperse PI21. The relaxation seen in those panels is the terminal relaxation of PI21, and the upturn noted at the low ω side of the panels reflects the relaxation of PI308 (high-M component) occurring at $\omega < 10$ s^{-1}. Clearly, the peaks of G'' and ε'' shift to lower ω and thus both of the viscoelastic and dielectric relaxation processes of PI21 are retarded with increasing ϕ_2 ($\geq$ 0.1). The DTD/CR mechanism working in the monodisperse PI21 system is restricted by the slower/longer PI308 chains to give this retardation. In relation to this point, it is noted that the peak shift is more significant for G'' than ε''. Namely, the restriction of DTD/CR gives a smaller effect for the dielectric relaxation than for the viscoelastic relaxation. This difference emerges because the terminal dielectric relaxation of the PI chain reflects a decay of the orientational memory of its end-to-end vector while the viscoelastic relaxation detects a decay of the isochronal orientational anisotropy of the Rouse segments: The orientational memory hardly decays but the isochronal anisotropy decays significantly on dilation of the tube that confines the chain.[16,23]

The magnitude of this retardation due to restriction of DTD/CR, represented as the ratios of the viscoelastic and dielectric relaxation times of PI21 in the blends to those in monodisperse PI21 system, $\tau_{G1}(\phi_2)/\tau_{G1}(0)$ and $\tau_{\varepsilon1}(\phi_2)/\tau_{\varepsilon1}(0)$, can be evaluated by superposing the G'' and ε'' curves of the blends on those of the monodisperse PI21 system. For this purpose, the G'' and ε'' data of the blends are reduced by intensity correction factors r (adjusting the G'' and ε'' peak height) and

shifted along the ω axis by factors λ to achieve the best superposition; cf. the bottom panels of Figures 5-10 and 5-11. (The r factor was close to the volume fraction of PI21.) The viscoelastic $\tau_{G1}(\phi_2)/\tau_{G1}(0)$ ratio, identical to the horizontal shift factor for the G'' curves, is plotted against ϕ_2 in Figure 5-12; cf. unfilled circles. For clarity of the plots, the dielectric $\tau_{\varepsilon 1}(\phi_2)/\tau_{\varepsilon 1}(0)$ ratio is not shown in Figure 5-12. Instead, this ratio is plotted against the viscoelastic ratio in Figure 5-13 (cf. circles).

For PI308/PI94 binary blends[31] having a higher M_1 (= $94._0\times10^3$; PI94) compared to the PI308/PI21 blends, a similar evaluation was made for the $\tau_{G1}(\phi_2)/\tau_{G1}(0)$ and $\tau_{\varepsilon 1}(\phi_2)/\tau_{\varepsilon 1}(0)$ ratios. These ratios are shown in Figures 5-12 and 5-13 with unfilled triangles. The evaluation was also made for the $\tau_{G1}(\phi_2)/\tau_{G1}(0)$ ratio for two series of binary blends of polystyrenes[27] (PS) having ($10^{-4}M_1$, $10^{-4}M_2$) = (3.6_3, $29._4$) and ($16._1$, $29._4$) and ϕ_2 in a range between 0.03 and 0.6. The results are shown in Figure 5-12 with unfilled diamonds and squares. (No dielectric $\tau_{\varepsilon 1}(\phi_2)/\tau_{\varepsilon 1}(0)$ ratio is available for PS/PS blends because PS chains have no type-A dipole.)

As seen in Figure 5-13, the $\tau_{G1}(\phi_2)/\tau_{G1}(0)$ and $\tau_{\varepsilon 1}(\phi_2)/\tau_{\varepsilon 1}(0)$ ratios for the PI/PI blends are well correlated with each other because both ratios represent the effect of the restriction of DTD/CR on the relaxation of the fast component. A rigorous molecular theory of DTD/CR, if available, would enable an accurately description of this correlation. However, no such theory is available at this moment. Thus, an empirical approach is adopted here to describe the plots shown therein with an empirical equation (solid line in Figure 5-13):

$$Q \equiv \left(\frac{\tau_{\varepsilon 1}(\phi_2)}{\tau_{\varepsilon 1}(0)} \right) = \left(\frac{\tau_{G1}(\phi_2)}{\tau_{G1}(0)} \right)^{0.3} \qquad \text{(A5-1-1)}$$

A relationship $\tau_{\varepsilon 1}(\phi_2)/\tau_{\varepsilon 1}(0) < \tau_{G1}(\phi_2)/\tau_{G1}(0)$ holds (cf. Figure 5-13) because the dielectric relaxation is not sensitive to DTD compared to the viscoelastic relaxation. The empirical exponent of 0.3 (< 1) appearing in eq A5-1-1 is a consequence of this relationship.

The viscoelastic $\tau_{G1}(\phi_2)/\tau_{G1}(0)$ ratio increases with increasing M_2/M_1 ratio and with increasing ϕ_2, as noted in Figure 5-12. This tendency reflects an obvious fact that the restriction of DTD/CR for the component 1 becomes less significant when the component molecular weights M_1 and M_2 become closer to each other and/or the high-M component 2 becomes dilute. (In an extreme cases of $M_2 \to M_1$ or $\phi_2 \to 0$, the blend reduces to the monodisperse system of the component 1 and the restriction of DTD/CR defined *with respect to this system* vanishes.) Thus, the M_2/M_1 ratio and ϕ_2 can be utilized as the empirical parameters that determine the $\tau_{G1}(\phi_2)/\tau_{G1}(0)$ ratio, *i.e.*, the parameters determining the magnitude of the retardation of the fast component relaxation due to the

restriction of DTD/CR. However, for the PI/PtBS blends examined in this chapter, the M_2/M_1 ratio and ϕ_2 cannot be conveniently utilized as such parameters because the PI and PtBS chains therein have different local frictions, which change with T differently. Thus, it is necessary to find the other parameter(s) that is experimentally measurable and can properly specify the $\tau_{G1}(\phi_2)/\tau_{G1}(0)$ ratio for PI, the fast component in the PI/PtBS blends.

For this purpose, the focus is placed on a ratio the viscoelastic relaxation times of the fast and slow components in the same blend, $\tau_{G2}(\phi_2)/\tau_{G1}(\phi_2)$. This ratio does not uniquely determine the $\tau_{G1}(\phi_2)/\tau_{G1}(0)$ ratio when ϕ_2 is varied. (Irrespective of the $\tau_{G2}(\phi_2)/\tau_{G1}(\phi_2)$ value, $\tau_{G1}(\phi_2)/\tau_{G1}(0) \to 1$ as $\phi_2 \to 0$.) Nevertheless, for a given ϕ_2 value, the $\tau_{G2}(\phi_2)/\tau_{G1}(\phi_2)$ ratio can be conveniently utilized as the empirical parameter determining the $\tau_{G1}(\phi_2)/\tau_{G1}(0)$ ratio, as explained below.

In Figure 5-12, the $\tau_{G2}(\phi_2)/\tau_{G1}(\phi_2)$ data obtained for respective PI/PI and PS/PS blends are shown with the filled symbols. Interpolation of these data as well as the $\tau_{G1}(\phi_2)/\tau_{G1}(0)$ data (unfilled symbols) gives the $\tau_{G2}(\phi_2)/\tau_{G1}(\phi_2)$ and $\tau_{G1}(\phi_2)/\tau_{G1}(0)$ values for different ϕ_2. Figure 5-14 shows a relationship between the $\tau_{G1}(\phi_2)/\tau_{G1}(0)$ and $\tau_{G2}(\phi_2)/\tau_{G1}(\phi_2)$ ratios obtained for different ϕ_2 as indicated. The plots obtained for different ϕ_2 are smoothly connected, suggesting that the $\tau_{G2}(\phi_2)/\tau_{G1}(\phi_2)$ ratio indeed works as the empirical parameter specifying the $\tau_{G1}(\phi_2)/\tau_{G1}(0)$ ratio for given ϕ_2.

It is also noted that the $\tau_{G1}(\phi_2)/\tau_{G1}(0)$ ratio tends to become constant for large $\tau_{G2}(\phi_2)/\tau_{G1}(\phi_2)$ values. This tendency naturally emerges because DTD/CR is fully restricted/saturated to a level determined by ϕ_2 once the $\tau_{G2}(\phi_2)/\tau_{G1}(\phi_2)$ ratio is increased to a certain critical value and a further increase of this ratio results in no change of the magnitude of restriction. The solid curves in Figure 5-14 shows an empirical equation mimicking this tendency,

$$\log\left(\frac{\tau_{G1}(\phi_2)}{\tau_{G1}(0)}\right) = B\ \tanh\left\{\alpha\left[\log\left(\frac{\tau_{G2}(\phi_2)}{\tau_{G1}(\phi_2)}\right)\right]^q\right\} \qquad \text{(A5-1-2)}$$

The coefficients (B, α, q) are (0.2, 0.23, 3) and (0.41, 0.2, 2.5) for ϕ_2 = 0.27 and 0.47, respectively. For PI/PtBS blends subjected to a correction of the DTD/CR mechanism, $\tau_{G2}(\phi_2)$ of PtBS can be approximated by the directly measurable $\tau_{GB}(\phi_2)$ of the blend. Eqs A5-1-1 and A5-1-2 combined with this harmless approximation can be utilized to estimate the $\tau_{G1}(\phi_2)/\tau_{G1}(0)$ ratio for PI.

References and Notes

1. Lodge, T. P.; McLeish, T. C. B. *Macromolecules* **2000**, 33, 5278-5284.
2. Miller, J. B.; McGrath, K. J.; Roland, C. M.; Trask, C. A.; Garroway, A. N. *Macromolecules* **1990**, 23, 4543-4547.
3. Chung, G. C.; Kornfield, J. A.; Smith, S. D. *Macromolecules* **1994**, 27, 964-973.
4. Alegria, A.; Colmenero, J.; Ngai, K. L.; Roland, C. M. *Macromolecules* **1994**, 27, 4486-4492.
5. Pathak, J. A.; Kumar, S. K.; Colby, R. H. *Macromolecules* **2004**, 37, 6994-7000.
6. Hirose, Y.; Urakawa, O.; Adachi, K. *Macromolecules* **2003**, 36, 3699-3708.
7. Zawada, J.A.; Fuller G.G., Colby R.H.; Fetters L.J., Roovers J. *Macromolecules* **1994**, 27 (23), 6851-6860
8. Zawada, J.A.; Fuller G.G., Colby R.H.; Fetters L.J., Roovers J. *Macromolecules* **1994**, 27 (23), 6861-6870
9. Haley, J. C.; Lodge, T. P. *J. Rheol.* **2004**, 48, 463-486.
10. Haley, J. C.; Lodge, T. P.; He, Y. Y.; Ediger, M. D.; von Meerwall, E. D.; Mijovic, J. *Macromolecules* **2003**, 36, 6142-6151.
11. Watanabe, H.; Matsumiya, Y.; Takada, J.; Sasaki, H.; Matsushima, Y.; Kuriyama, A.; Inoue, T.; Ahn, K. H.; Yu, W.; Krishnamoorti, R. *Macromolecules* **2007**, 40, 5389-5399.
12. Takada, J.; Sasaki, H.; Matsushima, Y.; Kuriyama, A.; Matsumiya, Y.; Watanabe, H.; Ahn, K. H.; Yu, W. *Nihon Reoroji Gakkaishi* **2008**, 36, 35-42.
13. Yurekli, K.; Krishnamoorti, R. *J. Polym. Sci. Part B: Polym. Phys.* **2004**, 42, 3204-3217.
14. Fetters, L. J.; Lohse, D. J.; Colby, R. H., *Chain Dimensions and Entanglement Spacings*, in Physical Properties of Polymer Handbook (2nd ed.), 2nd ed.; Mark, J. E., Ed. Springer: New York, **2007**; Chapter 25, pp 445-452.
15. Adachi, K. *Prog. Polym. Sci.* **1993**, 18, 585-622.
16. Watanabe, H. *Prog. Polym. Sci.* **1999**, 24, 1253-1403.
17. Watanabe, H. *Macromol. Rapid Commun.* **2001**, 22, 127-175.
18. Watanabe, H.; Matsumiya, Y.; Inoue, T. *Macromolecules* **2002**, 35, 2339-2357.
19. Pakula, T. *Dielectric and Mechanical Spectroscopy - a Comparison*, in Broadband Dielectric Spectroscopy (Kremer, F.; Schönhals A. Ed.), Springer: Berlin, **2003**; Chapter 16, pp. 597-623.
20. a) The coincidence of the dielectric and viscoelastic relaxation frequencies (within the factor of 2)[15-19] is a characteristic feature of the rubbery (global) relaxation of type-A polymers including PI. This coincidence is not found for the glassy (segmental) relaxation in polymeric/oligomeric materials[19,20a,20b] because of several factors that possibly include a difference between the viscoelastically and dielectrically active segments. b) McCrum, N. G.; Read, B. E.; Williams, G. *Anelastic and Dielectric*

Effects in Polymeric Solids, Dover: New York, **1967**, p. 300. c) Buchenau, U. J. *Non-Cryst. Solids* **2007**, 353, 3812-3819.

21. a) The global dielectric relaxation of PI chains detects the end-to-end vector fluctuation, as explained in eq 2-6. Thus, any heterogeneity over a length scale much shorter than the end-to-end distance is smeared in the global relaxation and can be just regarded as a factor determining a segmental friction averaged over the chain backbone. For this reason, the global dielectric mode distribution (being independent of this average friction) is insensitive to a change of the environment, unless the chains are subjected to strong thermodynamic/spatial confinements.[17] In contrast, the segmental relaxation detecting the dynamics at short length scales is very sensitive to changes in the environment;[21b,21c] for example, the segmental mode distribution broadens on dilution with a solvent. b) Jones, A. A.; Inglefield, P. T.; Liu, Y.; Roy, A. K.; Cauley, B. J. *J. Non-Cryst. Solids* 1991, 131-133, 556-562. c) Yada, M.; Nakazawa, M.; Urakawa, O.; Morishima, Y.; Adachi, K. *Macromolecules* 2000, 33, 3368-3374.
22. Ferry, J. D., *Viscoelastic Properties of Polymers*, 3rd ed.; Wiley: New York, **1980**; Chapter 11, pp 264-320.
23. Watanabe, H.; Ishida, S.; Matsumiya, Y.; Inoue, T. *Macromolecules* **2004**, 37, 1937-1951.
24. Inoue, T.; Okamoto. H.; Osaki, K. *Macromolecules* **1991**, 24, 5670-5675.
25. Okamoto, H.; Inoue, T.; Osaki, K. J. *Polym. Sci. Part B: Polym. Phys.* **1995**, 33, 417-424.
26. Inoue, T.; Matsui, H.; Osaki K. *Rheol. Acta* **1997**, 36, 239-244.
27. Watanabe, H.; Sakamoto, T.; Kotaka, T. *Macromolecules* **1985**, 18, 1008-1015.
28. Doi, M.: Edwards, S. F. *The Theory of Polymer Dynamics,* Oxford University Press: New York, 1986; Chapter 7, pp. 218-288.
29. Graessley, W. W. *Adv. Polym. Sci.* 1982, 47, 67-117.
30. McLeish, T. C. B. *Adv. Phys.* 2002, 51, 1379-1527.
31. Watanabe, H.; Ishida, S.; Matsumiya, Y.; Inoue, T. *Macromolecules* **2004**, 37, 6619-6631.

Table 5-1. Characteristics of samples

Code	$10^{-3}M_w$	M_w/M_n	$T_{r,bulk}^{\infty}$/°C	R/nm[a]
PI20[b]	19.9	1.10	30	12
PtBS16	16.4	1.02	171	7.7

a: The end-to-end distance of the chain was calculated by $R_X^2=[<R^2>/M]_X M_X$ (X = PI, PtBS) with $[<R^2>/M]_X$ = 6.79×10^{-3} and 3.61×10^{-3} for PI and PtBS, respectively.[14]

b: Supplied from Kuraray Co. The microstructure was 1,4-*cis*:1,4-*trans*:3,4=79:14:7.

Table 5-2. Degree of overlapping and iso-τ_s temperature of the components in blends and bulk

	w_{PtBS}	C_{PtBS}/C_{PtBS}*[a]	$T_{iso\text{-}PI}$/°C	$T_{iso\text{-}PtBS}$/°C
PI20/PtBS16	50%	2.3	63	43
PI20/PtBS16	30%	1.4	42	1
PI20/PtBS16[b]	20%	0.9	41	
PI20 (bulk)			30[c]	
PtBS16 (bulk)				171[c]

a: The overlapping concentration, $C_{PtBS}^* = \{M_{PtBS}/N_A\}/\{4\pi R_{g,PtBS}^3/3\}$, was evaluated from the root-mean-square radius of gyration $R_{g,PtBS}= \sqrt{R_{PtBS}^2/6}$.

b: $T_{iso\text{-}PtBS}$ could not be determined for the PI20/PtBS16 blend with w_{PtBS} = 20% because the modulus of PtBS16 in this blend was not obtained with acceptable accuracy.[12]

c: For bulk PI20 and PtBS16, the reference temperatures of the master curves (Figures 5-1 and 3-1(c)) were chosen to be T_{iso}. The local friction at respective T_{iso} is much larger (a difference $T_{iso}-T_g$ is much smaller) for bulk PtBS16 than for bulk PI20.

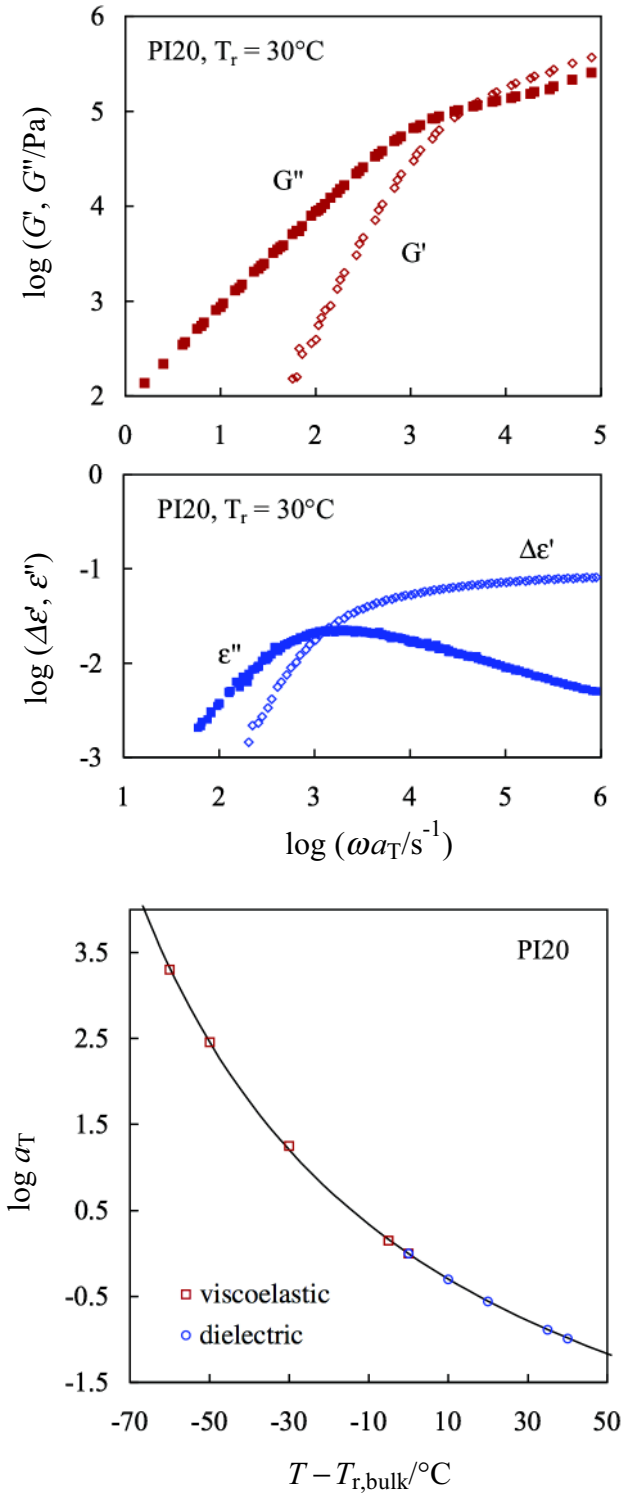

Fig. 5-1: **Top panel**: Frequency dependence of storage and loss moduli, G' and G'', decrease of dielectric constant from its static value, $\varepsilon_0-\varepsilon'$, and dielectric loss, ε'', obtained for bulk PI20 sample. All data are reduced at $T_{r,bulk}$ = 30°C. **Bottom panel**: Shift factors a_T obtained for the viscoelastic (squares) and dielectric (circles) data. The solid curve indicates WLF eq 3-2. The data were taken from Ref.11.

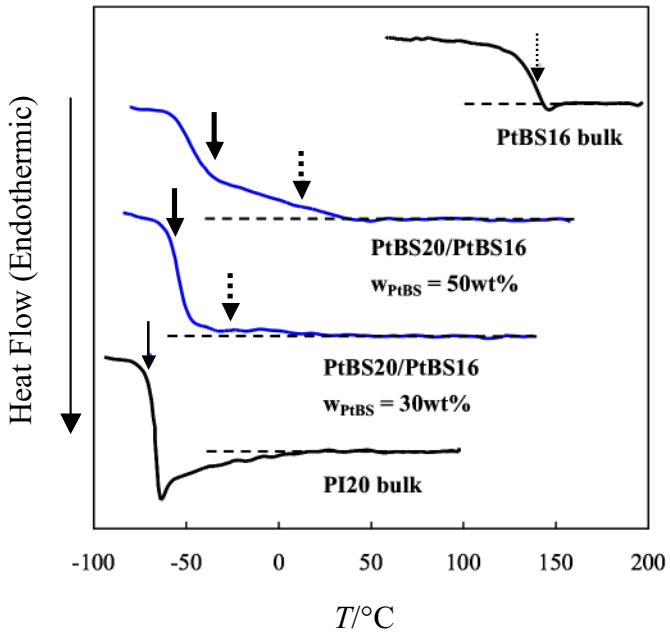

Fig. 5-2: DSC traces for PI20/PtBS16 blends with weight fraction of PtBS w_{PtBS} = 50wt% and 30wt%, and bulk PI20 and PtBS16 samples. Dashed lines are high-T baselines. Thin solid and dotted arrows indicate T_g of bulk PI20 and PtBS16 (−67 and +138°C, respectively). Thick solid and dotted arrows denote effective T_g of PI20 and PtBS16 in the blends expected from WLF analysis of the dielectric and viscoelastic data of the blends.

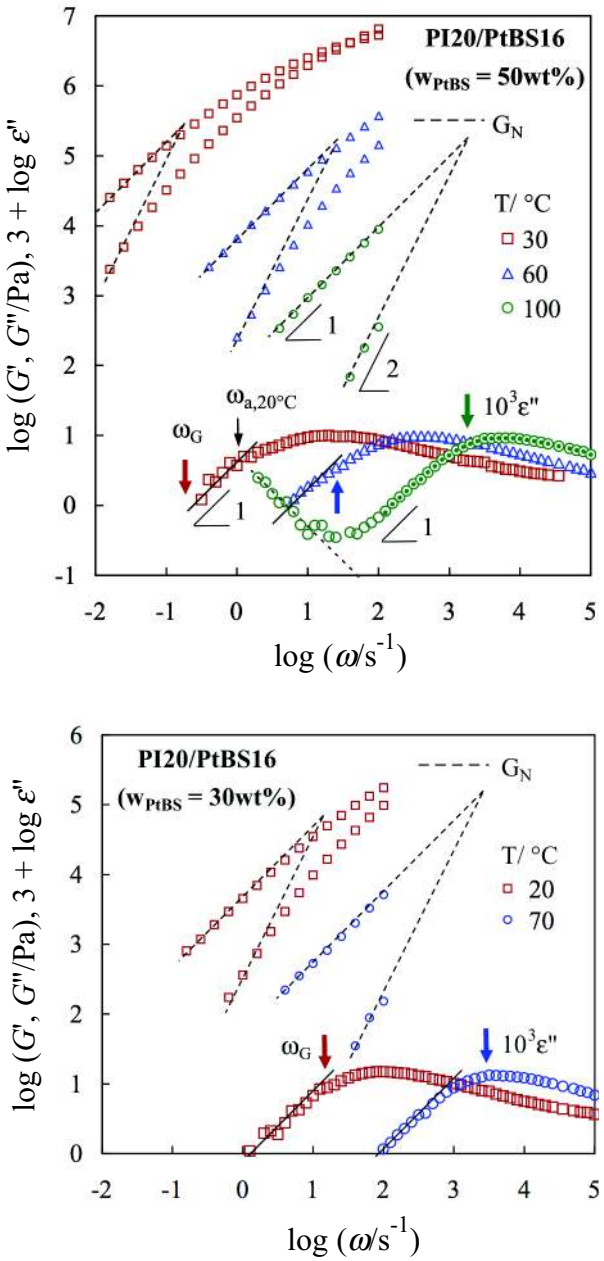

Fig. 5-3: Viscoelastic and dielectric behavior of PI20/PtBS16 blend with w_{PtBS} = 50wt% (top panel) and 30wt% (bottom panel) at representative temperatures as indicated. In both panels, the thick arrows indicate the average viscoelastic relaxation frequency of the blend, ω_G. The dashed lines indicate the plateau modulus G_N expected for the blends at the lowest T shown therein. In the top panel of the PI20/PtBS16 blend with w_{PtBS} = 50 wt%, the thin arrow indicates the characteristic frequency corresponding to the equilibration over entanglement mesh size a at 30°C. For the dielectric data at 100°C (top panel), large unfilled circle, dashed line (of slope = −1), and small filled circles indicate the raw ε'' data, the direct current (dc) contribution ε_{dc}'', and the residue $\varepsilon'' - \varepsilon_{dc}''$, respectively.

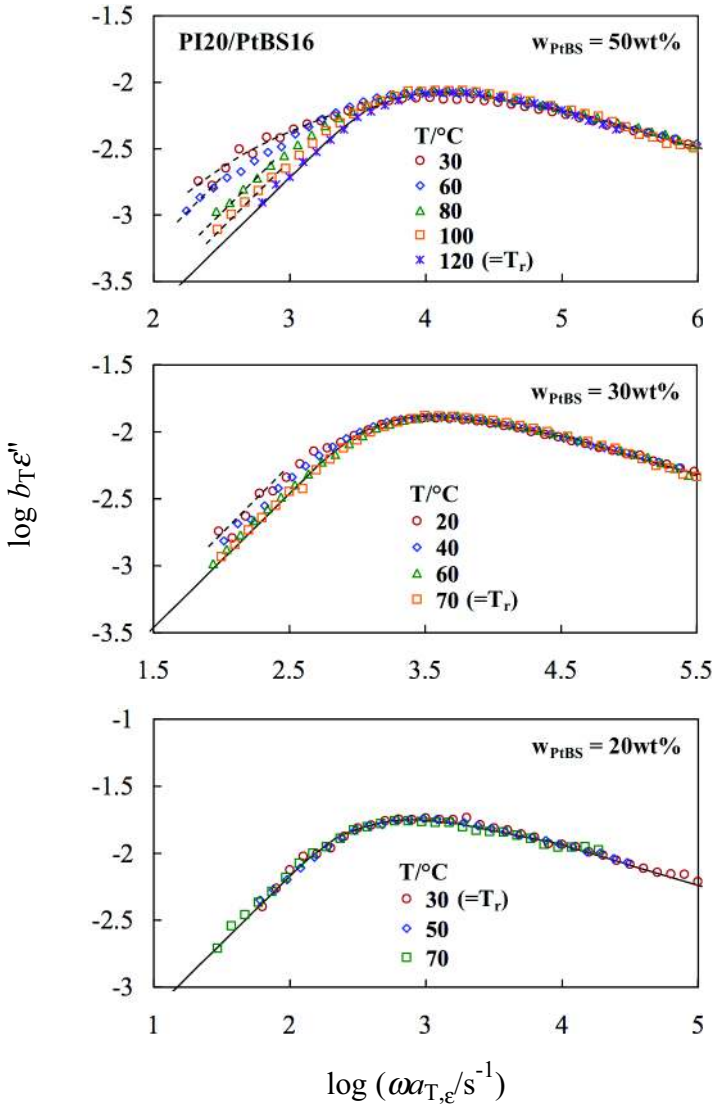

Fig. 5-4: Test of time-temperature superposability for the ε'' data of PI20/PtBS16 blends with w_{PtBS} = 50 wt%, 30 wt%, and 20 wt%. The ε'' data are multiplied by an intensity correction factor $b_T = T/T_r$ and shifted along the ω axis by a factor of $a_{T,\varepsilon}$ to superimpose their ε'' peak onto the peak at the reference temperature T_r as indicated. The solid curves indicate the normalized dielectric data of bulk PI20 shifted along the ω axis to match $\omega_{\varepsilon\text{-peak}}$ to that of the blend at T_r. The data of PI20/PtBS16 blend with w_{PtBS} = 20 wt% (bottom panel) were taken from Ref.12.

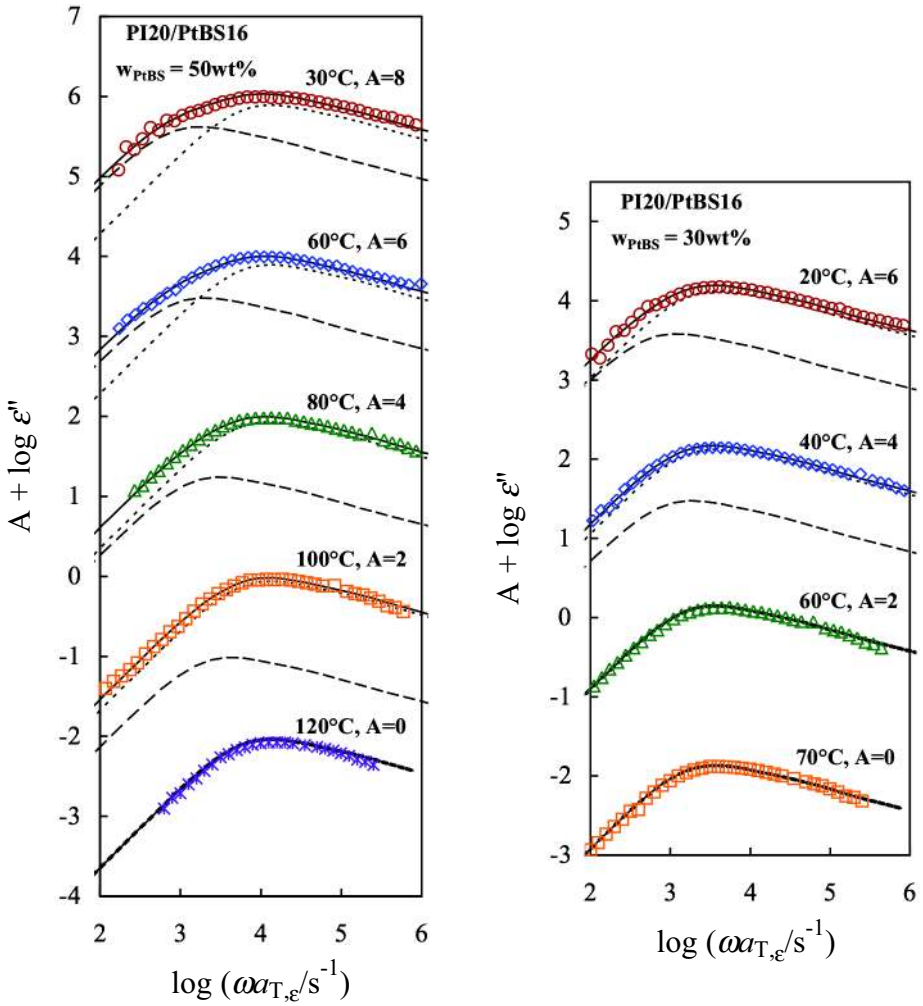

Fig. 5-5: Decomposition of raw ε'' data of PI20/PtBS16 with w_{PtBS} = 50% (symbols in the left panel) and 30% (symbols in the right panel) into contributions from the majority (dotted curves) and minority (dashed curves) of PI20 chains in the blends. The data are plotted against $\omega a_{T,\varepsilon}$ with $a_{T,\varepsilon}$ given in Figure 5-4 and the top panel of Figure 5-7. Solid curves indicate the sum of these contributions. For clarity of plots, the data and curves at different temperatures are shifted vertically by the factors A as indicated.

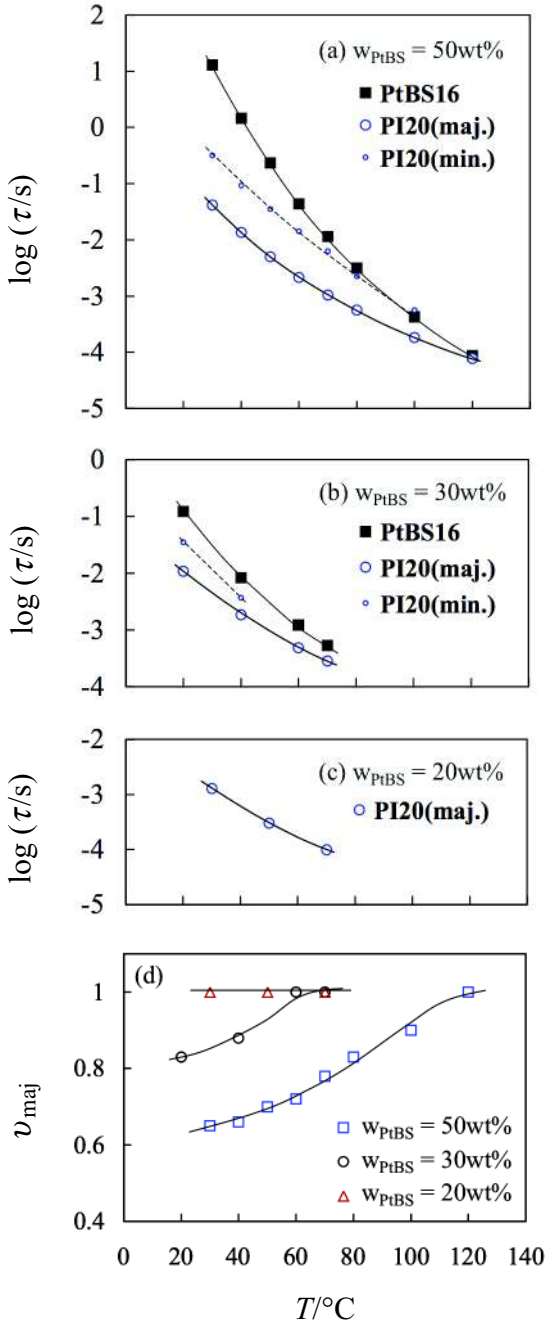

Fig. 5-6: **Top three panels**: Temperature dependence of dielectric relaxation times of the majority and minority of PI20 chains (large and small circles) and viscoelastic relaxation time the PtBS16 chains (filled squares) in PI20/PtBS16 blends with the PtBS concentrations w_{PtBS} as indicated.

Bottom Panel: Plots of the fraction of the majority of PI20 chains in the blends against temperature T. The curves are guide for eyes.

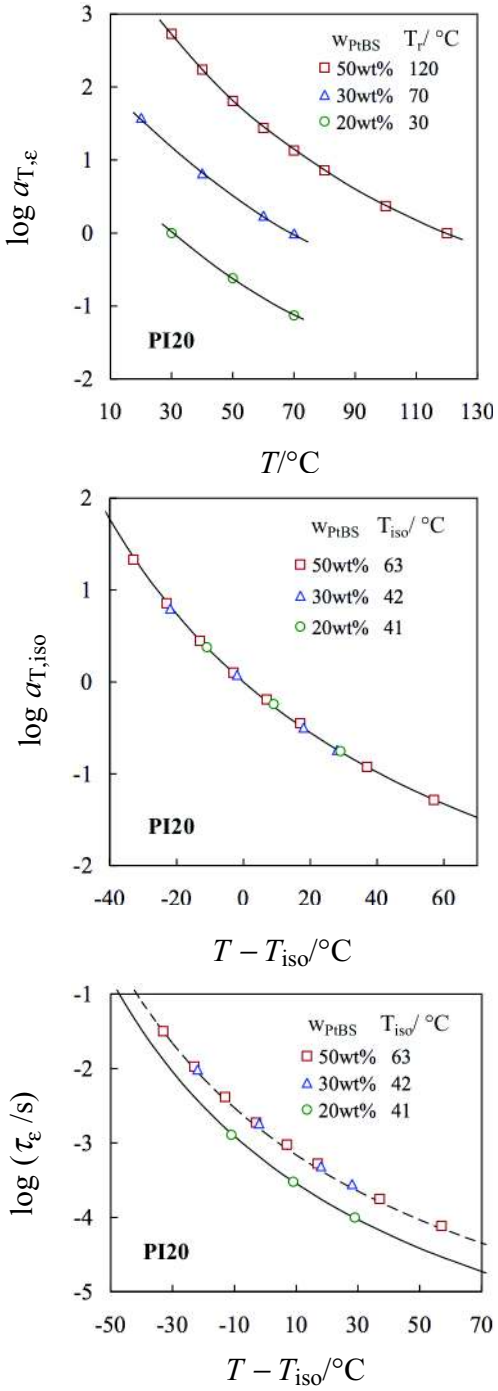

Fig. 5-7: **Top panel**: The time-temperature shift factor $a_{T,\varepsilon}$ for the ε" data (shown in Figure 5-4) plotted against the temperature T. **Middle panel**: The shift factor $a_{T,iso}$ of PI20 in the PI20/PtBS16 blends with w_{PtBS} = 20, 30, and 50 wt% plotted against a distance from the iso-τ_s temperature, $T - T_{iso\text{-}PI}$. The solid curve indicates a_T of bulk PI20 plotted against $T - T_{r,bulk}$ with $T_{r,bulk}$ = 30°C (WLF eq 3-2). **Bottom panel**: Dielectric relaxation time τ_ε of the majority of PI20 chains in the PI20/PtBS16 blends with w_{PtBS} = 20, 30, and 50 wt%. The τ_ε data are plotted against $T - T_{iso\text{-}PI}$. The solid curve indicates the τ_ε data of bulk PI20 plotted against $T - T_{r,bulk}$ ($T_{r,bulk}$ = 30°C). The dashed curve shows the bulk τ_ε data multiplied by a factor of 2.4.

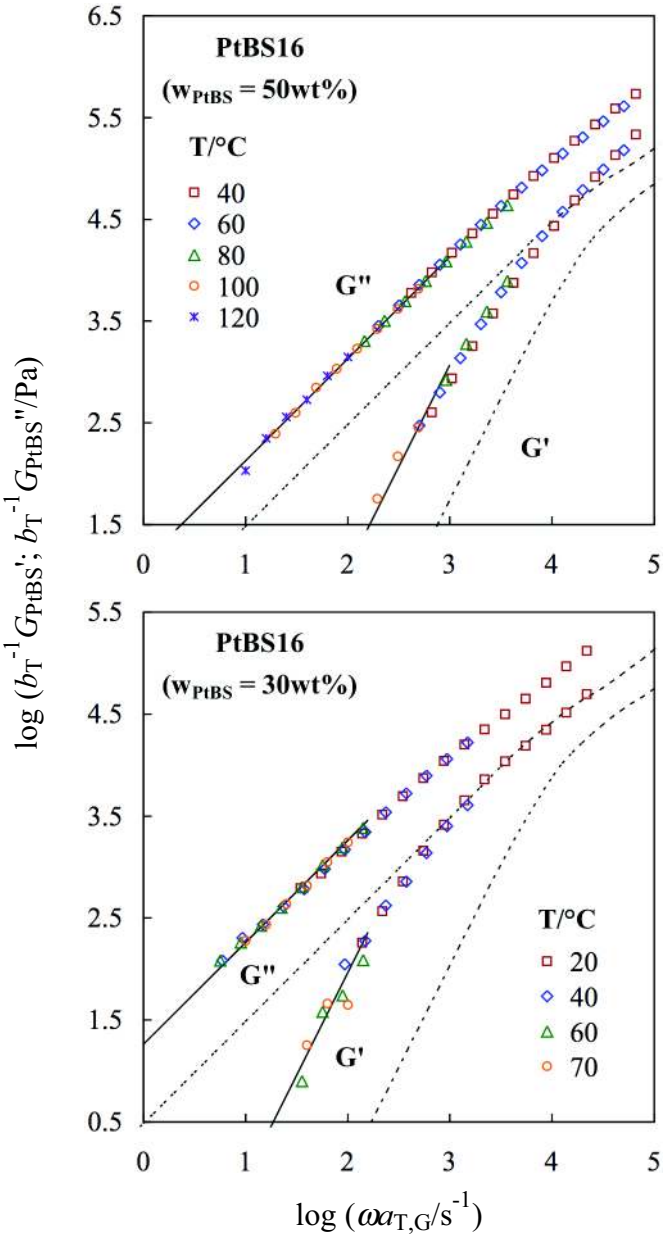

Fig. 5-8: Test of the time-temperature superposability for the $b_T^{-1} G_{PtBS}^{bld}$* data of the PtBS16 chains in the PI20/PtBS16 blends with w_{PtBS} = 50 and 30 w%, with $b_T = T/T_r$ being an intensity correction factor. The dotted curves indicate normalized modulus of bulk PtBS16 at the iso-τ_s temperature, $T_{iso\text{-}PtBS}$. The solid lines show the terminal tails of $G_{PtBS}^{bld}" \propto \omega$ and $G_{PtBS}^{bld}' \propto \omega^2$.

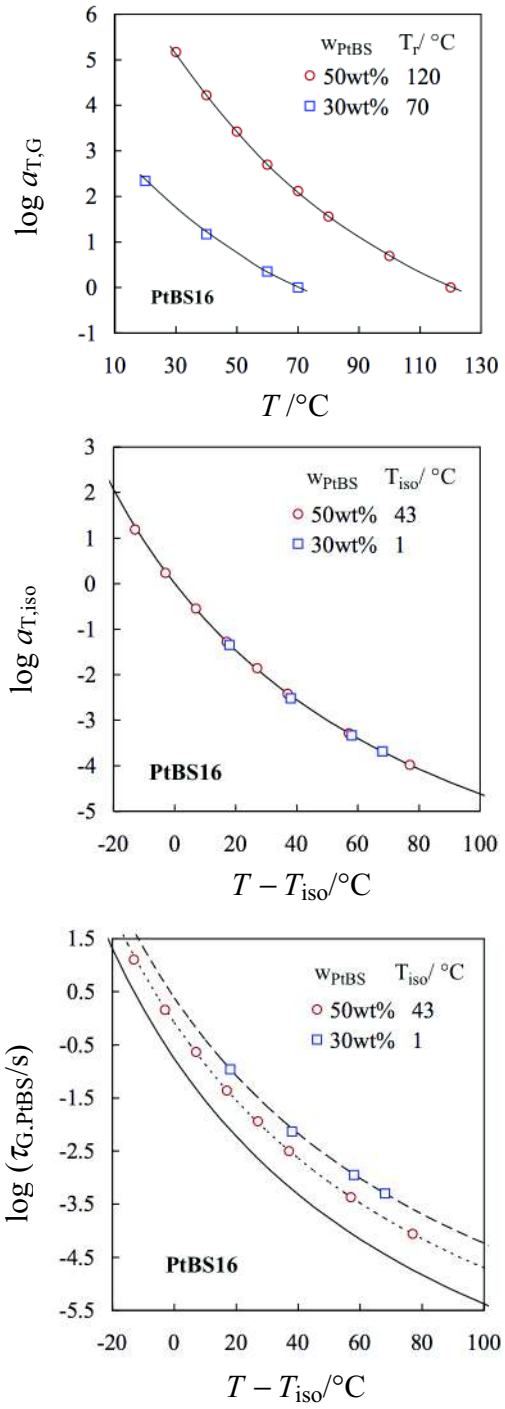

Fig. 5-9: **Top panel**: Plots of the time-temperature shift factor $a_{T,G}$ for G_{PtBS}^* data (shown in Figure 5-8) against the temperature T. **Middle panel**: Plots of a shift factor $a_{T,iso}$ of PtBS16 against a distance from the iso-τ_s temperature, $T - T_{iso\text{-}PtBS}$. The solid curve indicates a_T of bulk PtBS16 plotted against $T - T_{r,bulk}$ with $T_{r,bulk}$ = 171°C (WLF eq 3-3). **Bottom panel**: Viscoelastic relaxation time $\tau_{G,PtBS}$ of PtBS16 in the blends with w_{PtBS} = 30 and 50 wt%. These $\tau_{G,PtBS}$ data are plotted against $T - T_{iso\text{-}PtBS}$. The solid curve indicates $\tau_{G,PtBS}$ of bulk PtBS16 plotted against $T - T_{r,bulk}$ ($T_{r,bulk}$ = 171°C). The dotted and dashed curves, respectively, show the bulk $\tau_{G,PtBS}$ data multiplied by factors of 4.8 and 14.0.

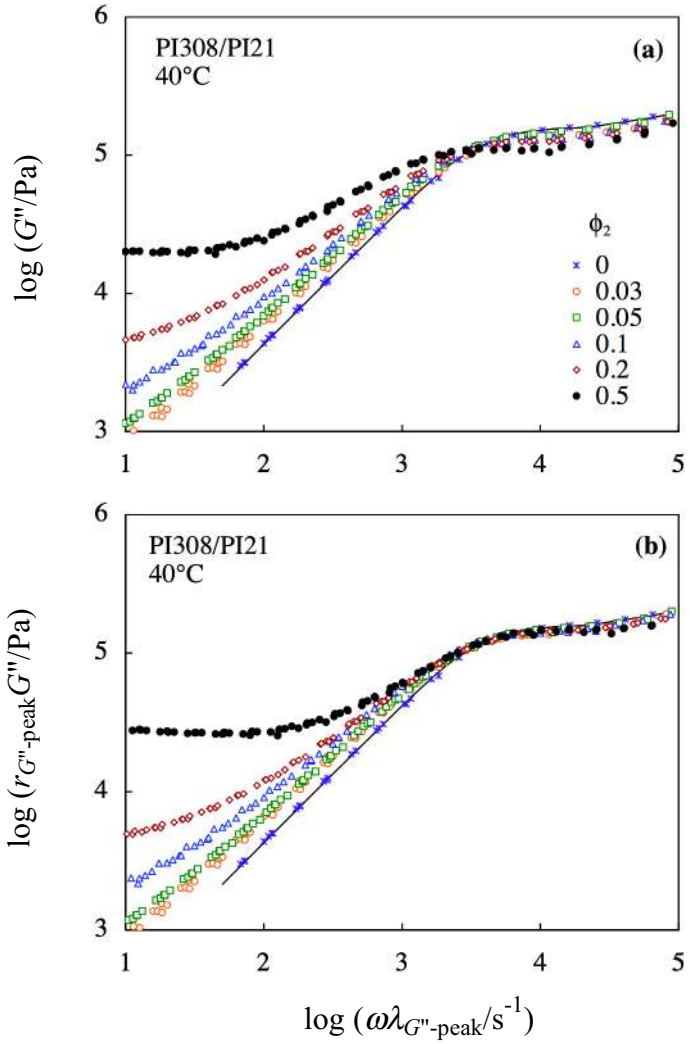

Fig. 5-10: **Top panel**: Angular frequency dependence of the loss modulus, G", obtained for a series of PI/PI binary blends with the component molecular weights of $10^{-3}M_1 = 21.4$ and $10^{-4}M_2 = 30.8$. The data were taken from Ref.23.

Bottom panel: Superposition of the G" curves shown in the top panel.

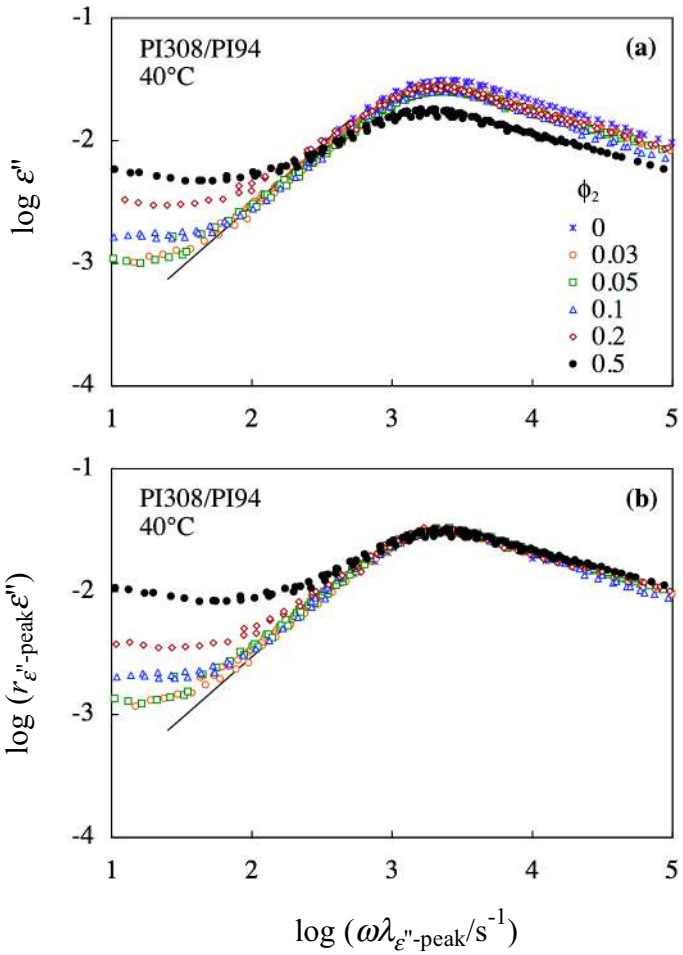

Fig. 5-11: **Top panel**: Angular frequency dependence of the dielectric loss modulus, ε'', obtained for a series of PI/PI binary blends with the component molecular weights of $10^{-3}M_1 = 21._4$ and $10^{-4}M_2 = 30._8$. The data were taken from Ref.23.

Bottom panel: Superposition of the ε'' curves shown in the top panel.

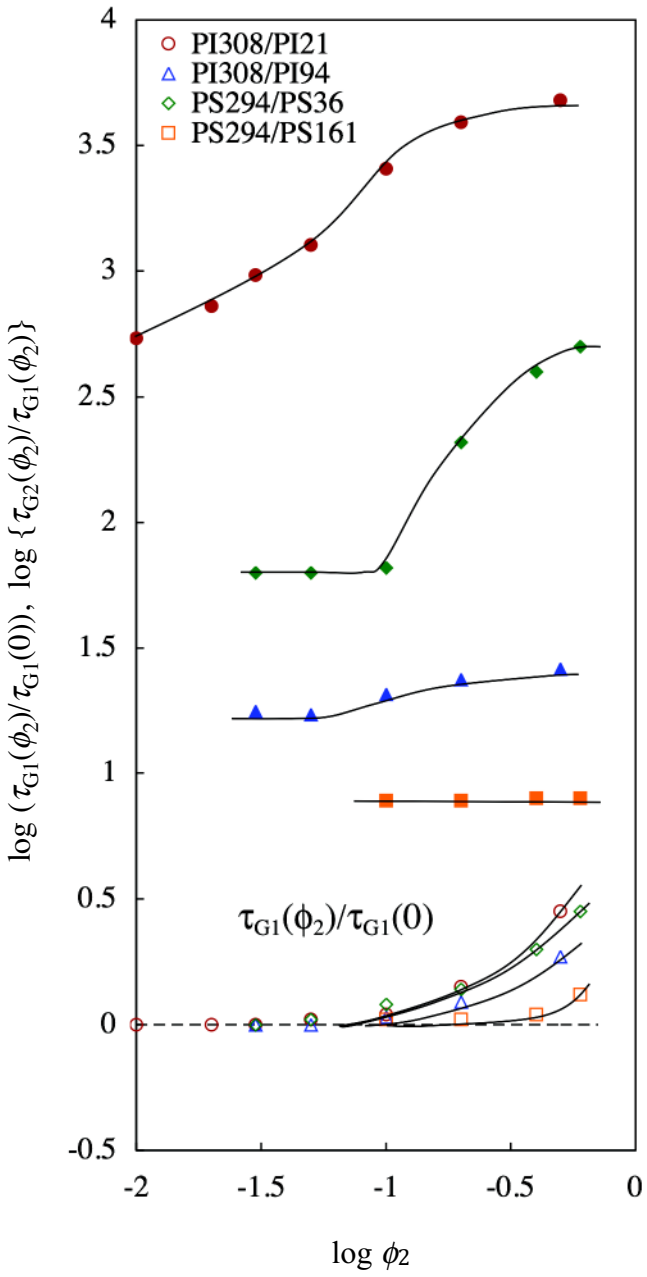

Fig. 5-12: Viscoelastic relaxation time ratios of fast component in blend and monodisperse bulk state, $\tau_{G1}(\phi_2)/\tau_{G1}(0)$ (unfilled symbols), and those of the slow and fast components in the same blend, $\tau_{G2}(\phi_2)/\tau_{G1}(\phi_2)$ (filled symbols). These ratios are plotted against volume fraction of the slow component, ϕ_2. The data were taken from Ref.23 (for PI308/PI21), Ref.31 (for PI308/PI94), and Ref.27 (for PS/PS).

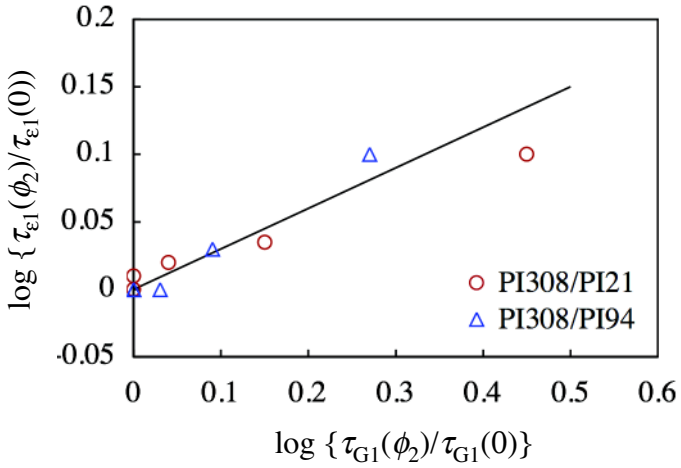

Fig. 5-13: Relationship between the $\tau_{\varepsilon 1}(\phi_2)/\tau_{\varepsilon 1}(0)$ and $\tau_{G1}(\phi_2)/\tau_{G1}(0)$ ratios for PI308/PI21 and PI308/PI94 blends. These ratios represent magnitudes of the retardation of the dielectric and viscoelastic relaxation of the fast component in these blends on restriction of DTD/CR. (This retardation is defined with respect to the monodisperse system of the fast component). The solid line indicates the empirical eq A5-1-1. The data were taken from Refs.23 and 31.

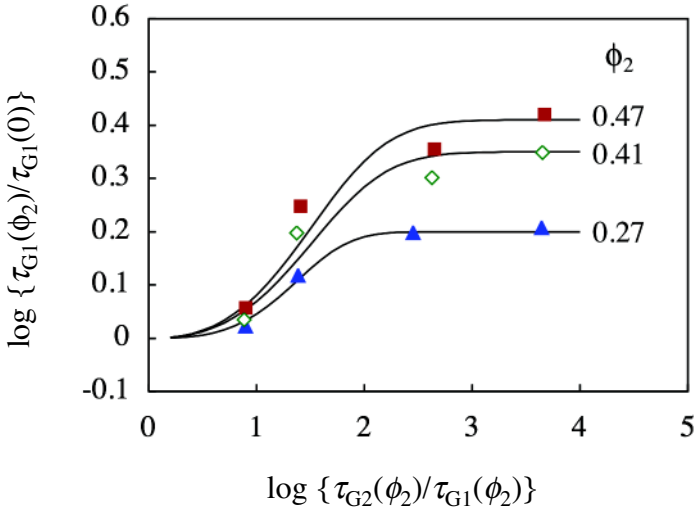

Fig. 5-14: Relationship between the $\tau_{G1}(\phi_2)/\tau_{G1}(0)$ and $\tau_{G2}(\phi_2)/\tau_{G1}(\phi_2)$ ratios for the blends with ϕ_2 as indicated. The plots were made by interpolating the data points in Figure 5-12. The $\tau_{G1}(\phi_2)/\tau_{G1}(0)$ ratio represents the magnitude of the retardation of the viscoelastic relaxation of the fast component in the blends due to restriction of DTD/CR, and the $\tau_{G2}(\phi_2)/\tau_{G1}(\phi_2)$ ratio specifies a difference of the relaxation times of the fast and slow components. The solid curves indicate the empirical eq A5-1-2.

Chapter 6 THERMO-RHEOLOGICAL BEHAVIOR OF PI/PTBS BLENDS: II

6-1 Introduction

Chapters 4 and 5 revealed several characteristic features of the component dynamics of polyisoprene/poly (*p-tert* butyl styrene) blends, as briefly summarized below.

The dielectrically-detected PI terminal relaxation in the blend is thermo-rheologically complex given that: (1) the PtBS motion is *much slower* than the PI motion to effectively quench the fluctuation of local friction (determined by the local composition) in the time scale of the global PI relaxation, and (2) the PI chain dimension is comparable to/smaller than the characteristic length of this frictional heterogeneity.[1-3] Furthermore, the PI relaxation was slower in the blends, by a factor of 2-3, than in the iso-τ_s bulk possibly because the slow PtBS chains disturbed the Rouse equilibration of the PI chains over the entanglement length (cf. Chapter 5).

The dynamics was also examined for the PtBS chains entangled with the PI chains. The viscoelastic modulus of the PtBS chains G_{PtBS}^{bld} *, obtained by subtracting the PI modulus G_{PI}^{bld} * from the blend modulus G_B*, was found to be thermo-rheologically simple given that the PI chains relaxed much faster than the PtBS chains thereby smearing the local frictional heterogeneity in the time scale of the PtBS relaxation.[1,3] Furthermore, the PtBS relaxation appeared to be slower in the blends, by a factor as large as one decade, than that in the iso-τ_s bulk.[3] This significant delay is attributable to the *pseudo-constraint release* (*pseudo-CR*) mechanism proposed in Chapter 5.[3]

There are several aspects to be further investigated. The high-M PI chains exhibited the thermo-rheologically simple behavior in Chapter 4, while low-M PI chains exhibited the thermo-rheologically complex behavior in Chapter 5, possibly because the characteristic length and time scales of the dynamic heterogeneity were larger than those of the low-M PI chains while smaller than those of the high-M PI chains. Thus, it is naturally expected that a crossover from thermo-rheologically complex to simple behavior occurs with increasing M_{PI} of the PI chains blended with the same PtBS chains. Furthermore, G_{PtBS}^{bld} * can be evaluated with smaller numerical uncertainty for larger M_{PtBS} (because G_{PtBS}^{bld} * approaches the raw G_B* data with increasing M_{PtBS}). For completeness, this chapter considers these points to examine the component dynamics in blends with a fixed PI/PtBS composition and different M_{PI}/M_{PtBS} ratios. It turned out that the thermo-rheological complexity of PI becomes less significant for larger M_{PI}, and G_{PtBS}^{bld} * can be evaluated without ambiguity for the blend with G_{PtBS}^{bld} * >> G_{PI}^{bld} * (PI relaxation much faster than the blend relaxation). The PtBS chains in those blends unequivocally exhibit the thermo-rheological simplicity as well as the retarded relaxation through the *pseudo-CR mechanism*. The entanglement

relaxation and pseudo-CR processes of the PI and PtBS chains therein were also examined for the blend with $G_{PtBS}^{bld} * \sim G_{PI}^{bld} *$. Details of the results are presented below.

6-2 Experimental

6-2-1 Materials

Three PI samples, PI3, PI53 and PI99, and a PtBS sample, PtBS42, were anionically synthesized. The methods for synthesizing and characterizing the samples were explained in Section 2-1. These samples as well as a commercially available PI20 (supplied from Kuraray Co.) sample and a previously synthesized PtBS70 sample[1] were utilized in this chapter. Their characteristics are summarized in Table 6-1.

The PI99/PtBS42, PI53/PtBS42, PI20/PtBS42, PI20/PtBS70 and PI3/PtBS42 blends having the PI content w_{PI} = 55.7wt% were prepared according to the method of Yurekli et.al.,[4] as explained in Section 2-1. This w_{PI} value was chosen to be the same as that of a PI53-PtBS42 diblock copolymer examined in Chapter 7. (The PtBS42 sample was a precursor of this copolymer sample.)

6-2-2 Measurements

Linear viscoelastic and dielectric measurements were conducted for the PI99/PtBS42, PI53/PtBS42, PI20/PtBS42 and PI20/PtBS70 blends, all having the PI content of w_{PI} = 55.7 wt%. For the PI3/PtBS42 blend, only the linear viscoelastic measurement was conducted.

The operation(s) and principle(s) for linear viscoelastic and dielectric measurements were explained in Section 2-2-2.

6-3 Results and Discussion

6-3-1 Overview of dynamic behavior of blends with $\tau_G >> \tau_\varepsilon$

Figure 6-1 compares the data of the storage and loss moduli, $G'(\omega)$ and $G''(\omega)$, the dielectric loss, $\varepsilon''(\omega)$, and the decrease of dynamic dielectric constant from its static value, $\Delta\varepsilon'(\omega) = \varepsilon'(0) - \varepsilon'(\omega)$, measured for the PI20/PtBS42 and PI20/PtBS70 blends having the same w_{PI}

(= 55.7 wt%) and same M_{PI} but different M_{PtBS}. These data are double-logarithmically plotted against the angular frequency, ω, and the comparison is made at the lowest and highest temperatures examined, T = 20 and 90°C. The $\Delta\varepsilon'(\omega)$ and ε'' data detecting exclusively the global motion of PI are multiplied by a factor of 10^3 and shown in a range of ω where the direct current contribution due to ionic impurities is neglibibly small.[3]

The PtBS chains in those blends have the molecular weight M_{PtBS} comparable to the entanglement molecular weight of bulk PtBS, $M_e^{\text{bulk PtBS}} = 37.6\times10^3$,[5] and are barely entangled in bulk. Nevertheless, the entanglement length a changes on blending, as discussed in Chapter 4. From the a value determined by eq 4-4, the corresponding M_e^{PtBS} and M_e^{PI} in the blends are evaluated as $M_e^X = M_e^{\text{bulk X}}(a / a_X^{\text{bulk}})^2$ (X=PI, PtBS). These M_e values are:

$$M_e^{PtBS} = 10.5\times10^3, \quad M_e^{PI} = 5.7\times10^3 \tag{6-1}$$

In Figure 6-1, the horizontal dashed lines indicate the entanglement plateau modulus G_N (= $C_{PI}RT/M_e^{PI} + C_{PtBS}RT/M_e^{PtBS}$; cf. eq 4-14) corresponding to above M_e values. At low T, the storage modulus G' does not show a plateau at this G_N but exhibits a power-law behavior together with the loss modulus, $G' \cong G'' \propto \omega^{\beta}$ with $\beta \cong 1/2$, and the moduli in this power-law zone are insensitive to M_{PtBS}; cf. the top panel of Figure 6-1. These features reflect the cooperative Rouse equilibration of the PI and PtBS chains within the entanglement length,[27] as discussed in Chapter 4.

The blends exhibit the terminal viscoelastic and dielectric relaxation characterized by the terminal tail,[6,7] G' ($\propto\omega^2$), G'' ($\propto\omega$), $\Delta\varepsilon'$ ($\propto\omega^2$), and ε'' ($\propto\omega$). The terminal viscoelastic and dielectric relaxation times, τ_G and τ_ε, are evaluated from these tails through eqs 2-26 and 2-31. The thick arrows in Figure 6-1 indicate the terminal viscoelastic relaxation frequency, $\omega_G = 1/\tau_G$. The terminal dielectric relaxation frequency, $\omega_\varepsilon = 1/\tau_\varepsilon$, was very close to a frequency ω_x where the $\Delta\varepsilon'$ and ε'' curves cross each other (since the terminal tails emerges immediately after this cross). Clearly, ω_G is much smaller than ω_x (= ω_ε). This fact indicates that the PI and PtBS chains are the fast and *much* slower components in the PI20/PtBS42 and PI20/PtBS70 blends and that the terminal viscoelastic relaxation of the blends is dominated by the PtBS chains.

This PtBS dominance can be also examined straightforwardly with the aid of a blending rule for the complex modulus G^* (= $G'+iG''$) introduced in Chapter 5.

$$G_B^*(\omega) = G_{PI,e}^{bld}*(\omega) + G_{PtBS}^{bld}*(\omega) \qquad \text{in frequency } \omega \text{ domain} \tag{6-2a}$$

$$G_B(t) = G_{PI,e}^{bld}(t) + G_{PtBS}^{bld}(t) \qquad \text{in time } t \text{ domain} \tag{6-2b}$$

with

$$G_{\mathrm{PI,e}}^{\mathrm{bld}}*(\omega)=\phi_{\mathrm{PI}}I_{\mathrm{PI}}\{\upsilon_{\mathrm{maj}}G_{\mathrm{PI}}^{\mathrm{bulk}}*(\omega Q_{\mathrm{maj}}^{2.33}/\lambda_{\mathrm{PI}}^{\mathrm{maj}})+(1-\upsilon_{\mathrm{maj}})G_{\mathrm{PI}}^{\mathrm{bulk}}*(\omega Q_{\mathrm{min}}^{2.33}/\lambda_{\mathrm{PI}}^{\mathrm{min}})\} \tag{6-3a}$$

$$G_{\mathrm{PI,e}}^{\mathrm{bld}}(t)=\phi_{\mathrm{PI}}I_{\mathrm{PI}}\{\upsilon_{\mathrm{maj}}G_{\mathrm{PI}}^{\mathrm{bulk}}(t\lambda_{\mathrm{PI}}^{\mathrm{maj}}/Q_{\mathrm{maj}}^{2.33})+(1-\upsilon_{\mathrm{maj}})G_{\mathrm{PI}}^{\mathrm{bulk}}(t\lambda_{\mathrm{PI}}^{\mathrm{min}}/Q_{\mathrm{min}}^{2.33})\} \tag{6-3b}$$

This rule is valid in the entanglement relaxation regime.[1-3] Eqs 6-2a and 6-3a are essentially the same as eqs 5-13 and 5-14 in Chapter 5, and eqs 6-2b and 6-3b represent the same blending rule in the time domain. Eqs 6-2a and 6-2b merely indicate the additivity of moduli of the PI chains ($G_{\mathrm{PI,e}}^{\mathrm{bld}}*(\omega)$, $G_{\mathrm{PI,e}}^{\mathrm{bld}}(t)$) and the PtBS chains ($G_{\mathrm{PtBS}}^{\mathrm{bld}}*(\omega)$, $G_{\mathrm{PtBS}}^{\mathrm{bld}}(t)$) in the blends, *i.e.*, the stress additivity. $G_{\mathrm{PI,e}}^{\mathrm{bld}}*(\omega)$ and $G_{\mathrm{PI,e}}^{\mathrm{bld}}(t)$ are the moduli for the entanglement relaxation of PI and include no contribution from the Rouse-equilibration. In eq 6-3, these moduli at T are approximated to have the same mode distribution as in bulk and expressed in terms of the moduli data of bulk PI at the same T, $G_{\mathrm{PI}}^{\mathrm{bulk}}*(\omega)$ and $G_{\mathrm{PI}}^{\mathrm{bulk}}(t)$. (This approximation, already made in Chapter 5, is valid for the terminal relaxation of the fast component in the blends, as noted from extensive data for entangled PI/PI blends.[6,8-10]) The moduli data of bulk PI may contain a contribution from the Rouse equilibration (completing at the time τ_a) in addition to $G_{\mathrm{PI,e}}^{\mathrm{bld}}*(\omega)$, but this Rouse contribution becomes negligible at low ω and long t, in particular for the relaxation modulus $G_{\mathrm{PI}}^{\mathrm{bulk}}(t)$ at long t because a modulus ratio for the Rouse equilibration and the entanglement relaxation rapidly decays with t as $\exp\left\{-t(\tau_a^{-1}-\tau_{\mathrm{ent}}^{-1})\right\}$ (τ_{ent} = entanglement relaxation time) and vanishes in the time scale of τ_{ent}.

The factors I_{PI} and λ's appearing in eq 6-3 represent corrections for the changes of the entanglement length a and dielectric relaxation time of PI, as explained earlier for eq 5-13. The Q factor, correcting a change of dynamic tube dilation/constraint release (DTD/CR) contribution to the relaxation of entangled PI, is evaluated from the τ_ε and τ_{G} data of blend and bulk PI with the aid of the empirical eq 5-7 in Chapter 5, with the numerical coefficients therein being given by (B, α, q) = (0.35, 0.2, 2.5) for the blends with the volume fraction of the slow component $\phi_2 = \phi_{\mathrm{PtBS}}$ = 0.41.

For evaluation of the factors of λ's appearing in eq 6-3, the dielectric ε'' data of the blend, triangles in Figure 6-2(a), are fitted with the $\varepsilon_{\mathrm{PI}}^{\mathrm{bulk}}{}''$ data of bulk PI multiplied by the PI volume fraction in the blend, ϕ_{PI} = 0.59. At low T (20°C), the dielectric mode distribution of the blend was broader than that of bulk PI. This fact indicates that the chains are classified into the minority and majority having different relaxation times: Namely, at low T, the PtBS motion is much slower than the PI motion to quench the dynamic frictional heterogeneity during the terminal relaxation process

of PI. Then, some PI chains (minority) in a PtBS-rich region feel the friction larger than the average (for the majority). Thus, the ε'' data are fitted with a sum of the contributions from the fast majority and the slow minority of PI in the blend, as explained in Chapter 5. The fitting was excellently achieved (with the fraction of PI in the fast majority $\upsilon_{maj} = 0.7$), as shown with the thin solid curve in the top panel of Figure 6-2(a) where the respective contributions are indicated with the thin dotted curves. In contrast, at high T (90°C), the dielectric mode distribution of the blend was very close to that of bulk PI and the ε'' data were satisfactorily fitted by one set of $\varepsilon_{PI}^{bulk}{}''$ for the majority ($\upsilon_{maj} = 1$), as shown with the thin solid curve in the bottom panel of Figure 6-2(a). In this way, the fitting of the ε'' data allowed determination of υ_{maj} and the frequency reduction factor (from bulk PI), λ_{PI}^{maj} and λ_{PI}^{min}, for the fast majority and the slow minority of PI chains. The υ_{maj} and λ were utilized in eq 6-3 to determine $G_{PI,e}^{bld}*$ of PI in the blend from $G_{PI}^{bulk}*$ data of bulk PI.

In Figure 6-2(a), the $G_B^*(\omega)$ data of the PI20/PtBS42 blend (squares) are compared with the modulus $G_{PI,e}^{bld}*(\omega)$ for the entanglement relaxation of PI20 therein (thick solid curves) estimated from the $G_{PI}^{bulk}*(\omega)$ data; cf. eq 6-3. Figure 6-2(b) shows the results of corresponding comparison of the relaxation moduli, $G_B(t)$ and $G_{PI,e}^{bld}(t)$ converted from the $G_B^*(\omega)$ and $G_{PI}^{bulk}*(\omega)$ data. For this conversion, the G^* data were first expressed as a sum of a set of single exponential modes[11] (with a logarithmic mode relaxation time span of $\log [\tau_{G,p}/\tau_{G,p+1}] = 0.1$; cf. eq 2-21) and then transferred into the time domain (cf. eq 2-20). The triangles show the dielectric relaxation function $\varepsilon(t)$ of the blend similarly converted from the ε'' data.

As noted in Figure 6-2(a), $G_{PI,e}^{bld}*(\omega)$ is much smaller than $G_B^*(\omega)$ in the entire ranges of ω and T. Correspondingly, $G_{PI,e}^{bld}(t)$ is much smaller than $G_B(t)$ at t and T examined; cf. Figure 6-2(b). These results indicate that the PtBS chains dominate the terminal viscoelastic relaxation of the blend. This was also the case for the PI20/PtBS70 blend having larger M_{PtBS}. Thus, for the PI20/PtBS42 and PI20/PtBS70 blends, the PtBS moduli obtained from the subtraction, $G_{PtBS}^{bld}*(\omega) = G_B*(\omega) - G_{PI,e}^{bld}*(\omega)$ and $G_{PtBS}^{bld}(t) = G_B(t) - G_{PI,e}^{bld}(t)$, are practically indistinguishable from the raw $G_B^*(\omega)$ and $G_B(t)$ data and hardly contain numerical uncertainty due to the subtraction; cf. small filled circles in Figures 6-2(a) and (b). These blends serve as the model systems that enable the unambiguous test of the thermo-rheological behavior of the PtBS chains therein. This test is made later for $G_{PtBS}^{bld}*(\omega)$ and $G_{PtBS}^{bld}(t)$ evaluated in the ranges of ω and t where the PI and PtBS chains have been Rouse-equilibrated within the entanglement segment to exhibit $G'(\omega)$, $G(t) \le G_N$: The blending rule considering this segment as the basic unit for the chain motion, eqs 6-2 and 6-3, is valid at those ω and t.

Now, the focus is placed on the Rouse-like power-law behavior seen at low T, $G' \cong G'' \propto \omega^{\beta}$ with $\beta \cong 1/2$, and the corresponding lack of the entanglement plateau at $G' = G_N$; cf. the top panel of Figure 6-1. This plateau prevails only when the global chain motion is much slower than the Rouse equilibration within the entanglement length a. In the PI/PtBS blends at low T, the slow PtBS chains hinder the fast PI chain from exploring the local conformations at lengths $\leq a$ within its intrinsic Rouse equilibration time thereby retarding the equilibration of the PI chain, as discussed in Chapter 4. If the time τ_a necessary for the cooperative Rouse equilibration of PI and PtBS is close to the terminal, entanglement relaxation time of PI, the power-law behavior associating to this equilibration masks the entanglement plateau. This molecular argument can be tested from comparison of τ_a and the dielectric τ_ε of PI, the former being evaluated from the continuous Rouse relationship, as explained in Chapter 4 (cf. eq 4-14).[12]

In the top panel of Figure 6-1, the thin arrow shows the Rouse equilibration frequency $\omega_a = 1/\tau_a$ evaluated from eq 4-14 applied to the G^* data at 20°C. The dielectric $\omega_\varepsilon = 1/\tau_\varepsilon$ of PI is very close to the frequency ω_x where the $\Delta\varepsilon'$ and ε'' curves cross each other, as explained earlier. Clearly, ω_a almost coincides with ω_x (= ω_ε). Thus, the PI20 chain in those blends fully relaxes immediately after it is Rouse-equilibrated together with the PtBS chain, which confirms the above molecular argument. This result becomes a key to later discussion of the PtBS relaxation in the blend.

In relation to the above result, it is noted that the Rouse equilibration is a local process occurring in length scales $\leq a$. Thus, the power-law behavior associating this process is expected to be insensitive to the component molecular weights M given that M is well above M_e. In fact, the G^* data in this power-law zone are indistinguishable for the PI20/PtBS42 and PI20/PtBS70 blends having different M_{PtBS}, as noted in the top panel of Figure 6-1. Furthermore, the G^* data of the PI99/PtBS42 blend having different M_{PI} (shown later in Figure 6-3) were also close to those of the PI20/PtBS42 and PI20/PtBS70 blends in the power-law zone. These results are consistent with the above expectation, lending support to the molecular picture of the retarded, cooperative Rouse equilibration of the PI and PtBS chains.

6-3-2 Overview of dynamic behavior of blends with $\tau_G \sim \tau_\varepsilon$

Figure 6-3 shows the G', G'', $\Delta\varepsilon'$, and ε'' data for the PI99/PtBS42 blend (w_{PI} = 55.7 wt%) at representative temperatures as indicated. (The $\Delta\varepsilon'$ and ε'' data are multiplied by a factor of 10^2.) The horizontal dashed line shows the entanglement plateau modulus G_N (= $C_{PI}RT/M_e^{PI}$ +

$C_{PtBS}RT/M_e^{PtBS}$; cf. eq 4-14) expected at 20°C. The thick arrows indicate the viscoelastic relaxation frequency $\omega_G = 1/\tau_G$ (cf. eq 2-26) evaluated for the blend at respective temperatures, and the thin arrow shows the Rouse-equilibration frequency $\omega_a = 1/\tau_a$ (cf. eq 4-14) at 20°C. The dielectric $\omega_\varepsilon = 1/\tau_\varepsilon$ of PI (with τ_ε being defined by eq 2-31) was very close to the frequency ω_x where the $\Delta\varepsilon'$ and ε'' curves cross each other.

As noted in Figure 6-3, the entanglement plateau is not observed at 20°C possibly because the power-law behavior due to the cooperative Rouse-equilibration of PI and PtBS masks the plateau. This feature is similar to that seen in Figure 6-1 for the lower-M_{PI} PI20/PtBS42 and PI20/PtBS70 blends. In fact, G^* data of the PI99/PtBS42 blend in this power-law zone are close to those of the latter two blends. However, important differences are also noted: For the PI99/PtBS42 blend, ω_G is close to the dielectric ω_ε (= ω_x) even at the lowest T examined, 20°C, and ω_ε is much lower than ω_a. The close coincidence of ω_G and ω_ε demonstrates a large contribution of the PI99 chains to the terminal viscoelastic relaxation of the blend, and the large separation between ω_ε and ω_a indicates that the PI99 chain exhibits the global relaxation well after its Rouse equilibration. A delicate hump of the G'' data, noted for the data points at ω =0.3-0.03s^{-1} that lie above the power-law line describing the data at $\omega > 1$s^{-1}, reflects this separation. (No corresponding hump is seen for the data of the PI20/PtBS42 blend in the top panel of Figure 6-2(a).) These differences are naturally related to the high molecular weight of PI99 ($M_{PI99} \cong 5M_{PI20}$) that results in the global motion much slower for PI99 than for PI20.

The significance of the PI99 contribution to the terminal viscoelastic relaxation of the blend can be further examined on the basis of the blending rule, eqs 6-2 and 6-3. The modulus $G_{PI,e}^{bld}$ * for the entanglement relaxation of PI99 was estimated from the τ_ε and τ_G data of blend and bulk PI99 and the G_{PI}^{bulk} * data of bulk PI99, as explained earlier for the low-M_{PI} blends; cf. eq 6-3. (For PI99, the slow minority content was negligibly small and $G_{PI,e}^{bld}$ * was estimated with υ_{maj} = 1.) The $G_{PI,e}^{bld}$ * data thus obtained are shown in Figure 6-3 with the thick solid curves. These curves are close to the G_B^* data of the PI99/PtBS42 blend in particular at high T, confirming the significant PI99 contribution to the G_B^* data in the terminal relaxation regime.

6-3-3 Thermo-rheological behavior of PI in blends

The dielectric $\Delta\varepsilon'$ and ε'' data of the PI/PtBS blends exclusively detect the global PI motion even for the case that the PI motion is much faster than the PtBS motion. (The Rouse equilibration within the entanglement length does not activate a change of the end-to-end vector except at the

chain ends and hardly affects the dielectric data.) Thus, those data enable a test of the thermo-rheological behavior of PI without any ambiguity in the entire range of T. In Figure 6-4, the time-temperature superposition is tested for the $\Delta\varepsilon'$ and ε'' data of the PI20/PtBS42, PI53/PtBS42, and PI99/PtBS42 blends. (The raw ε^* data of the PI53/PtBS42 are presented in Chapter 7.) The results for the PI20/PtBS70 blend were almost indistinguishable from those for the PI20/PtBS42 blend and not shown here. The reference temperature was chosen to be T_r = 90°C. The $\Delta\varepsilon'$ and ε'' data at respective T are multiplied by the intensity factor $b_T = T/T_r$ (with T and T_r in K unit) and shifted along the ω axis to achieve the best superposition at ω higher than the ε''-peak frequency, $\omega_{\varepsilon\text{-peak}}$. For clarity of the plots, only the data at representative T are shown, and the $\Delta\varepsilon'$ data are multiplied by a factor of $10^{1.5}$. For respective blends, the solid curves show the dielectric data of the PI components in the bulk state at 90°C. These bulk data are multiplied by the PI volume fraction in the blend, ϕ_{PI} = 0.59, and shifted along the ω axis to match $\omega_{\varepsilon\text{-peak}}$ with the blend data.

As noted in Figure 6-4, the shift is fairly successful for the ε'' data (even at $\omega < \omega_{\varepsilon\text{-peak}}$) while a non-negligible failure prevails for the $\Delta\varepsilon'$ data at $\omega < \omega_{\varepsilon\text{-peak}}$ in particular for the PI20/PtBS42 and PI53/PtBS42 blends. (Since $\Delta\varepsilon'$ is much more sensitive to slow dielectric modes compared to ε'',[7] the failure of the superposition is much more clearly resolved for $\Delta\varepsilon'$.) This failure is mostly related to the spatial frictional heterogeneity for the PI chains as discussed in Chapter 5:[1,3] At sufficiently low T where the PtBS motion is much slower than the PI motion, this heterogeneity survives during the terminal relaxation process of PI so that some PI chains (minority) stay in a PtBS-rich region and feel the friction larger than the average friction for the majority. This heterogeneity is smeared within a random coil of a high-M_{PI} chain having the end-to-end distance R_{PI} well above the correlation length of the heterogeneity. For this reason, the failure is less significant for the PI99 chain (bottom panel) than for the PI20 and PI53 chains (top and middle panel). This argument explains why the thermo-rheological complexity was clearly seen for low-M PI/PtBS blend in Chapter 5 while not for high-M PI/PtBS blend in Chapter 4.

The shift factor $a_{T,\varepsilon}$ utilized for the superposition in Figure 6-4 represents changes of the dielectric relaxation time τ_ε of the majority PI with T.[3] The top panel of Figure 6-5 shows the $a_{T,\varepsilon}$ data for the PI/PtBS blends as indicated (w_{PI} = 55.7 wt% for all blends). These data were subjected to a minor correction for a change of the DTD/CR contribution[3] to the PI relaxation with T (as explained earlier in Appendix 5-1) and then subjected to the standard WLF analysis (Appendix 3-1). This analysis enabled determination of the iso-τ_s temperatures $T_{iso\text{-}PI}$ where the Rouse segment of PI had the same relaxation time τ_s in the blend and in bulk. Specifically, $T_{iso\text{-}PI}$ for the PI chains in the blends that corresponds to $T_{r,bulk} = T_{iso\text{-}PI}^{bulk}$ = 30°C for bulk PI was found to be

$$T_{\text{iso-PI}} = 60°\text{C (for PI/PtBS blends with } w_{\text{PI}} = 55.7 \text{ wt\%}) \quad (6\text{-}4)$$

In the bottom panel of Figure 6-5, the shift factor $a_{\text{T,iso}}$ re-evaluated for this $T_{\text{iso-PI}}$ is plotted against a temperature difference, $T-T_{\text{iso-PI}}$. These $a_{\text{T,iso}}$ data are indistinguishable for the PI chains having the same w_{PI} but different M_{PI} (PI20, PI53, and PI99) and well described by the WLF equation for bulk PI shown with the solid curve (cf. eq 3-2). The coincidence of $T_{\text{iso-PI}}$ for those PI chains demonstrates that τ_s in the blends is determined by the local chemical composition irrespective of M_{PI}.

6-3-4 Thermo-rheological behavior and relaxation mechanism of PtBS in blends with $\tau_G >> \tau_e$

In the PI99/PtBS42 blend, the modulus $G_{\text{PI,e}}^{\text{bld}}*$ for the entanglement relaxation of PI is close to the $G_{\text{B}}*$ data at low ω (in particular at $T \geq 50°$C; cf. Figure 6-3) so that the PtBS modulus therein, $G_{\text{PtBS}}^{\text{bld}}* = G_{\text{B}}* - G_{\text{PI,e}}^{\text{bld}}*$ (cf. eq 6-2), cannot be evaluated with sufficient numerical accuracy. However, for the PI20/PtBS42 and PI20/PtBS70 blends, $G_{\text{B}}* \gg G_{\text{PI,e}}^{\text{bld}}*$ and thus $G_{\text{PtBS}}^{\text{bld}}*$ is evaluated with negligible uncertainty and practically coincides with $G_{\text{B}}*$. Thus, the $G_{\text{PtBS}}^{\text{bld}}*$ data for the PI20/PtBS42 and PI20/PtBS70 blends are utilized to test the thermo-rheological behavior and relaxation mechanism of the PtBS chains therein.

For convenience of this test, a PI3/PtBS42 blend (w_{PI} = 55.7 wt%) containing the oligomeric PI3 is chosen as the reference system. In this blend, the PtBS42 chains are not entangled among themselves because the M_{PtBS42} of these chains is well below the entanglement molecular weight in a PtBS solution with $\phi_{\text{PtPS}} = 0.41$ (corresponding to $w_{\text{PtBS}} = 44.3$ wt% in the blend),

$$M_{\text{e,PtBS}}^{\text{soln}} = M_{\text{e,PtBS}}^{\text{bulk}} / \phi_{\text{PtBS}}^{1.3} = 1.2\times10^5 \quad (6\text{-}5)$$

Furthermore, the oligomeric PI3 has $M_{\text{PI3}} < M_{\text{e}}^{\text{PI}}$ (= 5.7×10^3; cf. eq 6-1) and exhibits neither PI-PI nor PI-PtBS entanglement. Thus, the PI3/PtBS42 blend serves as the reference system showing the *intrinsic*, entanglement-free relaxation behavior of the PtBS42 chain affected only by the relaxation time τ_s of the Rouse segment of PtBS. The $G*$ data of this blend obeyed the time-temperature superposition at T/°C = 20-80 and ω/s^{-1} = 10^{-2}-10^{2} because the oligomeric PI3 relaxed much faster than PtBS42 and negligibly contributed to the data. These $G*$ data, reduced at T_r = 20°C, are shown in Figure 6-6, and the corresponding shift factor $a_{\text{T,G}}$ is shown later in Figure 6-9. The $G*$ data exhibit the Rouse/Zimm-like ω dependence, as expected for the non-entangled PtBS42 chain. These data serve as the reference data for the PtBS42 and PtBS70 chains in the non-entangled state, as explained later in more detail.

For the PI20/PtBS42 and PI20/PtBS70 blends (w_{PI} = 55.7 wt%), the moduli $G^{bld}_{PtBS}*(\omega)$ of the PtBS chains were evaluated in the range of ω where the $G'(\omega)$ data of the blends were below G_N and eqs 6-2 and 6-3 based on the entanglement concept is valid. In Figure 6-7, the modulus $G^{bld}_{PtBS}*(\omega)$ is reduced by the intensity factor, $b_T = T/T_r$ with T_r = 293 K (20°C), and shifted along the ω axis by a factor $a_{T,G}$ to make the best superposition. The corresponding shift of $G^{bld}_{PtBS}(t)$ is made in Figure 6-8. Good superposition is seen for $G^{bld}_{PtBS}*(\omega)$ and $G^{bld}_{PtBS}(t)$, in particular for the latter. A contribution of the Rouse equilibration within the entanglement length to the relaxation modulus $G^{bld}_{PtBS}(t)$, *even if it remains at short t*, decays rapidly as $\exp\left\{-t(\tau_a^{-1} - \tau_{ent}^{-1})\right\}$ and completely vanishes in the time scale of entanglement relaxation, τ_{ent}. Thus, the thermo-rheological simplicity seen in Figure 6-8 is conceptually more rigid than that seen in Figure 6-7.

The above results demonstrate the thermo-rheological simplicity of the PtBS dynamics in those blends. This simplicity prevailed because the PI20 chain therein relaxed much faster than the PtBS chains (cf. Figure 6-1) thereby allowing the PtBS relaxation mechanism to remain the same in the entire range of *T*.

The top panel of Figure 6-9 shows the *T* dependence of the shift factor $a_{T,G}$ utilized for the PI20/PtBS42 and PI20/PtBS70 blends in Figure 6-7. (The shift factor was the same for $G^{bld}_{PtBS}*(\omega)$ and $G^{bld}_{PtBS}(t)$.) The data for the PI20/PtBS42 and PI20/PtBS70 blends agree with each other, because τ_s of the Rouse segment of PtBS is determined by the chemical composition irrespective of M_{PtBS}. The $a_{T,G}$ data for the PI3/PtBS42 reference blend (shown with the diamond) exhibit a little weaker *T* dependence because the oligomeric PI3 plasticized the PtBS chains more strongly than the PI20 chains.

The $a_{T,G}$ data in the top panel of Figure 9 were subjected to the WLF analysis to determine the iso-τ_s temperatures $T_{iso\text{-}PtBS}$ for PtBS. Specifically, $T_{iso\text{-}PtBS}$ for the PtBS chains in the blends that corresponds to $T_{r,bulk} = T^{bulk}_{iso-PI}$ = 180°C of bulk PtBS was found to be:

$$T_{iso\text{-}PtBS} = 25°C \text{ in PI20/PtBS42 and PI20/PtBS70 blends} \quad (6\text{-}6a)$$

$$T_{iso\text{-}PtBS} = 22°C \text{ in PI3/PtBS42 blend} \quad (6\text{-}6b)$$

The difference between these $T_{iso\text{-}PtBS}$ values, 3°C, reflects an extra plasticization of PtBS due to the oligomeric PI3. Thus, for the PI20/PtBS42 and PI20/PtBS70 blends at a given *T*, the non-entangled PI3/PtBS42 blend is in the iso-τ_s state at a temperature, *T*–3. In the bottom panel of Figure 6-9, the shift factor re-evaluated for these $T_{iso\text{-}PtBS}$, $a_{T,iso}$, is plotted against a temperature difference, $T-T_{iso\text{-}PtBS}$. The $a_{T,iso}$ data are indistinguishable for the PtBS chains having the same w_{PI}

but different M_{PtBS} (PtBS42 and PtBS70) and well described by the WLF equation for bulk PtBS shown with the solid curve (cf. eq 3-3)

Now, the relaxation mechanism is to be discussed for the PtBS chains in the PI20/PtBS42, PI20/PtBS70, and PI53/PtBS42 blends. For this purpose, the G^* data of the non-entangled PI3/PtBS42 reference blend are useful. In the top panel of Figure 6-7, the data of this reference blend at 17°C (in the iso-τ_s state corresponding to the PI20/PtBS42 blend at 20°C) are shown with the dotted curves. The behavior of the PtBS70 chain in the non-entangled iso-τ_s state can be estimated by reducing and shifting the G^* data of the reference blend by the Rouse factors, *i.e.*, by the reduction factor of M_{PtBS42}/M_{PtBS70} (= 0.60) and the shifting factor of $\{M_{PtBS42}/M_{PtBS70}\}^2$ (= 0.36) along the ω axis. The reference data for the PtBS70 chain thus obtained are shown with the dotted curves in the bottom panel of Figure 6-7. These reference G^* data for the PtBS42 and PtBS70 chains were converted to the relaxation modulus $G(t)$ with the method[11] explained for Figure 6-2(b) and shown in Figure 6-8 with the dotted curves.

Clearly, the PtBS relaxation in the non-entangled, iso-τ_s state is faster, by a factor of 5, compared to that in the PI20/PtBS blends. This difference, also noted earlier in the Figure 5-8,[3] suggests that the PtBS relaxation is retarded by the moderately entangling PI20 chains. (The PI20 chain penetrates into/stitches neighboring PtBS chains to constrain the motion of these PtBS chains that are not entangled among themselves.[3])

In Figure 6-7, the solid curves indicate the reference G^* data in the non-entangled, iso-τ_s state that were shifted to lower ω to match the low-ω tails of the $G^{bld}_{PtBS}{}'$ data for the PI/PtBS blends. The solid curves in Figure 6-8 show the reference $G(t)$ data shifted to match long-t tails of the $G^{bld}_{PtBS}(t)$. These curves agree well with the $G^{bld}_{PtBS}{}^*$ and $G^{bld}_{PtBS}(t)$ data in the range of ω examined where $G^{bld}_{PtBS}{}' \cong G_B' < G_N$ and the concept of entanglement relaxation is valid. This agreement suggests that the PtBS chains in those blends exhibit the retarded Rouse/Zimm-like relaxation attributable to a *pseudo-constraint release* (pseudo-CR) mechanism discussed in Chapter 5.[3] Namely, the PtBS chains moderately entangled with (or stitched by) the PI20 chains relax on the global motion of the PI20 chain.

In relation to the above pseudo-CR mechanism of the PtBS chains in the PI20/PtBS42 and PI20/PtBS70 blends, it should be remembered that the PI20 chain fully relaxed immediately after its Rouse-equilibration within the entanglement length a, as evidenced from the close coincidence of ω_x ($\cong\omega_\varepsilon$) and ω_a explained earlier for Figure 6-1. Since this full relaxation of PI20 at the frequency $\omega_x \cong \omega_a$ activates the Rouse/Zimm-type pseudo-CR process for the PtBS chain, this process occurs smoothly after the Rouse equilibration of the PtBS chain at ω_a without a time lag.

This lack of the time lag results in a monotonic change of the ω dependence of the G^* data of the blend, without a hump in the G'' curve explained earlier, from the Rouse-equilibration regime to the pseudo-CR regime.

6-3-5 Relaxation mechanism of PtBS in blends with $\tau_G \sim \tau_\varepsilon$

The PtBS modulus $G^{bld}_{PtBS}*$ can not be evaluated accurately for the PI99/PtBS42 blend because the PI99 chain significantly contributes to the terminal viscoelastic relaxation of this blend in particular at high T, as explained earlier. Thus, the thermo-rheological behavior of the PtBS42 chain cannot be experimentally examined for this blend. Nevertheless, at low T (20°C) where the Rouse-equilibration frequency ω_a was experimentally determined (cf. thin arrow in Figure 6-3), the G^* data of the blend as a whole can be examined to test the relaxation mechanism of the PtBS42 chain, as discussed below.

In the PI99/PtBS42 blend, the PtBS42 chains are not entangled among themselves (cf. eq 6-5) but with the PI99 chains (cf. eq 6-1). The PI99 chains at 20°C exhibit the entanglement relaxation considerably slower than the Rouse-equilibration, as evidenced in Figure 6-3 where ω_ε ($\cong \omega_x$) was significantly lower than ω_a. Consequently, the PtBS42 chains in the blend appear to first relax partly through the Rouse-equilibration within the entanglement segment (together with the PI99 chains) and then completely through the pseudo-CR mechanism activated by the global motion of the PI99 chains. Differing from the situation in the low-M_{PI} blends (having $\omega_\varepsilon \cong \omega_a$), the PI99/PtBS42 blend has $\omega_\varepsilon << \omega_a$ and thus the pseudo-CR process therein should have occurred well after the Rouse-equilibration.

On the basis of the above molecular picture, the modulus of the PI99/PtBS42 is expected to be described by a model proposed earlier in Chapter 4 for entangled PI/PtBS blends (cf. eqs 4-15 to 4-17),[27] $G_B*(\omega) = G^{bld}_{PI}*(\omega) + G^{bld}_{PtBS}*(\omega)$. The PI and PtBS moduli, $G^{bld}_{PI}*(\omega)$ and $G^{bld}_{PtBS}*(\omega)$, included in the model can be written as:

$$G^{bld}_{PI}*(\omega) = \frac{C_{PI}RT}{M^{PI}_e}\sum_{p=1}^{N_R}\frac{i\omega\tau_a / r_p^2}{1+i\omega\tau_a / r_p^2} + \phi_{PI}I_{PI}G^{bulk}_{PI}*(\omega\lambda_{PI}Q^{2.33}) \quad (6\text{-}7a)$$

$$\text{with} \quad r_p = \sin\left\{\frac{p\pi}{2(N_R+1)}\right\}\sin^{-1}\left\{\frac{\pi}{2(N_R+1)}\right\} \quad (6\text{-}7b)$$

and

$$G^{\mathrm{bld}}_{\mathrm{PtBS}}{}^{*}(\omega) = \frac{C_{\mathrm{PtBS}}RT}{M^{\mathrm{PtBS}}_{\mathrm{e}}} \sum_{p=1}^{N_{\mathrm{R}}} \frac{i\omega\tau_a / r_p^2}{1 + i\omega\tau_a / r_p^2} + \frac{C_{\mathrm{PtBS}}RT}{M_{\mathrm{PtBS}}} \sum_{p=1}^{N_{\mathrm{CR}}-1} \frac{i\omega\tau_{\mathrm{CR}} / q_p^2}{1 + i\omega\tau_{\mathrm{CR}} / q_p^2} \tag{6-8a}$$

$$\text{with} \quad q_p = \sin\left\{\frac{p\pi}{2N_{\mathrm{CR}}}\right\} \sin^{-1}\left\{\frac{\pi}{2N_{\mathrm{CR}}}\right\} \tag{6-8b}$$

In eq 6-7a, the first summation term, dominating $G^{\mathrm{bld}}_{\mathrm{PI}}{}^{*}(\omega)$ at $\omega > \omega_a$, indicates the modulus for the Rouse-equilibration process having the mode relaxation time ratio r_p (eq 6-7b) and the slowest mode relaxation time τ_a (= $1/\omega_a$; determined in Figure 6-3). The number of the Rouse segments per entanglement segment N_{R} is evaluated from $M^{\mathrm{PI}}_{\mathrm{e}}$ (= 5.7×10^3 in the blend; cf. eq 6-1) and the molecular weight of the Kuhn segment of PI, $M^{\mathrm{PI}}_{\mathrm{Kuhn}}$ (= 130),[5] as $N_{\mathrm{R}} = M^{\mathrm{PI}}_{\mathrm{e}} / M^{\mathrm{PI}}_{\mathrm{Kuhn}} = 43$. The second, $\phi_{\mathrm{PI}} I_{\mathrm{PI}} G^{\mathrm{bulk}}_{\mathrm{PI}}{}^{*}(\omega\lambda_{\mathrm{PI}}Q^{2.33})$ term is identical to the modulus $G^{\mathrm{bld}}_{\mathrm{PI,e}}{}^{*}(\omega)$ for the entanglement relaxation of PI99 that has been evaluated earlier and shown in Figure 6-3 with the solid curves.

As for the PtBS modulus, the first summation term in eq 6-8a represents the Rouse-equilibration process common for PtBS42 and PI99 chains. The second summation term indicates the modulus for the pseudo-CR process that is modeled as the usual Rouse-type CR process[13] for N_{CR} entanglement segments per PtBS42 chain ($N_{\mathrm{CR}} = M_{\mathrm{PtBS}} / M^{\mathrm{PtBS}}_{\mathrm{e}} = 4$). The mode relaxation time ratio for this process, q_p, is described by eq 6-8b. Within the context of the Graessley model,[13] the terminal CR time, τ_{CR}, is related to the terminal viscoelastic relaxation time $\tau^{\mathrm{PI}}_{\mathrm{G}}$ of the PI99 chain that activates the CR process as (cf. Appendix 4-1):

$$\tau_{\mathrm{CR}} / q^2_{N_{\mathrm{CR}}-1} = \Lambda(z)\,\tau^{\mathrm{PI}}_{G} \quad \text{with} \quad \Lambda(z) = \frac{1}{z}\left(\frac{\pi^2}{12}\right)^z \tag{6-9}$$

The $q_{N_{\mathrm{CR}}-1}$ factor is given by eq 6-8b with $p = N_{\mathrm{CR}}-1$, $\tau^{\mathrm{PI}}_{\mathrm{G}}$ is evaluated for the $G^{\mathrm{bld}}_{\mathrm{PI,e}}{}^{*}(\omega)$ curve shown in Figure 6-3, and z is the local jump gate number typically in a range of z = 2-4.[13]

The model explained above is essentially identical to the model (eqs 4-15 to 4-17) developed for the high-M PI/PtBS blends in Chapter 4 in which the PI chains relaxed much faster than the PtBS chains (to have $\tau^{\mathrm{PI}}_{\mathrm{G}} = \tau^{\mathrm{PI}}_{\varepsilon}$) and the PtBS chains are entangled with the PI chains as well as among themselves. In contrast, in the PI99/PtBS42 blends examined in this chapter, the PI99 relaxation is just moderately faster than the PtBS42 relaxation (compare ω_{x} and ω_{G} at 20°C shown in Figure 6-3) and the PtBS42 chains are not entangled among themselves. Because of these differences, eqs 4-15 and 4-17 have been modified to eqs 6-7 to 6-9 by utilizing $\tau^{\mathrm{PI}}_{\mathrm{G}} \cong \tau^{\mathrm{PI}}_{\varepsilon}/2$ in eq 6-9 (instead of $\tau^{\mathrm{PI}}_{\mathrm{G}} = \tau^{\mathrm{PI}}_{\varepsilon}$ in eqs 4-15 and 4-17 for the high-M PI/PtBS blends where CR/DTD is

suppressed) and eliminating the PtBS-PtBS entanglement plateau in eq 4-16 (since the PtBS chains are not mutually entangled in the PI99/PtBS42 blend).

The values of model parameters appearing in eqs 6-7 to 6-9 are summarized in Table 6-2. The parameters, except the local jump gate number z, were known and/or evaluated from experimental data, as shown in the footnote of Table 6-2. Chapter 4 suggested that the data of several high-M PI/PtBS blends were well described by the model with z = 2 (a value in the typical range of z). Thus, the same value, z = 2, is utilized here to calculate $G_{\rm B}^*(\omega) = G_{\rm PI}^{\rm bld}*(\omega) + G_{\rm PtBS}^{\rm bld}*(\omega)$ from eqs 6-7 to 6-9. In Figure 6-10, the calculated and measured $G_{\rm B}^*$ are shown with the solid curves and symbols, respectively. Although the model does not reproduce the weak and slow relaxation reflected in the $G_{\rm B}'$ data at low ω, it well describes the dominant part of the $G_{\rm B}^*(\omega)$ data including the hump of $G_{\rm B}''$ at ω = 0.3-0.03 s^{-1} explained earlier for Figure 6-3. This result lends support to the molecular picture underlying the model, the cooperative Rouse-equilibration of the PI and PtBS chains followed by the considerably slower entanglement relaxation of PI and the pseudo-CR relaxation of PtBS activated by this PI relaxation.

Finally, it sounds appealing to apply the same model also to the low-$M_{\rm PI}$ PI20/PtBS blends at 20°C. The local CR process incorporated in the model can occur only after the entanglement segment is equilibrated (as discussed in Chapter 4). In the high-$M_{\rm PI}$ blend, Rouse-equilibration time τ_a (= 0.4 s; Table 6-2) is much shorter than $\Lambda(z)\,\tau_G^{\rm PI}$ (= 3.4 s) so that the CR-onset time τ^{**} can be evaluated as $\tau^{**} = \Lambda(z)\,\tau_G^{\rm PI}$ (cf. eq 6-9).[13] In contrast, the low-$M_{\rm PI}$ blends have $\tau_a \cong \tau_\varepsilon^{\rm PI} > \tau_{\rm G}^{\rm PI}$ (cf. Figure 6-1) and their τ^{**} cannot be evaluated in the same way. Thus, the above model needs to be modified for the low-$M_{\rm PI}$ blends. The pseudo-CR process for the PtBS chain in the low-$M_{\rm PI}$ blends occurs smoothly after the Rouse equilibration, as explained earlier. Thus, in the approximate but simplest modification, it is possible to express the PtBS modulus, $G_{\rm PtBS}^{\rm bld}*(\omega)$, in the Rouse form for the relaxation of a whole sequence of N Rouse segments in the PtBS chain ($N = M_{\rm PtBS}/M_{\rm Kuhn}^{\rm PtBS} >> 1$):

$$G_{\rm PtBS}^{\rm bld}*(\omega) = \frac{C_{\rm PtBS}RT}{M_{\rm PtBS}}\sum_{p=1}^{N-1}\frac{i\omega\tau_{\rm CR}/{q_p'}^2}{1+i\omega\tau_{\rm CR}/{q_p'}^2} \tag{6-10a}$$

$$\text{with}\quad q_p' = \sin\left\{\frac{p\pi}{2N}\right\}\sin^{-1}\left\{\frac{\pi}{2N}\right\} \tag{6-10b}$$

The terminal CR time $\tau_{\rm CR}$ in eq 6-10a is treated as an adjustable parameter (instead of z or $\Lambda(z)$ appearing in eq 6-9). The PI modulus, $G_{\rm PI}^{\rm bld}*(\omega)$, is not affected by this modification and given by eq 6-7 with the second term being replaced by $G_{\rm PI,e}^{\rm bld}*(\omega)$ for PI20 shown in the top panel of Figure 6-2(a) with the solid curves.

The parameters included in the modified model explained above are: τ_a, N_R, N (= $N_R N_{CR}$), and τ_{CR}. The first three parameters were determined experimentally in a way explained in the footnote of Table 6-2; τ_a = 0.4 s, N_R = 43, and N = 172. (These values are the same as those for the high-M_{PI} PI99/PtBS42 blend.) τ_{CR} is utilized as the adjustable parameter to calculate $G_B^*(\omega) = G_{PI}^{bld*}(\omega) + G_{PtBS}^{bld*}(\omega)$ for the PI20/PtBS42 blend. As shown in Figure 6-11, the G_B* calculated with τ_{CR} = 20s (solid curves) can mimic the data (symbols) considerably well, although non-trivial deviation (possibly due to the over simplification of the model) is still noted. This result further confirms the validity of the molecular picture, the cooperative Rouse-equilibration of the PI and PtBS chains followed by the entanglement relaxation of PI (occurring simultaneously with the equilibration in the low-M_{PI} PI20/PtBS42 blend) and the pseudo-CR relaxation of PtBS activated by this PI relaxation. Thus, the relaxation behavior of the low-M_{PI} and high-M_{PI} blends can be described/understood on a common basis.

6-4 Concluding Remarks

The viscoelastic and dielectric behavior was examined for the moderately entangled PI/PtBS blends (w_{PI} = 55.7 wt%) in the miscible state to examine the thermo-rheological behavior and the relaxation mechanisms of the component chains therein.

For these blends, the dielectrically detected PI dynamics exhibited the thermo-rheological complexity, in particular in the low-M_{PI} blends. This complexity was attributable to the dynamic frictional heterogeneity quenched by the slow PtBS chains during the time and length scales of the PI relaxation. The PI chains appeared to exhibit the entanglement relaxation affected by this frictional heterogeneity (that was smeared within high-M_{PI} PI chains) as well as the topological constraint from the slow PtBS chains.

For the low-M_{PI} blends, the viscoelastic data in the terminal relaxation regime were dominated by the slow PtBS chains. The PtBS modulus $G_{PtBS}^{bld*}(\omega)$ in those blends at low ω, being indistinguishable from the blend modulus and evaluated with negligible uncertainty, satisfied the time-temperature superposition. This thermo-rheological simplicity was attributed to the fast PI chains that smeared the frictional heterogeneity during the slow terminal relaxation of PtBS. Nevertheless, the PtBS chains showed no ordinary entanglement relaxation associated with the G'

plateau but exhibited Rouse/Zimm-like relaxation that was slower than the relaxation in a non-entangled, iso-τ_s reference state. This retarded Rouse/Zimm-like relaxation of PtBS was attributable to pseudo-constraint release mechanism activated by the global motion of the PI chains entangling with the PtBS chains. A simple model considering this mechanism described the G^* data of the low-M_{PI} and high-M_{PI} blends considerably well.

References

1. Watanabe, H.; Matsumiya, Y.; Takada, J.; Sasaki, H.; Matsushima, Y.; Kuriyama, A.; Inoue, T.; Ahn, K. H.; Yu, W.; Krishnamoorti, R. *Macromolecules* **2007**, 40, 5389-5399.
2. Takada, J.; Sasaki, H.; Matsushima, Y.; Kuriyama, A.; Matsumiya, Y.; Watanabe, H.; Ahn, K. H.; Yu, W. *Nihon Reoroji Gakkaishi (J. Soc. Rheol. Japan)* **2008**, 36, 35-42.
3. Chen, Q.; Matsushima, Y.; Masubuchi, Y.; Watanabe, H.; Inoue, T. *Macromolecules* **2008**, 41, 8694-8711.
4. Yurekli, K.; Krishnamoorti, R. J. *Polym. Sci. Part B: Polym. Phys*. **2004**, 42, 3204-3217.
5. Fetters, L. J.; Lohse, D. J.; Colby, R.H., Chain Dimensions and Entanglement Spacings, in *Physical Properties of Polymers Handbook, 2nd ed.;* Mark, J. E., Ed.; Springer: New York, **2007**; Chapter 25, pp 445-452.
6. Watanabe, H. *Prog. Polym. Sci.* **1999**, 24, 1253-1403.
7. Watanabe, H. *Macromol. Rapid Commun.* **2001**, 22, 127-175.
8. Watanabe, H.; Ishida, S.; Matsumiya, Y.; Inoue, T. *Macromolecules* **2004**, 37, 1937-1951.
9. Watanabe, H.; Ishida, S.; Matsumiya, Y.; Inoue, T. *Macromolecules* **2004**, 37, 6619-6631.
10. Watanabe, H.; Sawada, T.; Matsumiya, Y. *Macromolecules* **2006**, 39, 2553-2561.
11. Watanabe, H.; Matsumiya, Y.; Inoue, T *Macromolecules* **2002**, 35, 2339-2357.
12. Osaki, K.; Inoue, T.; Uematsu, T.; Yamashita, Y. J. *Polym. Sci. Part B: Polymer Phys*. **2001**, 39, 1704-1712.
13. Graessley, W.W. *Adv. Polym. Sci.* **1982**, 47, 67-117.

Table 6-1. Characteristics of samples

Code	$10^{-3}M_w$	M_w/M_n	$T^{\infty}_{r,bulk}$/°C
PI3	3.0	1.07	25
PI20	19.1	1.10	30
PI53	53.4	1.03	30
PI99	98.5	1.04	30
PtBS42	41.8	1.04	180
PtBS70	69.5	1.03	180

Table 6-2. Parameters utilized in the model (cf. eqs 6-7 to 6-9).

for PI99/PtBS42 (w_{PI} = 55.7 wt%) at 20°C	
τ_a/s [a]	0.4
τ_G^{PI}/s [b]	10.0
$10^{-3}M_e^{PI}$ [c]	5.7
$10^{-3}M_e^{PtBS}$ [c]	10.5
N_R [d]	43
N_{CR} [e]	4
τ_{CR}/s [f]	23.0
z [g]	2

a: evaluated from G^* data (cf. eq 4-14)

b: estimated from the modulus data for the entanglement relaxation of PI, $G^{bld}_{PI,e}(\omega) = \phi_{PI} I_{PI} G^{bulk}_{PI} * (\omega\lambda_{PI} Q^{2.33})$ shown in Figure 6-3.

c: given by eq 6-1

d: $N_R = M_e^{PI}/M_{Kuhn}^{PI}$

e: $N_{CR} = M_{PtBS}/M_{e,PtBS}$

f: evaluated from τ_G^{PI} and z (cf. eq 6-9)

g: z value utilized in eq 4-17.

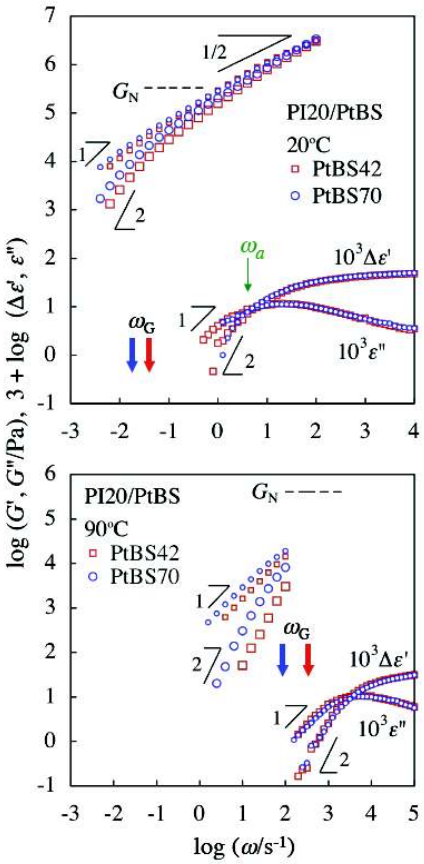

Fig. 6-1: Viscoelastic and dielectric behavior of the PI20/PtBS42 and PI20/PtBS70 blends (w_{PI} = 55.7 wt%) at 20 and 90°C. The horizontal dashed lines indicate the entanglement plateau modulus G_N expected for the blends. The thick arrows in both top and bottom panels indicate the viscoelastic terminal relaxation frequency of the blends, ω_G, and the thin arrow in the top panel, the frequency ω_a for the Rouse equilibration within the entanglement length a.

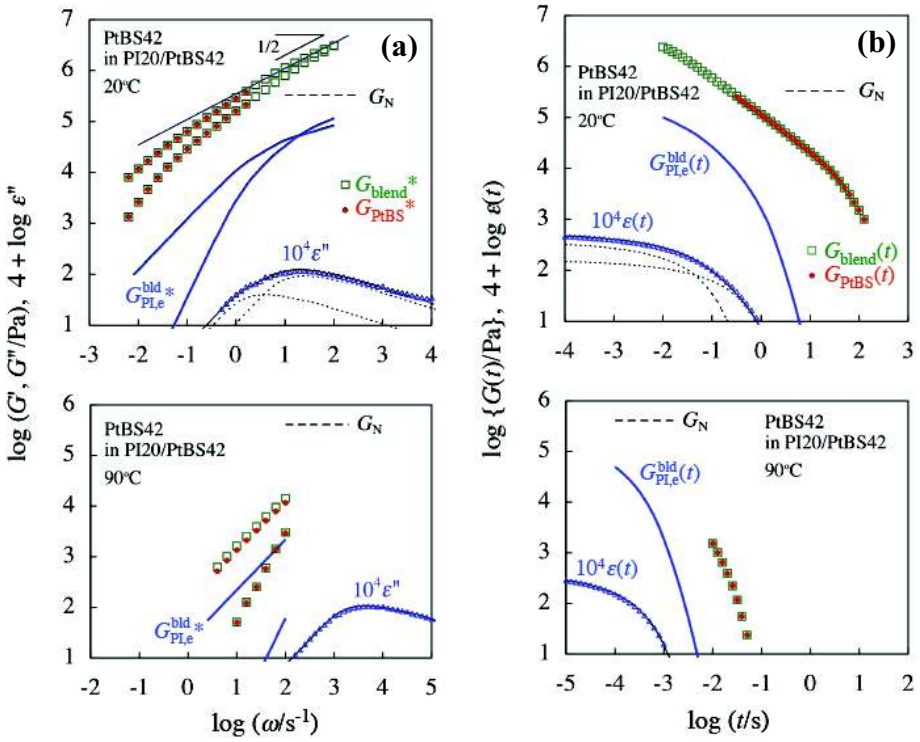

Fig. 6-2: **(a)** Comparison of the G_B* data of the PI20/PtBS42 blend (squares) and the modulus $G^{bld}_{PI,e}$* for the entanglement relaxation of PI20 therein (thick solid curves), the latter being estimated from the G^{bulk}_{PI}* data of bulk PI20 with the aid of the dielectric data (triangles). The horizontal dashed lines indicate the entanglement plateau modulus G_N expected for the blends. The small filled circles indicate $G^{bld}_{PtBS}*(\omega) = G_B*(\omega) - G^{bld}_{PI,e}*(\omega)$ evaluated in the range of ω where the PI and PtBS chains have been Rouse-equilibrated within the entanglement length. **(b)** The relaxation moduli of the blend and PI chains therein, $G_B(t)$, $G^{bld}_{PI,e}(t)$, converted from G_B* and $G^{bld}_{PI,e}$* shown in Figure 6-2(a), and the modulus $G^{bld}_{PtBS}(t) = G_B(t) - G^{bld}_{PI,e}(t)$ estimated for PtBS in the blend.

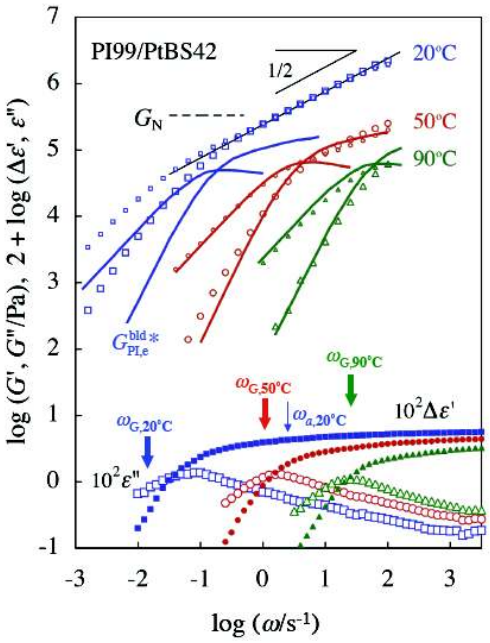

Fig. 6-3: Viscoelastic and dielectric behavior of the PI99/PtBS42 blend (w_{PI} = 55.7 wt%) at 20, 50, and 90°C. The horizontal dashed line indicates the entanglement plateau modulus G_N expected for the blend at 20°C. The thick arrows indicate the viscoelastic terminal relaxation frequency ω_G of the blend at respective T, and the thin arrow, the Rouse-equilibration frequency ω_a at 20°C. Solid curves indicate the modulus $G_{PI,e}^{bld}$ * of PI99 estimated from the G_{PI}^{bulk} * data of bulk PI99 with the aid of the dielectric data of the blend.

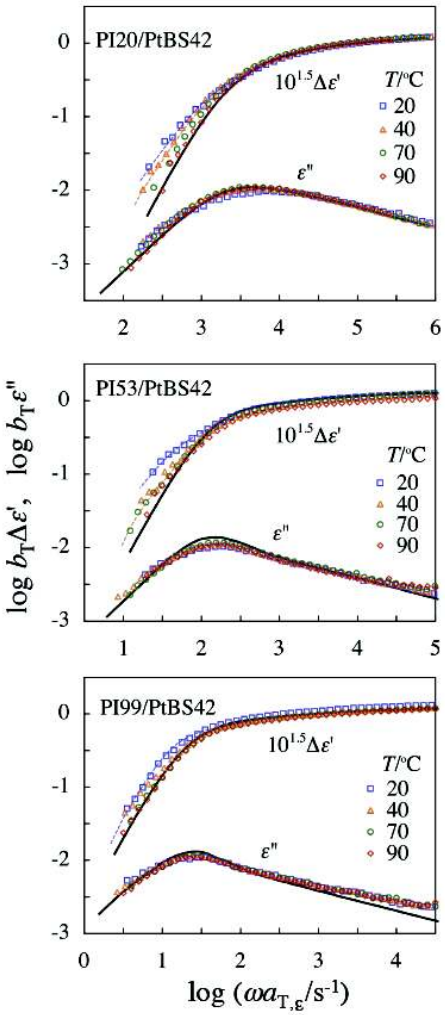

Fig. 6-4: Test of thermo-rheological behavior of PI in PI/PtBS blends as indicated. The reference temperature is chosen to be T_r = 90°C. The dielectric data of the blends (*i.e.*, of the PI chains therein) are shifted along the ω axis to achieve the best superposition at $\omega > \omega_{\varepsilon\text{-peak}}$. The thick solid curves indicate the dielectric data of bulk PI at 90°C multiplied by the PI volume fraction in the blend, ϕ_{PI} = 0.59, and shifted along the ω axis to match the ε''-peak frequency $\omega_{\varepsilon\text{-peak}}$ with the blend data.

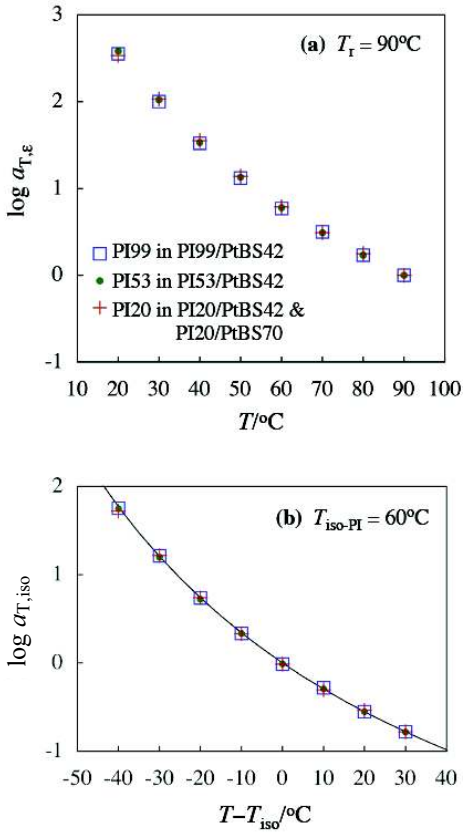

Fig. 6-5: **Top panel**: Shift factor $a_{T,\varepsilon}$ for the dielectric data of PI in the blends as indicated.

Bottom panel: Shift factor $a_{T,iso}$ for the dielectric data of PI defined with respect to the iso-τ_s temperature, T_{iso-PI} = 60°C. The solid curve indicates the WLF equation for bulk PI with $T_{r,bulk}$ = 30°C.

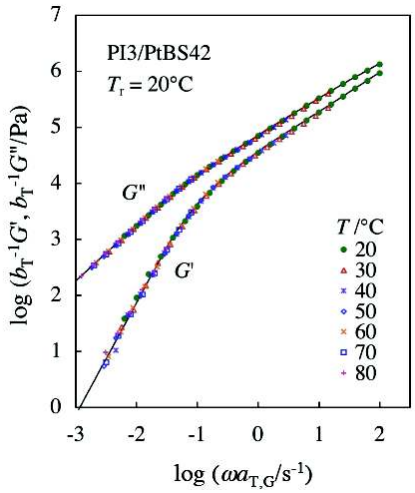

Fig. 6-6: Viscoelastic behavior of PI3/PtBS42 blend (w_{PI} = 55.7 wt%) at T_r = 20°C.

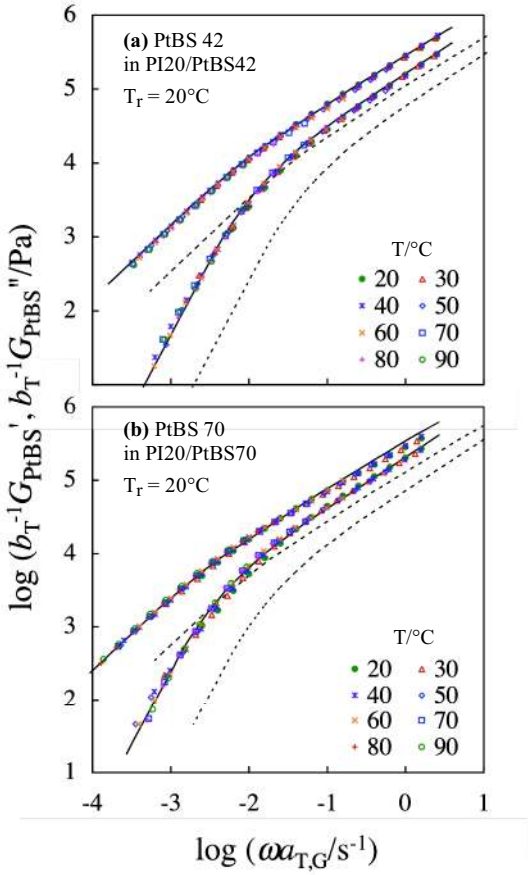

Fig. 6-7: Test of time-temperature superposability for the G_{PtBS}^{bld} * data of the PtBS42 and PtBS70 chains in the blends as indicated. The dotted curves show the modulus of these PtBS chains in the entanglement-free, iso-τ_s reference state. The solid curves indicate this reference behavior of the PtBS chains retarded by the PI chains.

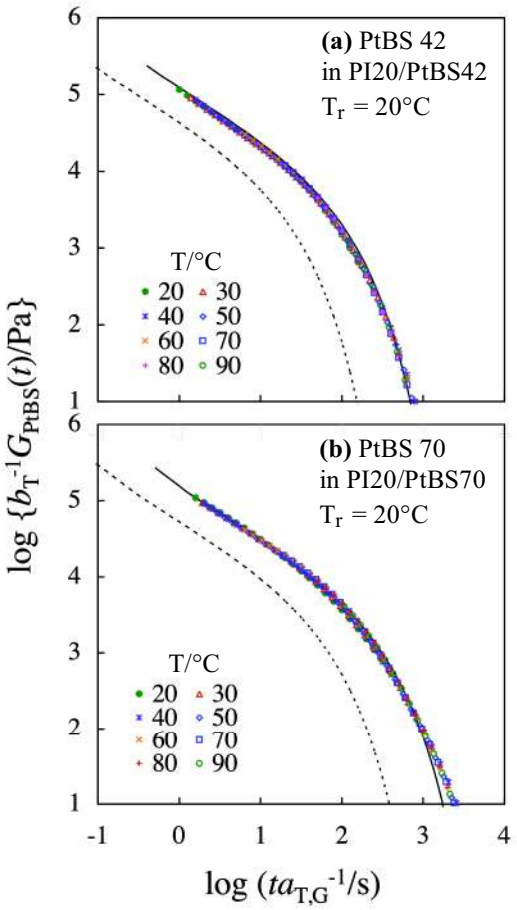

Fig. 6-8: Test of time-temperature superposability for the $G^{bld}_{PtBS}(t)$ data of the PtBS42 and PtBS70 chains in the blends as indicated. The dotted curves show $G^{bld}_{PtBS}(t)$ of these PtBS chains in the entanglement-free, iso-τ_s reference state. The solid curves indicate this reference behavior of the PtBS chains retarded by the PI chains.

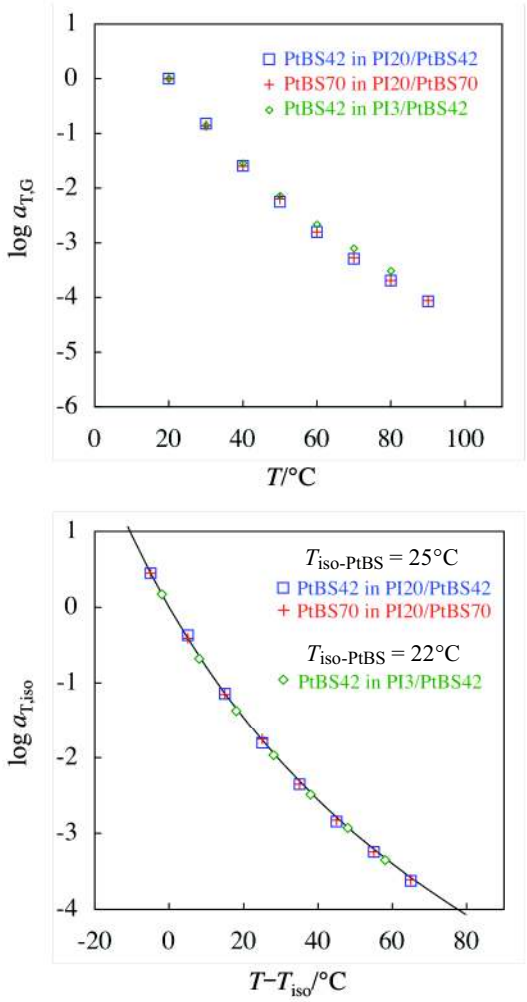

Fig. 6-9: **Top panel**: Shift factor $a_{T,G}$ for the viscoelastic data of PtBS in the blends as indicated.

Bottom panel: Shift factor $a_{T,iso}$ for the viscoelastic data of PtBS defined with respect to the iso-τ_s temperatures as indicated. The solid curve indicates the WLF equation for bulk PtBS with $T_{r,bulk}$ = 180°C.

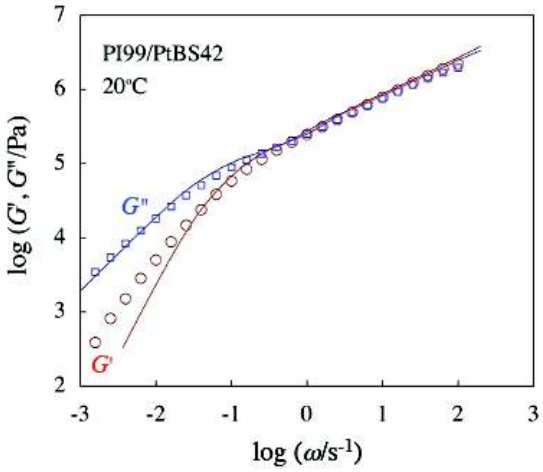

Fig. 6-10: Comparison of the G^* data of the PI99/PtBS42 blend at 20°C (symbols) with the model prediction (curves; eqs 6-7 to 6-9).

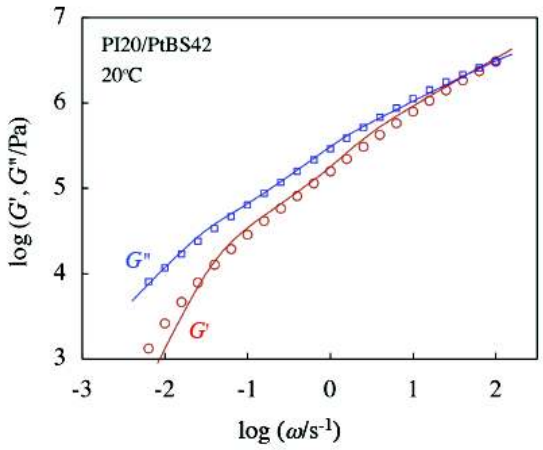

Fig. 6-11 Comparison of the G^* data of the PI20/PtBS42 blend at 20°C (symbols) with the model prediction (curves; eqs 6-7 and 6-10).

Chapter 7 DYNAMIC BEHAVIOR OF A PI-PTBS DIBLOCK COPOLYMER

7-1 Introduction

The molecular picture of miscible polymer blends[1-7] can be extended to disordered diblock copolymers by considering an effect(s) of the block junction.[8-15] Miscible blends of *cis*-polyisoprene (PI) and poly(vinyl ethylene) (PVE) and miscible PI-PVE copolymers exhibit similar segmental dynamics (cf. Figure 1-3) but quite different global dynamics: For the PI/PVE blends, the self-concentration usually leads to different temperature dependence of the global relaxation times of PI and PVE and accordingly to the thermo-rheological complexity for the terminal relaxation of the blend as a whole.[1,3,9,13,16-19] In contrast, the time-temperature superposition *approximately* works for the viscoelastic modulus G^* of the PI-PVE copolymers in the terminal regime,[8,9,12] leading to a qualitative interpretation that the block junction forces the PI and PVE blocks to relax cooperatively. Nevertheless, the time-temperature shift factor for G^* of the PI-PVE copolymer does not superpose the rheo-optical data.[8] Furthermore, the dielectric loss ε'' at low frequencies, exclusively detecting the global motion of the PI block, cannot be superposed with the shift factor determined for G^*.[9] Thus, rigorously speaking, the PI-PVE copolymers exhibit the thermo-rheological complexity. However, this complexity is rather weak thereby allowing G^* of the copolymer to be superposed approximately.

In relation to this point, distinct thermo-rheological complexity is expected to prevail even for the diblock copolymer *if* the temperature dependence of the local mobility is significantly different for the constituent blocks. This difference would allow one block (exhibiting the stronger dependence) to relax much more slowly compared to the other block at low T. Then, the slow block would effectively behave as an immobilized anchor for the fast block thereby forcing the latter to relax as a tethered chain. In contrast, at high T, the relaxation rate should become rather similar for the two blocks thereby forcing them to relax cooperatively and behave as a free (non-tethered) linear chain as a whole. Thus, the large difference of the temperature dependence of the block mobilities would result in a crossover between these types of relaxation (*crossover of the motional modes*), which should be observed as the thermo-rheological complexity not only for terminal relaxation of the copolymer chain as a whole but also for the relaxation of respective blocks.

PI and poly(*p-tert*-butyl styrene) (PtBS) having much larger T_g contrast than a pair of PI and PVE ($T_{g,PI}^{bulk} \cong -70°C$, $T_{g,PtBS}^{bulk} \cong 150°C$, $T_{g,PVE}^{bulk} \cong 0°C$) may serve as a good candicate for the blocks

utilized for a test of this molecular picture.[20-22] For the corresponding model material, the PI-PtBS copolymer, the global relaxation of the blocks should be affected by not only the PI-PtBS junction but also the frictional heterogeneity discussed in Chapters 5 and 6. Thus, it is necessary to separate these effects and focus on the junction effect. The PI/PtBS blend having the same composition and component molecular weights as the PI-PtBS copolymer serves as a reference system for specifying the frictional heterogeneity for the PI blocks: The concentration fluctuation giving this heterogeneity should be less significant for the copolymer than for the blend[24] so that the thermo-rheological complexity seen for the reference blend can be regarded as the upper bound complexity for the copolymer due to the fluctuation.

Following the above strategy, this chapter examines the viscoelastic, dielectric, and thermal behavior of a PI-PtBS diblock copolymer and its PI/PtBS reference blend. Experiments indicated that the dielectrically detected global relaxation of the PI block exhibited the thermo-rheological complexity due mainly to the junction effect, *i.e.*, the crossover of the motional modes for the PI block with T explained earlier. The viscoelastic data of the copolymer exhibited the complexity weaker than that for the PI block. Details of these results are presented/discussed below.

7-2 Experimental

7-2-1 Materials

A *cis*-polyisorene-poly(*p-tert*-butyl styrene) (PI53-PtBS42) diblock copolymer and a PI homopolymer sample (PI53) were anionically synthesized with *sec*-butyllithium (initiator) in benzene at 35°C. The methods of synthesizing and characterizing these samples were explained in Section 2-1. The characteristics of all these samples are summarized in Table 7-1, with the sample code number representing the molecular weight in unit of 1000. (The amounts of the monomer and initiator utilized for the synthesis were carefully adjusted to match the molecular weights of the PI53 homopolymer ($M_{PI} = 53.4 \times 10^3$) and the PI53 block.)

The microstructure determined from ^{1}H-NMR (Varian MERCURYplus AS400) were the same for the PI53 sample and the PI53 block of the copolymer, 1,4-*cis* : 1,4-*trans* : 3,4 = 78:14:8. This microstructure allowed the PI53 chain/block to be miscible with the PtBS42 chain/block in a wide range of T (≤250°C).

The materials subjected to thermal, viscoelastic, and dielectric measurements were the PI53-PtBS42 copolymer and a blend of PtBS42 (precursor of the PI53-PtBS42 copolymer sample) with PI53. The PI content in the blend was set identical to that of the copolymer, w_{PI} = 55.7 wt%. The PI53/PtBS42 blend, utilized as the reference material for the copolymer, was prepared according to the precipitation method explained in Section 2-1.[20,21]

7-2-2 Measurements

Linear viscoelastic, dielectric, and thermal (differential scanning calorimetry; DSC) measurements were conducted for the PI53-PtBS42 diblock copolymer as well as the PI53/PtBS42 reference blend, both having the PI content of w_{PI} = 55.7 wt%. The measurements were also conducted for the components of the blends, PI53 and PtBS42, in respective bulk states. The viscoelastic and dielectric data of these bulk components were shown in Chapter 3.

The linear viscoelastic and dielectric measurements were conducted at temperatures $20 \leq T/°C \leq 120$. For thermal measurements, the DSC traces were recorded for respective specimens (10~15 mg for each) at a heating rate of 10°C/min in a range of T between −120 and 250°C. The principles and operations of the measurements were explained in Section 2-2.

7-3 Results

7-3-1 Overview of dynamic behavior of PI-PtBS copolymer and PI/PtBS blend

Figure 7-1 shows the DSC traces measured for the PI53-PtBS42 copolymer and the PI53/PtBS42 reference blend having the same M_{PI}, M_{PtBS}, and w_{PI} (= 55.7 wt%; volume fraction ϕ_{PI} = 0.59 as evaluated on the basis of an assumption of volume additivity). For comparison, the profiles are shown also for the PI53 and PtBS42 bulk homopolymers. The horizontal dashed lines indicate the high-T baselines. The thin arrows indicate the glass transition temperatures $T_{g,PI}^{bulk}$ (= −65 °C) and $T_{g,PtBS}^{bulk}$ (= 147 °C) for bulk PI53 and PtBS42. The thick arrows denote the effective $T_{g,PI}^{eff}$ and $T_{g,PtBS}^{eff}$ of the PI and PtBS components in the blends estimated from the WLF analysis[28] of the time-temperature shift factors. The method of this analysis was explained in Appendix 3-1.[22]

The WLF analysis was made for the global (rubbery) relaxation process of PI and PtBS so that the resulting T_g^{eff} is related to the relaxation of the smallest motional unit of this process, *i.e.*, the Rouse segment, not the monomeric segment.[23]

Figure 7-1 clearly indicates that the PI53-PtBS42 copolymer and the PI53/PtBS42 reference blend exhibit similarly broad, almost two-step glass transitions. This broad transition reflects a broad distribution of local frictional environment for the monomeric segments due to the dynamic heterogeneity, as noted for a variety of miscible blends and disordered diblock copolymers.[1-9,12,22] The similarity of the glass transition behavior of the copolymer and blend demonstrates a similarity of the segmental dynamics therein. This similarity has been noted also for PI-PVE copolymers and PI/PVE blends (cf. Figure 1-3).[8,9,12]

Figure 7-2 shows the angular frequency (ω) dependence of the viscoelastic and dielectric data for the PI53-PtBS42 copolymer and the PI53/PtBS42 reference blend. The raw data of the dielectric loss, $\varepsilon''(\omega)$, in a range of ω where the direct current (dc) condution has negligible contribution (as explained in Chapter 5), and the decrease of the dynamic dielectric constant $\varepsilon'(\omega)$ from its static value $\varepsilon'(0)$, $\Delta\varepsilon'(\omega) = \varepsilon'(0) - \varepsilon'(\omega)$, are multiplied by a factor of 10^3 and compared with the data of storage and loss moduli, $G'(\omega)$ and $G''(\omega)$. For clarity of the plots, the ε'', G', and G'' data are shown only for representative T, and the $\Delta\varepsilon'$ data, only for the highest T.

In Figure 7-2, the copolymer and the blends (almost) exhibit the terminal viscoelastic and dielectric relaxation characterized with the power-law tails of the G' ($\propto \omega^2$), G'' ($\propto \omega$), $\Delta\varepsilon'$ ($\propto \omega^2$), and ε'' ($\propto \omega$) at low ω. The second-moment average (terminal) viscoelastic and dielectric relaxation times,[29] τ_G and τ_ε, were evaluated as: $\tau_G = [G'(\omega)/\omega G''(\omega)]_{\omega\to 0}$ and $\tau_\varepsilon = [\Delta\varepsilon'(\omega)/\omega\varepsilon''(\omega)]_{\omega\to 0}$ (cf. eqs 2-26 and 2-31).[29]

The dielectric relaxation of the copolymer and blends seen in Figure 7-2 is exclusively attributable to the global motion of the PI component therein, either the PI block or homo-PI chain. (The segmental relaxation of PI and PtBS occurs at high ω not covered in the experimental window.[30]) In contrast, the viscoelastic relaxation detects the global motion of the copolymer chain as a whole and/or all component chains in the blends. Thus, comparison of τ_ε and τ_G provides a clue for examining if PI dominates the terminal relaxation of the copolymer/blends. This comparison is made in Figure 7-3 where the τ_G and τ_ε data (filled circles and unfilled squares) of the copolymer and the blend are plotted against T.

In the PI53/PtBS42 blend, the PI and PtBS chains are not chemically connected and can relax at different times. Thus, the comparison of τ_G and τ_ε enables an assignment of the slow component. This comparison is made for τ's evaluated from different quantities (G^* and ε^*) of rather well entangled PI53 chains (having $M_{PI} \cong 10\, M_e^{\text{bulk PI}}$)[31] Thus, the behavior of entangled binary blends of linear PI is helpful for assigning the fast and slow components in the PI53/PtBS42 blend. Extensive experiments for the PI/PI blends[25-27,29,32] revealed that the viscoelastic $\tau_{G,slow}$ and dielectric $\tau_{\varepsilon,slow}$ defined for the slow component satisfy a relationship, $\tau_{G,slow}/\tau_{\varepsilon,slow} \cong 1/2$ (which reflects a considerable contribution of the constraint release/tube dilation relaxation[25,26]), and these $\tau_{G,slow}$ and $\tau_{\varepsilon,slow}$ data are close to the τ_G and τ_ε data of the blends as a whole. This relationship also holds for monodisperse linear PI systems in which all chains have the same relaxation time.[27,32] In contrast, $1/2 < \tau_{G,slow}/\tau_{\varepsilon,slow}$ (≤ 1) for the fast component in the PI/PI blends.[25,26] This behavior of PI/PI blends suggests that the terminal relaxation of PI in the PI/PtBS blend is slower or equally slow compared to the PtBS relaxation if $\tau_G/\tau_\varepsilon \cong 1/2$, while the PI relaxation is considerably faster than the PtBS relaxation if the τ_G/τ_ε ratio is well above 1/2, in particular in a case of $\tau_G/\tau_\varepsilon > 1$. (PtBS has no type-A dipole and thus the τ_G/τ_ε ratio for the PI/PtBS blend can be much larger than unity if PtBS relaxes much slower than PI.)

As seen in the bottom panel of Figure 7-3, the τ_G/τ_ε ratio for the PI53/PtBS42 blend is larger than unity and thus the PI relaxation is significantly faster than the PtBS relaxation at low $T \leq 50$°C. This ratio decreases to $\cong 1/2$ and thus the PI relaxation becomes comparable to (or slower than) the PtBS relaxation at higher T. This crossover reflects a difference in the temperature dependence of the local friction of the PI and PtBS chains.[21,22]

For the PI-PtBS copolymer, the τ_G/τ_ε ratio is close to unity even at the lowest T, 20°C, and decreases gradually to $\tau_G/\tau_\varepsilon \cong 1/2$ with increasing T. This behavior is qualitatively similar to but quantitatively different from the behavior of the PI53/PtBS42 blend (cf. bottom panel). This difference should reflect the connectivity between PI and PtBS blocks: The connectivity does not allow these block to relax in a *completely independent* way to have significantly different τ, although approximate independence can be realized at low T, as discussed later. For this reason, the temperature dependence becomes rather similar for τ_ε and τ_G of the copolymer, the former exclusively detecting the PI block relaxation while the latter representing the relaxation of the copolymer chain, *i.e.*, the connected sequence of the PI and PtBS blocks.

7-3-2 Thermo-rheological behavior of PI block

Figure 7-4 examines the thermo-rheological behavior (time-temperature superposability) for the $\Delta\varepsilon'$ and ε'' data of the copolymer and the blend, *i.e.*, of the PI53 block and PI53 chain therein. The reference temperature was chosen to be T_r = 363 K (= 90°C), and the data at the other temperatures were multiplied by an intensity correction factor, $b_T = T/T_r$ with T and T_r in K unit, and shifted along the ω axis by a factor $a_{T,\varepsilon}$. The thick solid curves in the bottom panel indicate the dielectric data of bulk PI53 at its $T_{r,bulk}$ = 303 K (= 30°C) multiplied by the intensity correction factor $b_T^o = T_{r,bulk}/T_r$ and the PI volume fraction in the blend $\phi_{PI} = 0.59$. The data of bulk PI53 thus reduced, $\phi_{PI} b_T^o \Delta\varepsilon_{PI}^{bulk\,\prime}(\omega/\Lambda_{PI})$ and $\phi_{PI} b_T^o \varepsilon_{PI}^{bulk\,\prime\prime}(\omega/\Lambda_{PI})$, are plotted against frequency ω, with the frequency reduction factor Λ_{PI} being chosen to match the ε''-peak frequencies $\omega_{\varepsilon\text{-peak}}$ for the PI chains in the blend and that in bulk.

The shift factor $a_{T,\varepsilon}$ for the plots in Figure 7-4 was chosen in a way that the $\Delta\varepsilon'$ and ε'' data were best superposed at $\omega > \omega_{\varepsilon\text{-peak}}$. This factor is plotted against T in Figure 7-5. The $a_{T,\varepsilon}$ data are almost indistinguishable for the copolymer and the blend, confirming the similarity of the friction of the Rouse segment (the motional unit for the global relaxation) for the PI block in the copolymer and PI chain in the blend.

For the copolymer as well as the blend, Figure 7-4 clearly indicates that the slow dielectric mode distribution broadens with decreasing T and the superposition fails for the dielectric data at low $\omega < \omega_{\varepsilon\text{-peak}}$. The broadening is more clearly noted for $\Delta\varepsilon'$ than for ε'' because slow modes are more sensitively reflected in $\Delta\varepsilon'$ than in ε''.[33] The molecular origin of this broadening is not exactly the same for the copolymer and blends, as discussed below.

As explained earlier in Chapter 5, the conditions necessary for the mode broadening and thermo-rheological complexity of the PI relaxation in a PI/PtBS blend to be observed are:[21,22] (1) the PtBS chains are not deeply overlapping with each other, (2) the average end-to-end distance R_{PI} of the PI chain is not much larger than the correlation length of concentration flucutation ($\sim R_{PtBS}$ of the low-M_{PtBS} PtBS chain), and (3) the terminal relaxation is much faster for the PI chain than for the PtBS chain. If the conditions (1) and (2) are satisfied, all PI chains cannot overlap with the PtBS chains to the same extent and thus a PI chain in a PtBS-rich region feels a larger friction compared

to the other PI chains out of this region. The resulting frictional distribution among the PI chains survives in the time scale of the global PI relaxation if the condition (3) is satisfied. This frictional heterogeneity naturally results in the mode broadening for the whole ensemble of the PI chains.[21,22] This molecular picture explains why the broadening seen for the PI53/PtBS42 blend ($C_{PtBS} \cong 3C_{PtBS}^*$)[34] is less significant than that for the the low-M blends ($C_{PtBS} \cong 2C_{PtBS}^*$) shown in Chapter 5 while more significant than that for the PI99/PtBS42 blend in Chapter 6.[22]

Now, the thermo-rheological behavior of the PI53-PtBS42 copolymer is examined; cf. top panel of Figure 7-4. Although the global dynamics of disordered copolymers is generally affected by the concentration fluctuation that results in the frictional heterogeneity,[35] the fluctuation should be weaker[24] and the corresponding thermo-rheological complexity should less significant for the copolymer than for the reference blend having the same composition and component molecular weights. Nevertheless, the broadening of dielectric data is more significant for the PI53-PtBS42 copolymer than for the PI53/PtBS42 blend. This observation cannot be explained from the molecular scenario explained above, because the conditions (1) and (2) are equally satisfied for these copolymer and blend while the condition (3) should be less valid for the copolymer exhibiting rather similar relaxation times of the PI block (τ_ε) and the copolymer as a whole (τ_G); cf. top panel of Figure 7-3. Thus, the strong dielectric broadening seen for the PI block should be mainly attributed to a crossover of the motional mode of the PI block with T due to the block connectivity. This crossover is further discussed below.

7-4 Discussion

7-4-1 Crossover of motional mode of PI block with T

For a linear diblock copolymer in the disordered state, the motion of one block (say PI block) is strongly affected by the other block (PtBS block) due to the block connectivity.[36-38] Strictly speaking, this effect of connectivity is to be represented as an internal boundary condition for the equation of motion for the copolymer chain, and the motion of the two blocks is described in terms of the eigenmodes associating this equation and thus correlated to each other. Specifically, the eigenmode relaxation times are the same but the eigenmode intensities can be different for the two blocks, as noted for homopolymer chains.[39-41] In this sense, it is impossible to define the “fast” and

"slow" blocks for the copolymer if just the eigenmode relaxation times are considered. However, if the eigenmode intensities are also considered, it is still possible to define the fast and slow blocks as those having small and large intensities for the slowest eigenmode. (This fact can be easily noted from a simple example for a linear homopolymer:[40] The chain end and the chain center always have the same slowest eigenmode relaxation time but the intensity of this eigenmode vanishes for the chain end. For this reason, the chain end relaxes much faster than the chain center.)

Since the effective T_g^{eff} is higher for PtBS42 than for PI53 in the copolymer as well as the blend (cf. Figure 7-1), a decrease of T results in stronger retardation of the PtBS42 relaxation. Thus, at low T, the PtBS42 block behaves as the slow block in the above sense, and the PI block would be effectively anchored by the PtBS42 block to behave as a tethered chain during the dominant part of its relaxation. For this case, it is reasonable to regard the PI block relaxation to be *approximately* independent from the PtBS block relaxation (although the real slowest part of PI relaxation would occur simultaneously with the PtBS relaxation because the PI and PtBS blocks have the same slowest eigenmode relaxation time). In contrast, at high T, the anchoring effect of PtBS should become weaker and finally vanish because of the stronger acceleration of the PtBS relaxation with increasing T. For this case, the PI and PtBS blocks would behave as portions of a free (non-tethered), linear chain and relax cooperatively.

This crossover of the motional mode of the PI block, from the tethered chain like behavior at low T to the linear chain like behavior at high T, appears to be the main mechanism of the strong dielectric broadening observed for the PI block. For a test of this molecular picture, the dielectric behavior of the PI block is compared with that of *equivalent* star-branched bulk PI (a model for tethered chain) and/or *equivalent* linear bulk PI. The following sections first specify the equivalent star/linear chains and then make the comparison.

7-4-2 Equivalent bulk PI chain defined for PI block

7-4-2-1 Entanglement length

For specifying the equivalent bulk PI chain for the PI block, the entanglement length a ($\propto M_e^{1/2}$) for the PI block is to be determined first. In Chapter 4, a mixing rule for the

entanglement length based on the concept of the packing length[22,31,42.43] has been proposed and experimentally confirmed (cf. eq 4-4).[30] This blending law gives

$$a = 6.2 \text{ nm } (\cong 1.07\, a_{\mathrm{PI}}^{\mathrm{bulk}}) \text{ for PI/PtBS with } w_{\mathrm{PI}} = 55.7 \text{ wt\%} \tag{7-1}$$

This a is common for all components in the PI/PtBS blend and PI-PtBS copolymer.

The a value given by eq 7-1 is considerably smaller than the $\left\langle R_{\mathrm{PtBS}}^2 \right\rangle^{1/2}$ and $\left\langle R_{\mathrm{PI}}^2 \right\rangle^{1/2}$ for the PtBS42 and PI53 chains (= 12.3 nm and 19.0 nm, as evaluated from $R_{\mathrm{X}}^2=[<R^2>/M]_{\mathrm{X}}M_{\mathrm{X}}$ (X =PI, PtBS) with $[<R^2>/M]_{\mathrm{X}} = 6.79\times10^{-3}$ and $3.61\times10^{-3}\mathrm{nm}^2$ for PI and PtBS, respectively).[31] Thus, the PtBS42 and PI53 chains are mutually constraining the large scale motion (*i.e.*, entangled), despite the PtBS42 molecular weight is close to M_{e} of bulk PtBS (= 37.6×10^3).

7-4-2-2 Relaxation time of Rouse segment

For comparison of the dielectric data for the PI block and the equivalent bulk PI chain, the relaxation time τ_{s} of the Rouse segment, the motional unit during the global relaxation process, needs to be specified.

For this purpose, Chapter 6 examined a set of PI/PtBS blends (including the PI53/PtBS42 blend) that have the same PI content as the PI53-PtBS42 copolymer (w_{PI} = 55.7 wt%).[44] The WLF analysis of the dielectric shift factor indicated that the iso-τ_{s} temperature $T_{\text{iso-PI}}$ is higher, by $\Delta T_{\text{iso-PI}}$ = 30°C, for PI in the PI/PtBS blends (w_{PI} = 55.7 wt%) than for bulk PI (cf. Figure 6-5). Since τ_{s} of the Rouse segment is *locally* determined just by the PI/PtBS composition, the PI53-PtBS42 copolymer and the PI/PtBS blends having the same w_{PI} should have the same τ_{s}. Thus, the iso-τ_{s} state for the Rouse segments of PI is achieved in these copolymer/blends and in bulk PI accordingly to a relationship,

$$\tau_{\mathrm{s}}^{\text{bulk PI}}(T) = \tau_{\mathrm{s}}^{\text{PI in b/c}}(T + \Delta T_{\text{iso-PI}}), \quad \frac{\zeta_{\mathrm{s}}^{\text{bulk PI}}(T)}{T} = \frac{\zeta_{\mathrm{s}}^{\text{PI in b/c}}(T + \Delta T_{\text{iso-PI}})}{T + \Delta T_{\text{iso-PI}}} \tag{7-2}$$

Here, ζ_{s} denotes the friction coefficient of the Rouse segment, the superscript "PI in b/c" stands for PI in the copolymer/blend systems, and $\Delta T_{\text{iso-PI}}$ = 30 K.

An *effective* glass transition temperature of PI53 in the blends, defined for the Rouse segment of PI through the WLF relationship (cf. Section 5-3) is expected to be higher, by $\Delta T_{\text{iso-PI}}$, than $T_{\text{g,PI}}$ (= −65°C) of bulk PI53. This $T_{\text{g,PI}}^{\text{eff}}$ (= −35°C), shown with the thick solid arrows in Figure 7-1, is located at the low-T side of the broad glass transition zone of the blend and copolymer, as expected. (The real glass transition occurs for the monomeric segments, and the real T_g is not necessarily identical to $T_{\text{g,PI}}^{\text{eff}}$ defined for the Rouse segments.[23] Nevertheless, a reasonable agreement is noted in Figure 7-1.)

As explained in Chapters 5 and 6, the dielectric data, detecting exclusively a global motion of PI, enable evaluation of the modulus corresponding to the entanglement relaxation of PI in the blend, $G_{\text{PI,e}}^{\text{bld}}*(\omega)$. From this $G_{\text{PI,e}}^{\text{bld}}*(\omega)$ and the $G_{\text{B}}*(\omega)$ data of the blends, the modulus of PtBS in the blend in a frequency range $G_{\text{B}}' \leq G_{\text{N}}$ (where the PI and PtBS chains have been Rouse-equilibrated within the entanglement segment) can be evaluated as $G_{\text{PtBS}}^{\text{bld}}*(\omega) = G_{\text{B}}*(\omega) - G_{\text{PI,e}}^{\text{bld}}*(\omega)$. In fact, in Chapter 6, $G_{\text{PtBS}}^{\text{bld}}*$ was evaluated for the PI/PtBS blends with w_{PI} = 55.7wt%, and the WLF analysis of the shift factor $a_{\text{T,G}}$ for those $G_{\text{PtBS}}*$ data gave the iso-τ_s temperature for the Rouse segment of PtBS in the blends, $T_{\text{iso-PtBS}}$ = 25°C that corresponds to the reference temperature of bulk PtBS, $T_{\text{r,bulk}}$ = 180°C (cf. Figure 6-9 and Appendix 7-4).[47] Thus, the Rouse segments of PtBS in the blends and copolymer at T are in the iso-τ_s state with respect to the segment in PtBS bulk at $T_{\text{iso-PtBS}}^{\text{bulk}} = T - \Delta T_{\text{iso-PtBS}}$ = T+155°C. The corresponding T_g^{eff} of PtBS, $T_{\text{g,PtBS}}^{\text{eff}} = T_{\text{g,PtBS}}^{\text{bulk}} + \Delta T_{\text{iso-PtBS}}$ = −8°C, is located at the high-T side of the broad glass transition of the blend/copolymer, as shown with the thick dotted arrows in Figure 7-1.

7-4-2-3 Equivalent star PI defined for PI block at low T

The PI block appears to behave as the tethered chain at low T. For this PI block, an *equivalent star PI* is defined as the bulk star PI having the *same* entanglement number N_e per arm ($N_e \propto M_{\text{arm}} / a^2$) as the PI block. The dielectric data is compared for the equivalent star PI and the PI block in the *iso-τ_e condition* where they have the same relaxation time τ_e of the entanglement segment. This choice is reasonable because the entanglement segment is the basic, motional unit for the global relaxation of entangled chains. τ_e is related to τ_s of the Rouse segment (smallest motional unit for the rubbery relaxation) as $\tau_e = \tau_s N_R^2$, where N_R is the number of the Rouse segments per entanglement segment.

From the entanglement length a for the PI block (eq 7-1), the arm molecular weight of the equivalent star PI is specified to be:

$$M_{\rm arm} = \left(\frac{a_{\rm PI}^{\rm bulk}}{a} \right)^2 M_{\rm PI\ block} = 46.0 \times 10^3 \ \text{for equivalent star PI} \qquad (7\text{-}3)$$

The iso-$\tau_{\rm s}$ temperature for this star PI defined with respect to the PI block at a temperature T is the same as that for the PI chains in the PI/PtBS blends ($w_{\rm PI}$ = 55.7 wt%) explained earlier: $T_{\rm iso\text{-}PI}^{\rm bulk} = T - \Delta T_{\rm iso\text{-}PI} = T - 30$ °C (cf. eq 7-2). Since the behavior of the equivalent star PI and the PI block are to be compared in the iso-$\tau_{\rm e}$ state, the dielectric data for the latter at T, $\varepsilon_{\rm PI\ block}^*(\omega;T)$, are not to be directly compared with the data for the former at this iso-$\tau_{\rm s}$ temperature, $\varepsilon_{\rm star}^*(\omega;T_{\rm iso\text{-}PI}^{\rm bulk})$, because of a difference of $N_{\rm R}$ ($\propto a^2$) for the copolymer and bulk PI: A minor shift is needed for the frequency of the equivalent star PI by a factor of $\lambda_a = (N_{\rm R}^{\rm PI\ block} / N_{\rm R}^{\rm star})^2 = (a / a_{\rm PI}^{\rm bulk})^4 = 1.3$ ($a / a_{\rm PI}^{\rm bulk} = 1.07$; cf. eq 7-1), and the shifted $\varepsilon_{\rm star}^*(\lambda\omega;T_{\rm iso\text{-}PI}^{\rm bulk})$ data are to be compared with the $\varepsilon_{\rm PI\ block}^*(\omega;T)$ data.

For the actual comparison, the dielectric (and viscoelastic) data are available in literature[27] for a series of 6-arm bulk star PI samples of various $M_{\rm arm}$. Among these chains, the star PI sample of $M_{\rm arm} = 59.0 \times 10^3$ (coded as PI(59)$_6$) is the closest, in the $M_{\rm arm}$ value, to the equivalent star PI specified above (cf. eq 7-3). Thus, the $\varepsilon_{\rm PI\ block}^*(\omega;T)$ data of the PI block are compared with the $\varepsilon_{\rm PI(59)_6}$ data for PI(59)$_6$ subjected to a correction for this $M_{\rm arm}$ difference (as well as for a as represented by the λ_a factor explained above):

$$\varepsilon_{\rm eqv}^*(\omega;T) \equiv \phi_{\rm PI} b_{\rm T}'' \varepsilon_{\rm PI(59)_6}^*(r_\tau \lambda_a \omega;T_{\rm iso\text{-}PI}^{\rm bulk}) \ \text{with} \ r_\tau = \frac{\tau_\varepsilon^{\rm eqv\text{-}star}}{\tau_\varepsilon^{PI(59)_6}} = 0.11 \qquad (7\text{-}4)$$

Here, the PI volume fraction $\phi_{\rm PI}$ (= 0.59) and the intensity factor $b_{\rm T}'' = T_{\rm iso\text{-}PI}^{\rm bulk} / T$ ($T_{\rm iso\text{-}PI}^{\rm bulk}$ and T in K unit) are multiplied to $\varepsilon_{\rm PI(59)_6}^*$ for correction of a difference of the dielectric intensities of the PI(59)$_6$ sample and the PI block. The $M_{\rm arm}$-correction factor, r_τ, was evaluated from the empirical equation for star PI shown in Appendix 7-1, $\tau_\varepsilon \propto M_{\rm arm}^{1.5} \exp\{1.4 \times 10^{-4} M_{\rm arm}\}$. The result of the comparison of the $\varepsilon_{\rm PI\ block}^*(\omega;T)$ data and $\varepsilon_{\rm eqv}^*(\omega;T)$ is later shown in Figures 7-7 and 7-8.

7-4-2-4 Equivalent linear PI defined for PI-PtBS copolymer at high T

At high T, the PI block appears to behave as a portion of a free linear chain and move cooperatively with the PtBS block. Thus, an *equivalent linear PI* is defined as the bulk PI chain having the same entanglement number N_e as the PI-PtBS copolymer, not just the PI block. Since the entanglement length a (= 6.2 nm; eq 7-1) is common for the PI and PtBS block (as discussed in Chapter 4 in relation to the cooperative Rouse equilibration),[30] N_e is evaluated from the mean square end-to-end distance of the copolymer, $\langle R^2 \rangle = \langle R^2_{PI53} \rangle + \langle R^2_{PtBS42} \rangle$ = 508 nm^2, as $N_e = \langle R^2 \rangle / a^2$ = 13.2. (This $\langle R^2 \rangle$ value was obtained under an assumption of the Gaussian conformation of the copolymer chain.)[31] The corresponding molecular weight of the equivalent linear PI is given by

$$M_{lin} = N_e M_e^{bulk\ PI} = 66.1 \times 10^3 \text{ for equivalent linear PI} \qquad (7\text{-}5)$$

This equivalent linear PI is hereafter referred to as PI66.

Now, a question is naturally asked: What the temperature for this equivalent PI66 should be when compared with the PI block at a given high T (say, 120°C). At low T, the PtBS block motion is essentially frozen in the time scale of the PI block relaxation, allowing a comparison of the data for the PI block and the equivalent star PI in the iso-τ_e state. However, at high T, the PtBS block moves cooperatively with the PI block to give an extra friction for the PI block motion, so that the iso-τ_e state defined just for the PI block/chain cannot be adopted as the state for the reasonable comparison. Thus, it is necessary to define an iso-τ_R^{chain} state where the Rouse relaxation time τ_R^{chain} is the same for the PI-PtBS copolymer and the equivalent linear PI66 chain. A comparison of the data of the PI block and PI66 chain can be made in the iso-τ_R^{chain} state on a sound physical basis. This comparison reduces to the comparison in the iso-τ_e state at low T, because the PI block and the equivalent star PI has the same N_e and the same τ_e thereby having the same τ_R^{chain} ($\propto N_e^2 \tau_e$) in this state.

For the PI block and the equivalent linear PI66, the iso-τ_R^{chain} state is conveniently specified by a frequency shift for the PI66 data at the iso-τ_s temperature at $T_{iso\text{-}PI}^{bulk} = T$–30°C (defined with respect to the data for the PI block at T). In the range of T examined, the friction coefficient of the entanglement segment of the PtBS block, $\zeta_e^{PtBS\ block}$, is larger than $\zeta_e^{PI\ block}$ of the PI block/equivalent PI. Thus, the Stockmayer-Kennedy (SK)[45] model (Appendix 7-3) for a bead-spring block chain,

applicable to disordered and unentangled block copolymers,[46] can be utilized to evaluate a τ_R^{chain} ratio for the PI53-PtBS42 copolymer at T and the equivalent PI66 chain at $T_{iso\text{-}PI}^{bulk}$. If the entanglement segments of the PI and PtBS blocks having the same a is utilized as the beads in the SK model, the viscoelastic τ_R^{chain} of the copolymer is given by[45]

$$\tau_R^{chain} = \frac{a^2 \zeta_e^{PtBS\ block} N_e^2}{6 k_B T} \frac{1}{\beta^2} \quad \text{with} \quad N_e = N_e^{PtBS} + N_e^{PI} \tag{7-6}$$

Here, $N_e^X (= \langle R_X^2 \rangle / a^2)$ is the number of entanglement segments (beads) per X block (X = PtBS, PI), and β is the smallest eigenvalue determined from

$$L^{1/2} \tan \beta\theta = -\tan \frac{\beta(1-\theta)}{L^{1/2}} \tag{7-7a}$$

with

$$L = \frac{\zeta_e^{PtBS\ block}}{\zeta_e^{PI\ block}} \tag{7-7b}$$

and

$$\theta = \frac{N_e^{PtBS}}{N_e} = \frac{\langle R_{PtBS42}^2 \rangle}{\langle R_{PtBS42}^2 \rangle + \langle R_{PI53}^2 \rangle} (= 0.30) \tag{7-7c}$$

The friction coefficient ratio L (eq 7-7b) is straightforwardly evaluated from the viscoelastic data of bulk PI and PtBS, as explained in Appendix 7-2: For example, L = 16.3 for the PI53-PtBS42 copolymer at T = 120°C. From the $L(T)$ value thus obtained and the θ value (eq 7-7c), eq 7-7a can be solved numerically to calculate $\beta(T)$.

The Rouse relaxation time of the equivalent PI66 chain at $T_{iso\text{-}PI}^{bulk}$ is given by $\tau_R^{PI66}(T_{iso\text{-}PI}^{bulk}) = \zeta_e^{bulk\ PI} \{a_{PI}^{bulk}\}^2 N_e^2 / 6\pi^2 k_B T_{iso\text{-}PI}^{bulk}$. Considering a relationship $\zeta_e^{bulk\ PI} = N_R^{bulk\ PI} \zeta_s^{bulk\ PI}$ and eq 7-2 (iso-τ_s relationship), this relaxation time can be expressed as $\tau_R^{PI66}(T_{iso\text{-}PI}^{bulk}) = \zeta_e^{PI\ block} \{a_{PI}^{bulk}\}^4 N_e^2 / 6\pi^2 k_B T a^2$. From this expression and eq 7-6, a ratio of $\tau_R^{PI\text{-}PtBS}$ of the PI53-PtBS42 copolymer at T to τ_R^{PI66} at $T_{iso\text{-}PI}^{bulk}$ is given by

$$\lambda' = \frac{\tau_R^{PI\text{-}PtBS}(T)}{\tau_R^{PI66}(T_{iso\text{-}PI}^{bulk})} = \frac{\pi^2 \zeta_e^{PtBS\ block}}{\beta^2 \zeta_e^{PI\ block}} \lambda_a \text{ with } \lambda_a = \left(\frac{a}{a_{PI}^{bulk}} \right)^4 (= 1.3) \tag{7-8}$$

From the above results, the comparison in the iso-τ_R^{chain} state can be made for the $\varepsilon_{PI\ block}^*(\omega;T)$ data of the PI53-PtBS42 copolymer at T and the shifted $\varepsilon_{PI66}^*(\lambda'\omega;T_{iso}^{bulk\text{-}PI})$ data of the equivalent PI66 at $T_{iso\text{-}PI}^{bulk} = T - \Delta T_{iso\text{-}PI} = T - 30°C$. However, two more points need to be considered for the actual comparison, *i.e.*, the lack of the type-A dipole in the PtBS block and the molecular weight of an available PI sample, as explained below.

Ordinary linear PI chains have the type-A dipoles parallel along the chain backbone. Thus, their polarization **P** is proportional to the end-to-end vector $\mathbf{R} = \mathbf{R}_1 + \mathbf{R}_2$ (cf. eq 2-6), where $\mathbf{R}_1$ is a vector connecting one end of the chain to a given segment and $\mathbf{R}_2$ is a vector connecting this segment to the other end; cf. Figure 7-6(a). For a special class of PI chains having the dipoles once inverted at the given segment, **P** is proportional to $\mathbf{R}_1 - \mathbf{R}_2$; cf. Figure 7-6(b). A *hypothetical* PI chain that has the type-A dipoles only in one block (cf. Figure 7-6(c)) corresponds to the PI-PtBS copolymer having no type-A dipole in the PtBS block. This hypothetical PI has $\mathbf{P} \propto \mathbf{R}_1$. For all these PI chains, the normalized dielectric relaxation function $\Phi(t)$ (= 1 at t = 0) is given by the auto-correlation of **P** and can be expressed as[29,32]

ordinary PI:
$$\Phi_{ord}(t) = \frac{\left\langle \{\mathbf{R}_1(t) + \mathbf{R}_2(t)\} \bullet \{\mathbf{R}_1(0) + \mathbf{R}_2(0)\} \right\rangle}{\left\langle \mathbf{R}^2 \right\rangle} \tag{7-9}$$

dipole-inverted PI:
$$\Phi_{inv}(t) = \frac{\left\langle \{\mathbf{R}_1(t) - \mathbf{R}_2(t)\} \bullet \{\mathbf{R}_1(0) - \mathbf{R}_2(0)\} \right\rangle}{\left\langle \mathbf{R}^2 \right\rangle} \tag{7-10}$$

hypothetical PI:
$$\Phi_{part}(t) = \frac{\left\langle \mathbf{R}_1(t) \bullet \mathbf{R}_1(0) \right\rangle}{\left\langle \mathbf{R}_1^2 \right\rangle} \tag{7-11}$$

Here, $\langle ... \rangle$ indicates the average at equilibrium. (In the denominator of eqs 7-9 and 7-10, the Gaussian feature of the chain, $\langle \mathbf{R}_1(t) \bullet \mathbf{R}_2(t) \rangle = 0$ at any time t at equilibrium, has been considered.) The dielectric $\Delta\varepsilon'(\omega)$ and $\varepsilon''(\omega)$ are proportional to the sine- and cosine-Fourier transformation of $\Phi(t)$ (cf. eq 2-18b).[29,32]

The dipole-inverted PI samples have been actually synthesized and their dielectric behavior has been examined.[40,41] In contrast, the hypothetical, partially dipole-labeled PI cannot be synthesized. Nevertheless, for a special case that the hypothetical PI chain is dipole-labeled in *half* of its backbone, eqs 7-9 to 7-11 allow a simple expression of $\Phi_{half\text{-}label}(t)$ as

$$\Phi_{\text{half-label}}(t) = \frac{1}{2}\left\{\Phi_{\text{ord}}(t) + \Phi_{\text{sym-inv}}(t)\right\} \tag{7-12}$$

Here, $\Phi_{\text{ord}}(t)$ and $\Phi_{\text{sym-inv}}(t)$ are the dielectric relaxation functions for the ordinary and symmetrically dipole-inverted linear PI chains having the same molecular weight M and exhibiting the same motion as the *half-label* PI chain of interest. The dielectric behavior has been investigated for such a pair of the ordinary and dipole-inverted PI49 with M = 48.8×10^3 ($\cong 10M_e^{\text{PI bulk}}$). The dielectric relaxation mode distribution is the same for these ordinary and symmetrically dipole-inverted PI but the relaxation is faster for the latter by a factor ≅ 4.[40,41] Thus, and $\Phi_{\text{sym-inv}}(t)$ and $\Phi_{\text{ord}}(t)$ satisfy a relationship, $\Phi_{\text{sym-inv}}(t) = \Phi_{\text{ord}}(4t)$, and eq 7-12 is rewritten as

$$\Phi_{\text{half-label}}(t) = \frac{1}{2}\left\{\Phi_{\text{ord}}(t) + \Phi_{\text{ord}}(4t)\right\} \tag{7-13}$$

In the PI53-PtBS42 copolymer, the PtBS42 block occupies 30% of the backbone measured in terms of the number of entanglement segments (cf. eq 7-7c). This fraction is different from but fairly close to the fraction (50%) considered in eq 7-13. Thus, as the best approximation at this moment, a comparison is made, on the basis of eq 7-13, for the $\varepsilon_{\text{PI block}}^*(\omega;T)$ data of the PI53-PtBS42 copolymer at T and $\{\varepsilon_{\text{PI66}}^*(\lambda'\omega;T_{\text{iso-PI}}^{\text{bulk}}) + \varepsilon_{\text{PI66}}^*(\lambda'\omega/4;T_{\text{iso-PI}}^{\text{bulk}})\}/2$ of the equivalent PI66 at $T_{\text{iso-PI}}^{\text{bulk}} = T - \Delta T_{\text{iso-PI}}^{\text{bulk}} = T$–30°C. Since the dielectric data are available for the ordinary and dipole-inverted PI49 samples[40] but not for PI66, the actual comparison is made for the $\varepsilon_{\text{PI block}}^*(\omega;T)$ data and the data obtained for the ordinary PI49 sample,

$$\varepsilon_{\text{eqv}}^*(\omega;T) \equiv \frac{\phi_{\text{PI}} b_T''}{2}\left\{\varepsilon_{\text{PI49}}^*(r_\tau'\lambda'\omega;T_{\text{iso-PI}}^{\text{bulk}}) + \varepsilon_{\text{PI49}}^*(r_\tau'\lambda'\omega/4;T_{\text{iso-PI}}^{\text{bulk}})\right\} \tag{7-14}$$

In eq 7-14, the PI volume fraction ϕ_{PI} and the intensity factor $b_T'' = T_{\text{iso}}^{\text{bulk-PI}}/T$ are multiplied for correction of a difference of the dielectric intensities of the PI49 sample and the PI block (as done in eq 7-4). A minor correction factor r_τ' for the molecular weight difference between PI49 and the equivalent PI66 is evaluated as

$$r_\tau' = \left(\frac{M_{\text{PI66}}}{M_{\text{PI49}}}\right)^{3.5} = 2.9 \tag{7-15}$$

The result of the above comparison is later shown in Figures 7-7 and 7-9.

7-4-3 Comparison of dielectric behavior of PI-PtBS copolymer and equivalent PI

7-4-3-1 Comparison of τ_ε

In Figure 7-7, the dielectric $\tau_\varepsilon(T)$ data of the PI53-PtBS42 copolymer at various T (circles)[47] are compared with $\tau_\varepsilon^{\rm eqv}(T)$ of the equivalent star and linear PI obtained from $\varepsilon_{\rm eqv}^*(\omega;T)$ defined by eqs 7-4 and 7-14. This $\varepsilon_{\rm eqv}^*(\omega;T)$ was evaluated from the available data for the bulk $PI(59)_6$ and PI49 samples at $T-\Delta T_{\rm iso\text{-}PI} = T-30$°C, as explained earlier. The $\tau_\varepsilon(T)$ data of the copolymer are close to $\tau_\varepsilon^{\rm eqv}(T)$ of the equivalent star and linear PI at low and high T, respectively, and the crossover between these asymptotes is noted at intermediate T. This result lends support to the molecular picture that the PI53 block behaves as the equivalent star and linear chains at low and high T. Thus, the thermo-rheological complexity of the dielectric data for the copolymer at low ω (top panel of Figure 7-4) is mainly attributable to the crossover of the motional mode, as discussed earlier.

7-4-3-2 Comparison of relaxation mode distribution at lowest T (20°C)

As shown in eq 7-4, the dielectric $\varepsilon_{\rm PI(59)_6}^*(\omega;T_{\rm iso\text{-}PI}^{\rm bulk})$ data of the star $PI(59)_6$ sample[27] reduced at $T_{\rm iso\text{-}PI}^{\rm bulk} = -10$°C (263 K) are utilized to evaluate $\varepsilon_{\rm eqv}^*(\omega;T)$ for the equivalent star PI at $T = 20$°C (293 K). In the top panel of Figure 7-8, the $\Delta\varepsilon_{\rm eqv}'(\omega)$ and $\varepsilon_{\rm eqv}''(\omega)$ of the equivalent star PI (solid curves) are compared with the $\Delta\varepsilon'(\omega)$ and $\varepsilon''(\omega)$ data of the PI53-PtBS42 copolymer at 20°C. The filled triangles indicate plot of the $\Delta\varepsilon'(\omega)$ data of the PI53/PtBS42 reference blend with $w_{\rm PI}$ = 55.7 wt% at 20°C (in the iso-$\tau_{\rm s}$ state). For clear comparison, this plot is slightly shifted upward in the double logarithmic scale so that it agrees with the $\Delta\varepsilon'(\omega)$ plot for the copolymer (unfilled squares) at the highest ω in the panel. The bottom panel compares the modulus data of the PI53-PtBS42 copolymer (symbols) and the PI53/PtBS42 blend (curves) at 20°C.

The copolymer chain has $N_{\rm e}$ =13.2 entanglements per chain, as explained earlier. The corresponding plateau modulus sustained by both PI and PtBS blocks is evaluated to be $G_{\rm N} = \nu_{\rm chain}N_{\rm e}k_{\rm B}T = 3.3\times10^5$ Pa ($\nu_{\rm chain}$ = chain number density). As noted in the bottom panel of Figure 7-8, $G' > G_{\rm N}$ at $\omega > 2$ s^{-1} and the Rouse-like power-law behavior, $G' \cong G'' \propto \omega^{1/2}$, is observed in this high-ω zone. Thus, at $\omega > 2$ s^{-1}, the PI and PtBS blocks appear to equilibrate themselves within the entanglement length a through the cooperative Rouse mechanism, as discussed for high-M blends in Chapter 4. Consequently, the entanglement relaxation occurs at $\omega < 2$ s^{-1}. The dominant part of the dielectric relaxation of the PI block is observed in this low-ω zone (top panel), which is

consistent with the molecular picture that that the PI53 block essentially behaves as a star arm at low T.

As first noted in the top panel of Figure 7-8, the dielectric relaxation is significantly slower for the PI53 block of the copolymer (unfilled symbols) than for the PI53 chain in the blend (filled triangle). This result demonstrates that the PI block motion is strongly constrained by the PtBS block (even compared to the PI motion in the blend) at 20°C. Furthermore, the curves for the equivalent star PI are close to the $\Delta\varepsilon'(\omega)$ and $\varepsilon''(\omega)$ data of the copolymer. This result lends support to the above molecular picture.

Despite this success of the molecular picture, it should be again emphasized that the PI and PtBS blocks do have the same, slowest eigenmode relaxation time and the PI block relaxation is much faster than the PtBS block relaxation only in a sense that the intensity of the slowest eigenmodes is smaller for the PI block. Consequently, the *real slowest* relaxation process of the PI block should occur simultaneously with that process of the PtBS block, and the PtBS block cannot be regarded as the fixed anchor for the PI block during this process.

In relation to this point, it is noted that G' of the copolymer decreases to the entanglement plateau modulus expected for the case of simple dilation of entanglement mesh by the relaxed PI block, $G_N^{dil} = \phi_{PtBS}^{2.3} G_N = 4.3 \times 10^4$ Pa, with decreasing ω to ω_c = 0.06 s^{-1}; cf. the arrow in the bottom panel. This viscoelastic feature suggests that the PtBS block begins to exhibit rather significant motion/relaxation at such low $\omega \leq \omega_c$. The terminal part of the dielectric relaxation of the PI block does occur in this range of ω, suggesting that the motion of the PtBS block affects (accelerates) the PI relaxation at those ω. Indeed, a hint of this acceleration can be noted as the downward deviation of the $\Delta\varepsilon'(\omega)$ data of the PI block from the equivalent PI curve at those ω. In addition, because of the block connectivity, the PtBS segment near the PI-PtBS junction would be more significantly plasticized by the PI segments compared to the other PtBS segments far from the junction. The junction point fluctuation due to this extra plasticization might enhance the difference between the PI block and star PI. Thus, the full relaxation behavior of the PI block at low T is close but not identical to that of the equivalent star PI.

7-4-3-3 Comparison of relaxation mode distribution at highest T (120°C)

As shown in eq 7-14, the dielectric $\varepsilon_{PI49}^*(\omega; T_{iso\text{-}PI}^{bulk})$ data of the linear PI49 sample[40] reduced at $T_{iso\text{-}PI}^{bulk}$ = 90°C are utilized to evaluate $\varepsilon_{eqv}^*(\omega; T)$ for the equivalent, half-labeled linear PI at T = 120°C. The top panel of Figure 7-9 compares the $\Delta\varepsilon_{eqv}'(\omega)$ and $\varepsilon_{eqv}''(\omega)$ of this equivalent PI

(solid curves) with the data of the PI53-PtBS42 copolymer at 120°C (unfilled symbols). The bottom panel compares the modulus data of the PI53-PtBS42 copolymer (symbols) and the PI53/PtBS42 blend (curves) at 120°C.

At low ω where the dominant part of the dielectric relaxation of the PI block is observed, G' of the copolymer is well below the entanglement plateau modulus sustained by both PI and PtBS blocks, $G_N = \nu_{chain} N_e k_B T = 4.4\times10^5$ Pa (at 120°C); cf. bottom panel. This fact indicates that the entanglement segment of the size a (= 6.2 nm; cf. eq 7-1) behaves as the internally equilibrated motional unit for the dielectrically detected global relaxation process of the copolymer. Thus, the dielectric data of the equivalent linear PI, being evaluated with the entanglement segment as the basic motional unit (cf. eqs 7-7 and 7-8), can be unequivocally compared with the copolymer data.

The mean-square end-to-end distance $\langle R^2 \rangle$ is not exactly the same for the PI and PtBS blocks and no complete agreement can be expected for the data of the copolymer and the equivalent linear PI chain, the latter having the dipoles in its *half* backbone. Nevertheless, the dielectric data of the equivalent PI agree with the copolymer data surprisingly well; cf. top panel. This result strongly suggests the basic validity of the molecular picture that the PI53 block at high T behaves as a portion of free linear chain (subjected to an extra friction from the PtBS block).

7-4-4 Dynamics of copolymer chain

For the PI53-PtBS42 copolymer, the PtBS block dynamics is also a subject of interest. However, it is impossible to dielectrically examine the global motion of the PtBS block having no type-A dipole. Furthermore, for the *mutually connected* PI and PtBS blocks, no simple blending law is available for the viscoelastic moduli sustained by respective blocks. For this reason, this section focuses on the behavior of the PI-PtBS copolymer chain as a whole to discuss the relaxation of the PtBS block just qualitatively.

7-4-4-1 Viscoelastic relaxation time of the copolymer

Figure 7-10 compares the terminal viscoelastic relaxation times τ_G of the PI53-PtBS42 copolymer (unfilled squares) and the PI53/PtBS42 blend (unfilled circles), both having the same PI content (w_{PI} = 55.7 wt%). In the copolymer and blend at the same T, the iso-τ_s state is achieved not only for the Rouse segment of PI but also for that of PtBS. The relaxation times of the PI53 and PtBS42 chains in the blend are also shown for comparison; cf. unfilled diamonds and filled

triangles. These relaxation times are evaluated from the modulus of PI and PtBS in the PI53/PtBS42 blend, $G_{PI,e}^{bld}$* and G_{PtBS}^{bld}* (cf. eq 2-26). The evaluation of $G_{PI,e}^{bld}$* and G_{PtBS}^{bld}*, explained in detail in Chapter 6 (cf. eqs 6-2a and 6-3a), is briefly summarized for the PI53/PtBS42 blend in Appendix 7-4.

At low T, τ_G is similar for the copolymer, blend, and the PtBS42 chain in the blend but significantly smaller for the PI53 chain in the blend, which is in harmony with the earlier discussion for the PI block relaxation: Namely, at low T, the PtBS42 block is the "slow" block defined by considering both of the relaxation time and intensity of eigenmodes and thus behaves as the anchor during the dominant part of the PI block relaxation. Consequently, at the onset of the terminal relaxation of the copolymer (where the PI block has relaxed considerably), the connectivity with the PI53 block would not significantly affect the PtBS42 block motion. Then, τ_G of the PtBS42 block is expected to be close to τ_G of the copolymer and also to τ_G of the PtBS42 chain in the blend being free from the connectivity effect. This expectation is in harmony with the low-T data in Figure 7-10. However, it should be also noted that the viscoelastic data of the copolymer and blend at low ω are close but not identical to each other; cf. the bottom panel of Figure 7-8. This result suggests that the PI block has some effect on the relaxation of the copolymer/PtBS block possibly because the real slowest relaxation of the PI block occurs cooperatively with the PtBS42 block, as discussed earlier.

In contrast, at high T, τ_G of the copolymer is larger than τ_G's of the blend and the PI53 and PtBS42 chains therein, as clearly noted in Figure 7-10. Thus, the PtBS42 and PI53 blocks connected to each other appears to relax cooperatively thereby allowing the copolymer chain to behave as the equivalent linear chain that has a larger M and relaxes more slowly compared to the PI53 and PtBS42 chains in the blend. This effect of the block connectivity makes a significant contrast between the relaxation of the copolymer and blend at high T.

At intermediate T, τ_G of the copolymer exhibits a crossover between the two asymptotic cases discussed above. This crossover of τ_G, due to the crossover of the motional mode of the PI block and the corresponding change in the PtBS block motion, cannot be described by the molecular models available at this moment.

7-4-4-2 Thermo-rheological behavior of the copolymer

In Figure 7-11, the storage and loss moduli, G' and G'', measured for the copolymer at various T are reduced by an intensity correction factor, $b_T = T/T_r$ (T and T_r in K unit), and shifted along ω

axis by a factor of $a_{T,G}$ to achieve the best superposition of their low-ω tails. The reference temperature is chosen to be T_r = 363 K (90°C). The G'' data are multiplied by a factor of 10 in order to avoid heavy overlapping with the G' data. In Figure 7-12, the viscoelastic shift factor $a_{T,G}$ utilized for this superposition is compared with the dielectric shift factor $a_{T,\varepsilon}$ achieving the superposition of the $\Delta\varepsilon'$ and ε'' data of the copolymer (cf. Figure 7-5).

As noted in Figure 7-11, a fairly good superposition is achieved for the G' and G'' data of the copolymer. However, a close inspection reveals a failure of superposition at intermediate to high ω; cf. the data at $\omega a_{T,G}/s^{-1} = 10^2 - 10^5$. This delicate failure possibly reflects the change of the motional mode of the PI block with T (from the tethered chain like motion at low T to the free chain like motion retarded by the PtBS block friction at high T) and the corresponding change for the PtBS block motion. The copolymer dynamics should be thermo-rheologically complex because of these changes of the motional modes. However, this viscoelastic complexity is much less significant compared to the dielectric complexity (cf. Figure 7-4), as also noted for miscible PI-PVE block copolymers.[9]

The difference of the viscoelastically and dielectrically observed thermo-rheological complexities of the PI-PtBS copolymer is related to a fact that the dielectric data just detect the global motion of the PI block while the viscoelastic data are contributed from both PI and PtBS blocks. The change in the motional mode of the PI block with T is directly reflected in the dielectric complexity. With this change, the PI contribution to the terminal relaxation of the copolymer is enhanced while the PI contribution to the fast relaxation becomes less significant with increasing T. Correspondingly, the PtBS contributions to the slow and fast parts of the copolymer relaxation become less and more significant with increasing T. These changes of the PI and PtBS contributions tend to cancel each other, which possibly resulted in the weak viscoelastic complexity seen in Figure 7-11.

The viscoelastic shift factor $a_{T,G}$ of the copolymer is evaluated from the low-ω moduli data. Thus, the $a_{T,G}$ data of the copolymer at low T are expected to reflect the motion of the PtBS block (much slower than the motion of the PI block) while the data at high T correspond to the cooperative motion of the PI and PtBS blocks. This expectation is in harmony with the observation that $a_{T,G}$ at low T is larger and more strongly dependent on T compared to $a_{T,\varepsilon}$ reflecting the the PI block motion while $a_{T,G}$ at high T is very similar, in the T dependence as well as the magnitude, to the dielectric $a_{T,\varepsilon}$ reflecting the PI block motion at any T; cf. Figure 7-12. This result again lends support to the molecular picture that the PI block essentially behaves as the tethered chain at low T while as a portion of the free linear chain at high T.

7-5 Concluding Remarks

Linear viscoelastic and dielectric behavior was examined for a disordered PI53-PtBS42 diblock copolymer and the PI53/PtBS42 reference blend having the same PI content (w_{PI} = 55.7 wt%). For these samples, the dielectric data characterize the global motion of PI block/chain, while the viscoelastic data detect the relaxation of all components in the blend/copolymer systems.

Comparison of the dielectric and viscoelastic terminal relaxation times suggested that the relaxation of the PI and PtBS blocks of the copolymer is affected by the anti-plasticization and plasticization due to respective partner blocks, as similar to the situation in the PI/PtBS blends. However, more importantly, the block relaxation was strongly affected by the connectivity between the blocks. This connectivity effect, being absent in the blends, forced the PI block to relax essentially as the tethered chain (anchored by the slow PtBS block) at low T while as a portion of free linear chain at high T (where the PI and PtBS blocks relax cooperatively). This change of the motional mode of the PI block with T led to the thermo-rheological complexity of the dielectric data that was much more significant compared to the complexity observed for the PI/PtBS reference blend. The corresponding complexity was noted also for the viscoelastic data of the copolymer. However, this viscoelastic complexity was much less prominent than the dielectric complexity, possibly because viscoelastic changes due to the changes of the relaxation mechanisms of the PI and PtBS blocks tend to cancel each other.

Appendix 7-1 Dielectric Relaxation Time of PI

The PI53 block of the PI53-PtBS42 copolymer is expected to essentially behave as the arm of star chain at low T and as a portion of a free, non-tethered linear chain at high T. A test of this molecular picture requires data of the dielectric relaxation time of star/linear homo-PI chains. These data are summarized below.[27]

The data for the terminal dielectric relaxation time, τ_ε defined by eq 2-31, are available for a series of entangled 6-arm star PI and linear PI in bulk state at 40°C.[27] These τ_ε data were reduced to 30°C with the aid of the WLF equation for bulk PI (eq 3-2) and plotted against the span molecular weight $2M_{\rm arm}$ (for star PI) and/or the total molecular weight M (for linear PI) in Figure 7-13. (The WLF shift is identical for the star and linear PI.[27]) The plots in the range of M, $2M_{\rm arm} > 50\times10^3$ (well entangled regime) are described by empirical equations shown with the curves:

$$\tau_\varepsilon/{\rm s} = 2.0\times10^{-10} M_{\rm a}^{1.5} \exp\left\{1.4\times10^{-4} M_{\rm a}\right\} \text{ for star PI at 30°C} \qquad \text{(A7-1-1)}$$

$$\tau_\varepsilon/{\rm s} = 7.9\times10^{-19} M^{3.5} \text{ for linear PI at 30°C} \qquad \text{(A7-1-2)}$$

These equations were utilized to evaluate τ_ε of the equivalent star and linear PI in the iso-τ_ε and iso-$\tau_{\rm R}^{\rm chain}$ states, respectively.

Appendix 7-2 Viscoelastic Relaxation Times of PI and PtBS

The evaluation of $\tau_{\rm R}^{\rm chain}$ of the copolymer at T requires a value of a ratio L of frictional coeffeicients for the entanglement segments of the PtBS and PI blocks, *i.e.*, $L = \zeta_{\rm e}^{\rm PtBS\ block}(T)/\zeta_{\rm e}^{\rm PI\ block}(T)$ appearing in eq 7-7. The data for the terminal viscoelastic relaxation time $\tau_{\rm G}^{\rm bulk}$ (defined by eq 2-26) of monodisperse bulk PI and PtBS can be utilized to evaluate this ratio. As an example, the top panel of Figure 7-14 shows the $\tau_{\rm G}^{\rm bulk}$ data for bulk PI at $T_{\rm iso\text{-}PI}^{\rm bulk}$ = 90°C and bulk PtBS at $T_{\rm iso\text{-}PtBS}^{\rm bulk}$ = 275°C plotted against the $M/M_{\rm e}^{\rm bulk}$ ratio (unfilled symbls). These $T_{\rm iso\text{-}PI}^{\rm bulk}$ and $T_{\rm iso\text{-}PtBS}^{\rm bulk}$ are the iso-$\tau_{\rm s}$ temperature defined with respect to the Rouse segments of the PI and PtBS blocks at T = 120°C.

The filled circles in the top panel of Figure 7-14 indicate the $\tau_{\rm G}^{\rm bulk\ PtBS}(T_{\rm iso\text{-}PtBS}^{\rm bulk})$ data multiplied by 3.7×10^{-3}. As noted from the coincidence of those circles and squares ($=\tau_{\rm G}^{\rm bulk\ PI}(T_{\rm iso\text{-}PI}^{\rm bulk})$), the $\tau_{\rm G}$ data of bulk PI and PtBS exhibit very similar M dependence, $\tau_{\rm G} \propto M^2$ for $M/M_{\rm e}^{\rm bulk} < 1$

(unentangled behavior) and $\tau_G \propto M^{3.5}$ for $M / M_e^{bulk} > 1$ (entangled behavior). However, the magnitude of τ_G is different for the bulk PI and PtBS having the same M / M_e^{bulk} value, which essentially reflects the difference of $\zeta_e^{bulk\ PI}(T_{iso\text{-}PI}^{bulk})$ and $\zeta_e^{bulk\ PtBS}(T_{iso\text{-}PtBS}^{bulk})$. This difference of τ_G can be utilized to evaluate the $\zeta_e^{PtBS\ block}(T) / \zeta_e^{PI\ block}(T)$ ratio for the PtBS and PI blocks of the copolymer at *T*, as explained below.

The τ_G data of unentangled bulk PI and PtBS at *T* can be expressed in the Rouse form,

$$\tau_G = \left[\frac{G'}{\omega G''} \right]_{\omega \to 0} = \frac{\left\{ a_X^{bulk} \right\}^2 \zeta_e^{bulk\ X}(T)}{90 k_B T} \left(\frac{M}{M_e^{bulk\ X}} \right)^2 \quad (X = PI, PtBS) \tag{A7-2-1}$$

where $\zeta_e^{bulk\ X}(T)$ ($\propto N_R^{bulk\ X} \propto \left\{ a_X^{bulk} \right\}^2$) is the friction coefficient of the entanglement segment of the size a_X^{bulk} in the bulk X system at *T*. (With the aid of the relationships for the chain friction coefficient $\zeta^{chain} = \zeta_e^{bulk\ X} M / M_e^{bulk}$ and for the chain size $\left\langle R^2 \right\rangle = \left\{ a_X^{bulk} \right\}^2 M / M_e^{bulk}$, τ_G can be rewritten from the usual Rouse expression (eq A4-1-2) into the form of eq A7-2-1.) Thus, for the bulk PI and PtBS having the *same* M / M_e^{bulk} ratio, eq A7-2-1 gives

$$\frac{\tau_G^{bulk\ PtBS}(T_{iso\text{-}PtBS}^{bulk})}{\tau_G^{bulk\ PI}(T_{iso\text{-}PI}^{bulk})} = \frac{T_{iso\text{-}PI}^{bulk} \left\{ a_{PtBS}^{bulk} \right\}^2}{T_{iso\text{-}PtBS}^{bulk} \left\{ a_{PI}^{bulk} \right\}^2} \frac{\zeta_e^{bulk\ PtBS}(T_{iso\text{-}PtBS}^{bulk})}{\zeta_e^{bulk\ PI}(T_{iso\text{-}PI}^{bulk})}$$

$$= \frac{\left\{ a_{PtBS}^{bulk} \right\}^4}{\left\{ a_{PI}^{bulk} \right\}^4} \frac{\zeta_e^{PtBS\ block}(T)}{\zeta_e^{PI\ block}(T)} \tag{A-7-2-2}$$

The derivation of eq A7-2-2 utilized the proportionality, $N_R \propto a^2$, and the following iso-τ_s relationship (cf. eq 7-2):

$$\frac{\zeta_e^{bulk\ X}(T_{iso\text{-}X}^{bulk})}{T_{iso\text{-}X}^{bulk}} = \frac{\zeta_s^{bulk\ X}(T_{iso\text{-}X}^{bulk})}{T_{iso\text{-}X}^{bulk}} N_R^{bulk\ X}$$

$$= \frac{\zeta_s^{X\ block}(T)}{T} N_R^{bulk\ X}$$

$$= \frac{\zeta_e^{X\ block}(T)}{T} \left(\frac{a_X^{bulk}}{a} \right)^2 \tag{A7-2-3}$$

The $\zeta_e^{PtBS\ block}(T) / \zeta_e^{PI\ block}(T)$ ratio for the entanglement segments of the PtBS and PI blocks can be evaluated from the data for the $\tau_G^{bulk\ PtBS}(T_{iso\text{-}PtBS}^{bulk}) / \tau_G^{bulk\ PI}(T_{iso\text{-}PI}^{bulk})$ and $a_{PtBS}^{bulk} / a_{PI}^{bulk}$ ratios with the aid of

eq A7-2-2: For example, the data in the top panel of Figure 7-14 give $\zeta_e^{\text{PtBS block}}(T)/\zeta_e^{\text{PI block}}(T)$ = 16.3 at T = 120°C. The bottom panel shows plots of the $\zeta_e^{\text{PtBS block}}(T)/\zeta_e^{\text{PI block}}(T)$ ratio thus obtained. This ratio changes with T according to the WLF feature of $\tau_G^{\text{bulk X}}$ (X = PI, PtBS) described by the eqs 3-2 and 3-3. The $\zeta_e^{\text{PtBS block}}/\zeta_e^{\text{PI block}}$ ratio is utilized to specify the iso-τ_R^{chain} state, as explained for eqs 7-6 to 7-8.

Appendix 7-3 Stockmay-Kennedy (SK) Model

Stockmay and Kennedy[45] derived in a generalized bead-spring model (SK model) applicable to non-entangled ABA triblock and AB diblock copolymers. The theoretical analysis for the AB diblock copolymers is briefly summarized below.

The SK model considered a diblock copolymer composed of A and B block having number of segments (beads) N_A and N_B, respectively. The *beads* of A and B blocks have different frictional coefficient, $\zeta_{s,A}$ and $\zeta_{s,B}$, and the springs associated to A and B blocks have, in general, different force constant, κ_A and κ_B. Then, from the force balance and the requirement of coincidence of spatial position of A and B blocks at the junction point, the SK model gives a characteristic equation for the eigenvalue β:

$$\varphi L^{1/2}\tan\beta\theta = -\tan\frac{\beta(1-\theta)}{L^{1/2}} \qquad \text{(A7-3-1)}$$

with $L = \zeta_{s,A}/\zeta_{s,B}$, $\varphi = \kappa_A/\kappa_B$, and $\theta = N_A/(N_A+N_B)$. However, the slow dynamic behavior does not depend on the choice of the bead size, b_R. Thus, b_R and the spring force constant ($=3k_BT/b_R^2$) can be chosen to be the same for two blocks. Then, eq A7-3-1 is simplified to:[46]

$$L^{1/2}\tan\beta\theta = -\tan\frac{\beta(1-\theta)}{L^{1/2}} \quad \text{with } \theta = \frac{R_A^2}{R_A^2+R_B^2} \qquad \text{(A7-3-2)}$$

where R_A^2 and R_B^2 are the mean square end-to-end distance of A and B blocks.

The eigenvalue β is numerically obtained from eq A7-3-2, and the relaxation time for the p-th normal mode is written in terms of β_p as:

$$\tau_p = \tau_{1A}(\pi/2\beta_p)^2 \qquad \text{(A7-3-3)}$$

Here $\tau_{1A} = \zeta_{s,A}(N_A + N_B)^2 b_R^2/6\pi^2 k_B T$ is the longest viscoelastic Rouse relaxation time of a hypothetical A chain that has the same chain size as AB block copolymer and is in an iso-τ_s state

defined with respect to A block. Thus, SK model can be utilized to calculate the Rouse time of diblock copolymer as long as the friction coefficient and the mean-square junction-to-end distance are known for A and B blocks.

Appendix 7-4 Viscoelastic relaxation of PI and PtBS in the reference blend

In the PI53/PtBS42 blend, the PtBS42 relaxation is slower/equally slow compared to the PI53 relaxation in the entire range of T examined (cf. Figure 7-3). Thus, the PtBS modulus in the blend can be evaluated from the $G_B^*(\omega)$ data of the blend and the G_{PI}^{bulk} * data of bulk PI53 at T with the aid of a blending law explained in Chapter 6 (cf. eqs 6-2 and 6-3):

$$G_B^*(\omega) = G_{PI,e}^{bld}*(\omega) + G_{PtBS}^{bld}*(\omega) \tag{A7-4-1}$$

$$G_{PI,e}^{bld*}(\omega) = \phi_{PI} I_{PI} G_{PI}^{bulk*}(\omega Q^{2.33} / \lambda_{PI}) \tag{A7-4-2}$$

Here, I_{PI} (= $\left\{a_{PI}^{bulk} / a\right\}^2$ = 0.88) represents the decrease of the entanglement plateau modulus G_N on blending of PI and PtBS, ϕ_{PI} (= 0.59) is the PI volume fraction in the blend, Q is a factor specifying an increase of τ_ε of PI in the blend due to restriction of DTD/CR, λ_{PI} is a ratio of the dielectric relaxation time of bulk PI53 to that of PI53 in the blend. For the PI53/PtBS42 blend, the thermo-rheological complexity is moderate for ε'' data of the blend (cf. Figure 7-4). Thus, a contribution of the slow minority PI has been neglected in eq A7-4-2.

The time-temperature superposability was tested of the PtBS modulus data obtained above by utilizing the low-ω G_{PtBS}^{bld}" data as a guide for the superposition. The results are shown in Figure 7-15, where G_{PtBS}^{bld} * at respective T is reduced by the intensity correction factor $b_T = T/T_r$ (with T_r = 293K) and plotted against a reduced frequency $\omega a_{T,G}$. The superposition fails moderately, possibly because of a change of the motional mode of the PtBS42 chain with T: PtBS42 relaxes much more slowly compared to PI53 at low T, but this difference of the relaxation rates decreases with increasing T to enhance the topological effect of PI53 on the PtBS relaxation and induce this change of the motional mode. (This situation is qualitatively similar to that for the moderate thermo-rheological complexity seen for the PI-PtBS copolymer; cf. Figure 7-11).

In Chapter 6, G_{PtBS}^{bld} * was obtained for the PI20/PtBS42 and PI20/PtBS70 blends having the same content of PtBS, w_{PtBS} = 44.3wt%, as the PI53/PtBS42 blend. For these blends, the relaxation of PtBS was much slower than that of PI and the G_{PtBS}^{bld} * data exhibited the thermo-rheological simple behavior (cf. Figure 6-7). The standard WLF analysis of the shift factor $a_{T,G}$ for those

G_{PtBS}^{bld} * data gave the iso-τ_s temperature for the Rouse segment of PtBS in the blend, $T_{iso\text{-}PtBS}$ = 25°C that corresponded to the reference temperature of bulk PtBS, $T_{r,bulk}$ = 180˚C (cf. Figure 6-9).

In Figure 7-16, the $a_{T,iso}$ data defined with respect to $T_{iso\text{-}PtBS}$ = 25°C for the PI53/PtBS42 blend is plotted against $T - T_{iso\text{-}PtBS}$ (cf. small triangles). For comparison, the $a_{T,iso}$ data obtained for the PI20/PtBS42 and PI20/PtBS70 blends are also shown (cf. large circles and squares). The plots for these three blends agree well and are described by the WLF equation for bulk PtBS (eq 3-3) with $T_{r,bulk} = T_{iso\text{-}PtBS}$ = 180°C (solid curve), suggesting that the approximate superposition utilizing the low-ω G_{PtBS}^{bld}" data as a guide in Figure 7-15 have reflected the correct $T_{iso\text{-}PtBS}$ with a rather small uncertainty.

References and Notes

1. Lodge, T. P.; McLeish, T. C. B. *Macromolecules* **2000**, 33, 5278-5284.
2. Chung, G. C.; Kornfield, J. A.; Smith, S. D. *Macromolecules* **1994**, 27, 964-973.
3. Alegria, A.; Colmenero, J.; Ngai, K. L.; Roland, C. M. *Macromolecules* **1994**, 27, 4486-4492.
4. Kumar, S. K.; Colby, R. H.; Anastasiadis, S. H.; Fytas, G. *J. Chem. Phys.* **1996**, 105, 3777-3788.
5. Wetton, R. E.; Macknight, W. J.; Fried, J. R.; Karasz, F. E. *Macromolecules* **1978**, 11, 158-165.
6. Liang, K. M.; Banhegyi, G.; Karasz, F. E.; Macknight, W. J. *J. Polym. Sci. B: Polym. Phys.* **1991**, 29, 649-657.
7. Miura, N.; MacKnight, W. J.; Matsuoka, S.; Karasz, F. E. *Polymer* **2001**, 42, 6129-6140.
8. Arendt, B. H.; Krishnamoorti, R.; Kannan, R. M.; Seitz, K.; Kornfield, J. A.; Roovers, J. *Macromolecules* **1997**, 30, 1138-1145.
9. Hirose, Y.; Urakawa, O.; Adachi, K. *J. Polym. Sci. B: Polym. Phys*. **2004**, 42, 4084-4094.
10. Roovers, J.; Toporowski, P. M. *Macromolecules* **1992**, 25, 3454-3461.
11. Roovers, J.; Wang, F. *J. Non-Crystalline Solids* **1994**, 172, 698-704.
12. Kanetakis, J.; Fytas, G.; Kremer, F.; Pakula, T. *Macromolecules* **1992**, 25, 3484-3491.
13. Chung, G. C.; Kornfield, J. A.; Smith, S. D. *Macromolecules* **1994**, 27, 5729-5741.
14. He, Y. Y.; Lutz, T. R.; Ediger, M. D. *Macromolecules* **2003**, 36, 8040-8048.
15. He, Y. Y.; Lutz, T. R.; Ediger, M. D.; Lodge, T. P. *Macromolecules* **2003**, 36, 9170-9175.

16. Haley, J. C.; Lodge, T. P.; He, Y. Y.; Ediger, M. D.; von Meerwall, E. D.; Mijovic, J. *Macromolecules* **2003**, 36, 6142-6151.
17. He, Y. Y.; Lutz, T. R.; Ediger, M. D. *Macromolecules* **2004**, 37, 9889-9898.
18. Hirose, Y.; Urakawa, O.; Adachi, K. *Macromolecules* **2003**, 36, 3699-3708.
19. Urakawa, O. *Nihon Reoroji Gakkaishi* (*J. Soc. Rheol. Japan*) **2004**, 32, 265-270.
20. Yurekli, K.; Krishnamoorti, R. *J. Polym. Sci. B: Polym. Phys.* **2004**, 42, 3204-3217.
21. Watanabe, H.; Matsumiya, Y.; Takada, J.; Sasaki, H.; Matsushima, Y.; Kuriyama, A.; Inoue, T.; Ahn, K. H.; Yu, W.; Krishnamoorti, R. *Macromolecules* **2007**, 40, 5389-5399.
22. Chen, Q.; Matsumiya, Y.; Masubuchi, Y.; Watanabe, H.; Inoue, T. *Macromolecules* **2008**, 41, 8694-8711.
23. Zhao, J. S.; Ediger, M. D.; Sun, Y.; Yu, L. *Macromolecules* **2009**, 42, 6777-6783.
24. Bates, S. F; Fredrickson, G. H. *Annu. Rev. Phys. Chem.* **1990**, 41, 525-557.
25. Watanabe, H.; Ishida, S.; Matsumiya, Y.; Inoue, T. *Macromolecules* **2004**, 37, 1937-1951.
26. Watanabe, H.; Ishida, S.; Matsumiya, Y.; Inoue, T. *Macromolecules* **2004**, 37, 6619-6631.
27. Watanabe, H.; Matsumiya, Y.; Inoue, T. *Macromolecules* **2002**, 35, 2339-2357.
28. Ferry, J. D., *Viscoelastic Properties of Polymers*, 3rd ed.; Wiley: New York, **1980**; Chapter 11, pp 264-320.
29. Watanabe, H. *Macromol. Rapid Commun.* **2001**, 22, 127-175.
30. Watanabe, H.; Chen, Q.; Kawasaki, Y.; Matsumiya, Y.; Inoue, T.; Urakawa, O. *submitted to Macromolecules*
31. Fetters, L. J.; Lohse, D. J.; Colby, R.H., *Chain Dimensions and Entanglement Spacings*, in *Physical Properties of Polymers Handbook*, 2nd ed.; Mark, J. E., Ed.; Springer: New York, 2007; Chapter 25, pp 445-452.
32. Watanabe, H. *Prog. Polym. Sci.* **1999**, 24, 1253-1403.
33. Weak and slow dielectric modes are more sensitively detected by $\Delta\varepsilon'$ than by ε'', as explained for Figure 7-4.
34. In the PI/PtBS42 blend with w_{PI} = 55.7 wt%, the PtBS42 chain has the mass concentration, C_{PtBS} = 0.41 g cm^{-3} and the overlapping concentration of PtBS42 is $C_{PtBS}^* = \{M_{PtBS}/N_A\}/\{4\pi R_{g,PtBS}^3/3\}$ = 0.13 g cm^{-3}, with $R_{g,PtBS} = \sqrt{R_{PtBS}^2/6}$ the root-mean-square radius of gyration.
35. Karatasos, K.; Anastasiadis, S. H.; Semenov, A. N.; Fytas, G.; Pitsikalis, M. Hadjichristidis, N. *Macromolecules* **1994**, 27, 3543-3552.
36. Adachi, K.; Nishi, I.; Doi, H.; Kotaka, T. *Macromolecules* **1991**, 24, 5843-5850.
37. Yao, M. L.; Watanabe, H.; Adachi, K.; Kotaka, T. *Macromolecules* **1992**, 25, 1699-1704.
38. Stühn, B.; Stickel, F. *Macromolecules* **1992**, 25, 5306-5312.
39. Yoshida, H.; Watanabe, H.; Adachi, K.; Kotaka, T. *Macromolecules* **1991**, 24, 2981-2985.

40. Watanabe, H.; Urakawa, O.; Kotaka, T. *Macromolecules* **1993**, 26, 5073-5083.
41. Watanabe, H.; Urakawa, O.; Kotaka, T. *Macromolecules* **1994**, 27, 3525-3536.
42. Fetters, L. J.; Lohse, D. J.; Richter, D.; Witten, T. A.; Zirkel, A. *Macromolecules* **1994**, 27, 4639-4647.
43. Fetters, L. J.; Lohse, D. J.; Graessley, W. W. *J. Polym. Sci. Part B: Polym. Phys.* **1999**, 37, 1023-1033.
44. Chen, Q.; Matsumiya, Y.; Watanabe, H. Accepted by *Polymer Journal.*
45. Stockmayer, W. H.; Kennedy, J. W. *Macromolecules* **1975**, 8, 351-355.
46. Yao, M. L.; Watanabe, H.; Adachi, K.; Kotaka, T. *Macromolecules* **1992**, 25, 1699-1704.
47. The $\tau_\varepsilon(T)$ of the copolymer, defined by eq 2-31, were evaluated from the low-ω tails of the dielectric data that violated the time-temperature superposition. Thus, the temperature dependence of $\tau_\varepsilon(T)$ is a little different from the dependence of the dielectric shift factor $a_{T,\varepsilon}$, the latter being obtained from the dielectric data at high $\omega \geq \omega_{\varepsilon\text{-peak}}$.

Table 7-1. Characteristics of Samples.

Code	$10^{-3}M_{PI}$	$10^{-3}M_{PtBS}$	M_w/M_n
PI53-PtBS42	52.6	41.8	1.08
PI53	53.4		1.03
PtBS42[a]		41.8	1.04

a: precursor of PI53-PtBS42 copolymer

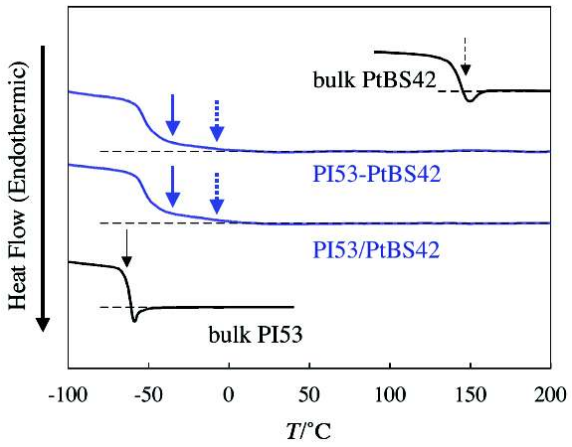

Fig. 7-1: DSC traces for the PI53-PtBS42 diblock copolymer and the PI53/PtBS42 blend. Thin solid and dashed arrows denote the glass transition temperature of bulk PI53 ($T_{g,PI}^{bulk}$ = −65°C) and bulk PtBS42 ($T_{g,PtBS}^{bulk}$ = 147°C), respectively. The thick solid and dotted arrows, respectively, show the effective $T_{g,PI}^{eff}$ and $T_{g,PtBS}^{eff}$ for the Rouse segments of PI and PtBS in the blends/copolymer expected from the WLF analysis.

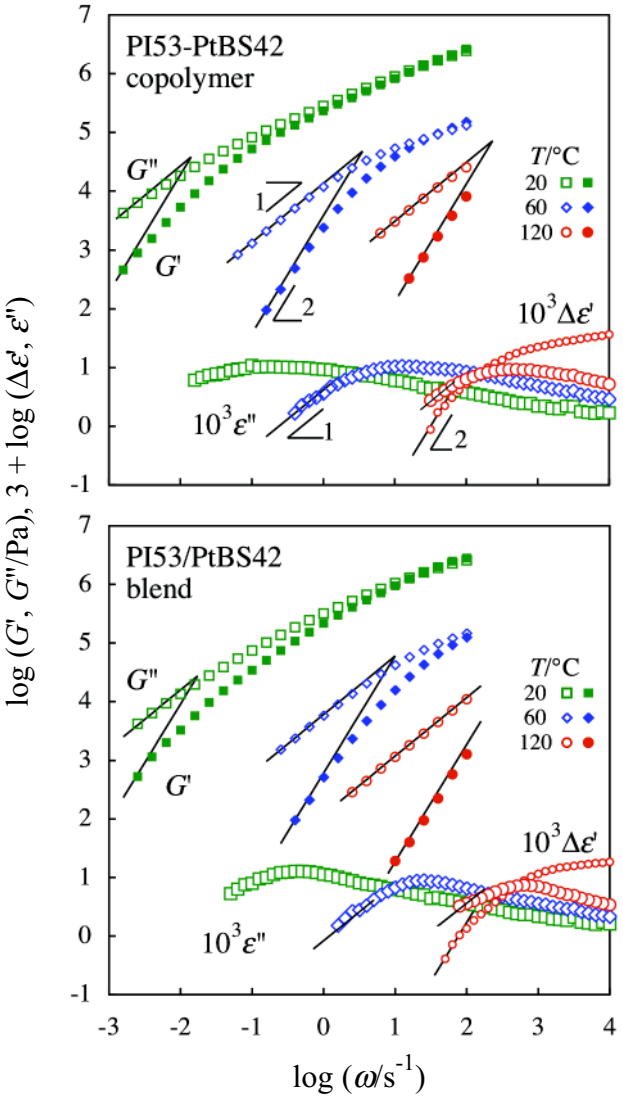

Fig. 7-2: Viscoelastic and dielectric behavior of PI53-PtBS42 diblock copolymer and PI53/PtBS42 blend. Only the raw ε'' data at moderately high ω where the dc conduction was negligible are shown.

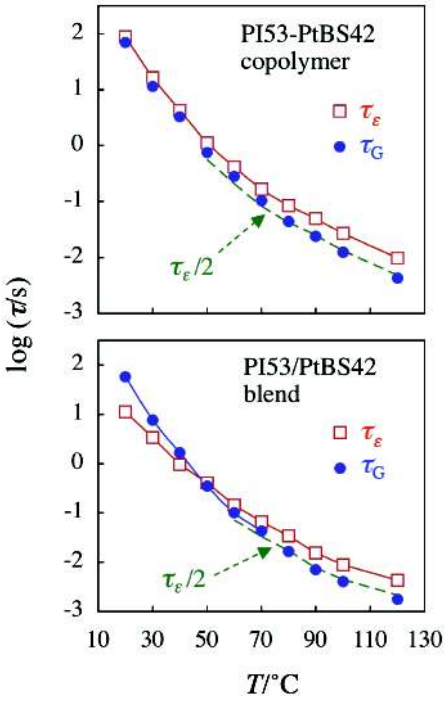

Fig. 7-3: Comparison of the dielectric and viscoelastic terminal relaxation times, τ_ε and τ_G, obtained for the PI53-PtBS42 copolymer and the PI53/PtBS42 blend at various T.

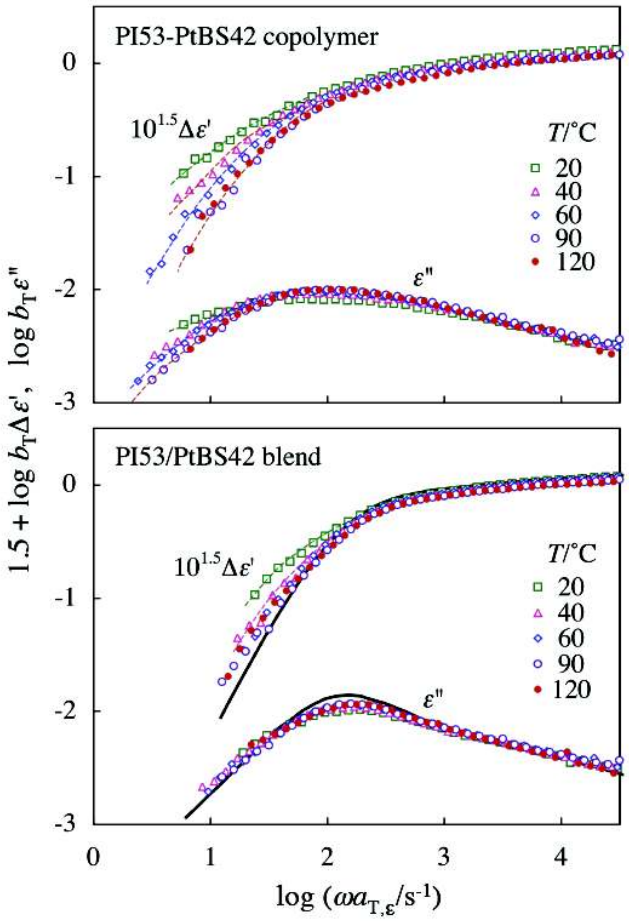

Fig. 7-4: Test of the time-temperature superposability for the dielectric $\Delta\varepsilon'$ and ε'' data for the PI53-PtBS42 copolymer and the PI53/PtBS42 blend. These data are multiplied by the intensity correction factor $b_T = T/T_r$ (with the reference temperature of T_r = 363K) and shifted along the ω axis by a factor of $a_{T,\varepsilon}$ to achieve the best superposition at $\omega > \omega_{\varepsilon\text{-peak}}$. (The $\Delta\varepsilon'$ data are further multiplied by a factor of $10^{1.5}$ to avoid heavy overlapping with the ε'' data.) The solid curve in the bottom panel indicate the dielectric data of bulk PI53 shifted along the ω axis to match their $\omega_{\varepsilon\text{-peak}}$ with $\omega_{\varepsilon\text{-peak}}$ of the blends.

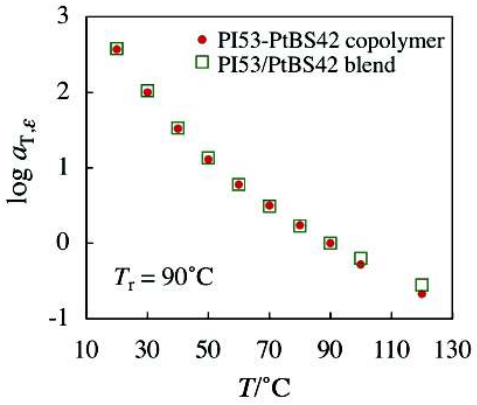

Fig. 7-5: Shift factor $a_{T,\varepsilon}$ utilized for superposition of the dielectric data for the PI53-PtBS42 copolymer and PI53/PtBS42 blend (cf. Figure 7-4). The $a_{T,\varepsilon}$ data, defined with respect to T_r = 90°C, are plotted against T.

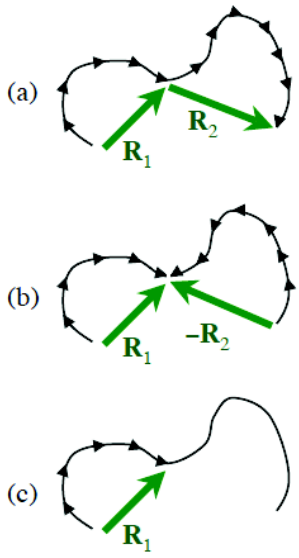

Fig. 7-6: Schematic illustration of (a) ordinary PI having the type-A dipoles aligned along the chain backbone in the same direction from one end to the other, (b) a special class of PI having once-inverted dipoles, and (c) hypothetical PI having the type-A dipole only in a portion of the backbone.

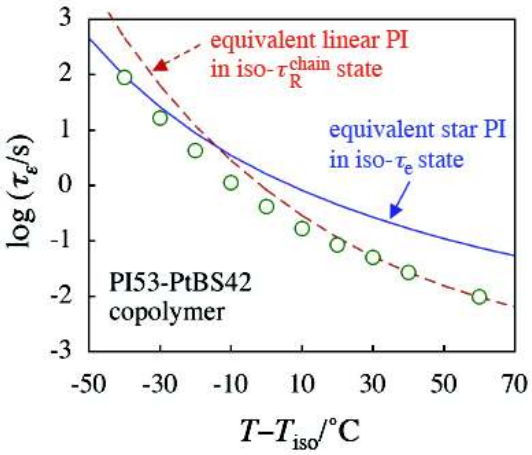

Fig. 7-7: Comparison of the τ_ε data of PI53-PtBS42 copolymer at various T (circles) with the τ_ε expected for equivalent PI, the star PI ($M_a = 46.0\times10^3$; solid curve) and linear PI ($M = 66.1\times10^3$; dashed curve). The arm of the equivalent star PI has the same entanglement number N_e as the PI53 block, while the equivalent linear PI chain has N_e being identical to N_e for the copolymer chain as a whole. The τ_ε data of the equivalent star PI are compared in the iso-τ_e state (defined for the entanglement segment), while the data of the equivalent linear PI are compared in the iso-τ_R^{chain} state (defined for the chain as a whole).

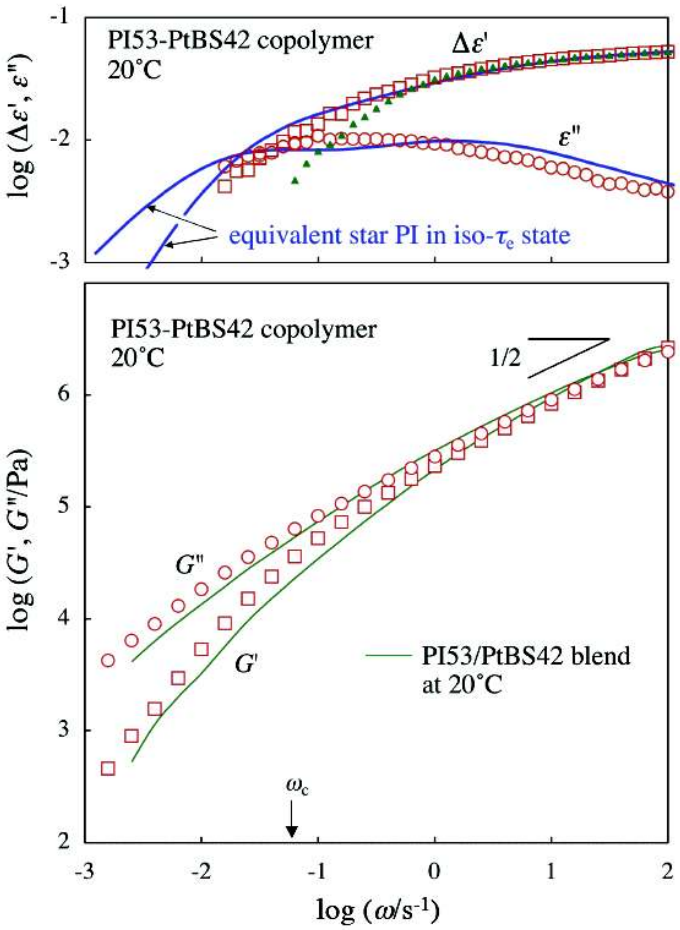

Fig. 7-8: **Top panel:** Comparison of the dielectric $\Delta\varepsilon'$ and ε'' data for the PI53-PtBS42 copolymer at 20°C (unfilled symbols) and the equivalent star PI ($M_{arm} = 46.0 \times 10^3$; solid curves) having the arm entanglement number identical to that for the PI53 block. The comparison is made in the iso-τ_e state defined for the entanglement segment of PI. The filled triangles show the $\Delta\varepsilon'(\omega)$ data of the PI53/PtBS42 blend at 20°C (in the iso-τ_e state). For clear comparison, this $\Delta\varepsilon'(\omega)$ plot is slightly shifted upward in the double logarithmic scale so that it agrees with the $\Delta\varepsilon'(\omega)$ plot for the copolymer (unfilled squares) at the highest ω in the panel.

Bottom panel: Comparison of the viscoelastic G' and G'' data for the PI53-PtBS42 copolymer (unfilled symbols) and the PI53/PtBS42 blend (curves) at 20°C.

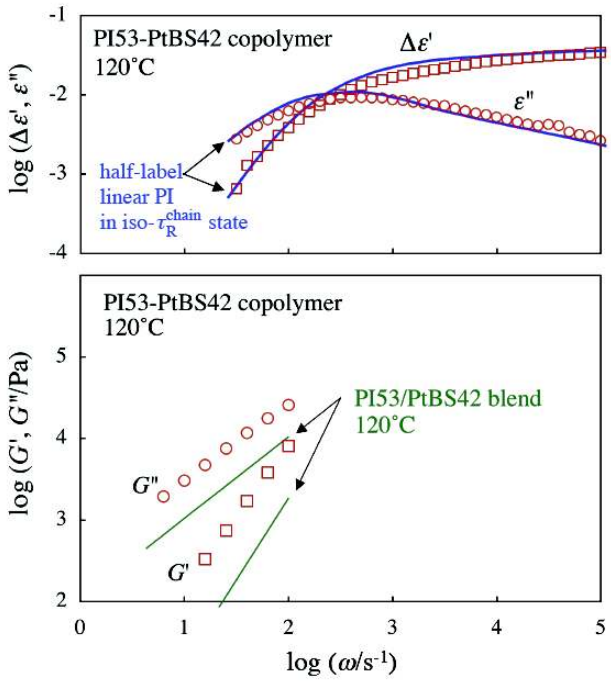

Fig. 7-9: **Top panel:** Comparison of the dielectric $\Delta\varepsilon'$ and ε'' data for the PI53-PtBS42 copolymer at 120°C (unfilled symbols) and the equivalent linear PI (M = 66.1×10^3; thick solid curves) having the entanglement number identical to that for the copolymer chain as a whole. The comparison is made in the iso-τ_R^{chain} state where the equivalent linear PI and the PI-PtBS copolymer have the same longest Rouse relaxation time.

Bottom panel: Comparison of the viscoelastic G' and G'' data for the PI53-PtBS42 copolymer (unfilled symbols) and the PI53/PtBS42 blend (curves) at 120°C.

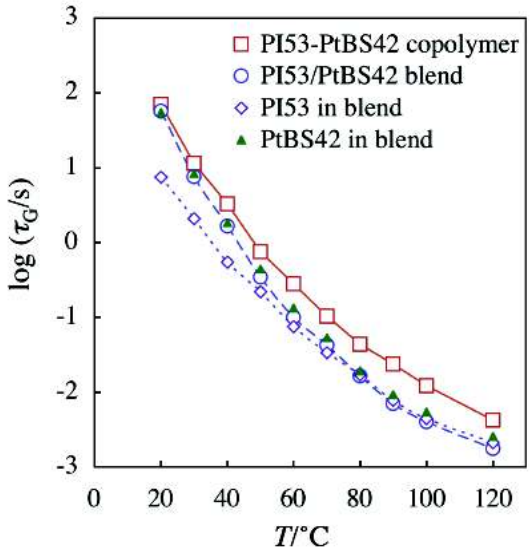

Fig. 7-10: Comparison of the viscoelastic terminal relaxation time τ_G for the PI53-PtBS42 copolymer, the PI53/PtBS42 blend, and the PI53 and PtBS42 chains in the blend.

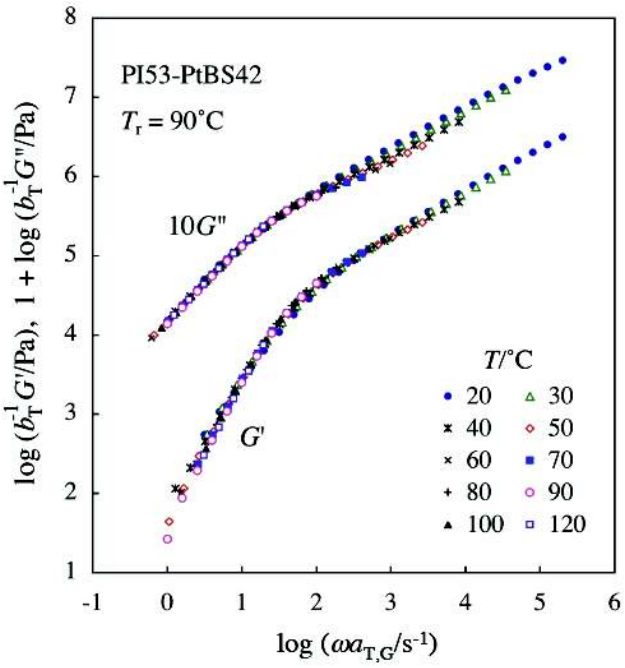

Fig. 7-11: Test of time-temperature superposability for the viscoelastic G' and G'' data for the PI53-PtBS42 copolymer. The data are reduced by the intensity factor, $b_T = T/T_r$ (with T_r = 363 K), and superposed in their low-ω tails. The G'' data are multiplied by a factor of 10 to avoid heavy overlapping with the G' data.

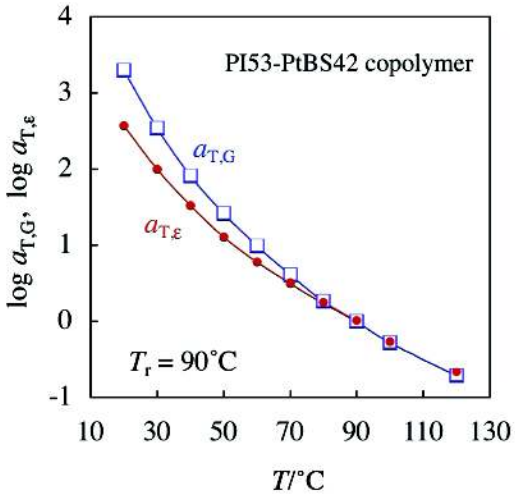

Fig. 7-12: Comparison of the viscoelastic and dielectric shift factors $a_{T,G}$ and $a_{T,\varepsilon}$ for the PI53-PtBS42 copolymer utilized for the superposition in Figures 7-11 and 7-4.

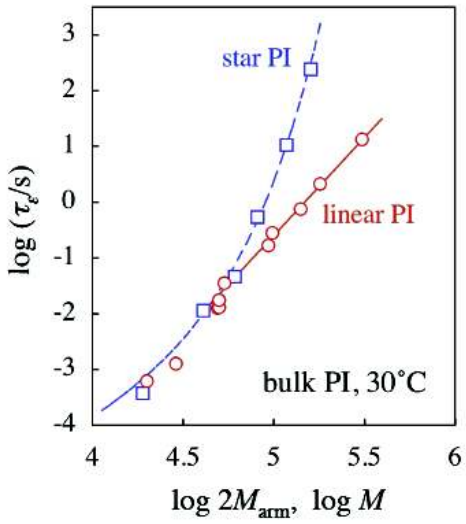

Fig. 7-13: Plots of the dielectric relaxation time data[27] for 6-arm star PI (squares) and linear PI (circles) at 30°C against the span molecular weight $2M_{arm}$ (for star PI) and/or total molecular weight M (for linear PI). The dashed curve and solid line indicate empirical equations (eqs A7-1-1 and A7-1-2) in the well entangled regime (M, $2M_{arm}$ >50×10^3).

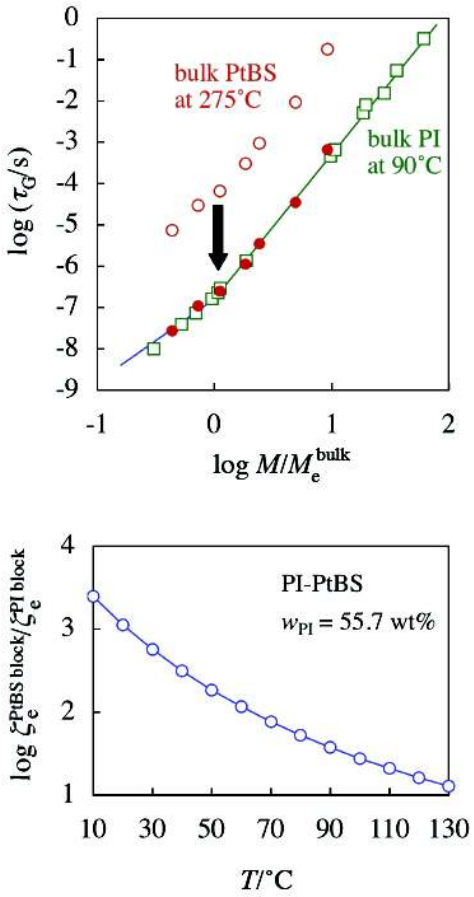

Fig. 7-14: **Top panel:** Comparison of viscoelastic τ_G for bulk PI at $T_{\text{iso-PI}}^{\text{bulk}} = T - \Delta T_{\text{iso-PI}}$ = 90°C (unfilled squares) and bulk PtBS at $T_{\text{iso-PtBS}}^{\text{bulk}} = T - \Delta T_{\text{iso-PtBS}}$ = 275°C (unfilled circles). These $T_{\text{iso-PI}}^{\text{bulk}}$ and $T_{\text{iso-PtBS}}^{\text{bulk}}$, respectively, are the iso-τ_s temperatures for the Rouse segments of PI and PtBS in the PI/PtBS blend (and copolymer) at T = 120°C. The filled circles indicate the τ_G data for bulk PtBS multiplied by a factor of 3.7×10^{-3}.

Bottom panel: A ratio of the friction coefficients of the entanglement segments of the PtBS and PI blocks, $\zeta_e^{\text{PtBS block}}(T) / \zeta_e^{\text{PI block}}(T)$, evaluated from the τ_G data of bulk PI and PtBS. This ratio is plotted against T.

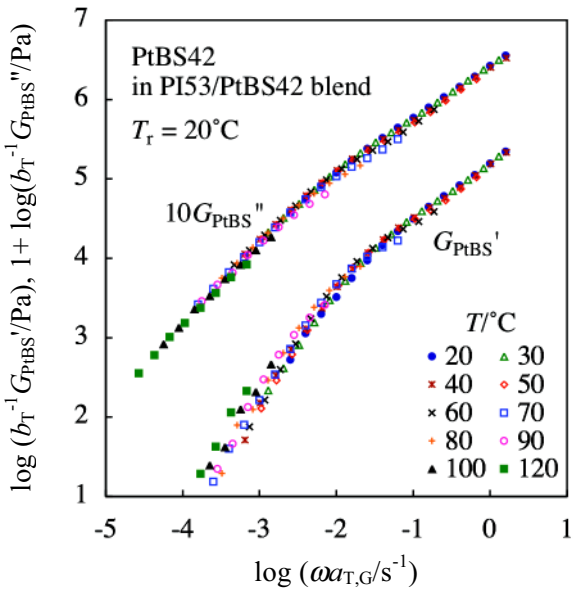

Fig. 7-15: Test of the time-temperature superposability for the viscoelastic modulus data of the PtBS42 chains in the PI53/PtBS42 blend. The reference temperature is T_r = 20°C. The data are reduced by the intensity factor, $b_T = T/T_r$ (with T_r = 293 K), and superposed by utilizing the low-ω G^{bld}_{PtBS}" data as a guide. The G^{bld}_{PtBS}" data are multiplied by a factor of 10 to avoid heavy overlapping with the G^{bld}_{PtBS}' data.

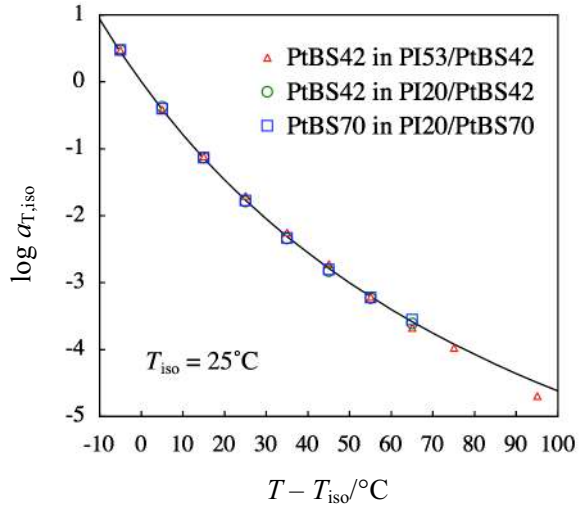

Fig. 7-16: Shift factor $a_{T,iso}$ defined with respect to the iso-τ_s temperature T_{iso} = 25°C for PtBS in the PI53/PtBS42 (Figure 7-15), PI20/PtBS42, and PI20/PtBS70 blends. All these blends have the same PI content, w_{PI} = 55.7 wt%. The solid curve indicates the WLF equation for PtBS bulk with $T_{r,bulk}$ = 180°C.

Chapter 8 SUMMARY AND CONCLUSIONS

This thesis attempts to discuss two fundamental questions from experimental viewpoint; (1) how does the blending modify the dynamic behavior, in particularty the terminal dynamics, of each component in a miscible polymer blend, and (2) what is the role of the junction point in a diblock copolymer. Obviously, the effects of blending and/or the junction can be magnified if two components have a large contrast in their basic dynamic parameters, *e.g.*, the segmental friction of their Rouse segments, ζ_s, and the entanglement mesh size, a.

From this point of view, miscible blends and a disordered diblock copolymer composed of polyisoprene (PI) and poly(*p-tert* butyl styrene) (PtBS) were chosen as model systems, since bulk PI and PtBS have a large contrast on the glass transition temperature, T_g^{bulk}, and the entanglement mesh size, a^{bulk}. The blending should change the local environment for each component to modify these parameters and affect the component dynamics. This thesis is devoted to the understanding of this effect in the PI/PtBS blends as well as the junction effect in the disordered PI-PtBS diblock copolymer. The principal results and conclusions are summarized below.

Chapter 3 analyzed the linear visocelasitic mode distribution of bulk PI and PtBS samples. The contribution of the glassy and Rouse fluctuation modes were subtracted from the complex modulus (G^*) data to evaluate the modulus G_{ent}^* exclusively reflecting the entanglement relaxation. It turned out that the terminal mode distribution of G_{ent}^* and the corresponding compliance J_{ent} are rather insensitive to M and agree with those of high-M chains in a range of M near the onset of entanglement.

Chapter 4 was devoted for a test of the mixing rule of entanglement length, a, and of the entanglement dynamics of well-entangled high-M PI and PtBS chains in the blends. The PI and PtBS were the fast and slow components, and the dynamics of these chains was found to change significantly with temperature T. At high T, the blend exhibited two-step entanglement plateau of the storage modulus $G'(\omega)$, and the plateaus at high and low angular frequencies (ω) were attributed, with the aid of the dielectric data, to the entanglement among all component chains and that between the PtBS chains, respectively. The entanglement length a characterizing the high-ω plateau was well described by a simple mixing rule proposed in this thesis, $a = n_{PI} a_{PI}^{bulk} + n_{PtBS} a_{PtBS}^{bulk}$, with n_X being the number fraction of Kuhn segments of the components X (= PI, PtBS). This mixing rule is consistent with the current molecular picture relating the entanglement density to the packing length p ($\cong 1/20a$). The validity of the mixing rule was confirmed also from the rheo-optical data. At low T, the blend exhibited the Rouse-like power-law behavior of storage and loss moduli, $G' = G'' \propto \omega^{1/2}$, in the range of ω where the high-ω plateau was supposed to emerge. This

lack of the high-ω plateau was attributed to retardation of the Rouse equilibration of the PI chain over the entanglement length a due to the hindrance from the slow PtBS chains: The PI and PtBS chains appeared to be equilibrated *cooperatively/simultaneously* at a rate essentially determined by PtBS. This molecular picture was further confirmed by the rheo-optical data.

Chapters 5 and 6 were devoted to investigation of the relationship(s) between the frictional/dimensional contrast of the PI and PtBS chains and their thermo-rheological behavior in the blends. For most of the blends studied, PI was the fast component and its terminal relaxation exhibited the thermo-rheological complexity being related to the frictional heterogeneity due to slow PtBS chains that was quenched in the time scale of the global motion of PI. Some PI chains (minority) were located in a PtBS-rich region to feel a higher friction compared to the other PI chains (majority). A difference of the relaxation times of the minority and majority changed with T, which naturally resulted in the thermo-rheological complexity of the whole ensemble of the PI chains. The frictional heterogeneity for the global motion of the PI chains became less significant on reduction of the dynamic contrast between the PI and PtBS chains through increases of the PI content (Chapter 5) and/or the PI chain dimesion (Chapter 6). In contrast, the PtBS chains exhibited thermo-rheological simple behavior when their relaxation was much slower than the PI relaxation, possibly because the fast motion of PI had smeared the dynamic heterogeneity to allow all PtBS chains to feel a uniform frictional environment. The relaxation of either PI or PtBS chains in the blends was slower than that in respective iso-frictional non-entangled states. The delay of the PI relaxation in the blends was related to the Rouse equilibration of PI over the entanglement mesh size hindered by the slower PtBS chains (as discussed in Chapter 4). The delay of the PtBS relaxation was related to the topological constraint from the PI chains: The PtBS chains exhibited no ordinary entanglement relaxation associated with a plateau of the storage modulus. Instead, the PtBS chains exhibited Rouse/Zimm-like relaxation that was slower, by a factor of about one decade, than the relaxation in the iso-frictional bulk state. This retarded Rouse/Zimm-like relaxation of the PtBS chains was attributable to *pseudo-constraint release* mechanism activated by the global motion of the PI chains entangling with the PtBS chains.

Chapter 7 was devoted to study of the junction effect on the dynamics of a PI-PtBS diblock copolymer in the disordered state. The dielectric data of the PI block exhibited prominent thermo-rheological complexity. Since the PI and PtBS blocks behaved as the fast and slow blocks at low T while these blocks exhibited equally fast motion at high T, this complexity was related partly to the dynamic frictional heterogeneity for the PI block resulting from this motional difference of the blocks. However, it turned out that the complexity was more importantly related to the connectivity (junction) between the PI and PtBS blocks: Namely, the PI block essentially behaved as a tethered

chains at low T (where the slow PtBS block effectively anchored the PI block) while the two blocks behaved as portions of a free linear chain at high T (where this anchoring effect was weakened). This change in the motional mode of the PI block dominated the thermo-rheological complexity of the PI block, as confirmed from comparison of the dielectric data of the copolymer and equivalent PI chains. These results lent support to the transition of the dynamic behavior of the PI block due to the motional contrast and connectivity of the PI and PtBS blocks.

List of Publications

I. *Publications Included in This Thesis*

1. "Component Dynamics in Polyisoprene/Poly(*4-tert*-butylstyrene) Miscible Blends"
   Chen, Q.; Matsumiya, Y.; Masubuchi, Y.; Watanabe, H.; and Inoue, T.
   Macromolecules **2008**, 41, 8694-8711.

2. "Viscoelastic Mode Distribution of Moderately Entangled Linear Polymers"
   Chen, Q.; Uno, A.; Matsumiya, Y.; and Watanabe, H.
   Nihon Reoroji Gakkaishi (J. Soc. Rheol. Japan) **2010**, 38, 187-193.

3. "Rheological Characterization of Polymeric Liquids"
   Watanabe, H.; Matsumiya, Y.; Chen, Q.; and Yu, W.
   Comprehensive Polymer Science, 2nd Ed., edited by Krzysztof Matyjaszewski and Martin Möller, Elsevier, Oxford, UK, **2011**, in press (Chapter 2).

4. "Dynamics of Polyisoprene-Poly(*p-tert*-butyl styrene) Diblock Copolymer in Disordered State"
   Chen, Q.; Matsumiya, Y.; Masubuchi, Y.; Watanabe, H., and Inoue, T.
   Macromolecules, submitted.

5. "Entanglement Dynamics in Miscible Polyisoprene/Poly(*p-tert*-butyl styrene) Blends"
   Watanabe, H.; Chen, Q.; Kawasaki, Y.; Matsumiya, Y.; Inoue, T.; and Urakawa, O.
   Macromolecules, submitted.

6. "Dynamics in Miscible Blends of Polyisoprene and Poly(*p-tert*-butyl styrene): Thermo-Rheological Behavior of Components"
   Chen, Q.; Matsumiya, Y.; Hiramoto, K.; and Watanabe, H.
   Polymer Journal, **2011**, in press.

II. *Other Publications*

1. "Nonlinear Behavior of a Drop undergoing Large Amplitude Oscillatory Shear Flow"
   Chen, Q.; Yu, W.; and Zhou, C.X.
   Chinese Journal of Theoretical and Applied Mechanics **2007**, 39, 528-532.

2. "Rheological Properties of Immiscible Polymer Blends Under Parallel Superposition Shear Flow"
   Chen, Q.; Yu, W.; and Zhou, C.X.
   Journal of Polymer Science Part B-Polymer Physics **2008**, 46, 431-440.

3. "Transient Stresses and Morphology of Immiscible Polymer Blends under varying Shear Flow"
   Chen, Q.; Yu, W.; and Zhou, C.X.
   Colloids and Surfaces A: Physicochemical and Engineering Aspects **2008**, 326, 175-183.

Acknowledgements

This thesis is based on the study carried out under the direction of Professor Hiroshi Watanabe, Institute for Chemical Research, Kyoto University, from 2007 to 2010.

The auhor wishes to express his sincere gratitude to Professor Hirohsi Watanabe, for his patient guidance, invaluable advice, and constant encouragement throughout this work.

The author also wishes to express his thanks to Professor Yumi Matsumiya, Institute for Chemical Research, Kyoto University, for her helpful advice and collaboration.

The author is sincerely grateful to Professor Tadashi Inoue, Department of Macromolecular Science, Osaka University, for his invaluable discussions and helpful advice, and Professor Yuichi Masubuchi, Institute for Chemical Research, Kyoto University, for his helpful suggestion and encouragement.

Thanks are also due to Mr. Kazushi Horio for his kind help and friendly cooperation, to Ms. Eri Mishima for her valuable collaboration, and to all members in Watanabe Lab for their friendship.

The author is grateful for the financial support from the Japan Society for Promotion of Science from 2009 to 2011.

Finally, the author thanks his wife, Ying, for her care and constant encouragement, and his sister and parents for their support.

Quan Chen